Measuring the Mass of the W Boson with the Last $3.7\,\mathrm{fb}^{-1}$ of Tevatron Data.

Michelle Brochmann

A dissertation
submitted in partial fulfillment of the
requirements for the degree of

Doctor of Philosophy

University of Washington

2017

Reading Committee:

Gordon Watts, Chair

Shih-Chieh Hsu

Marcel den Nijs

Program Authorized to Offer Degree:
Department of Physics

University of Washington

Abstract

Measuring the Mass of the W Boson with the Last $3.7\,\mathrm{fb}^{-1}$ of Tevatron Data.

Michelle Brochmann

Chair of the Supervisory Committee:
Dr. Gordon Watts
Department of Physics

This thesis presents the results of an analysis of the $3.7\,\mathrm{fb}^{-1}$ of Tevatron proton-antiproton data collected with the DZero (D0) Detector at Fermilab during the "RunIIb34" period, with the goal of extracting an improved measurement of the W boson mass, which is currently measured to a precision of $\approx 20\,\mathrm{MeV}$. The measurement is performed on events with one W boson which decays to an electron and a neutrino. Using a template technique, the mass is measured from three distributions that are correlated with the W boson mass: the transverse electron momentum, p_T^e, the transverse W mass, m_T, and the neutrino momentum, which appears as missing transverse energy, $\not{E}_T$. A test measurement using this technique is successfully performed on a mock dataset generated with a Monte Carlo simulation. In the data, we find unexpected azimuthally dependent inconsistencies between the early and late parts of the data taking period. Implications for the completion of the data measurement are discussed.

TABLE OF CONTENTS

LIST OF FIGURES

LIST OF TABLES

ACKNOWLEDGMENTS

Many thanks to my advisor, Dr. Gordon Watts for his patience and guidance. Thank you also to the members of the D0 W mass group, especially Jan Stark, Jakub Cúth, Jenny Holzbauer, Rafael Lopes de Sá, and Hengne Li. Thank you to my family, friends, and teachers for supporting me throughout the years.

DEDICATION

To my mom.

Chapter 1

INTRODUCTION

The purpose of this chapter is to place the measurement of the W boson mass in the context of theoretical and experimental particle physics. First we give a brief introduction to the Standard Model with an overview of the fundamental particles and their interactions, as well as the quantities of interest for scientific measurement and theoretical prediction. We then describe the particle interactions in the context of field theory, with particular attention to the weak interaction and the role of symmetry breaking via the Higgs boson in the manifestation of the vector boson masses. Then we will present the equations which describe the expected interaction rates of the W boson, and distributions of measureable observables, at the Tevatron. Finally, we will discuss the motivation for this analysis, and present an overview of the previous calculations and measurements of the W boson mass.

1.1 The Particles and Interactions of the Standard Model

The Standard Model describes the interactions of the smallest known indivisible particles in nature. There are two main types of particles, the matter particles, or “fermions”, and the interaction particles, or “bosons”, which mediate the transmission of conserved quantities between the matter particles. These particles are catalogued, with their charges, electromagnetic spins, and masses, in Figure 1.1.

The fermions consist of the quarks and leptons. The quarks, which have fractional charges (relative to the charge of the electron, which defines a unit of charge), are depicted in the violet boxes. The lightest and most common, and therefore considered to be part of the “first generation” of fermions, are the up and down quark, which make up the protons and neutrons which form the nuclei of atoms, which in turn make up most of the physical

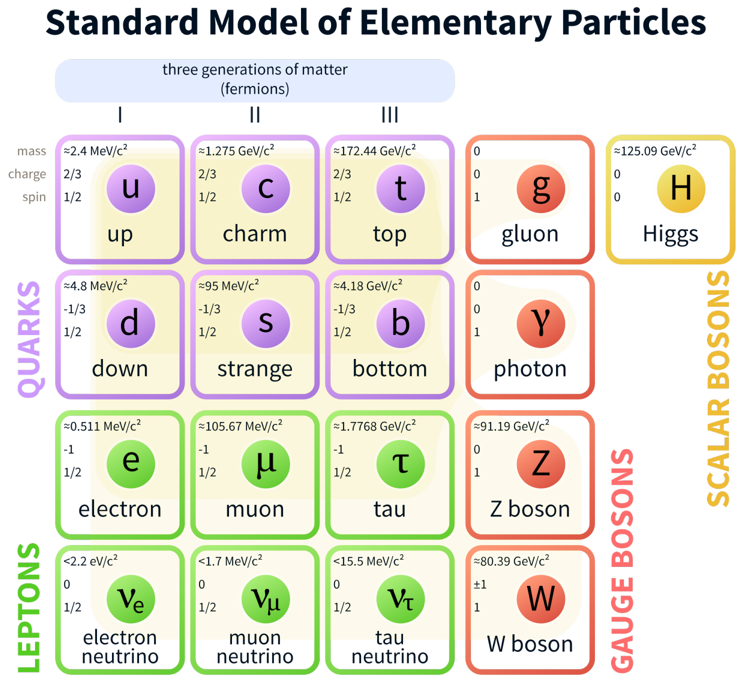

Figure 1.1: The known fundamental particles of the Standard Model.

objects we see in every day life. The "second generation" quarks are the charm and strange quarks. The "third generation" quarks, the heaviest quarks we know of, are the top and bottom quarks. The massive leptons are also ranked according to mass in generations, with the electron being the lightest, the muon being heavier, and the tau being the heaviest. These three leptons each have charge -1 (negative by convention). Each of the massive leptons have a (nearly) massless neutrino partner, simply called the electron neutrino, the muon neutrino, and the tau neutrino. The neutrinos are chargeless.

There are four gauge bosons which mediate the interactions between the particles. (The reason for the "gauge" label will be explained in Section 1.2.) The most well known gauge boson is the massless photon, the "light" particle, which transmits the electromagnetic force. Only electromagnetically charged particles interact via the electromagnetic interaction, i.e. the quarks, the massive leptons, and the charged gauge bosons (described next) can

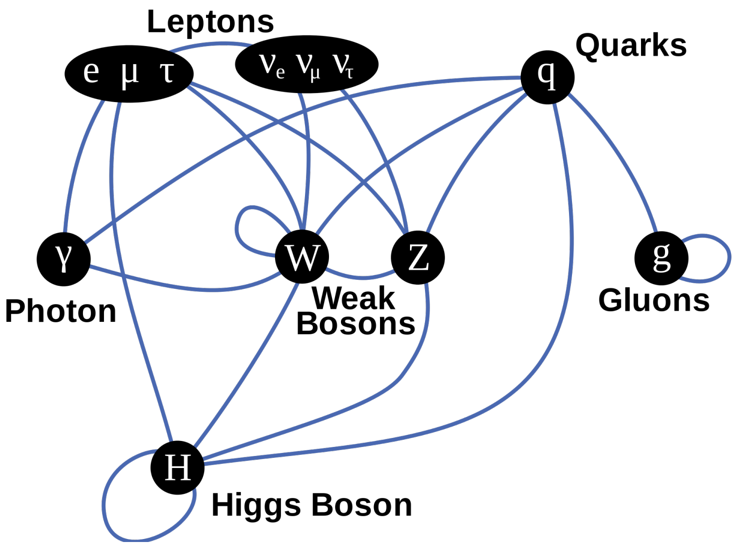

Figure 1.2: Connecting lines indicate allowed interactions between the fundamental particles.

exchange photons. The weak interaction is transmitted by the massive weak gauge bosons - the charged $W^{\pm}$ and the neutral Z. All fermions can interact via the weak force. The electromagnetic and weak interactions are unified in the "electroweak" interaction before symmetry breaking (discussed in Section 1.2). The final type of gauge boson is the massless gluon which transmits the strong force, for which the conserved charge is "color". There are three types of conserved "color" charge, red, green, and blue. Only particles with color charge can interact via the strong force, so quarks can exchange gluons, and gluons, which also have color charge, can self-interact.

Finally, the scalar Higgs boson is responsible, via electroweak symmetry breaking, for the masses of the weak bosons, and for part of the mass of the leptons and quarks, as will be described in Section 1.2.All massive particles interact via the Higgs field. A schematic diagram of the particle interactions, with connecting lines indicating whether particles can interact with each other, is shown in Figure 1.2.

The mass (or masslessness) of a non self-interacting force transmitter indicates the range of the interaction. The $W\pm$ and Z particles, which transmit the weak force, are massive, corresponding to the short range of the weak interaction, $\approx 10^{-17} - 10^{-16}\,\mathrm{m}$. In contrast, electromagnetic force is transmitted by massless photons and hence has infinite range. In principle, the color force of massless gluons also has infinite range, however, the incredible strength of this force combined with the fact that gluons self-interact results in an effective range of the color force of $10^{-15}\,\mathrm{m}$.

The Standard Model is a unified description of three of the four fundamental forces: the weak, electromagnetic, and strong interactions. It unfortunately does not describe gravity. It describes the relationships between the masses of the particles and the characteristics of their interactions. These characteristics include collison cross sections, decay rates, branching ratios, and the kinematics of these interactions. The relationships prescribed by the Standard Model can be derived using field theory.

1.2 Field Theory

In the classical limit of field theory, the evolution of a system is governed by the principle of least action. This principle states that the expected path of a system is the one that minimizes the "action", a quantity which describes the difference between the kinetic and potential energy of the system, integrated over time:

$$S = \int L dt = \int (T - V) dt = \int \mathcal{L}(\phi, \partial_\mu \phi) d^4x \tag{1.1}$$

where the first equality states that the action S is the integral of, L, the Lagrangian, over t, time, the second equality substitutes the difference between the kinetic energy, T, and the potential energy, V, for L, and the last equality converts the one-dimensional integral into a four-dimensional space-time integral over $\mathcal{L}$, the Lagrangian density as a function of one, or more, fields, $\phi_{(i)}$, and the derivative of the field(s), $\partial_\mu \phi_{(i)}$. The interactions of a system of particles are governed by the form of the terms in $\mathcal{L}(\phi, \partial_\mu \phi)$.

By minimizing the action over an infinitesimal length of time, δt, we can derive the Euler-Lagrange equations of motion:

$$\partial_\mu \left(\frac{\partial \mathcal{L}}{\partial(\partial_\mu \phi)} \right) - \frac{\partial \mathcal{L}}{\partial \phi} = 0 \tag{1.2}$$

At the quantum level of field theory (QFT), the system follows all possible paths that lead from the initial to the final state, even paths which do not conserve energy and momentum. (The measured initial and final states must still conserve energy and momentum.) The probability for the initial state to transition to the final state is the proportional to the integral of the action over all possible paths. This is the reason "off-shell" interactions, such as beta decay, in which a virtual W boson is emitted from a transitioning quark and decays into an electron and neutrino with combined energy that is only a fraction of the W mass, can occur. The multiplicity of all the paths leading from an intial to a final state is proportional to the probability of that transition. This governs cross sections for particle interactions and decay rates.

If the Lagrangian of a system is unchanged under a transformation of the system, it is symmetric under the transformation. There is a conserved quantity associated with all continuous symmetries (i.e. symmetries under continuous transformations). The Standard Model Lagrangian is symmetric under Lorentz transformations, which include translations, rotations, and boosts (shifts to a moving reference frame). These symmetries correspond, respectively, to conservation of momentum, angular momentum, and energy.

The Standard Model Lagrangian is also symmetric under CPT, meaning that it is unchanged when it is operated on by all three of the following discrete transformations together: charge conjugation, parity, and time reversal. Individual parts of the SM Lagrangian are also symmetric under subsets of CPT. Electromagnetism and the strong force are invariant uncer C, P, and T individually. The weak force violates all three symmetries.

Another kind of symmetry that we can have is a "local gauge symmetry". This is the invariance of a Lagrangian under a space and time dependent transformation governed by a Lie group applied to the field(s) of the Lagrangian.

1.2.1 An example of symmetry breaking: QED from the U(1) symmetry

As an example, we will examine the Lagrangian of a free fermion. By requiring that the Lagrangian is invariant under U(1) local gauge transformations, we will derive the

Lagrangian of quantum electrodynamics (QED).

$$\mathcal{L} = \bar{\psi}(x)(i\partial\!\!\!/ - m)\psi(x) \tag{1.3}$$

where $\bar{\psi}(x)$ is the field of the anti-fermion, $\psi(x)$ is the field of the fermion, and $\partial\!\!\!/$ is $\gamma^\mu \partial_\mu$, where γ^μ are the 4x4 Dirac gamma matrices

$$\gamma^\mu = \begin{pmatrix} 0 & \sigma^\mu \\ -\sigma^\mu & 0 \end{pmatrix} \tag{1.4}$$

where σ^μ are Pauli spin matrices. Having U(1) symmetry means the Lagrangian is invariant under a complex rotation of the wave function, with local phase $\alpha(x)$

$$\psi(x) \to \psi'(x) = e^{-i\alpha(x)}\psi(x) \;\text{ and }\; \bar{\psi}(x) \to \bar{\psi}'(x) = e^{i\alpha(x)}\bar{\psi}(x) \tag{1.5}$$

The mass term of the Lagrangian is clearly invariant under this transformation, however, in its current form, the derivative term is not - it "breaks" the symmetry. Therefore, we must change to a gauge covariant derivative, $D_\mu = \partial_\mu + ieA_\mu(x)$, where e is the fermion charge and where the gauge field $A_\mu(x)$ is defined to transform under the rotation:

$$A_\mu(x) \to A'_\mu(x) = A_\mu(x) - \frac{1}{e}\partial_\mu \alpha(x) \tag{1.6}$$

When the field and the derivative transform according to these rules, the Lagrangian is invariant. The field A_μ is actually the electromagnetic potential which describes Maxwell's equations, and whose corresponding gauge boson is the photon. Its propagation is included via the gauge invariant term $F_{\mu\nu}Fe^{\mu\nu}$, where $F_{\mu\nu} = \partial_\mu A_\nu - \partial_\nu A_\mu$.

The final QED Lagrangian is then

$$\mathcal{L}_{\text{QED}} = \bar{\psi}(x)(iD\!\!\!\!/ - m)\psi(x) - \frac{1}{4}F_{\mu\nu}F^{\mu\nu} \tag{1.7}$$

A mass term for a field $A_\mu(x)$ would look like $mA_\mu A^\mu$, but there is no such term in the QED Lagrangian. This corresponds to the photon having no mass.

The Standard Model is a gauge theory based on the symmetry group

$$SU(3) \otimes SU(2) \otimes U(1) \tag{1.8}$$

where the $SU(3)$ symmetry describes the coupling of the color charge to the quarks and gluons, the $SU(2)$ symmetry describes the coupling of the weak isospin to left-handed fermions (and right-handed antifermions), and the $U(1)$ symmetry describes the coupling of the weak hypercharge to all fermions. The electromagnetic and weak interactions are unified under the $SU(2) \otimes U(1)$ symmetry as the electroweak interaction. The strong sector, which describes the interactions of quarks and gluons, the conserved charge is color, is invariant under $SU(3)$ transformations. It is relevant to this dissertation in the sense that it is responsible for the QCD background, and also in the sense that in the $p\bar{p}$ interactions, the strong force is involved in the collisions which break apart the protons and antprotons. Ultimately, however, the focus of this dissertation is the W boson, a mass eigenstate which results from symmetry breaking of the electroweak interaction by the scalar Higgs Field.

1.2.2 Electroweak theory

In the previous section, we introduced the concept of gauge symmetry breaking by adding a term to the Lagrangian, and restoring it by adding a new field via a gauge covariant derivative. In this section, we will explore the effect of adding a Higgs term to the electroweak Lagrangian.

We require the electroweak Lagrangian to be invariant under $SU(2)_T \times U(1)_Y$, in order to conserve the weak isospin, T, which appears in units of $\frac{1}{2}$ and the weak hypercharge, Y, which appears in units of $\frac{1}{3}$. These quantities are related to electrical charge, Q, which comes in units of 1 via $Y \equiv Q - T^3$.

Experimentally, we observe that $W^{\pm}$ bosons only decay to left-handed fermions and right-handed antifermions. Therefore we treat left-handed and right-handed particles differently. The fields of fermions and antifermions are described by four-component "bispinors":

$$\psi = \begin{pmatrix} \psi_1 \\ \psi_2 \\ \psi_3 \\ \psi_4 \end{pmatrix} = \begin{pmatrix} \phi \\ \chi \end{pmatrix} \quad \text{where } \phi = \begin{pmatrix} \phi_1 \\ \phi_2 \end{pmatrix} \quad \text{and } \chi = \begin{pmatrix} \chi_1 \\ \chi_2 \end{pmatrix} \tag{1.9}$$

where the "bi-spinor" is, by convention, to have the same handedness as its first spinor component.

Since the particles whose interactions we are investigating are, in general, not at rest, we must treat the spin in the context of the motion of the particles. Therefore, we work not with eigenstates of spin, but of chirality. Eigenstates of chirality are the relativistic limit of eigenstates of helicity. Helicity is spin projected onto momentum:

$$\lambda = \frac{1}{2}\frac{\vec{\sigma} \cdot \vec{p}}{|\vec{p}|} \tag{1.10}$$

and has eigenvalues of $\pm\frac{1}{2}$. Helicity is the only spin-dependent value that commutes with (i.e. has the same eigenstates as) the Hamiltonian, but, because it depends on the direction of motion[1], it is not Lorentz-invariant for massive particles. Chirality, on the other hand, does not commute with the Hamiltonian, but it is Lorentz invariant. Its eigenstates (which approach helicity eigenstates in the relativistic limit) are the eigenstates of $\gamma^5 = \gamma^0\gamma^1\gamma^2\gamma^3$, with eigenvalues of $+1$ (right-handed) and -1 (left-handed). We can project the ψ states into left-handed and right-handed components:

$$\psi_L = \frac{1}{2}(1-\gamma^5)\psi \tag{1.11}$$

$$\psi_R = \frac{1}{2}(1+\gamma^5)\psi \tag{1.12}$$

$$\bar{\psi}_L = \frac{1}{2}\bar{\psi}(1+\gamma^5) \tag{1.13}$$

$$\bar{\psi}_R = \frac{1}{2}\bar{\psi}(1-\gamma^5) \tag{1.14}$$

---

[1] i.e. it is susceptible to "spin-flipping"

The left-handed fermion fields are doublets of SU(2) weak isospin.

$$l_L = \begin{pmatrix} \nu_L^e \\ e^- \end{pmatrix}, \begin{pmatrix} \nu_L^\mu \\ \mu^- \end{pmatrix}, \begin{pmatrix} \nu_L^\tau \\ \tau^- \end{pmatrix} \tag{1.15}$$

$$q_L = \begin{pmatrix} u_L \\ d'_L \end{pmatrix}, \begin{pmatrix} c_L \\ s'_L \end{pmatrix}, \begin{pmatrix} t_L \\ b'_L \end{pmatrix} \tag{1.16}$$

The complex conjugates are the right-handed antifermion fields. The left-handed fermion and right-handed antifermion fields transform under $SU(2) \times U(1)$ according to

$$f_L \;\; \rightarrow \;\; e^{-i(\xi^0 + \xi^a \tau_a)} f_L \;\text{ and }\; \bar{f}_L \rightarrow e^{i(\xi^0 + \xi^a \tau_a)} \bar{f}_L \tag{1.17}$$

where the τ_a are the Pauli spin matrices.

The right-handed fermions are singlets:

$$l_R = e_R, \mu_R, \tau_R \tag{1.18}$$

$$q_R = u_R, d_R, c_R, s_R, b_R, t_R \tag{1.19}$$

and transform only under $U(1)$:

$$f_R \;\; \rightarrow \;\; e^{-i\xi^0} f_R \;\text{ and }\; \bar{f}_R \rightarrow e^{i\xi^0} \bar{f}_R \tag{1.20}$$

We do not include right-handed neutrinos or left-handed antineutrinos in our theory because we have not yet found compelling experimental evidence that they exist.

For the charged leptons, the mass eigenstates are the same as the weak isospin eigenstates. This is not true for neutrinos, but we will not discuss neutrino mixing here. The quark mass eigenstates are different from weak isospin eigenstates. The weak isospin eigenstates for quarks are related to the quark mass eigenstates ("mixed") by the Cabibbo-Kobayashi-Masakawa (CKM) matrix:

$$\begin{pmatrix} d' \\ s' \\ b' \end{pmatrix} = \begin{pmatrix} V_{ud} & V_{us} & V_{ub} \\ V_{cd} & V_{cs} & V_{cb} \\ V_{td} & V_{ts} & V_{tb} \end{pmatrix} \begin{pmatrix} d \\ s \\ b \end{pmatrix} \approx \begin{pmatrix} \cos\theta_C & \sin\theta_C & 0 \\ -\sin\theta_C & \cos\theta_C & 0 \\ 0 & 0 & 1 \end{pmatrix} \begin{pmatrix} d \\ s \\ b \end{pmatrix} \tag{1.21}$$

where $\theta_C = 13.1^\circ$ is the Cabibbo angle.

1.2.3 Electroweak Vector Gauge Bosons

W^1_μ, W^2_μ, W^3_μ, and B_μ are the massless gauge boson fields. They are the eigenstates of weak isospin before they have been "mixed" by the Higgs boson. The W^a_μ states couple to the left-handed isospin current,

$$J^a_\mu = \frac{1}{2}\bar{\psi}_L \gamma_\mu \tau_a \psi_L \tag{1.22}$$

where τ_a are the Pauli spin matrices, ψ_L is the isospin doublet, and $\bar{\psi}_L = \psi^\dagger_L \gamma^0$ is the adjoint of ψ_L. B_μ couples to the weak hypercharge current, which includes both chiralities:

$$J^Y_\mu = Y\bar{\psi}\gamma_\mu\psi \tag{1.23}$$

The leptonic Lagrangian is

$$\mathcal{L}_{\text{EW}} = \bar{\psi}_L \gamma^\mu \mathcal{D} \psi_L + \bar{\psi}_R \gamma^\mu \mathcal{D}_R \psi_R - \frac{1}{4} W^a_{\mu\nu} W^{a\mu\nu} - \frac{1}{4} B_{\mu\nu} B^{\mu\nu} \tag{1.24}$$

where

$$\begin{aligned} \mathcal{D} &= \left(i\partial_\mu - \frac{g}{2}\tau^a W^a_\mu - g' Y_W B_\mu\right) && (1.25) \\ \mathcal{D}_R &= \left(i\partial_\mu - g' Y_W B_\mu\right) && (1.26) \end{aligned}$$

are the gauge covariant derivatives for the left- and right-handed leptonic fields, and

$$\begin{aligned} W^a_{\mu\nu} &= \partial_\mu W^a_\nu - \partial_\nu W^a_\mu + g\epsilon^{abc} W^b_\mu W^b_\nu && (1.27) \\ B_{\mu\nu} &= \partial_\mu B_\nu - \partial_\nu B_\mu && (1.28) \end{aligned}$$

are the terms which describe the propagation of the fields (analogous to Maxwell's equations for electromagnetic fields), and g (g') is the coupling constant between the weak isospin current and the W (B) field.

For the Lagrangian to be invariant under a $SU(2) \times U(1)$ gauge transformation of the lepton fields, the W triplet must transform under $U(1)$ and $SU(2)$ via

$$\begin{aligned} W^a_\mu &\rightarrow W^a_\mu - \frac{1}{e}\partial_\mu \xi^0 && (1.29) \\ W^a_\mu &\rightarrow W^a_\mu + g\epsilon_{abc} W^b_\mu \xi^c + \partial_m u \xi^a && (1.30) \end{aligned}$$

while the B singlet must transform under $U(1)$ via

$$B_\mu \rightarrow B_\mu - \frac{1}{e}\partial_\mu \xi^0 \tag{1.31}$$

Note that this Lagrangian contains no mass terms for any of the fields; no gauge covariant derivative has been developed which would allow it to contain mass terms and still be invariant under a gauge transformation. However, experimentally we observe massive gauge bosons. These arise through spontaneous symmetry breaking by the Higgs field, an isospin doublet of complex scalar fields

$$\phi = \begin{pmatrix} \phi_1 \\ \phi_2 \end{pmatrix}, \quad \phi^\dagger = (\phi_1^\star, \phi_2^\star) \tag{1.32}$$

The U(1) transformation adds a phase to both members of the doublet while the SU(2) transformation rotates the field between components of the isospin doublet. As a scalar field, it is permitted to have a mass without costing the Lagrangian its gauge symmetry.

The Higgs field is included in the Lagrangian via the term

$$\mathcal{L}_{\text{Higgs}} = |\mathcal{D}\phi|^2 - V(\phi) \tag{1.33}$$

where we assign the hypercharge operator (included in $\mathcal{D}$) on the ϕ doublet as $Y_\phi = +1$, and the electric charge operator (also included in $\mathcal{D}$) on the ϕ doublet as $Q = \frac{1}{2}(\sigma + Y) = \begin{pmatrix} 1 & 0 \\ 0 & 0 \end{pmatrix}$. The eigenmodes of these operators imply two charged ($Q = \pm 1$) and two scalar bosons.

$$V(\phi) = -\mu^2 \phi^\dagger \phi + \frac{\lambda}{2}\left(\phi^\dagger \phi\right)^2 \tag{1.34}$$

We require $\mu^2 > 0$, in order for the Higgs field to have a non-zero expectation value: $v = \sqrt{\frac{\mu^2}{\lambda}}$. The vacuum state of ϕ, found by minimizing $V(\phi)$, can be written as

$$\langle \phi \rangle = \frac{1}{\sqrt{2}} \begin{pmatrix} 0 \\ v \end{pmatrix} \tag{1.35}$$

With the addition of the Higgs term, the Lagrangian can be re-written in a form that contains mass terms.

The covariant derivative can be written in terms of the mixed fields as

$$\begin{aligned} D_\mu &= \partial_\mu + i\frac{g}{\sqrt{2}}(W_\mu^+\tau^+ + W_\mu^-\tau^-) && (1.36) \\ &+i\frac{1}{\sqrt{g^2+g^{'2}}}Z_\mu\left(g^2\tau^3 - g^{'2}Y\right) + ieA_\mu(\tau^3+Y) && (1.37) \end{aligned}$$

where $e = g\sin\theta_W = g'\cos\theta_W$ and $\tau^\pm = \frac{1}{2}(\sigma^1 \pm i\sigma^2)$, τ^3 and Y are the operators for isospin and weak hypercharge.

The interaction terms of the Lagrangian can be written in terms of the mixed fields as

$$\begin{aligned} \mathcal{L} &= -eQ\bar{\psi}\gamma^\mu\psi A_\mu - \frac{g}{2\sqrt{2}}\bar{\psi}_L\gamma^\mu(\tau^+W_\mu^+ + \tau^-W_\mu^-)\psi_L && (1.38) \\ &-\frac{g}{2\cos\theta_W}\bar{\psi}\gamma^\mu(g_V - g_A\gamma^5)\psi Z_\mu \end{aligned}$$

where g_V and g_A are the vector and axial-vector couplings:

$$\begin{aligned} g_V^f &= \tau_f^3 - 2Q_F\sin^2\theta_W && (1.39) \\ g_A^f &= \tau_f^3 && (1.40) \end{aligned}$$

which describe the degree to which the Z boson interacts differently with right- and left-handed particles.

Note that the $W^\pm$, like the W^a, couple only to left-handed currents. Note also that Z couples to left-handed and right-handed currents with different strengths.

$$\mathcal{L}_{\text{EW}} = \mathcal{L}_{\text{leptons}} + \mathcal{L}_{\text{gauge}} \qquad (1.41)$$

The gauge Lagrangian is

$$\mathcal{L}_{\text{gauge}} = -\frac{1}{4}F_{\mu\nu}^l F^{l,\mu\nu} - \frac{1}{4}f_{\mu\nu}f^{\mu\nu} \qquad (1.42)$$

where

$$F^l_{\mu\nu} = \partial_\mu W^l_\nu - \partial_\nu W^l_\mu - g\epsilon^{lmn} W^m_\mu W^n_\nu \tag{1.43}$$

$$f^l_{\mu\nu} = \partial_\mu B_\nu - \partial_\nu B_\mu \tag{1.44}$$

are the non-Abelian and Abelian field strength tensors.

The leptonic and gauge Lagrangians, and hence their sum, are Lorentz invariant under the transformation of two distinct local gauge symmetry groups: the non-Abelian $SU(2)_L$ of weak isospin and the Abelian $U(1)_Y$ of weak hypercharge.

The Yukawa term is the interaction term between the fermions and the Higgs field which breaks the chiral symmetry and provides the lepton masses:

$$\mathcal{L}_{\text{Yukawa}} = -G_e \left[\bar{\psi}_R \phi^\dagger \psi_L + \bar{\psi}_L \phi \psi_R\right] \tag{1.45}$$

where the Yukawa constant G_e is arbitrary, i.e. unconstrained by the symmetries.

We find from the form of the rewritten Lagrangian that there are now three massive gauge bosons: the charged W bosons and the neutral Z boson. We also find the massless, chargeless, photon.

The vacuum state of the Higgs field has broken the electroweak symmetry of the Lagrangian. The Lagrangian that includes the Higgs term is gauge invariant under the group $U(1)$ only, but now it includes massive bosons (and leptons). The four bosons form mass eigenstates which we call $W^\pm_\mu$, Z_μ, and A_μ. These physical states are related to the eigenstates of the $SU(2) \otimes U(1)$ gauge group, W^a_μ and B_μ, where $a \in [1, 2, 3]$, via

$$W^\pm_\mu = \frac{1}{\sqrt{2}} \left(W^1_\mu \pm i W^2_\mu\right) \tag{1.46}$$

and

$$\begin{pmatrix} Z_\mu \\ A_\mu \end{pmatrix} = \begin{pmatrix} \cos\theta_W & \sin\theta_W \\ -\sin\theta_W & \cos\theta \end{pmatrix} \begin{pmatrix} W^3_\mu \\ B_\mu \end{pmatrix} \tag{1.47}$$

where θ_W is the weak mixing angle:

$$\cos\theta_W = \frac{g}{\sqrt{g^2 + g'^2}} \quad \text{or} \quad \sin\theta_W = \frac{g'}{\sqrt{g^2 + g'^2}} \tag{1.48}$$

At tree level,

$$\cos\theta_W = \frac{M_W}{M_Z} \tag{1.49}$$

where M_W and M_Z are the masses of the physical W and Z bosons. At tree level, we can also say

$$M_W = \frac{1}{2}vg \tag{1.50}$$

$$M_Z = \frac{v}{2}\sqrt{g^2 + g'^2} \tag{1.51}$$

The fermions also acquire mass from the Higgs field,

$$m_f = \frac{\kappa_f v}{\sqrt{2}} \tag{1.52}$$

where the κ_f must be determined experimentally. At tree level, the weak mixing angle[2] relates the masses of the W and Z bosons

$$\sin^2\theta_W = 1 - \left(\frac{M_W}{M_Z}\right)^2 \approx 0.226 \tag{1.53}$$

These relationships allow the tree-level masses of the W and Z bosons to be determined in terms of three experimentally determined quantities: the fine structure constant, $\alpha = \frac{e^2}{4\pi} = \frac{1}{137.04}$, the Fermi coupling constant, $G_F = 1.66 \times 10^{-5}\ \mathrm{GeV}^{-2}$, and the weak mixing angle, θ_W.

1.2.4 The W Mass from the Muon Decay Time

The determination of the true masses requires renormalizing the Standard Model Lagrangian, which is beyond the scope of this dissertation. We will only briefly describe how this process adds radiative corrections which depend on the Higgs and top quark masses, which makes the value of the W mass, in addition to being sensitive to the mass of the Z boson and the electric charge-coupling, sensitive to the Higgs and top quark masses (in addition to dependencies of higher order corrections). In the “old Fermi four-fermion theory”,

---

[2] θ_W can also be defined as a function of higher orders in the calculation

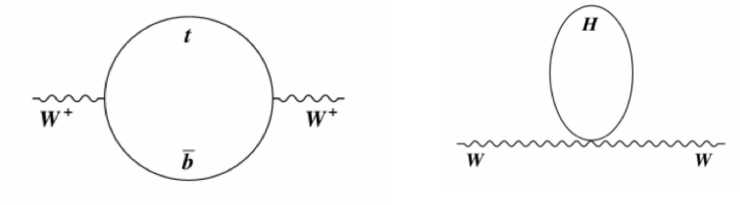

Figure 1.3: The Feynman diagrams for the leading contribution to the W mass from the top quark (left, plus charge conjugate) and the Higgs boson (right).

which is the effective theory of the electroweak fermion interaction, the muon decay time is related to other observables of the Standard Model via

$$\tau_\mu^{-1} = \frac{G_F^2 m_\mu^5}{192\pi^3} F\left(\frac{m_e^2}{m_\mu^2}\right)\left(1 + \frac{3m_\mu^2}{5M_W^2}\right)(1 + \Delta q_{\text{QED}}) \tag{1.54}$$

where[3]

$$F(x) = 1 - 8x - 12x^2 \ln x + 8x^3 - x^4 \tag{1.55}$$

and q_{QED} contains QED corrections only,

An expression for calculating the W mass from the other quantities can be derived by calculating the equivalent expression for the muon decay time in the Standard Model and comparing it to the equation from the effective field theory, which results in the following relationship:

$$M_W\left(1 - M_W^2/M_Z^2\right) = \frac{\pi\alpha}{\sqrt{2}G_F}(1 + \Delta r) \tag{1.56}$$

where $\alpha = e^2/4\pi$ is the fine structure constant, and Δr contains the full radiative corrections (including those in Figure 1.3). The full radiative corrections have been calculated to two-loop order[31], and the fermionic corrections have been calculated to four-loop order[16].

---

[3] $\frac{3m_\mu^2}{5M_W^2}$ comes from the W propagator and not the Fermi theory. The numerical effect is negligible (even considering current precision of G_F).

1.2.5 Quantum Chromodynamics - a very Brief Overview

Quantum Chromodynamics (QCD) is a theory governed by Lie group SU(3). It is relevant to this experiment in the sense that it governs the distribution of the vector boson momentum. It is also used to predict the QCD background. QCD describes the strong force interaction via the conserved color charge between the gluons and quarks. We will not go into great detail in this dissertation, but simply state the form of the Lagrangian for completeness:

$$\mathcal{L} = \bar{q}(i\gamma^{\mu} D_{\mu} - m)q - \frac{1}{4} G^{a}_{\mu\nu} G^{a\mu\nu} \tag{1.57}$$

where $D_{\mu} = \partial_{\mu} + i g_s T_a G^{a}_{\mu}$ is the covariant derivative, G^{a}_{μ} is the gluon field, T_a is the generator of the SU(3) Gauge Group, g_s is the QCD coupling, and f_{abc} defines the structure of the gauge group via

$$[T_a, T_b] = i f_{abc} T_c \tag{1.58}$$

The term

$$G^{a}_{\mu\nu} = \partial_{\mu} G^{a}_{\nu} - \partial_{\nu} G^{a}_{\mu} - g_s f_{abc} G^{b}_{\mu} G^{c}_{\mu} \tag{1.59}$$

describes the gluon propagation, analogous to the way Maxwell's Equations describe the propagation of the electromagnetic field.

The strong force grows with distance, unlike the electroweak force. Quarks are strongly held together by "color confinement". If a strong enough (or near enough) force manages to pull them apart, $q\bar{q}$ pairs will be created from vacuum to hadronize (i.e. form new particle states energetically which are energetically favorable due to minimizing gluon separation) with the newly separated quarks. At short distances, electroweak and strong force behave similarly, allowing for the electroweak decay ("asymptotic freedom").

1.3 Motivation

All of the fundamental particles of the standard model have now been measured, including the Higgs mass, and the model is now over-constrained, meaning that we can check its applicability to nature by testing whether it predicts the same relationships between

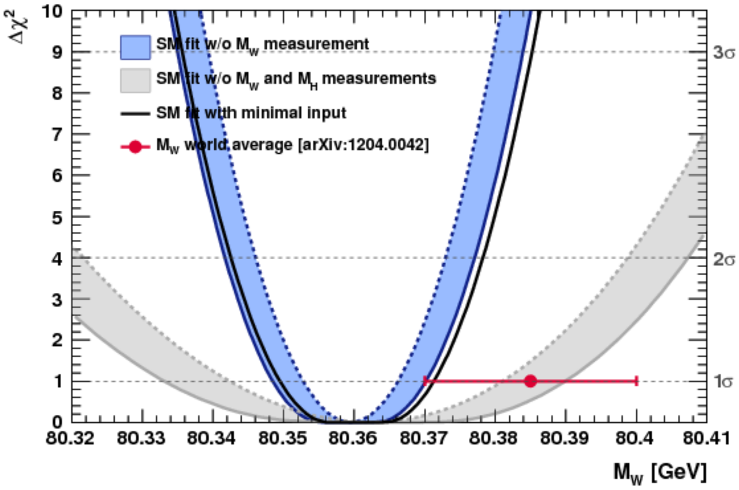

Figure 1.4: The predicted value of the W boson mass compared with the measured world average, based on a χ^2 method calculated from the pulls shown in Figure 1.6[17].

various quantities that have been measured experimentally. The W boson is unique in that the experimental uncertainty on its mass has not yet been decreased to be less than the uncertainty of the theoretical predicted value, meaning that increasing of the precision of its measurement will add to our understanding of the Standard Model's adequacy in describing nature as we observe it. There is a small tension between the predicted and experimentally measured values of the mass, as can be seen from the χ^2 dependency on the W mass in Figure 1.5 and the W and top quark mass in Figure 1.4. These χ^2 discriminants have been calculated from a sum of the squared pulls for the electroweak precision observables as shown in Figure 1.6. Given the current state of knowledge, the W mass is the observable whose measurement most effectively can further constrain the Standard Model, therefore continuing to decrease the experimental uncertainty on this physics quantity is a crucial part of continued validation of the Standard Model.

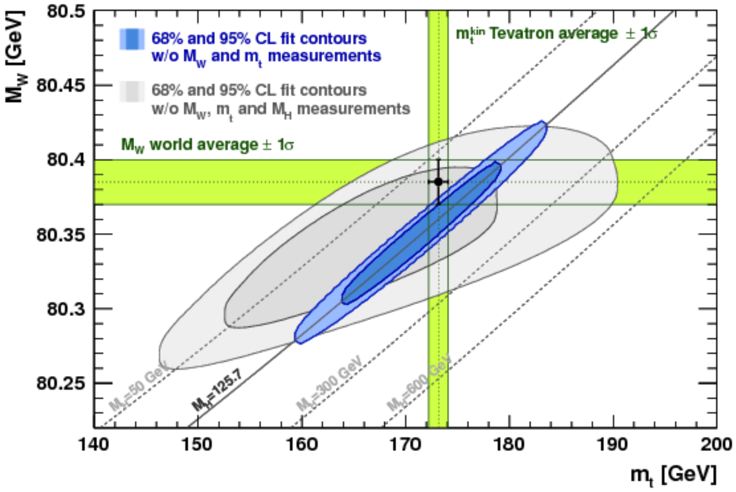

Figure 1.5: The predicted value of the W boson and top quark masses compared with the measured world averages, based on a χ^2 method calculated from the pulls shown in Figure 1.6[17].

1.4 W Boson Production at the Tevatron

W bosons are produced at the Tevatron primarily through the following interactions:

$$d\,(p_d) + \bar{u}\,(p_u) \longrightarrow W^- \longrightarrow e^-\,(p_e) + \bar{\nu}\,(p_\nu) \tag{1.60}$$

$$\bar{d}\,(p_d) + u\,(p_u) \longrightarrow W^+ \longrightarrow e^+\,(p_e) + \nu\,(p_\nu) \tag{1.61}$$

Both the W and Z bosons appear as resonances at the tevatron. This means that the particle is not stable, and always decays after a finite amount of time. The average of the time to decay is called the lifetime. The lifetime is inversely related to the decay width (i.e. the invariant mass width) of the resonance, which can be approximated by a Breit-Wigner spectrum.

To get the differential cross section for any process (i.e. transition), we must com-

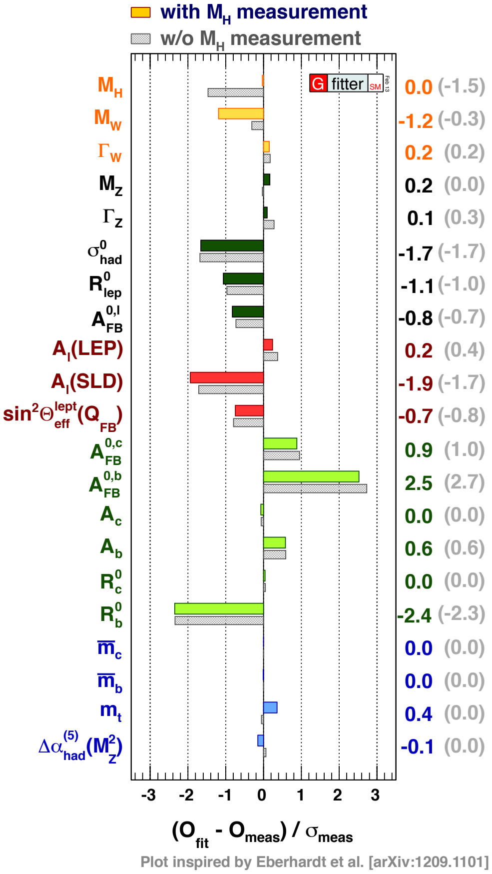

Figure 1.6: The pull plots describing the tensions between the observed and expected values for various observables of the Standard Model.

pute the scattering matrix $S_{fi} = \langle f|S|i\rangle$.[4]

The differential cross section is

$$d\sigma = |\bar{\mathcal{M}}|^2 \frac{p}{32\pi^2 s^{3/2}} d\Omega. \tag{1.63}$$

To determine the spin-averaged amplitude for a particular process we use the Feyn-

---

[4] Which is normalized according to:

$$S_{fi} = \delta_{fi} + (2\pi)^4\delta^4(P_f - P_i)(-i\mathcal{M}_{fi}) \prod_{j=f,i} \frac{1}{\sqrt{2E_j}} \tag{1.62}$$

man rules. The probability of a transition is $dp \propto |\bar{\mathcal{M}}|^2$. At tree level, we have two types of vertices and one type of propagator.

The leptonic-W vertex factor is:

$$-i\frac{g}{2\sqrt{2}}\bar{e}\gamma^{\mu}(1-\gamma_5)\nu W_{\mu}^{-} = -i\sqrt{\frac{G_F M_W^2}{\sqrt{2}}}\bar{e}\gamma^{\mu}(1-\gamma_5)\nu W_{\mu}^{-} \text{ plus CC} \tag{1.64}$$

The quark-W vertex factor is:

$$-i\frac{g}{2\sqrt{2}}\bar{u}\gamma^{\mu}(1-\gamma_5)d'W_{\mu}^{-} = -i\sqrt{\frac{G_F M_W^2}{\sqrt{2}}}\bar{u}\gamma^{\mu}(1-\gamma_5)d'W_{\mu}^{-} \text{ plus CC} \tag{1.65}$$

We have one propagator:

$$\frac{1}{m^2 - m_W^2 + im_W\Gamma_W} \tag{1.66}$$

These are combined and squared to get:

$$\left|\mathcal{M}\left(d\bar{u} \to e^-\nu\right)\right|^2 = 16\left(2\sqrt{2}G_F M_W^2\right)^2 |V_{ud}|^2 \frac{\left(p_u \cdot p_e\right)^2}{\left(\left(p_u + p_e\right)^2 - M_W^2\right)^2 + M_W^2\Gamma_W^2} \tag{1.67}$$

where $|V_{ud}|$ is the CKM matrix element.

If we define θ^* as the polar angle of electron (positron) emission in the rest frame of the $W\pm$ boson, measured relative to the incident direction of the incident antiproton (proton),

$$\left(p_u \cdot p_e\right)^2 = \frac{M_W^4}{16}\left(1 + \cos\theta^*\right) \tag{1.68}$$

which leads to

$$\cos\theta* = \sqrt{1 - \frac{4p_T^{e2}}{M_W^2}} \tag{1.69}$$

When we average over the W^+ and W^- bosons, we get an angular distribution of combined electrons and positrons:

$$\frac{1}{\sigma}\frac{d\sigma}{d\cos\theta^*} = \frac{3}{8}\left(1 + \cos^2\theta^*\right) \tag{1.70}$$

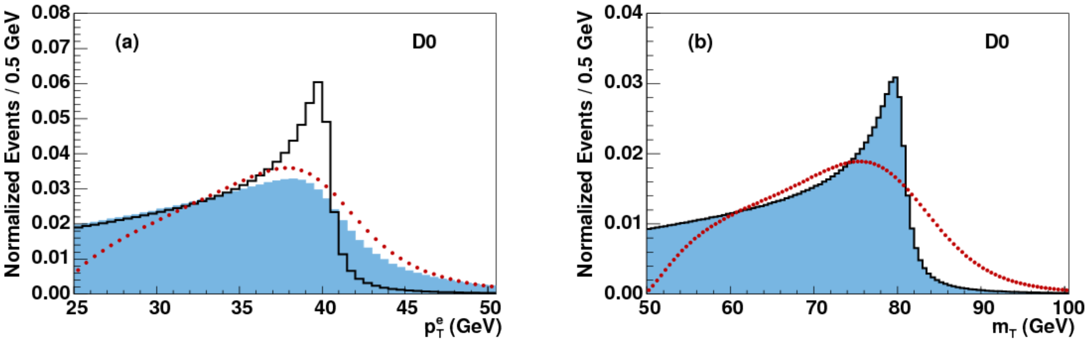

Figure 1.7: Normalized differential cross sections for the decay of a W boson in the rest frame for the p_T^e (a) and m_T (b) observables. The blue shaded regions show the effect of the p_T^W distribution at the Tevatron, and the red points show the effect of the detector response.

Transforming variables, gives us:

$$\frac{1}{\sigma}\frac{d\sigma}{dp_T^{e2}} = \frac{3}{M_W^2}\left(\frac{1-4p_T^{e2}}{M_W^2}\right)^{-1/2}\left(\frac{1-2p_T^{e2}}{M_W^2}\right) \tag{1.71}$$

which is strongly peaked at $p_T^e = \frac{M_W}{2}$, known as the “Jacobian peak” or “Jacobian edge”, seen in Figure 1.7.

Our strategy for measurement is to accurately determine the position of the peak. The neutrino distribution is the same as the electron distribution, and there is a similar peak in the transverse mass distribution, where $M_T^2 = 2p_T^e p_T^\nu(1-\cos\Delta_{e\nu})$.

Since the W boson is not decaying from rest, the peaks for the neutrino and electron transverse momentum are modified by the W boson p_T distribution (p_T^W) at the Tevatron. The peaks for the transverse momentum quantities and the transverse mass are affected by both electroweak corrections from FSR and by QCD corrections from ISR.

The transverse boson momentum at the Tevatron is small, $q_T \ll Q$, where $q_T = p_T^W$ is the transverse momentum of the W boson, and $Q = m_W$ is the mass of the W boson.[5] Because it is small, the calculation is more complicated than if it were large. To calculate

---

[5] These are the variable names used when performing the QCD production cross section.

the transverse momentum distribution via QCD is beyond the scope of this dissertation, but we reproduce results here:

$$\frac{d\sigma}{dq_T^2} = \alpha_S \left(A \frac{\ln \left(Q^2/q_T^2 \right)}{q_T^2} + B \frac{1}{q_T^2} + C \left(q_T^2 \right) \right) \tag{1.72}$$

where A and B are calculated perturbatively. The first two terms diverge at small transverse boson momentum, exhibiting singular behavior of the invariant amplitude when a soft gluon is emitted. The integral is regularized by virtual corrections at every order, but first factor is large when

$$\alpha_s \ln \frac{Q^2}{q_T^2} \gtrsim 1 \rightarrow q_T \lesssim 10\,\mathrm{GeV} \tag{1.73}$$

there is divergence at every perturbation order:

$$\frac{1}{\sigma}\frac{d\sigma}{q_T^2} \simeq \left[A_1 \alpha_S \ln \frac{Q^2}{q_T^2} + A_2 \alpha_S^2 \ln^3 \frac{Q^2}{q_T^2} + \cdots + A_n \alpha_S^n \ln^n \frac{Q^2}{q_T^2} + \cdots \right] \tag{1.74}$$

so, for low boson transverse momentum convergence cannot be achieved at fixed order. The series can be resummed in impact parameter space, as was first discovered by Collins, Soper and Sterman,[26] using the "CSS formalism" used by the `RESBOS` simulation described in Chapter 4, where the cross section for W and Z production is calculated via

$$\begin{aligned} \left(\frac{d\sigma(h_1 h_2 \rightarrow V(\rightarrow \ell_1 \bar{\ell}_2) X)}{dQ^2 dy dq_T^2 d\phi_V d\cos\theta d\phi} \right)_{\mathrm{res}} &= \frac{1}{96\pi^2 S} \frac{Q^2}{(Q^2 - M_V^2)^2 + Q^4 \Gamma_V^2 / M_V} \\ &\times \Bigg\{ \frac{1}{(2\pi)^2} \int d^2 b e^{i \vec{q}_T \cdot \vec{b}} \sum_{j,k} \tilde{W}_{j\bar{k}}(b_*, Q, x_1, x_2, \theta, \phi, C_1, C_2, C_3) \tilde{W}_{j\bar{k}}^{NP}(b, Q, x_1, x_2) \\ &\qquad + Y(q_T, Q, x_1, x_2, \theta, \phi, C_4) \Bigg\} \end{aligned} \tag{1.75}$$

where

$$x_1 = e^y Q/\sqrt{s} \ \text{ and } \ x_2 = e^{-y} Q/\sqrt{s} \tag{1.76}$$

are the parton momentum fractions, and $\sqrt{s}$ is the center-of-mass energy of the hadrons h_1 and h_2, and V represents the W or the Z.

The renormalization group invariant quantity $\tilde{W}_{j\bar{k}}(b)$ sums to all orders in α_S the singular terms that behave like q_T^{-2} or $q_T^{-2} \ln(q_T^2/Q^2)$ as $q_T \rightarrow 0$. To avoid the Landau pole, we introduce a cutoff at large values of b by replacing the impact parameter in $\tilde{W}_{j\bar{k}}(b)$ with

$$b_* = \frac{b}{\sqrt{1+(b/b_{\max})^2}} \tag{1.77}$$

This region cannot be calculated perturbatively, but we can introduce a phenomenological non-perturbative form factor

$$\tilde{W}^{NP}_{j\bar{k}}(b, Q, x_1, x_2) \tag{1.78}$$

For this analysis, we use the “BNLY” parametrization as form factor, which has been fitted to Tevatron Run I data[38].

$$\tilde{W}_{j\bar{k}}(b) = \exp\left[(-g_1 - g_2\ln(Q/Q_0) - g_1 g_3 \ln(100x_1x_2))b^2\right] \tag{1.79}$$

The values we use in our simulations are

$$g_1 = 0.21^{+0.01}_{-0.01} \text{ and } g_2 = 0.68^{+0.01}_{-0.02} \text{ and } g_1 = -0.6^{+0.05}_{-0.04} \tag{1.80}$$

1.5 Previous Calculations

First published calculation of the W mass was performed by Marciano and Sirlin [45], and recently reviewed in [52].

The most up-to-date calculation is the full two-loop-order calculation, but fermionic corrections in three and four loops are also known[16].

When Equation 1.56 is used to predict the value of the W boson mass, there are 4 MeV of uncertainty due to uncalculated higher order corrections. This calculation is usually done in the “on-shell” renormalization scheme, using the physical mass as the renormalized mass which leads to all renormalized equations having a direct physical interperetaion[51].

The relationship between the on-shell, or “pole”, mass and the $\bar{\text{M}}$S (modified minimum subtraction mass), is known to two-loop precision[35][36].

Before the Higgs mass was measured, Equation 1.56 was used to predict its value. Now, it is a powerful test of relationship between the W and top quark masses.

1.6 Previous Measurements

The W boson mass was first measured by the UA1[11] and UA2[12] collaborations with data from CERN's Super Proton Synchrotron (SPS), using similar methods to those used for the current analysis. These two measurements, 81 ± 5 GeV by UA1 and $80 + 10 - 6$ GeV by UA1, resulted in a Nobel Prize. The H1[57] and Zeus[25] collaborations at HERA performed early measurements as well, but the first "precision" measurements were done at LEP and the Tevatron.

At LEP, the ALEPH[48], DELPHI[9], L3[10], and OPAL[8] collaborations measured the W mass in the $e^+e^- \rightarrow W^+W^- \rightarrow q\bar{q}q\bar{q}$ and $e^+e^- \rightarrow W^+W^- \rightarrow q\bar{q}l\nu$ channels by reconstruction of the invariant mass of the decay products. The result of these measurements had a combined precision of 31 MeV.

At the Tevatron, the D0 and CDF collaborations measured the W mass using similar strategies, but different calibration procedures. CDF measured the mass from in the $W \rightarrow e\nu$ and $W \rightarrow \mu\nu$ channels, with 19 MeV of uncertainty[4]. CDF's measurement using the m_T observable from the muon channel was the most precise individual measurement W mass, until the recent measurent by ATLAS, which achieved similar precision. The D0 collaboration measured the mass in the electron channel only, to a precision of 23 MeV.

The current world average is dominated by Tevatron RunII and LEP measurements. The various contributions to this average can be seen in Figure 1.8. It was 80.385 ± 0.015 GeV[1] prior to the latest ATLAS measurement, the result of which is shown in Figure 1.9.

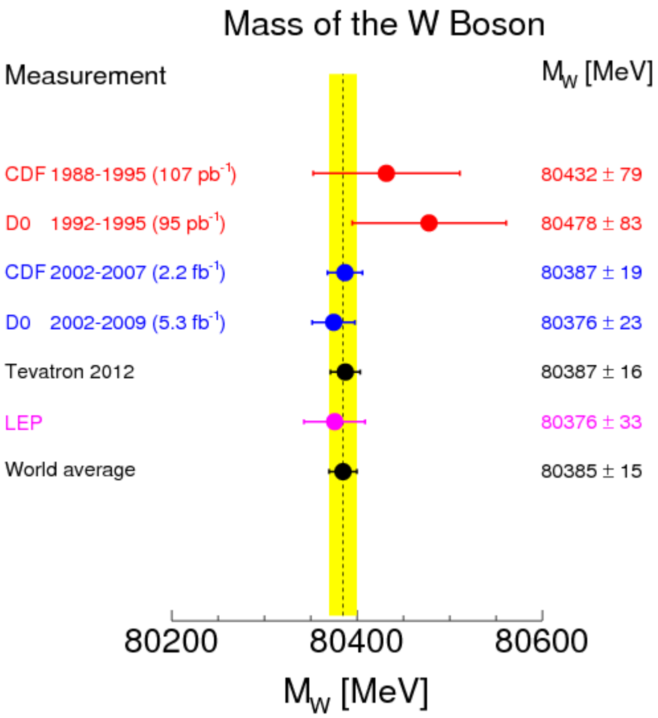

Figure 1.8: Previous measurements and world average of W mass before ATLAS measurement.

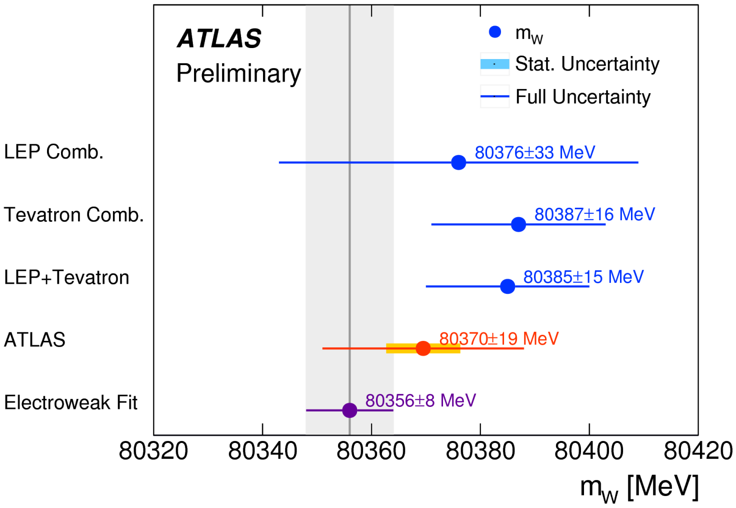

Figure 1.9: December 2016 ATLAS measurement of the W mass.

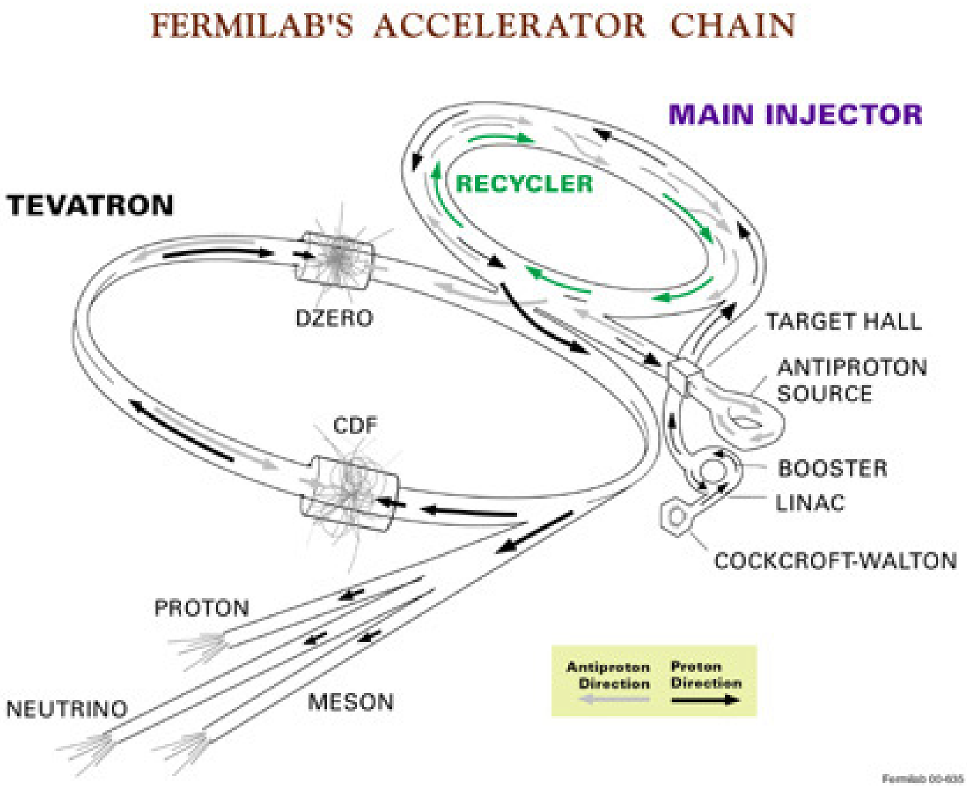

Figure 2.1: The Fermilab accelerator chain

Chapter 2

EXPERIMENTAL APPARATUS

2.1 The Fermilab Tevatron Collider

Between 2002 and 2011, the Tevatron produced proton-antiproton collisions at a center-of-mass energy of 1.96 TeV. The Tevatron collider was the last in a chain of accelerators which produced protons and antiprotons and accelerated them from production to interaction point. (Fig. 2.1)

Tevatron operation was divided into “epochs” or “runs”. RunI took place from 1992 to 1996, with $120\,\mathrm{pb}^{-1}$ recorded, during which CDF and D0 independently observed the top quark. RunII lasted from 2001 to September 2011, and was separated into RunIIa and RunIIb by a break from April to June 2006 during which improvements were made both to the accelerator complex and the D0 detector. During RunII, a total of 11.9 fb^{-1} was delivered, of which D0 recorded 10.7. (In contrast, the CDF measurement used only 2.2 fb^{-1}; they achieved similar precision by using muons in addition to electrons.) The recording efficiency of $\approx 90\%$ was limited by the trigger framework dead time (Section 2.4) and temporary detector problems.

The protons started life as the nuclei of hydrogen atoms in a gas. The gas was ionized to have one extra electron per hydrogen atom, and the ions were accelerated inside inside a Cockroft-Walton accelerator (see Figure 2.1 to 750 keV. The ions were further accelerated in the LINAC (an RF linear accelerator) to 400 MeV, when they were passed through a carbon foil to strip off their electrons leaving free protons. Next, they were accelerated to 8 GeV in the Booster (a circular accelerator), where they were stored until approximately 5×10^{12} protons were available. Then, they were transferred to the Main Injector (another circular accelerator) where they were accelerated to 150 GeV. From the Main Injector they were routed into the Tevatron, where they were accelerated to their final energy of 980 GeV.

To produce antiprotons, protons from the Main Injector were collided with a Ni-Cu target, producing particle showers from which antiprotons were collected with a high-gradient lithium lens. The lithium lens was a 3.6 cm diameter and 15 cm long cylinder of lithium metal with constant (10^6A) axial current resulting in the azimuthal magnetic field (with a gradient of 5 T/cm) which collimated the beam. After passing through the lithium lens, the antiprotons were injected into the Debuncher ring where their large energy spread was narrowed by stochastic cooling. The antiprotons were then transferred to the Accumulator ring where they were accelerated to 8 GeV. When $60-70\times10^{10}$ antiprotons were accumulated, they were transferred to the Recycler Ring where they were cooled further, stochastically and with an electron beam. From there they went to the Main Injector, where, like the protons, they were accelerated to 150 GeV for injection into the Tevatron. The Recycler Ring was named for one of its original purposes, which was to recycle the difficult-to-produce antiprotons. It was not, however, used for this purpose, for two reasons: 1) the extraction and cooling of antiprotons from the Tevatron after a store never reached a satisfactory efficiency, and 2) antiproton production “from scratch” exceeded expectations, as described next.

Only about one antiproton could be produced for every 10^5 protons incident on the Ni-Cu target; this was the limiting factor for the number of antiprotons in the ring during a store (whereas the limiting factor for protons was the capacity of the ring). However, the low production efficiency was significantly mitigated by factors including a high proton beam intensity on the Ni-Cu target and using electron cooling in addition to stochastic cooling, as well as improvements to the lithium lens and Debuncher during the 2006 upgrade. After this upgrade, the production of antiprotons almost doubled so that there were 127×10^9 antiprotons per bunch, compared with 270×10^9 protons per bunch.

2.2 The Tevatron Bunch Structure and Luminosity

Each fill of the Tevatron was called a “store”, and each store lasted approximately 16 hours. The protons and antiprotons travelled in opposite directions in a single vacuum pipe (unlike proton-proton beams at the LHC which require separate pipes) and were kept in different helical orbits overlapping only at the collision points by electrostatic separators. One of the advantages of a single vacuum pipe is that, when focused at the interaction points at D0 and CDF (at point B0 on the other side of the ring), the crossing angle is nearly zero and the beams collide nearly head-on, which maximizes the number of collisions. A disadvantage is that when the beams are not physically isolated, the proton and antiproton beams have a defocusing effect (essentially, knocking each other out of orbit) which is strongest near the interaction point where the orbits overlap.

The typical instantaneous luminosity during a store was $\mathcal{L} \approx 200 \times 10^{30}\mathrm{cm}^{-2}\mathrm{s}^{-1}$, but could be as much as $\mathcal{L} \approx 430 \times 10^{30}\mathrm{cm}^{-2}\mathrm{s}^{-1}$. Over the course of a store, the luminosity would decrease as protons were lost to interactions and vacuum imperfections. When the luminosity had decreased beneath useful levels, the store was sent to a beam dump. The beam-beam interaction described above was responsible for 40% of the luminosity loss during a store. The rest of the luminosity loss was mainly due to collisions at the interaction point, and vacuum imperfections (mainly interactions with renegade nitrogen molecules)[49][50].

Protons and antiprotons traveled around the ring in packets called "bunches". They were accelerated by a time-space pattern of longitudinally focusing pulses, or "acceleration radio-frequencey (RF)", operating at 53.104 MHz, or one pulse every 18.85 ns. A pulse was called a "bucket", because each one could hold a bunch of particles in its moving electromagnetic potential. With a revolution frequency of 47.713 kHz, or 21 μs per revolution, there were 1113 RF buckets around the ring. The buckets were further divided into ticks of 7 consecutive buckets each, for 159 ticks. Only the first bucket in a tick was allowed to hold a bunch, but not all ticks held bunches. A store in RunI had 6 equally-spaced bunches each of protons and antiprotons while a store in RunII had 2×36 bunches divided into 3 "superbunches" of 12 bunches each. A superbunch contained one bunch for every three ticks, and superbunches were separated by 17 ticks (nearly 20 including all the empty buckets after the last bunch in a superbunch), or $\approx 2.64\mu$s. The RunI configuration resulted in bunch crossings every 3500 ns at a CoM of 1.8 TeV, while the RunII configuration had bunch crossings every 393 ns, at a CoM of 1.96 TeV.

In the absence of a crossing angle, instantaneous luminosity is given by [18]

$$\mathcal{L} = \frac{fBN_pN_{\bar{p}}}{2\pi(\sigma_p^2 + \sigma_{\bar{p}}^2)} F(\sigma_l/\beta^*) \tag{2.1}$$

where f is revolution frequency, B is the number of bunches per beam, $N_{p(\bar{p})}$ is the number of protons (anti-protons) per bunch, $\sigma_{p(\bar{p})}$ is the RMS size of the proton (anti-proton) beam, F is a form-factor that depends on ratio of σ_l to β^*, σ_l is the bunch length, and β^* is beta function at interaction point. In this dissertation and in many publications, instantaneous luminosity is expressed in units of $I_0 = 10^{30}\,\mathrm{cm}^{-2}\mathrm{s}^{-1} = 1\mu\mathrm{b}^{-1}\,\mathrm{s}^{-1}$, i.e. one "microbarne" per second.

The luminosity $\mathcal{L}$ is related to average number of interactions per beam crossing $\bar{N}_{LM}$ via

$$\mathcal{L} = \frac{f}{\sigma_{\mathrm{LM}}} \bar{N}_{LM} \tag{2.2}$$

where σ_{LM} is the inelastic luminosity cross section corrected by the Luminosity Monitors acceptance and efficiency. A tick was considered to contain an interaction at D0 if there was a coincidence signal in both Luminosity Monitors during that tick (see Section 2.3.5). The number of interactions per revolution n could not be measured directly, but followed a Poisson distribution with mean $\bar{N}_{LM} = \mathcal{L}\sigma_{\mathrm{LM}}/f$.

Knowing the fraction of beam crossings with no collisions, we can exploit the relationship $P(0)_{\mathrm{turn}} = e^{-\bar{N}_{LM}}$ to find

$$\mathcal{L} \;=\; -\frac{f}{\sigma_{\mathrm{LM}}} \ln\left(P_{\mathrm{turn}}\left(n=0\right)\right) \tag{2.3}$$

A tick, or even a turn, was too short a period of time to measure luminosity, but a hypothetical probability of no interactions during a turn assuming perfectly constant conditions could be calculated from the number of coincidences in the luminosity monitors ΔLM over a pre-determined period of time called the Luminosity Block (LB) and lasting Δticks ticks. In general, the LB lasted 60 s, corresponding to 455 million ticks. [1]

$\bar{N}_{LM}$ was not constant from tick to tick: not every tick contained a bunch, and individual bunches varied in size. However, a given pair of proton and antiproton bunches which collided at tick i of a revolution would collide at tick i of every revolution. The luminosity block was short enough that the instantaneous luminosity for the two bunches colliding at tick i didn't change appreciably over its duration, but was long enough to neglect the statistical fluctuations in the LM count. Thus we can average over 159 measurements each lasting the duration of the LB and integrating LM coincidences for a particular i, to

---

[1] The LB number (LBN) was also incremented upon run or store transitions, TFW or SCL initialization, or by request. Raw data files were opened and closed on LBN boundaries[5].

find

$$\mathcal{L} = -\frac{f}{\sigma_{\mathrm{LM}}} \sum_{i=1}^{159} \ln\left(1 - 159 \cdot \frac{\Delta \mathrm{LM}_i}{\Delta \mathrm{ticks}_i}\right) \qquad (2.4)$$

2.3 The Run II D0 Detector

The D0 Detector[5] was made up of several important subsystems, including the central tracking detector (CTD), the uranium/liquid-argon calorimeters, the forward proton detector (FPD), the luminosity monitors (LMs), preshower detectors, and the muon spectrometer, as well as the trigger system which interfaced with all these components to orchestrate when and what data to record. All of these components will be described in this section, although the most important for the W mass measurement were the CTD and the calorimeters. The detector surrounded the D0 beam pipe which was made of beryllium, 2.37 m long, and with an outer diameter of 38.1 mm and wall thickness of 0.508 mm.

2.3.1 Central Tracking Detector

The Central Tracking Detetor (CTD) consisted of a center scintillating-fiber tracker (CFT) and a silicon microstrip tracker (SMT) inside a 2 T solenoidal magnet. The latter two components were added during the 2006 upgrade, when the radiation damaged CFT was also replaced. The magnetic field allowed for track-based momentum measurement of charged particles, used to calibrate the calorimeter and identify electrons via the energy-momentum (E/p) ratio. The CTD provided vertexing with a high resolution of 35 μm and tracking information for leptons and jets which was also used for triggering (see Section 2.4).

2.3.1.1 Silicon Microstrip Tracker

The Silicon Microstrip Tracker (SMT) was designed to have almost as much coverage in η as the calorimeter and muon systems. Its length corresponded to the size of the ≈ 25 cm interaction region. As seen in Figure 2.3, the central portion is divided lengthwise

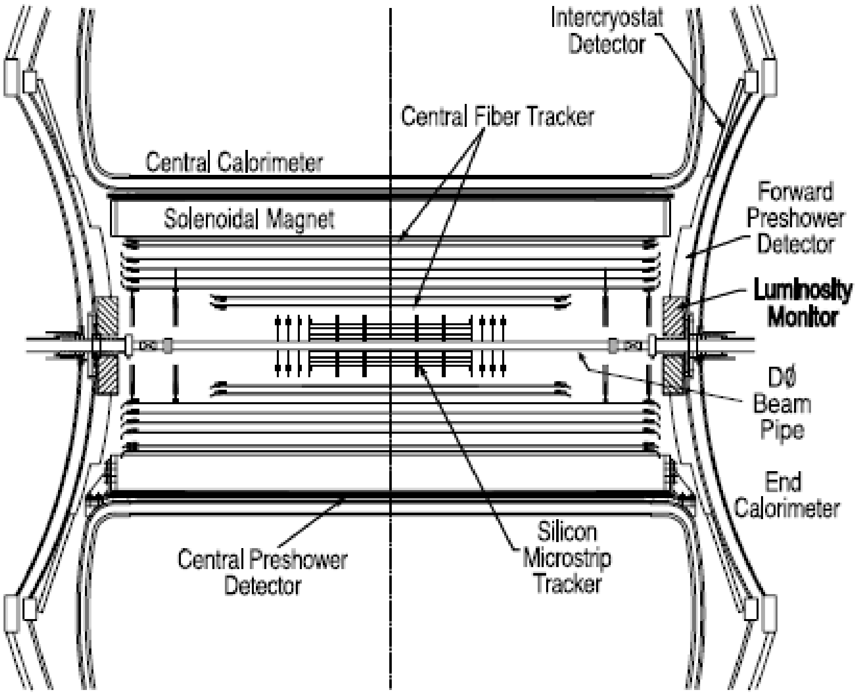

Cross sectional view of the Run IIa D0 tracking system.

Figure 2.2: Cross-sectional view of the D0 detector in the $x - z$ plane. The main focus is the central tracking cystem, but the solenoid, the preshower detectors, luminosity monitor, and the calorimeters are also shown[5].

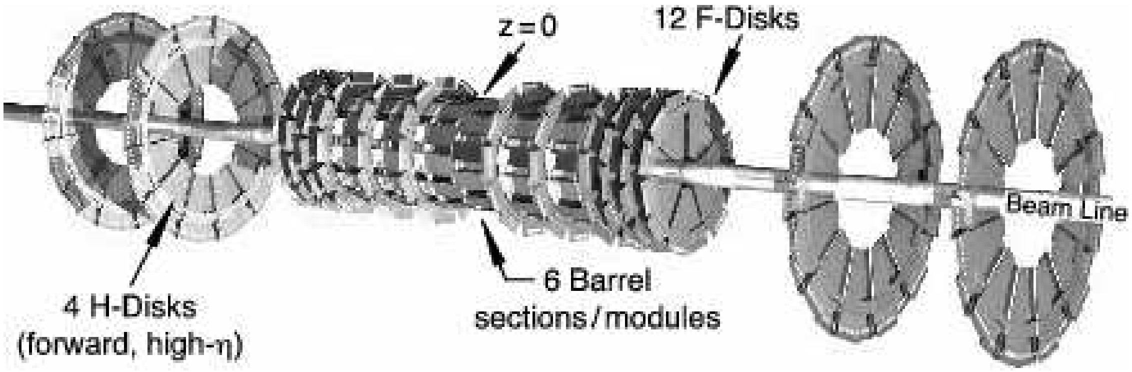

Figure 2.3: The silicon microstrip tracker[5].

into six "barrels" with centers at $z = 6.2$, 19.0, and 31.8 cm. Each barrel is capped with a flat "F-disk" on the high-z end, at 12.5, 25.3, and 38.2 cm. There are three more F-disks in front of and behind the central barrel region, at $z = 43.1$, 48.1, and 53.1 cm. Finally, there are four large-diameter "H-disks" at $z = \pm 100.4\,\text{cm}$ and $z = \pm 121.0\,\text{cm}$, the far-forward and far-backward regions of the SMT. The disks and barrels can track particles in the $r - \phi$ plane, while only the disks can track particles in the $r - z$ plane. The barrels each have four layers of silicon sensors in a "ladder" configuration; the inner two layers have 12 ladders each while the outer two layers have 24 ladders each, for a total of 432 ladders. The F-disks are composed of 12 double-sided wedge-shaped sensors each, for a total of 144 F-wedges, and the H-disks are composed of 24 back-to-back pairs of single-sided "half-wedges"each, for a total of 96 full H-wedges. The trapezoidal wedges overlap as they are arranged around the disks, resulting in a 30° stereo angle for the F-disks and a 15° stereo angle for the H-disks.

2.3.1.2 Central Fiber Tracker

The CFT consisted of 2 inner cylinders 1.66 m long and 6 outer cylinders 2.52 m long arranged as in Figure 2.2. It surrounded the SMT, occupying the radial space from 20 to 52 cm. The outer cylinder covered $\eta \lesssim 1.7$ (the inner cylinders covered a somewhat larger range). Each of the 8 cylinders supported one doublet layer (Figure 2.4) of 835 μm diameter fluorescent dye doped polystyrene (PS) scintillating fibers oriented along the beam direction (the "axial", or "z"-, layer) and an additional doublet layer oriented at a ±3° angle relative to the first layer (the "stereo", or "u"-(positive ϕ)/"v"-(negative ϕ) layer). The cylinders alternated between u- and v- layers, with an innermost u-layer. The scintillating fibers were coated with 90% reflective sputtered aluminum coating one one end and the other end was coupled to 7.8-11.9 m long clear (undoped) PS fiber waveguides which led to visible light photon counters (VLPCs)[2]. About 200 km of scintillating fiber and 800 km of clear fiber was used in the CFT! The CFT had an inherent doublet layer resolution of $\approx 100\,\mu$m as long as individual fiber positions were known to $50\,\mu$m. The fast L1 hardware triggered (see section 2.4.3) on discriminator signals from the axial doublet layers, such as number of track

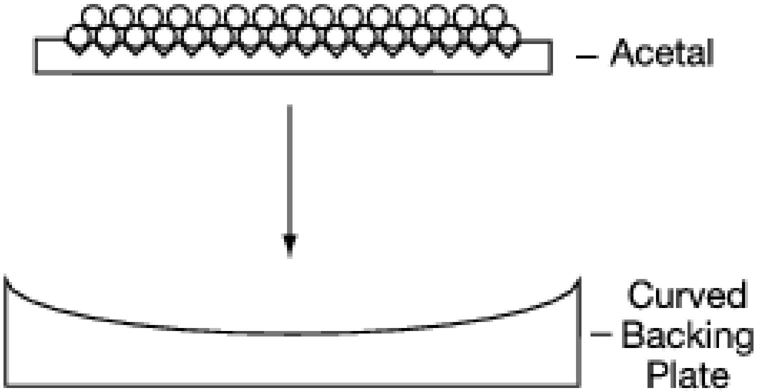

Figure 2.4: The curved scintillating fiber ribbon fabrication process. A 1/16” thick was prepared with precisely spaced (between 928 and 993 μm, depending on the radius of the corresponding support cylinder) grooves, the ribbon was attached to a curved backing plate of the appropriate radius, and 256 fibers are inlaid in an offset double layer. Note that not all 256 fibers are shown, and that there was also a top layer holding the fibers in place[5].

candidates above specified p_T thresholds (min 1.5 GeV/c)). The L2 trigger also used track candidates, and if the event passed L2 triggering, the full CFT readout information was read out.

2.3.2 Solenoidal and Toroidal Magnets

The D0 toroid system, which was part of the muon system already in place during RunI, consisted of one central and two end toroids, as shown in Figure 2.6. The central toroid was a square annulus 109 cm thick, with an inner surface about 318 cm from the beamline,

---

[2] The $n = 1.59$ polystyrene fibers (PS) were doped with 1% (by weight paraterphenyl (PT) (an organic flourescent dye) and 3-hydroxyflavone (3HF) (a wave-shifter dye) at 1500 ppm. Excitations in PS were transferred to the PT via non-radiative dipole-dipole interaction. PT fluoresces at ca 340 nm with decay time of a few ns. The mean free path in PS at this wavelength is only a few hundred microns, but 3HF picks up the light and reemits it as 530 nm light, which is readily transmitted through the fiber. The PS fibers were double-clad, with a 25 μm inner layer of $n = 1.49$ polymethylmethacrylate (PMMA), and a 25 μm outer layer of $n = 1.42$ fluoro-acrylic. The PMMA inner layer was a mechanical interface between the inner core and outter cladding, which were mechanically incompatible. The scintillating fiber had an attenuation length of 5m and the clear fiber an attenuation length of 8m.

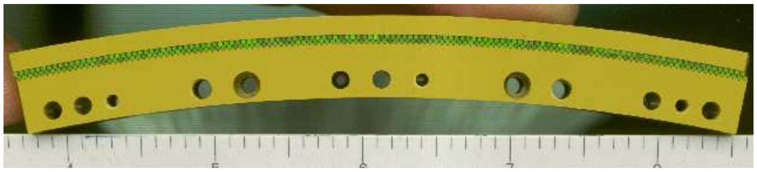

Figure 2.5: A CFT fiber ribbon mass terminated via a v-groove connector. Light transmission between this connector and the waveguides is 95% with optical grease[5].

and covered region $|\eta| \lesssim 1$. It was constructed in three sections - a center bottom section, and two C-shaped side sections. It was wound with 20 coils of ten turns each. The two end toroids, also square, occupied the spaces with $454 \leq |z| \leq 610$ cm. The inner surfaces were about 91 cm from the beam line, and the outer surfaces 426 cm from the beam line in x and y. The toroids were operated in series during RunI and RunII, and during RunI a current of 2500 A was used, and the magnetic fields in the central and end toriods were 1.9 and 2.0 T. During RunII, because momentum could now be measured in the central tracker, the current was decreased to 1500 A, with a magnetic field decrease of 6%.

The D0 superconducting solenoidal magnet, added during the upgrade prior to RunII, was designed to optimize momentum resolution $\delta p_T/p_T$ and tracking pattern recognition based on RunI detector constraints. At 2.73 m long and 1.42 m in diameter, it maximized use of the available space inside the CC. It was as thin as possible to maximize the available tracking volume, and to optimize the performance of CPS detector, was one radiation length in thickness at normal incidence ($\eta = 0$). It was designed to operate safely and stably at either polarity, both for cancellation of systematic uncertainties and for asymmetry measurements. Two layers of superconductor windings (in ribbons, each containing 18 superconducting strands as seen in Figure 2.7) were necessary to achieve the required current of 4749A for the intended 2.0 T central field (only a 1.9 T field was used at run time, since a cracking noise was heard when the magnet was operated full intensity [43]), and field uniformity was maximized by appropriately increasing the density of the windings

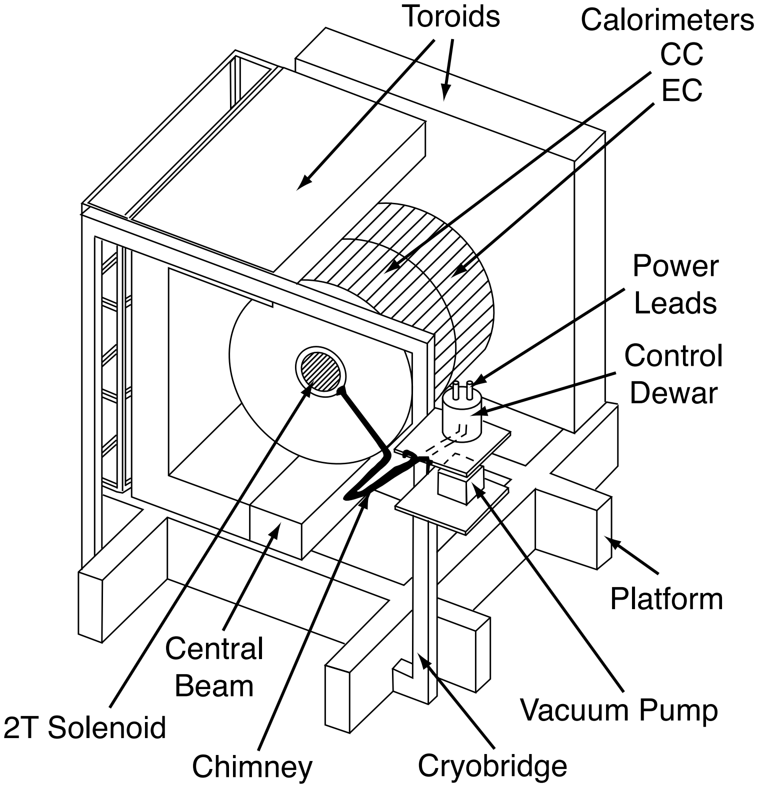

Figure 2.6: A cut-away view of the D0 solenoid inside the central calorimeter. Only one end calorimeter and parts of the muon chambers and toroid system are shown. Note the positions of the central beam, support platform, service chimney, and control dewar[5].

(by narrowing the ribbons) at the ends of the coil.

2.3.3 Muon System

The D0 muon system consisted of the central muon system, covering $|\eta| \lesssim 1.0$, and the forward muon systems, covering $1.0 \lesssim |\eta| \lesssim 2.0$. All had three layers of drift chambers, an A layer outside the calorimeters and inside the toroids, and a B and C layer outside the toroids. The drift chambers were made of rectangular extruded aluminum tubes, and were typically $2.8 \times 5.6\,\mathrm{m}^2$. The drift tubes were filled with a gas of 84% argon, 8% methane, and 8% CF_4, which was exchanged and filtered at a rate of three volumes per day. The central

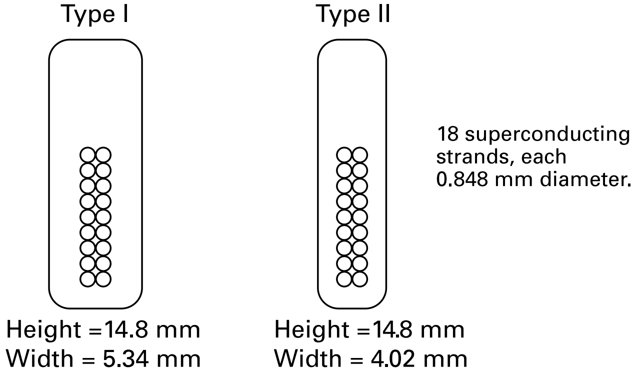

Figure 2.7: Cross sections of the two superconducting ribbons used in the solenoidal magnet. The narrower ribbon was used at the end of the coil, to increase the current density there[5].

muon system used proportional drift tubes (PDTs) that had been used in RunI, while the new forward muon system used mini drift tubes (MDTs). Approximately 55% of the central region was covered by three layers of PDTs, and close to 90% was covered by at least two layers. The A- and C-layer of the central muon system and all layers of the forward muon system were equipped with scintillation counters. The 630 in the central muon system were "Aϕ Counters", and the 4214 in the forward regions were "Pixel Counters". The muon system also included a "cosmic cap" and "bottom" scintillation counters, for the purpose of detecting and discriminating against cosmic ray muons at the trigger level. The scintillation counters of the muon system were calibrated and monitored by an LED-based pulser system.

2.3.4 Forward Proton Detector

The purpose of the FPD was to detect elastically scattered protons and antiprotons, track them (with a position resolution of 130 μm), and measure their momentum. The Forward Proton Detector (FPD) consisted of 18 position detectors arranged as in Figure 2.9. As seen in Figure 2.10, each position detector contained three pairs of scintillating fiber layers, one oriented vertically and two at ±45° from vertical. The fiber stack in a single layer of a pair was offset with respect to that of the other layer to provide full coverage. The

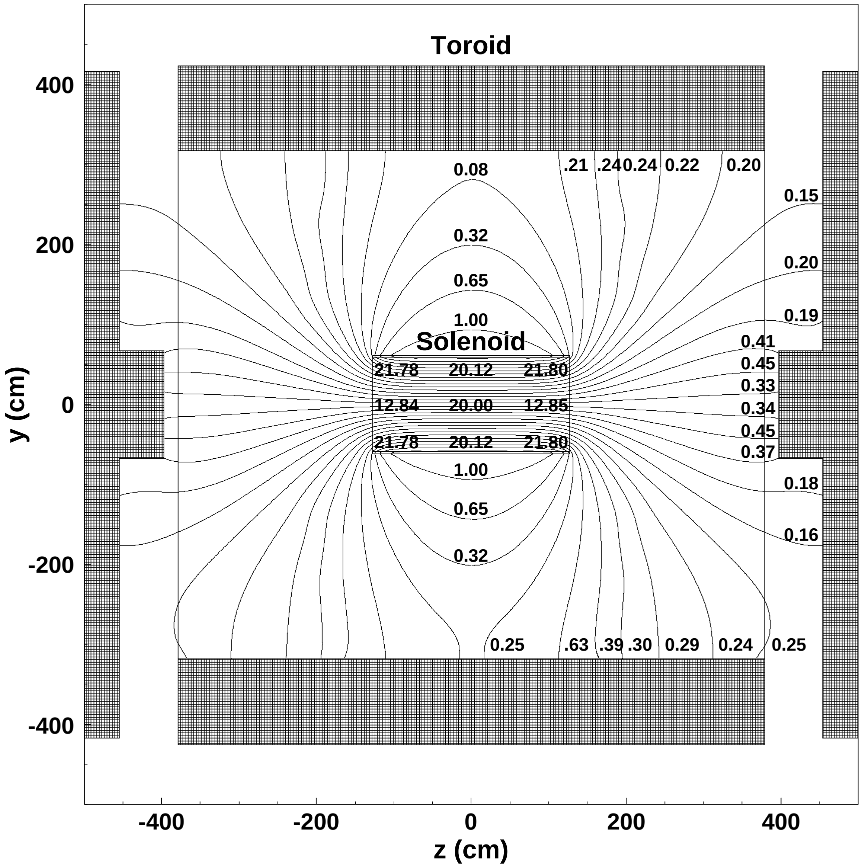

Figure 2.8: A side view of the D0 magnetic field in kG. Both the toroidal and solenoidal magnets are at full current (1500 A and 4749 A, respectively). The fields in the central and end toroids are ≈ 1.8 and ≈ 1.9 T, respectively. Note the top to bottom asymmetry in the field. There is also asymmetry in the x direction. These asymmetries were not desired, but were unavoidable due to structural support requirements in the detector[5].

scintillating fibers were read out into 16-channel multi-anode photomultipliers (MAPMTs). The position detectors also each contained a layer of trigger scintillator, read out into a fast photomultiplier tube. The muon LED system was also used to calibrate the FPD.

The position detectors could be moved, via "Roman pots", in and out of the ultra-high vacuum inside stainless steel "castles" which resided in the beam line, and of which there

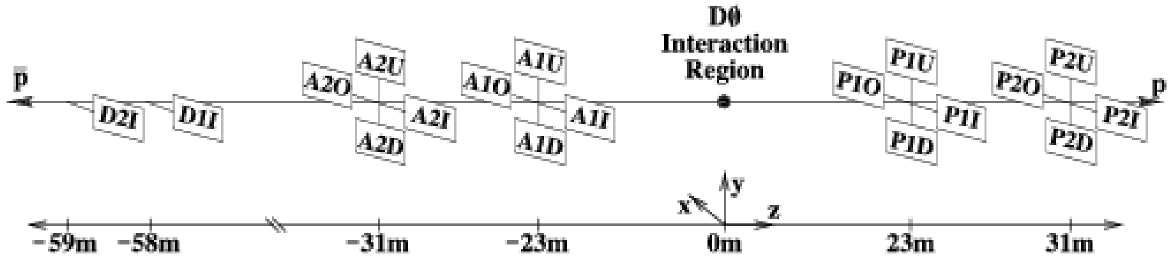

Figure 2.9: The Forward Proton Detector layout. Quadrupole castles are designated with a three-symbol code: P (A) when on the p ($\bar{p}$) side; a number designating the station location; U for up, D for down, I for in, O for out. D1I and D2I are the dipole castles[5].

were six as described in the caption of Figure 2.9. The quadrupole castles (Figure 2.11) were connected to the ultra-high vacuum of the beam pipe via bellows, and their position could be adjusted in all directions over a range of 15 mm with an accuracy of 0.1 mm. The detectors in their pots were separated from the beam pipe vacuum by 200 μm-thick stainless steel windows.

2.3.5 Luminosity Monitor

The Luminosity Monitor (LM) was situated at the high η region for maximum sensitivity, catching particles deflected in the softest of interactions. For a valid luminosity signal, at least one in-time hit in both north and south Luminosity Monitors was required. In addition to measuring luminosity, it provided fast vertex estimation and a halo veto. The vertex estimation was calculated via $z_v = \frac{c}{2}(t_- - t_+)$, where t_+ and t_- were the times-of-flight for particles hitting the LMs at $z = \pm 140\,\text{cm}$. The LMs had a temporal resolution of about 0.3 ns, mainly due to light path variation across the scintillator. Beam-beam collisions required hits in the temporal window 6.4 ns around the interaction point (IP), or $z_v \lesssim 100\,\text{cm}$. At about three times the size of the typical luminous region ($|z_v| \lesssim \pm 40\,\text{cm}$), this would catch nearly all $p\bar{p}$ collisions. Beam halo particles tended to have $t_- - t_+ \approx 9\,\text{ns}$, or $|z_v| \approx 140\,\text{cm}$

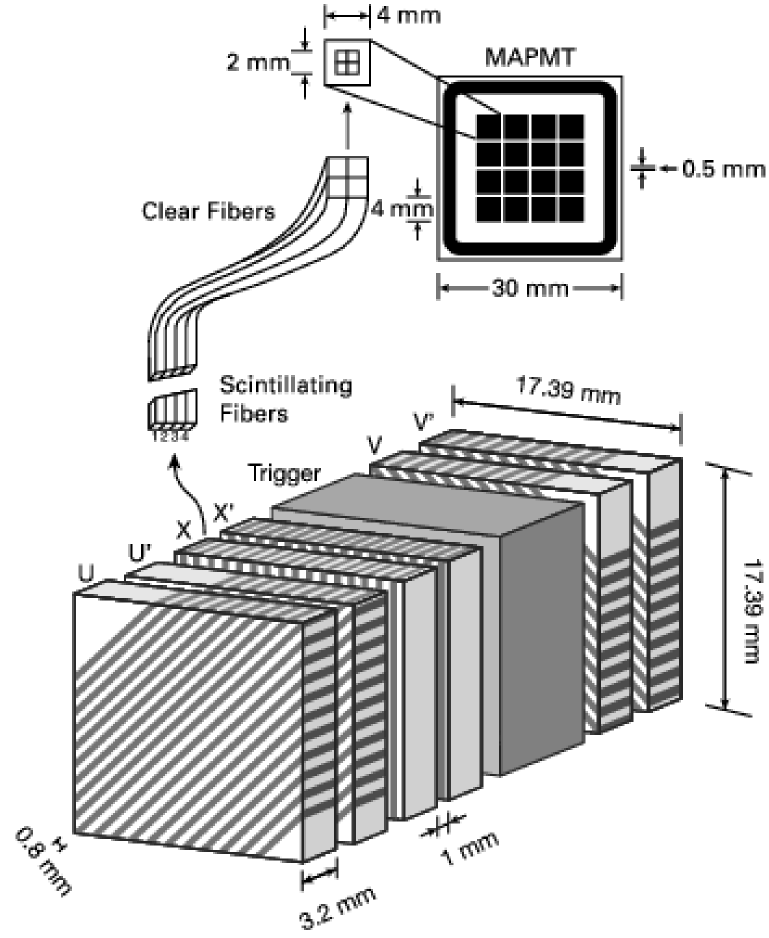

Figure 2.10: Forward Proton Detector scintillating structure composition and connection to the multi-anode photomultiplier[5].

(although in this case, technically there was no vertex). These were automatically eliminated by the $z_v \lesssim 100\,\text{cm}$ requirement. More than six halo particles per bunch crossing would result in a halo veto, as in this case the detector would be too noisy for an accurate luminosity measurement. All other crossings were called "live crossings" and sent to the L1 trigger. The LM was considered to be "Level 0" of the D0 trigger system[24].

The LM had a coverage of $2.7 < |\eta| < 4.4$ and consisted of two arrays of scintillation counters attached to the D0 ECs, as seen in figure 2.12. There were 24 wedges per array, read

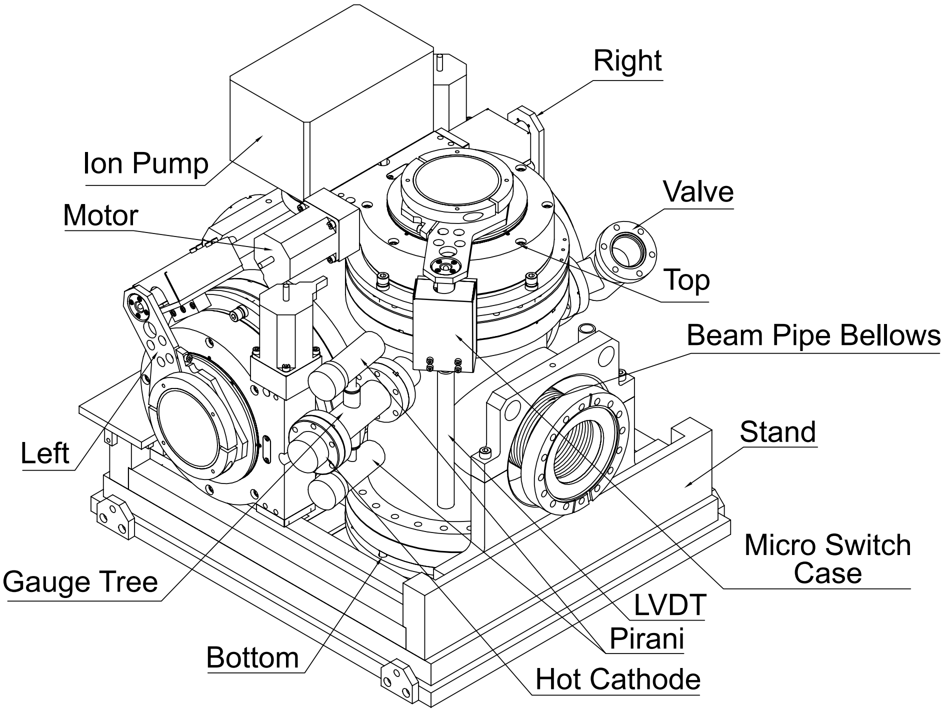

Figure 2.11: FPD quadrupole castle[5].

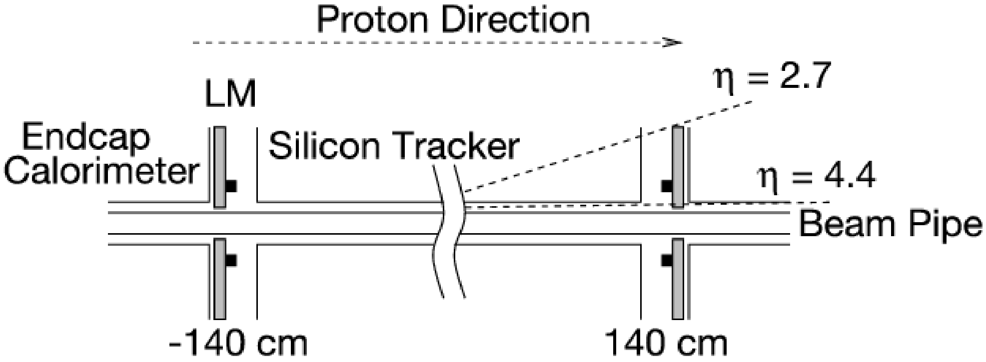

Figure 2.12: The location of the LMs in the D0 detector[5].

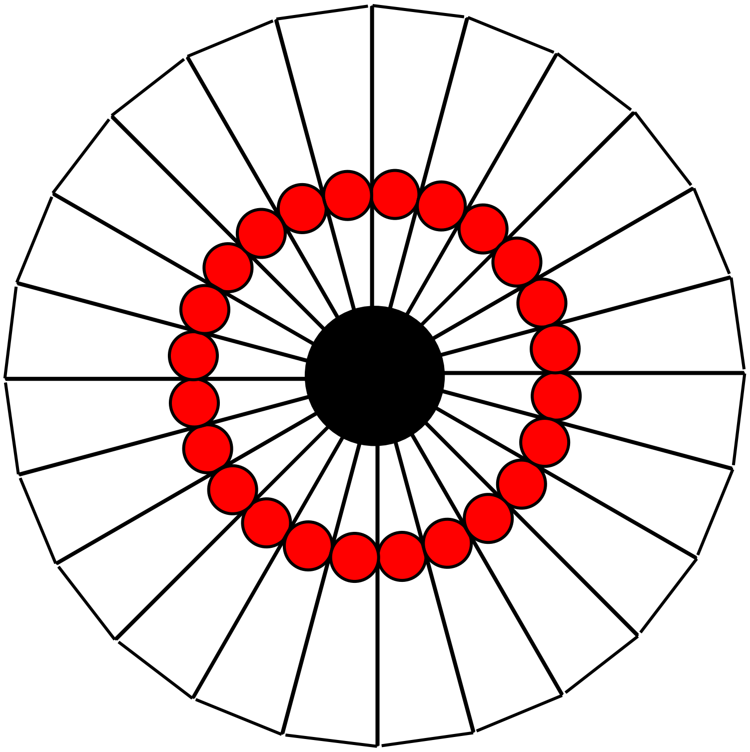

Figure 2.13: The geometry of the LM counters, including the locations of the PMTs (solid dots)[5].

out to PMTs mounted directly on face of scintillators, as seen in figure 2.13. The LM had no magnetic shielding, and was in a 1 T field when the solenoid was on; this reduced its gain by a factor of ≈ 30. This close to the beam, the PMTs were irradiated by $\approx 25\,\mathrm{krad/fb^{-1}}$, so instead of borosilicate glass, fused quartz windows which are much less susceptible to radiation, were used. The scintillator itself was irradiated by up to $\approx 300\mathrm{krad/fb^{-1}}$ at the inner edge. This would degrade the scintillator somewhat, and $\approx 10\%$ light loss was expected after $\approx 3\,\mathrm{fb^{-1}}$. The scintillation counters were held in light-tight enclosures, two per LM (east and west), with twelve counters per enclosure. They were read out to preamps with $5\times$ gain inside enclosure. The enclosure was purged with nitrogen gas to protect them from helium to which borosilicate glass is permeable.

2.3.6 The D0 Calorimetry System

The D0 calorimetry system consists of three sampling calorimeters, including the inter-cryostat detector attached to the endcaps.

2.3.6.1 Liquid Argon Calorimeters

There were three liquid-argon (LAr) calorimeters, each inside its own cryostat maintained at 90.7±0.1 K. The central calorimeter (CC) covered $|\eta| \lesssim 1.0$ and the north and south endcap calorimeters (ECN and ECS) extended the coverage to $|\eta| \sim 4.0$. Each calorimeter contained an electromagnetic section followed by fine and coarse hadronic sections (FH and CH). The CC and endcap (EC) EM calorimeters used, respectively, 3 mm and 4 mm plates of nearly pure depleted uranium as absorbers, while the FH used 6 mm plates of uranium-niobium 2% alloy and the CH used 46.5 mm plates of copper/steel in the CC/EC. The signal boards in all but the smallest angle modules in the EC are made of two sheets of 0.5 mm G-10 fiberglass, sandwiching an inner copper layer milled into a segmented readout pattern. The small angle monolithic EM and hadronic modules have single multilayer printed circuit boards to avoid the significant dead regions that would occur with individual signal boards per cell. The absorber plates are grounded and the signal boards are held at a positive high voltage, typically 2.0 kV. The LAr gap between the absorber and the signal board is 2.3 mm, with approximately 450 ns electron drift time. A schematic of a typical cell can be seen in Figure 2.14.

The cells were arranged in "pseudo-projective" towers with the centers of cells lying along projective rays and the cell boundaries are perpendicular to absorber plates, as seen in Figure 2.16. The resulting offset of subsequent layers of cells provided hermiticity. The projective sizes of the towers in the EM and hadronic modules were $\Delta\eta = 0.1$ and $\Delta\phi = 2\pi/64 \approx 0.1$, except at larger η, where cell sizes were increased to avoid tiny cells, and at the third layer of the EM modules which were located at the typical EM shower maximum, and therefore twice as finely segmented in both η and ϕ for more precise location of shower

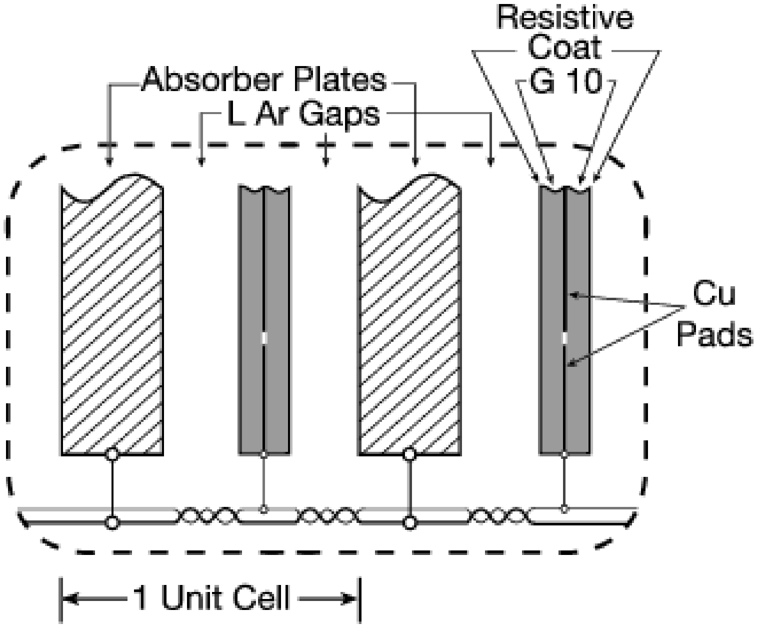

Figure 2.14: Schematic view of the absorber plates (grounded), signal boards (connected to high voltage), and liquid argon gap in the calorimeter. Several unit cells are ganged together to form a single readout cell[5].

centroids. The transverse sizes of the readout cells were in general comparable to transverse size of showers: 1-2 cm for EM showers and 10 cm for hadronic showers.

The CC and EC EM calorimeters each had four layers, from inside to outside, the CC layers were 1.4, 2.0, 6.8 and $9.8X_0$ thick (where X_0 is the radiation length), and the EC layers were 1.6, 2.6, 7.9, and $9.3X_0$ thick. In addition, the material in front of the CC had thickness $4X_0$ while in front of the EC at $\eta = 2$, there was $4.4X_0$ of material. In the CC, the thicknesses of the three FH and single CH hadronic layer were, respectively, 1.3, 1.0, 0.76, and 3.2 λ_A thick (where λ_A is the nuclear interaction length). In the EC (see Figure 2.15), both the FH and CH inner module had inner and outer radii of 3.92 and 86.4 cm. The FH portion had four readout cells, each $1.1\lambda_A$ thick, and the CH had a single readout cell $4.1\lambda_A$ thick. The middle EC hadronic module had four FH cells, each $0.9\lambda_A$ thick, and a CH single readout cell $4.4\lambda_A$ thick. The outer EC hadronic module had stainless steel absorber plates

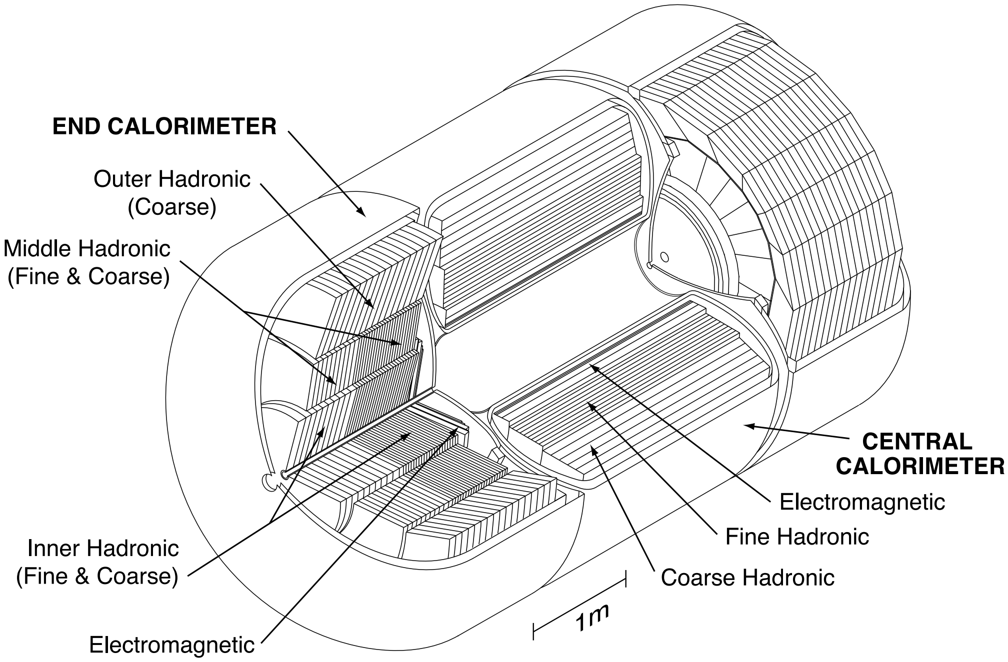

Figure 2.15: Cutaway, isometric diagram of the structure of the D0 central and end calorimeters[5].

of total thickness about $6\lambda_A$, inclined at 60° with respect to the beam axis, as seen in Figure 2.16.

2.3.6.2 Inter-Cryostat Detector

Due to the geometry of the three separate cryostats holding the detector components, there was incomplete coverage in pseudorapidity region $0.8 < |\eta| < 1.4$. In addition, there was substantial unsampled material in this region which by starting showers early degrades the resolution of energy measurements. To remedy this, extra sampling layers called "massless gaps" were attached to the external surfaces of the end cap calorimeters, in front of first layer of uranium. Whereas in RunI the full $0.8 < |\eta| < 1.4$ was covered, space was needed for SMT and CFT cabling in RunII, so the size of the extra sampling layers was decreased to cover region $1.1 < |\eta| < 1.4$. These extra layers formed modules called the

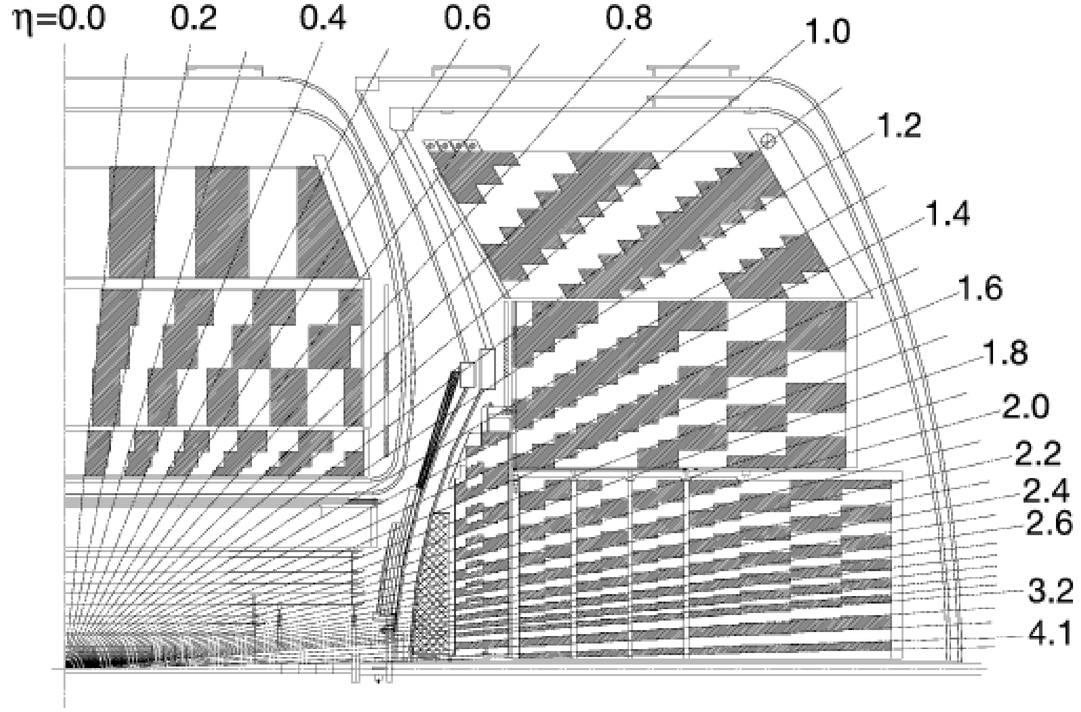

Figure 2.16: Side view of one quadrant of the D0 calorimeter, showing the calorimeter segmentation and tower definition in the CC and EC. Lines of constant pseudorapidityshow the (η_{det}) coverage of cells and projected towers. The solenoid and tracking detectors can also be seen in the inner part of the detector[6].

Inter-Cryostat Detectors (ICDs), one on each endcap. They were composed of 12 0.5" thick scintillating tiles, as shown in Figure 2.17, each covering $\Delta\eta \times \Delta\phi \approx 0.3 \times 0.4$ and separated via epoxy filled grooves into 12 $\Delta\eta \times \Delta\phi \approx 0.1 \times 0.1$ subregions, as seen in Figure 2.18.

Each subtile was read out via two 0.9 mm wavelength shifting fibers, and a third fiber, used to inject light during calibration, was also attached. These fibers ran in a 3.5mm groove along the outside edge of the subtile, and were in turn mated to 1.0mm clear optical fibers at outer radius of the tile. These clear fibers passed through a light tight "fiber backplane" and iron block (for magnetic shielding) into a drawer in a low magnetic field

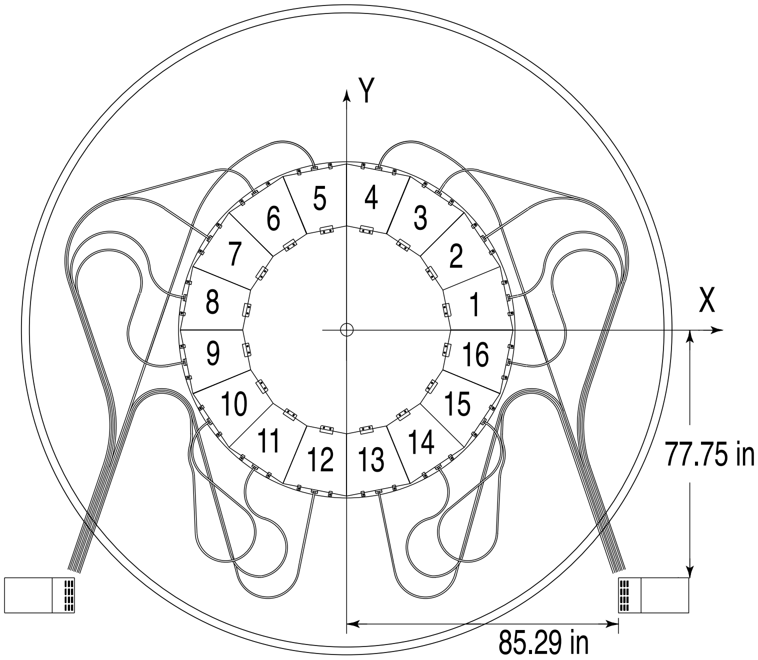

Figure 2.17: The ICD tiles are radially arranged on the surfaces of the endcap cryostats. The iron block and fiber backplane assemblies which contain the ICD electronics and PMTs are shown on each side[5].

region where they terminated in the photocathodes of PMTs.

2.3.6.3 The Central and Forward Preshower Detectors

The Central and Forward Preshower Detectors (CPS and FPS) performed both tracking and calorimetry, enhancing spatial matching between tracks and calorimeter showers, and aided in electron id and background rejection during triggering and offline reconstruction. CPS and FPS signals could be used for offline correction of EM energy measurement from losses in the solenoid and other upstream dead material. The axial layers were used to provide fast energy and position measurements which could be included in the L1 trigger, and all three layers could be used in L2 and L3.

Each preshower detector was made of sheets composed of 1280 parallel strips of

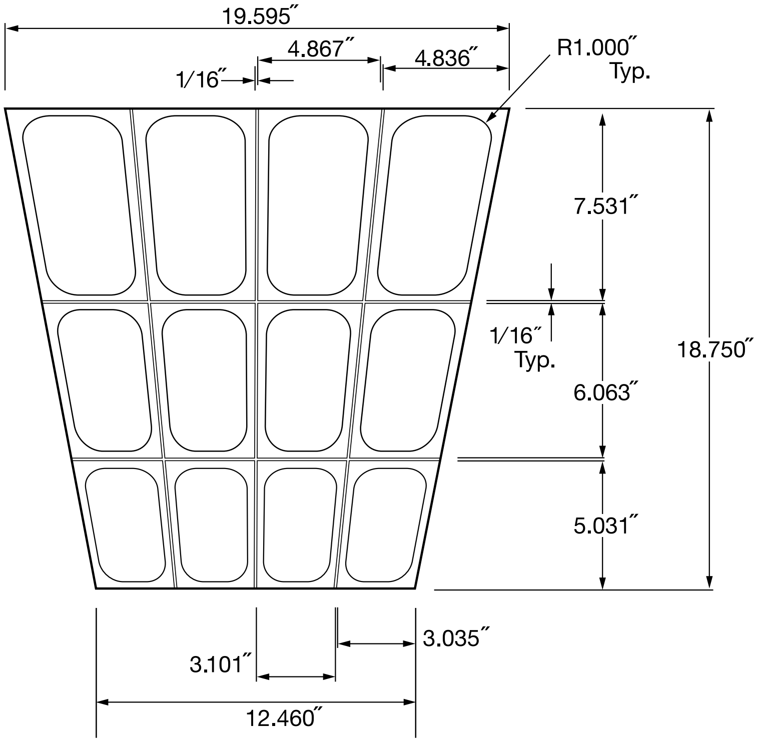

Figure 2.18: Diagram of the subdivision of an ICD tile. The WLS fibers are embedded along the edges of each of the twelvetrapezoidal subtiles[5].

scintillator.[3]The scintillator strips had a triangular cross section and were interleaved as shown in Figure 2.19, and sandwiched between 1/30 inch stainless sheets. The overlap and lack of dead space between strips allowed for improved measurement via strip-to-strip interpolation. Each strip had a wavelength shifting (WLS) fiber at its center, to collect and carry light to the end of the strip, where the fibers were grouped in bunches of 16 and connected to clear lightguide fibers going to VLPC cassettes. The WLS fibers split at $z = 0$ and read out from each end resulting in 2560 readout channels per layer - eighty sectors of sixteen-fiber groups. As in the CFT (2.3.1.2), the WLS and clear fibers were 835 μm diameter multiclad fibers.

---

[3] The strips were extruded polystyrene plastic doped with 1% p-terphenyl and 150 ppm diphenyl stilbene (similar to Bicron BC-404 scintillator). For optical isolation they were machine wrapped with aluminized

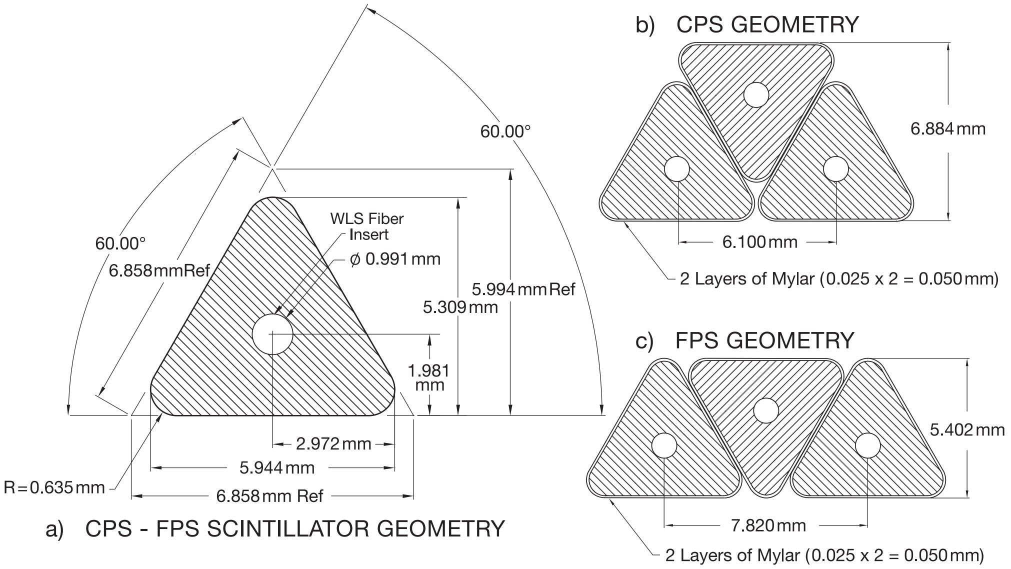

Figure 2.19: End view of the layout of the CPS and FPS scintillator strips, showing the cross sectional structure of the strips. The embedded wavelength-shifting fibers run through the centers of the strips, perpendicular to the page, as denoted by the circles[5].

The central preshower detector (CPS) had three concentric cylinder layers of the scintillator sheets in an axial-u-v geometry (with a u stereo angle of 23.774° and a v stereo angle of 24.016°) in the 5 cm gap between the solenoid and the central calorimeter, with an inner radius of 28.25 inches and an outer radius of 29.21 inches. The CPS covered $|\eta| < 1.3$. Each layer was divided into eight 45° octants, of which an "unwrapped" view can be seen in Figure 2.20.

Outside the solenoid and inside the CPS was a lead radiator cylinder, 7/32 inches, or approximately one radiation length, thick, 96 inches long, covering $\eta < 1.31$. The lead was covered with a layer of stainless steel, 1/32 inches thick, and 103 inches long. The solenoid itself was 0.9 X_0 thick, for a total of approximately two radiation lengths before the CPS at

---

mylar and the ends were painted white to enhance reflectivity.

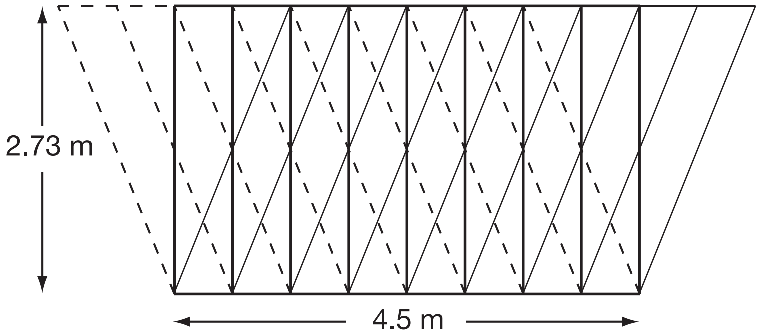

Figure 2.20: View of the CPS if it were unwrapped in a plane. Each rectangular (trapezoidal) module forms one octant of the corresponding axial (stereo) layer. The stereo octant edges align precisely with the axial octant edges[5].

normal incidence ($\eta = 0$), increasing to four radiation lengths at larger angles.

The North and South forward preshower detectors (FPS) were mounted on the spherical heads of the endcap calorimeters, between the LMs and the ICDs, and were shaped to conform to the calorimeter geometry. Each had coverage of $1.5 < \eta < 2.5$. Each FPS had two layers of scintillator, each layer consisting of two planes, each divided into 8 22.5° wedges of active material alternating with 8 wedges of inactive material, and the active material wedges in one layer are offset from those in the other layer so that there are no ϕ cracks. The active material itself is composed of two sublayers of nested scintillator strips with a stereo angle of 22.5° with respect to one another.also Between the two layers was a $2X_0$-thick absorber divided into 48 wedges covering 7.5° and weighing approximately 5 lbs. each. Each wedge consisted of a 2/8”-thick stainless-steel supportive plate sandwiched by two plates of lead.

The upstream layer was known as the “minimum ionizing particle” (MIP) layer - it measured the (η,ϕ,z) location of charged particle tracks from their minimum ionizing signal. It covered $1.5 < |\eta| < 2.5$. The downstream layer was known as the “shower layer”. The lighter particles, including chargeless particles such as photons, would shower in the absorber producing an energy cluster, typically about three strips wide, which was

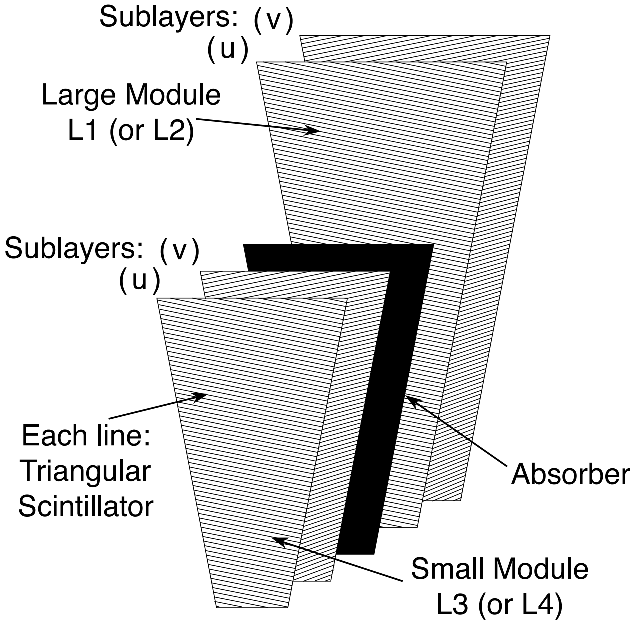

Figure 2.21: One ϕ-segment of a FPS module. Two large and two small modules, each consisting of overlapping $u - v$ MIP and shower layers, surrounded the lead and stainless steel absorber. Only one large and one small module is shown[5].

measured and matched with MIP signal, while heavier particles which do not shower so readily would usually deposit a MIP signal in the downstream layer as well. The absorber and the downstream layer covered $1.65 < |\eta| < 2.5$. Note that the region $1.5 < |\eta| < 1.65$ of the FPS, covered by the MIP layer but not the absorber or the downstream layer, was in the approximately $3X_0$ thick shadow of the solenoidal magnet coil.

2.3.6.4 Calorimeter Readout System

There was a total of 47,032 calorimeter electronics channels (of the 55,296 available) connected to the physical readout modules in the cryostats. Timing was crucial due to the bunch crossing time of 396 ns and the electron drift time of 450 ns. The system was upgraded before RunII to cope with the significant reduction in the Tevatrons bunch spacing, and could handle a minimum bunch crossing time of 132 ns (or 7.57 MHz). There were three stages of readout:

1) "Front end electronics": Detector signals were transported to preamps located on the cryostats via low-impediance ($30\,\Omega$) coaxial cable - these had been replaced for RunII to match ($30\,\Omega$) preamp input impedance, and to equalize lengths to minimize spread of signal arrival times. The preamps were "transimpedance" - charge to voltage hybrid amplifiers, and two pre-amp gain paths - $\times 1$ and $\times 8$ - were available to increase dynamical range. The 55,296 preamps were contained in twelve boxes with ninetysix motherboards per box, and fortyeight preamps per motherboard. Because access to these boxes were limited, there were two low noise commercial power supplies per box, a primary plus a backup. Because the calorimeter cells varied in impedance, fourteen species of preamp were required to give approximately the same output waveform for all cells. The motherboards were printed in eight layers, which were separated by solid copper ground or power planes to minimize noise pickup and cross talk. The motherboards also housed 10 kΩ and 20 kΩ 0.1% precision resistors used for calibration voltage pulses, with six preamps pulsed at once. These electronics were all magnetically shielded from the local residual magnetic field of a few hundred gauss.

2) "Signal shaping and trigger pickoff": A single preamp output was the integral of the detector signal, with a rise time of $\approx 450\,$ns and a recovery of 15 μs. The outputs of the preamps were transported via twisted-pair cables to analog signal shaping and storage circuits on baseline subtractor (BLS) boards. The BLS removed low frequency noise and minimized pileup by using only the first 260 ns of charge (about 2/3) collected by the preamp for signal shaping. This was converted with a shaper circuit to a unipolar signal with peak at $\approx 320\,$ns and recovery time of 1.2 μs. The converted signals were sampled every 132 ns (for three samples per bunch crossing), including a sample at the $\approx 320\,$ns peak. Baseline subtraction was accomplished by subtracting the signal from three samples (396 ns) earlier. After subtration, the signal was digitized by a 12-bit successive approximation ADC. Because of uncertainty in the subtraction, large negative energy signals could occur; this happened more in RunII than in RunI due to increased pileup, so much so that in RunII, there was an explicit luminosity dependence of some calorimeter based measurements. At the shaper

Layer	Pedestal RMS (ADC)	Pedestal RMS (MeV)
CC(EM1)	3.1	48
EC(EM1)	3.2	50
CC(EM3)	2.0	25
CC(FH1)	6.6	80
CC(CH)	6.4	297

Table 2.1: Some typical calorimeter pedestal RMS values, given in ADC units and MeV[43].

inputs, faster shaped analog sums of the signals from 0.2×0.2 trigger towers were also picked off (via resistor packs on BLS boards) to provide prompt inputs to the L1 and L2 calorimeter trigger system. The resistor packs were configured based on a sampling weight optimization study maximizing 1) electron resolution and 2) jet resolution, for the channels included in the trigger (CH sections did not contribute). The BLSs used switched capacitor arrays (SCAs) as analog storage devices; these held the signals for ca $4\,\mu$s until the L1 trigger decision was made, and could hold them up to 25 ms longer (on average 2 ms) for a L2 decision.

3) Digitization: the precision BLS signals were transmitted via analog bus, driven by analog drivers, over 130 m of twisted pair cable to the analog-to-digital converters (ADCs). The digital signals entered the data acquisition system for the L3 trigger decision and storage to tape.

Between stores, values of calorimeter pedestal signals were measured, with RMS σ (due to thermal noise) a function of the capacitance of each cell. For some typical pedestal values, see Table 2.1 The pedestal was subtracted from each readout signal. For most events, a 1.5σ zero-suppression was applied to all cells. During reconstruction, only signals with positive energies above 2.5σ were kept, and at a later stage, the high-level T42.5 algorithm further suppressed energies above 4σ unless the cell was a 3D neighbor of another cell above 4σ.

Driven by a special trigger based solely on the accelerator clock, the calorimeter was also sampled sequentially in each tick with a bunch crossing at constant low exposure; these zero-bias events were collected without any zero-suppression.

2.3.6.5 Anomalous Currents

During run time, the response of the calorimeter detectors would vary due to anomalous currents, of which there were two significant sources. One was due to high currents in the detectors during periods of high luminosity causing a decrease in the voltage drop across the liquid argon gap, the other from "dark current" due to insulating buildup on absorber surfaces.

An insulating layer of uranium oxide would form on the absorber surfaces during manufacture, and these layers collected argon ions in the detector. As the layer of argon ions built up, the field across this layer increased the number of electrons tunneling through the oxide into the gap and thereby increased the current in resistive coats. Known as the "Malter process", this effect was first seen in aluminum oxide at room temp (resisitivity $1.0 \times 10^{1}4\,\Omega$ cm), with a rate comparable to that of uranium oxide at 83K, (resistivity $1.4 \times 10^{1}6\,\Omega$ cm). When the current became high enough, the ions were quenched, and the process began anew.

The Malter effect, plus the effect of high luminosity currents across the high resistivity coating of the signal boards, led to luminosity dependence in the liquid argon calorimeter gain. There was also an η dependence as well, due to the voltage being fed from corners of calorimeter modules.

Understanding the behavior of these anomalous currents is crucial to a proper calibration of the calorimeters.

2.4 Triggering

The D0 trigger system was composed of hardware and software modules which sampled information from the various detector subsystems, and decided, based on this information, when to record detector data in high detail. It had three levels, with each successive level examining fewer events in greater detail. The Level 1 trigger (L1) had an average acceptance rate of 2 kHz (though in RunII, L1Cal could exceed 10kHz), the Level 2 trigger (L2) accepted events at a rate of 1 kHz; all data blocks for accepted events were fully digitized and sent to the Level 3 (L3) "farm" of microprocessors with sophisticated algorithms which performed fast reconstruction of high level objects on which decisions were based. L3 events were accepted at 50 Hz and these events were recorded for offline reconstruction. Due to their high acceptance frequency, L1 and L2 minimized deadtime with FIFO pipelining of event data awaiting a L2 decision or being transferred to L3 farm. Overall coordination and control of the triggering system was handled by the D0 central coordination program (COOR). COOR coordinated all trigger configuration and programming requests. Global trigger lists, containing requirements and parameters for all triggers used by the experiment, were specified using this application as were more specific trigger configurations (many of these would operate simultaneously) used for calibration and testing[5].

The trigger framework (TFW) collected single-bit signals[4] of which there were a maximum of 256 - from all the L1 trigger outputs of various detector modules. Using global D0 timing and control signals it coordinated these signals to form a maximum of 128 trigger terms (each with a separate associated programmable "beam condition" trigger requirement), decided whether or not to accept a particular event for further examination. Individual triggers could be combined to create more complex triggers. Whereas RunI only allowed for hardware "AND"ing of device outputs for individual L1 trigger terms, Run II also used software to create "pseudoterms" including "OR" operations at the L1 level. This allowed sharpening of trigger curves and reduction of combinatorial backgrounds and thus low p_T triggers. The TFW was also responsible for prescaling[5] and vetoing events. The trigger control computer (TCC) was in charge of setting up initializing the TFW before each run.

---

[4] These single-bit signals are referred to as "primitives" by the author's advisor.

[5] i.e. reducing the recording rate of very frequent events by simply ignoring some fraction of them.

2.4.1 Level 1

For the L1 calorimeter trigger (L1CAL), triggering depended in part on the fast pickoffs (see Section 2.3.6.4) of the following values:

- Global variables: $\sum E_T$ (sum of all tower E_Ts) and/or $\not{E}_T$, each with four thresholds.
- Local variables: counts of single EM and EM+H towers exceeding four possible thresholds. There were two EM count limits and four EM+H count limits.
- Large tiles: counts of partial sums (covering 4×8 trigger towers, or 1.28 in $\eta \times \phi$ space) of tower E_T, exceeding four possible thresholds. There were two EM+H count limits.

The L1 forward proton detector trigger (L1FPD) checked for small-angle scattered protons or antiprotons from diffractively-produced events. Coincidences in hits between both position detectors in a single FPD spectrometer might correspond to a single diffractive event, while two coincidences in a back-to-back configuration might signify elastic diffraction, and other two-spectrometer configurations might signify double pomeron production - any of these could cause an L1 trigger. Hits with large multiplicities were rejected since these were most likely from the beam halo.

The central track trigger (L1CTT) used field programmable gate arrays (FPGAs) with fast discriminator data from the CFT, CPS and FPS to reconstruct the trajectories of charged particles by comparing CFT hits with 20,000 predefined track equations and matching CFT tracks with CPS clusters, as seen in figure 2.22. Triggering decisions are based on momentum thresholds and cluster requirements. This trigger was optimized for making fast decisions at the L1 level using the CFT/CPS axial layers and the FPS, but the electronics also stored event data such as sorted lists of tracks and preshower clusters for later L2/L3 readout, or for use as seeds by other D0 trigger systems. L1CTT has a maximum latency of $2.5\,\mu$s.

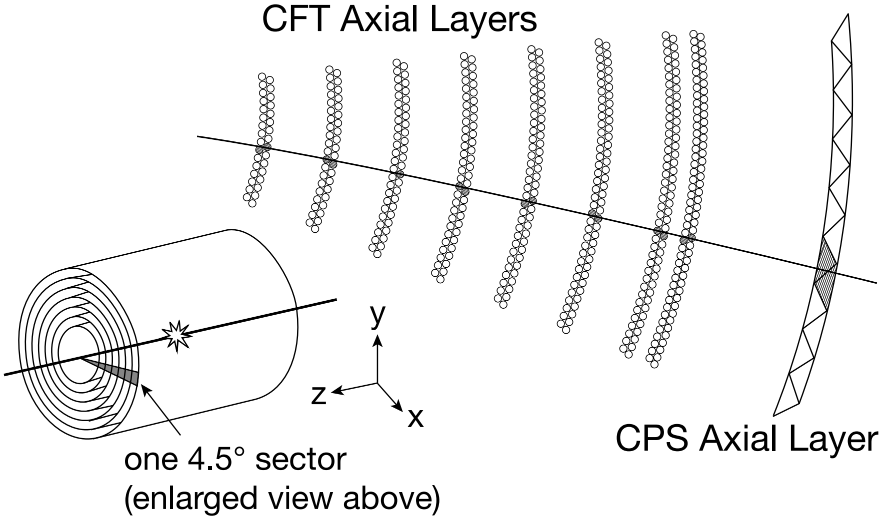

Figure 2.22: Transverse schematic (CPS is further from the CFT than shown, see Figure 2.2) view of a single 4.5° sector of the full CFT and CPS (see lower left of figure). A track is overlaid on the eight CFT axial doublet layers and CPS axial layer. The L1 trigger requires a match to a predefined equation with a fiber hit on all eight CFT axial layers and a CPS cluster match[5].

The L1 muon system trigger (L1Muon) used FPGAs to compare output from 60,000 muon channels (wire chambers and scintillation counters) and up to 480 tracks from L1CTT for every bunch crossing and search for patterns consistent with muons. L1Muon had a latency of about $3.20\,\mu$s[23].

2.4.2 Level 2

The L2 trigger could handle input rates of up to 10 kHz and had a maximum accept rate of 1 kHz. It had preprocessors for each detector subsystem to form higher quality physics objects and a global processor (L2Global) which integrated data and tested for correlations in physics signatures across detector subsystems. Events which passed L2 were tagged for full readout and further analysis in the L3 trigger.

The L2 calorimeter trigger (L2Cal) preprocessor identified jets, electrons, and photons, and calculated event $\not{E}_T$ from using the E_T data from the 2560 calorimeter trigger towers. Jet cluster energies were measured from groups of 5×5 calorimeter trigger towers centered on seed towers from L1, with algorithms for separating or discarding overlapping jets. The list of jets was passed to L2Global. The energies of electrons and photons were measured by summing the E_T of the seed tower with the E_T of the highest energy neighbor tower, and comparing it with the energy of a 3×3 tower centered on the seed tower to reduce background. Electron candidates were sent to L2Global. The $\not{E}_T$ algorithm could use different tower E_T thresholds and η ranges.

The L2 Muon trigger (L2Muon) used calibration and more precise timing information to improve the quality of the muon candidates. It received the L1Muon output and data from approximately 150 front-end modules (from the PDTs, MDTs, and the scintillation counters). The muon candidates contained the track p_T, η and ϕ coordinates, and quality and timing information.

The L2 preshower detectors trigger (L2PS) compared signals of early shower development in the CPS and FPS with tracks and calorimeter clusters. At L2, CPS and FPS were treated separately. CPS axial clusters were tagged by L1 with the presence (possible electron) or absence (possible photon) of a CFT track. At L2, clusters in the other two stereo layers of the CPS that lined up with the axial clusters were sought, and if found, the three centroids were compared to produce an (η, ϕ) coordinate for the cluster. These coordinates were binned to match up with calorimeter trigger towers with $\Delta\eta \times \Delta\phi = 0.2 \times 0.2$. Any preshower hit within 0.05 of a trigger tower was designated a calorimeter match. A similar process of matching between preshower clusters and calorimeter towers was done with the FPS and the EC.

The L2 central track trigger (L2CTT) used track information from the L1CTT and refined the p_T measurements using the additional hit and tracking information available from the CFT at L2, with an optional mode to also use input from the L2STT (see below). It determined the azimuthal angle with respect to the beamline, ϕ_0, and calculated the expected azimuthal angle at EM3 due to the solenoidal magnetic field. Isolation values were also calculated to help identify tau leptons. The L2 tracks were passed to L2Global sorted by p_T; if input from L2STT was used, the list was also sorted by impact parameter.

The SMT did not provide trigger input until L2. The SMT track trigger (L2STT) utilized the much finer spatial resolution of the SMT to improve the position and momentum measurement of charged particle tracks found by the CFT. It used only the (r,ϕ) information from three of the four layers of axial SMT strips together with the inner and outer layer of the CFT to precisely measure the impact parameter of tracks. This measurement helped identify long-lived particles, such as B hadrons, at L2.

2.4.3 Level 3

Level 3 triggering was performed in software, on a farm of commodity CPUs. Physics objects are created with "object specific software algorithms" and triggering was performed based on the following characteristics of these objects:

- Level 3 jets and electrons: The L3 jet tool used high precision calorimeter and vertex data with a jet cone algorithm and rejection of hot cells to identify jets with high efficiency, as can be seen in Figure 2.23. E_T, EM/H fraction and transverse shower shape were used to distinguish electrons from hadronic jets, achieving jet rejection factors of 20-50.

- Level 3 muons: At Level 3, track-finding algorithms linked segments constructed from wire and scintillator hits to identify three-dimensional muon tracks, which were matched with tracks in the CFT. Cosmic ray muons were discriminated against based on timing characteristics deduced from their velocities and candidate tracks, as well as association with an incoming track.

- Level 3 $\not\!\!E_T$: At Level 3, the $\not\!\!E_T$ was calculated in more detail, via individual cells in pseudorapidity ring sums, and corrected for a non-$(0,0,0)$ vertex when possible. This

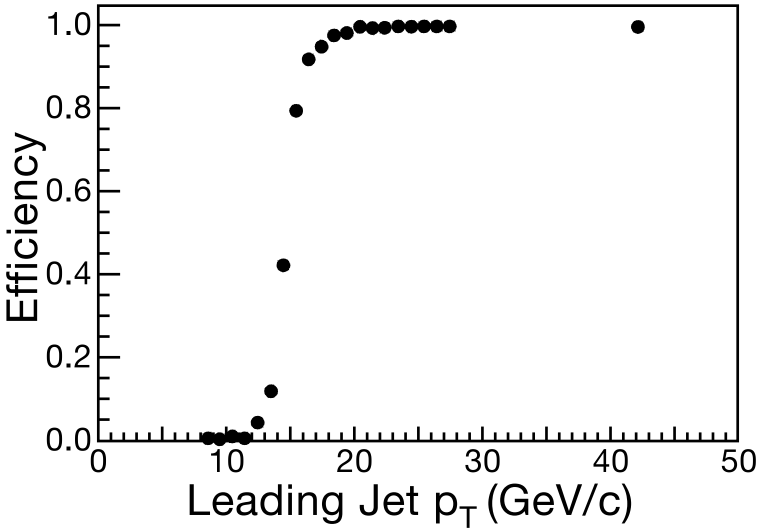

Figure 2.23: Efficiency of the L3 jet trigger as a function of the offline leading jet p_T. Note the turn-on due to the online selection cut of 15 GeV/c applied by the L3 filter. Statistical errors are plotted, but for most points are obscured by the symbol[5].

provided e.g. stricter selection of top quark events and redundancy for selection of W boson events.

- Level 3 tracking: At this level, more detailed information from the trackers was fed through more complex algorithms. CFT tracks were fit in two steps, first to circular arcs S in the $r - \phi$ plane, and then to "straight" lines in the $S - z$ plane. SMT tracks were fit to helical paths in a single step.

- Level 3 relational filters: At this level, the measurements from multiple physics objects could be combined in any way to derive quantities such as invariant mass, relative angle, and scalar E_T sums. Additional selections were made based on these combinations. The D0 single electron trigger, described in Section 2.4.4, was such a filter.

Trigger	L1	L2	L3
E1_SHT5 (v16)	$E_T > 19$ GeV	$E_T > 25$ GeV or $E_T > 19$ GeV and likelihood	$E_T > 25$ GeV cut and shower shape requirements
E1_SHT7	$E_T > 19$ GeV	$E_T > 25$ GeV or $E_T > 19$ GeV and likelihood	$E_T > 27$ GeV cut and shower shape requirements

Table 2.2: Single EM triggers - from [19]

2.4.4 The D0 Single Electron Trigger

In collecting data for the W mass measuremnt, the D0 single electron trigger was crucial. Two different unprescaled triggers were used E1˙SHT25 (v16) and E1˙SHT27. The L1 and L2 stages of the two triggers were identical: a calorimeter electron cluster with transverse energy greater than 19 GeV for L1, and a further cut at 25 GeV for L2, unless the cluster satisfied a shape-based likelihood criterion (see Section 5.2.3.1). L3 however, could vary. During the beginning of a store, when InstLumi was high, the experiment used the E1_SHT7 trigger with L3 p_T cut of 27 GeV to reduce QCD background and keep trigger rates acceptable. Later in the store, when InstLumi decreased, the experiment used the E1_SHT5 trigger with L3 p_T cut of 25 GeV.

Chapter 3

MEASUREMENT STRATEGY

3.1 Event Characteristics

W and Z bosons are produced at the Tevatron mainly through valence quark-antiquark annihilations with smaller contributions from the quark sea. The initial state radiation is mostly soft gluons, but sometimes the gluons have enough energy to create hadron jets; this leads to a long tail of bosons with high p_T. After the collision, conservation of momentum (which is zero in the transverse direction) means that the boson p_T (measured from its decay products) must be balanced by the collective transverse momentum of all other event products ("hadronic recoil").

Both W and Z production is exploited in the W mass measurement. As the measurement sample we use the electron channel of the W boson decay, $p\bar{p} \rightarrow (W^{\pm} \rightarrow e^{\pm}\nu) + X$, and as the calibration sample we use the electron channel of the Z boson decay, $p\bar{p} \rightarrow (Z \rightarrow ee) + X$. The size of the $Z \rightarrow ee$ sample is limited by its relatively small branching fraction $\mathrm{BR}\,(Z \rightarrow ee)\,/\mathrm{BR}\,(W \rightarrow e\nu) = 0.31$. Note that in this dissertation, "electron" means "electron or positron" unless specifically noted.

Candidate W boson decay events are characterized by measurements of i) the transverse electron momentum $\vec{p}_T^{\,e}$, ii) the transverse hadronic recoil $\vec{u}_T$, and iii) the missing transverse energy, $\vec{\not{E}}^{T} = -\left(\vec{p}_T^{\,e} + \vec{u}_T\right)$ (also referred to as "MET" in this dissertation), corresponding to the energy of the decay neutrino which escapes without leaving any signal in the detector. Candidate Z boson decay events are characterized by measurements of i) the transverse electron momenta p_T^{e1} and p_T^{e2}, and ii) the transverse hadronic recoil u_T. Electrons (and neutrinos) from W and Z boson decays typically have transverse momentum of about half the mass of the decaying boson, and are well isolated in the calorimeter. Electrons may

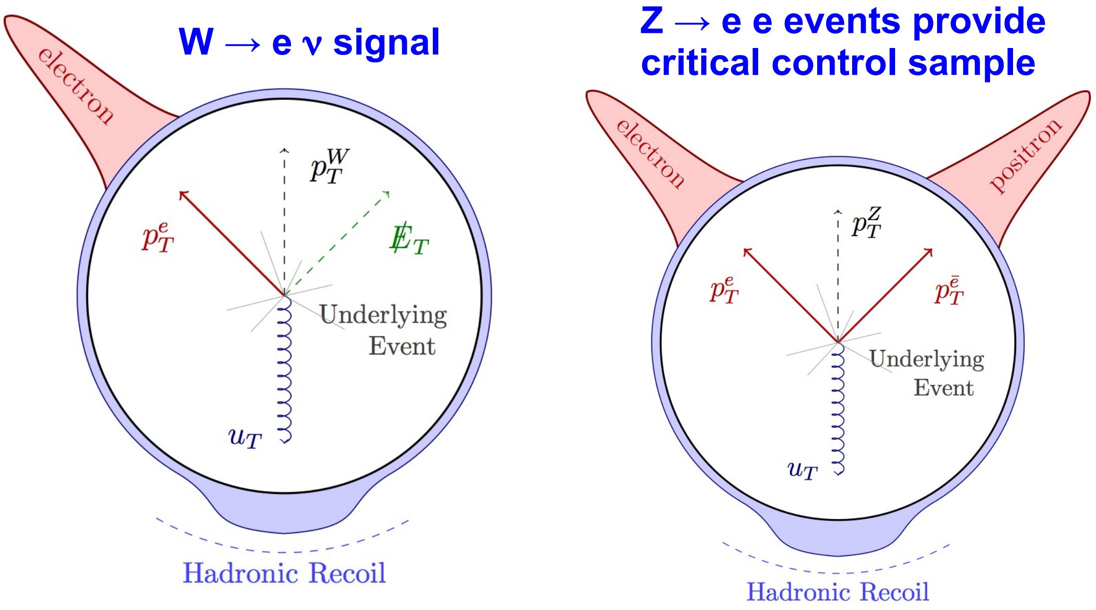

Figure 3.1: Schematic of transverse quantities from $W \to e\nu$ and $Z \to ee$ events in the D0 detector.

radiate one or more photons via final state radiation (FSR), or by bremsstrahlung in dead material before the calorimeter. At the Tevatron, W and Z decays were the primary source of high p_T, isolated electrons, allowing for a clean sample selection.

The electron in a sample W candidate event (and at least one of the two electrons in a Z candidate event) is required to have $|\eta_{\text{det}}| < 1.05$, whereas the hadronic recoil is measured from all other particles with $|\eta_{\text{det}}| < 4.2$. Particles with $|\eta| > 4.2$ were not measured by the calorimeters, but their contribution to the recoil transverse momentum is negligible. The D0 calorimeter provided a precise measurement of electron energies, with an average resolution of 4.5% across the angular and energy spectrum of electrons used in the measurement.

3.2 Mass Measurement Strategy

We measure the W mass from distributions of the magnitudes of the following three kinematic observables: i) the W transverse mass, m_T, ii) the electron transverse momentum,

p_T^e, and iii) neutrino transverse momentum, $\not\!\!E_T$. Transverse quantities were used because, in a $p\bar{p}$ collision, the longitudinal momentum of the center-of-mass of interacting parton pairs is undetermined due to the shape of the parton density function (PDF) at relativistic speeds, and therefore, the longitudinal momentum of the neutrino is impossible to deduce. While in theory longitudinal electron momentum information from the tracker could be used, for this study, it was not.

Using three distributions measured from the same data sample increases the precision of the measurement - the less correlation between the different measurements, the more powerful the combination of the results. The systematic uncertainties of the m_T and p_T^e measurements are only weakly correlated: the m_T spectrum is dominated by the detector resolution via the recoil energy measurement, while the p_T^e spectrum is mainly affected by the transverse momentum of the W boson, and hence by the kinematics of the recoil system and initial-state radiation, as seen in Figure 3.2. The $\not\!\!E_T$ measurement is moderately correlated with the other two measurements and has a significantly worse resolution, but still adds some precision to the measurement.

The measurement strategy is to compare the measured distributions to predicted distributions whose shapes depend on M_W, and determine M_W from the best match. Because of complicated detector acceptance, scaling, and resolution effects, the distributions of the measured variables cannot be calculated analytically. Therefore, Monte Carlo simulations with varied W masses must be used to generate test distributions, called "templates". Very high statistics of $\approx 10^9$ events are necessary to characterize all the systematic uncertainties with negligible statistical uncertainty. The detailed D0 detector simulation (FullMC) is too slow to generate many samples of this size, and in addition it does not reproduce the detector performance in data with sufficient precision to measure the W boson mass. Therefore, a parameterized Monte Carlo simulation (FastMC) has been developed to generate large samples on a reasonable time scale. To check that the FastMC is sufficiently accurate for the measurement of the W boson mass, we test for "closure", which means that when we perform a test measurement of the W boson mass using FullMC data with FastMC templates, we

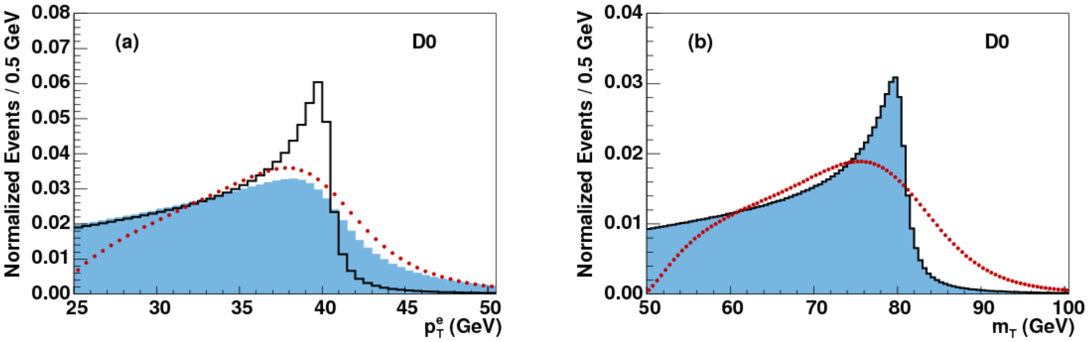

Figure 3.2: The (a) p_T^e and (b) m_T spectra for simulated W bosons with various levels of detector effects simulated. The solid lines show the spectra without detector resolution effects for W bosons with transverse momentum $p_T^W = 0$. The shaded area shows the spectra without detector resolution effects for W bosons with the range of p_T^W seen at the Tevatron. The points show the spectra with detector resolution effects for W bosons with the range of p_T^W seen at the Tevatron.

get the same value of the W mass out that the FullMC used to generate events.

An added benefit to the parameterized FastMC is that, while the FullMC does not perfectly simulate data, the FastMC can be tuned to match the data even better than the FullMC can. Therefore, we create two versions of the FastMC: one which is tuned with information from the FullMC generated sample, and a modified version of the first tune which is adjusted to match the data. The tuning procedure is described in detail in Chapter 7.

We mainly use $Z \to ee$ events (in FullMC and data) to determine the FastMC parameters. For example, the EM calorimeter energy scale used for simulation is based on a detailed study of the shape of the Z mass peak in data or FullMC. Since the calibration depends on the Z mass which has been measured with high precision[3], the measurement can be thought of as a measurement of the ratio of W to Z mass. Hower, since the W mass is about 20% lower than the Z mass, care must be taken to ensure that the EM calorimeter energy scale is valid at the lower average energies of the W electrons. A FullMC simulation of the $Z \rightarrow \nu\nu$ process is also used to aid in determination of some of the hadronic recoil parameters, as described in Section 7.4.1.

Once the detector response is well parameterized, the W mass is determined with a "binned likelihood" method. Distributions of the three observables, m_T, p_T^e, and $\not{E}_T$, are constructed from the data sample and from FastMC samples generated with a range of input W masses in increments of 10 MeV. For each observable, the data distribution is compared with the FastMC distributions ("templates") for that observable by calculating the log-likelihood using the Poisson probability that bin i which has m_i template events would have n_i observed (data) events. The total likelihood is the product of individual bin probabilities:

$$\mathcal{L} = \prod_{i=1}^{N} \frac{e^{-m_i} m_i^{n_i}}{n_i!} \tag{3.1}$$

and taking the negative natural logarithm gives

$$-\ln \mathcal{L} = \sum_{i=1}^{N} \left(-n_i \ln m_i + m_i + \ln\left(n_i!\right)\right) \tag{3.2}$$

The fitting program `MINUIT` is then used to find W mass which maximizes likelihood, interpolating between the $\left(m_{W_i}, -\ln \mathcal{L}_\rangle\right)$ pairs.

3.3 Blinding the W Mass to Avoid Bias

Because we do not want to bias our measurement procedure towards a particular desired outcome of the W mass measurement, we use a blinding procedure by which we add a random, recoverable number between ±2GeV to the mass in the process of the calculation. This is performed in the code, so we do not see the value of the random number. This allows us to perform studies of systematic effects ("sensitivity methods"). The same number is added to the mass for both RunIIb3 and RunIIb4, so we can see tensions between the measurements from the two samples despite the blinding. When we have developed our measurement strategy to a satisfactory level, we "unblind" our measurement, recovering the final value for the measurement of the W boson mass in data.

3.4 Systematic Uncertainties

The effects of systematic uncertainties in the parametrization (see Chapter 7) on the W boson mass are determined using an ensemble of pseudo-experiments simulated in fastMC. To determine the systematic uncertainty on the W mass due to the uncertainty on a given parameter, pseudo-experiments are generated in which that parameter is varied independently in steps of multiples of $\pm 0.5\sigma$, where σ is the one standard deviation uncertainty for the parameter under study) while holding all other parameters constant.

For each variation, M_W is determined using the standard fit method comparing the unmodified distribution to the templates generated by the pseudo-experiment. This yields a value M_{W_i} for each variation δ_i. The set of (δ_i, M_{W_i}) pairs is fitted to a straight line. For all systematic uncertainties in this measurement, we verify that the linear regime assumed by this procedure is a valid approximation. The slope of the line determines the systematic uncertainty in M_W as in the usual error propagation:

$$\sigma^2_{M_W}(X) = \left(\frac{\partial M_W}{\partial X}\right)^2 \sigma^2_X \tag{3.3}$$

where σ_X is the uncertainty in the determination of the parameter X in the simulation. If a set of parameters are correlated, then the uncertainty in M_W due to the set of parameters $\vec{X}$ is

$$\sigma^2_{M_W}\left(\vec{X}\right) = \sum_{i,j} \left(\frac{\partial M_W}{\partial X_i}\right) C^X_{ij} \left(\frac{\partial M_W}{\partial X_j}\right) \tag{3.4}$$

where C^X is the correlation matrix for the parameters $\vec{X}$.

3.5 Conventions

A momentum vector $\vec{p}$ in the D0 standard coordinate is represented using a right-handed Cartesian coordinate system, p_x, p_y, p_z, where $\hat{z}$ is the direction of the proton beam and $\hat{y}$ points upward. It is convenient to use a cylindrical coordinate system in which the same vector is given by the magnitude of its components perpendicular to the beam (transverse momentum) p_T, its azimuthal angle ϕ, and p_z. In spherical coordinates, the polar angle θ is sometimes replaced by the pseudorapidity $\eta = \ln\left(\tan\frac{\theta}{2}\right)$. When refering to instrumental effects, sometimes it is convenient to define η_{det} as the pseudorapidity of the particle determined as if it had been produced at the center of the calorimeter.

3.6 Additional Kinematic Variables

In $Z \to ee$ decays, the di-electron momentum is $\vec{p}_{ee} = \vec{p}^{e_1} + \vec{p}^{e_2}$ and the invariant mass is $m_{ee} = \sqrt{2E^{e_1} \cdot E^{e_1}\,(1 - \cos\omega)}$, where ω is the opening angle between electrons. When working with $Z \to ee$ data, it is useful to define a coordinate system in transverse plane first introduced by UA2[12] and reproduced in Figure 3.3. These coordinates depend on the electron directions, but not their energies. The $\hat{\eta}$ axis is the inner bisector of the electron momenta, and $\hat{\xi}$ is perpendicular to $\hat{\eta}$. These variables describe the balance of momentum in events and are of particular use when determining final adjustments to the FastMC simulations (Section 7.4.5). For $W \to e\nu$ decays, to study the correlation between the recoil system and the electron direction, one useful quantity is the projection of the recoil system's transverse momentum onto the direction of the electron transverse momentum: $u_{\|} = \vec{u}_T \cdot \hat{p}^e_T$, and another useful quantity is the magnitude of the remaining component, perpendicular to the electron direction: $u_{\perp} = \vec{u}_T \cdot (\hat{p}^e_T \times \hat{z})$. (See Figure 3.3) These quantities can also be calculated for each electron from a $Z \to ee$ event. The $u_{\|}$ observable, because it describes the degree of "overlap" between electron energy and recoil energy, has significant correlation with electron efficiency and energy measurement, and both $u_{\|}$ and $u_{\perp}$ distributions are used to check the quality of the FastMC simulations.

Another useful quantity which reflects the total hadronic activity in the calorimeter is the Scalar E_T or SET: the scalar sum of all transverse energies in the calorimeter, except electron energy. Its average value is correlated with the instantaneous luminosity (InstLumi). Its significance is discussed in Section 7.2.4 and other parts of Section 7.2.

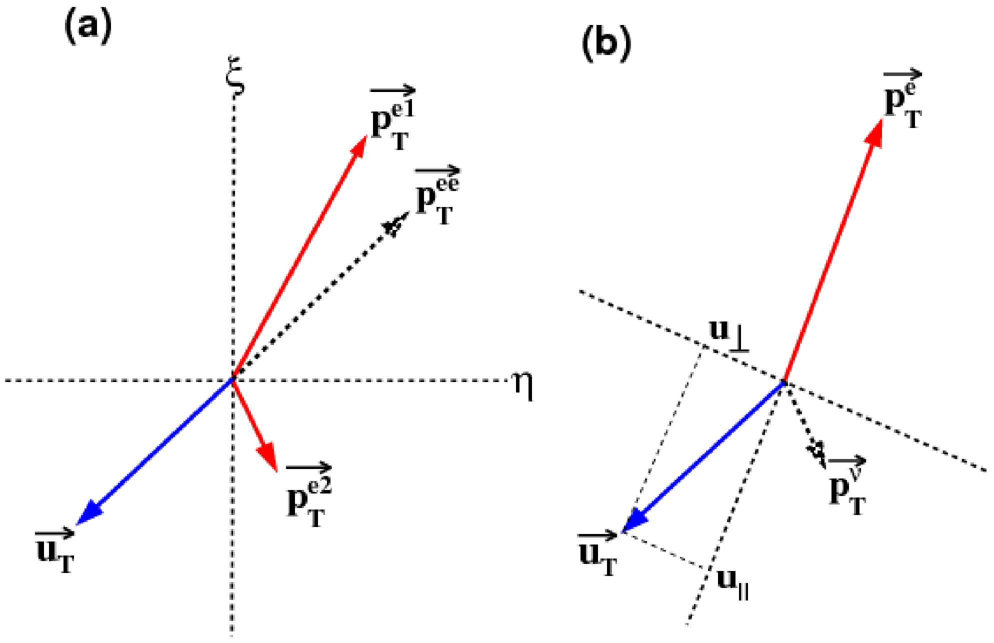

Figure 3.3: (a) Definition of η and ξ axes for $Z \to ee$ events. (b) Definition of $u_\parallel$ and $u_\perp$. The variable $u_\parallel$ is negative when opposite to the electron direction. See Section 3.6 for more information.

Chapter 4

COLLIDER DATA, FULLMC SAMPLES, AND GENERATORS FOR FASTMC

Some important aspects of the collider data and simulated data samples are discussed in this chapter. In the first section, we describe the data samples used to measure the W mass and to tune the FastMC simulations. In the second section, we describe various FullMC samples which are used to tune the FastMC simulations described in detail in Chapter 7 and also used as mock data to test the accuracy and precision of our analysis strategy. In the third section we describe the event generators which are used to simulate the $p\bar{p}$ collisions for the FullMC and the FastMC simulations.

4.1 Collider Data Samples

For this analysis, we use three main samples of events from the $3.7\,\text{fb}^{-1}$ of collider data, with special selections applied, called "skims." The sample from which we measure the W mass is called the "EM+MET" skim, the sample we use to tune our FastMC simulations is called the "2EM" skim, and the sample we use to estimate background contribution is called the "EMJET" skim. The selection requirements for the three skims, which are each separated into a RunIIb3 and a RunIIb4 sample, are described below.

EM+MET:

- One EM object with $p_T > 20\,\text{GeV}$, $|\eta_{\text{det}}| < 1.2$, and EMF > 0.9
- $\not\!\!E_T^{\text{raw}} > 20\,\text{GeV}$

2EM:

- Two EM objects, each with $p_T > 20\,\mathrm{GeV}$, EMF > 0.9, and ISO < 0.2

EMJET:

- One EM with $p_T > 20\,\mathrm{GeV}$, $|\eta_{\mathrm{det}}| < 1.2$, EMF > 0.9, and ISO < 0.2
- One jet with $p_T > 20\,\mathrm{GeV}$, $|\eta_{\mathrm{det}}| < 0.8$, or $1.5 < |\eta_{\mathrm{det}}| < 2.5$, $0.05 <$ EMF < 0.95, CHF < 0.4, HCR < 10, n90 > 10

Where EMF is the electromagnetic fraction, ISO is the isolation, CHF is the coarse hadronic fraction, HCR is the hot cell ratio which is proportional to the fraction of hot cells in the measurement cone, and n90 is the number of jets with 90% of the total p_T^{jet}.

The last $3.7\,\mathrm{fb}^{-1}$ of data are split into a RunIIb3 and a RunIIb4 sample for each skim.

4.2 FullMC Samples

FullMC events are created in two steps. First, the collision is simulated with a particle physics simulator (the "generator", which is described in Section 4.3). The output of the generator is a list of the products of the collision(s), their particle ids, and their four-momenta. Then, a full detector simulation processes this output, simulating the interaction of the particles with the detector, in particular, the tracker and the calorimeter. The output of the full detector simulation contains the tracker hits and calorimeter energy deposits, in the same format as the output from a full collider run, so that the same reconstruction process can be applied to FullMC as it is to collider data.

4.2.1 Detector Simulation

`GEANT` (GEometry ANd Tracking) is a software package used for the simulation of the passage of particles through matter using Monte Carlo methods with our current best understanding of material physics. The D0 version is often referred to as `D0gstar`[1]. The output of the generators - the list of particle four-vectors - are passed to `GEANT`, which simulates their interaction with the detector. The output is passed to the `D0sim`[2] software for Analog-Digital Converter (ADC) simulation, resulting in the final sample on which "data" reconstruction is performed.

We simulate the energy of other $p\bar{p}$ interactions in the detector with an overlay of non zero-suppressed Zero Bias (unzsup ZB) events from recorded collider data. To perform the overlay for a given event, an unzsup ZB data event chosen randomly from a library of unzsup ZB collider data events with the appropriate luminosity profile (indicated by LBN, see Section 2.2), its raw cell energy is added to the raw cell energy from `D0gstar`, and the sum is converted to ADC counts with standard zero-suppression applied (Section 2.3.6.4). This energy is converted to calorimeter energy sums in the reconstruction process (Chapter 5).

Standard `D0reco` is used for the FullMC reconstruction with a primary vertex reconstructed from the reconstructed charged particles as is done with collider data. For the single electron/photon sample used for the geometrical energy correction and for the photon radiation studies (Chapter 6 and Sections 7.2.2 and 7.3.1), the transverse energies are calculated using the generated primary vertex rather than the reconstructed vertex.

Table 4.1 describes the MC samples used in this study, including the corresponding integrated luminosity. Note that for the simulated events, a much higher Integrated Luminosity (with the same InstLumi profile) is available, allowing for precise measurements for tuning the FastMC and testing the analysis procedure. The Minimum Bias sample was pro-

---

[1] "`GEANT` Simulation of the Total Apparatus Response"

[2] Version 20.17.03 is used for RunIIb3 samples and version 20.19.02 is used for RunIIb4 samples.

Process	$\int \mathcal{L}dt$	# Events	Description
$Z \to ee$	RunIIb3: 43 fb^{-1} RunIIb4: 51.8 fb^{-1}	12.8 M 15.4 M	Underlying Event Turned on
$W \to e\nu$	RunIIb3: 20 fb^{-1} RunIIb4: 24 fb^{-1}	50.2 M 60.4 M	Underlying Event Turned on
$Z \to \nu\nu$		10 M 10 M	
Min Bias		54.7 M 53.6 M	
Single Neutrino		21 M 21 M	"ZB-only" sample
Single Electron			Unknown # Events

Table 4.1: The `GEANT` FullMC samples that were generated for RunIIb34.

duced from inelastic $p\bar{p}$ events generated by `PYTHIA` and processed with `GEANT`. The Single Neutrino sample, described in detail in Section 7.4.1, is used to calculate the hard recoil in $Z \to ee$ events. ZB overlay is applied for all samples.

4.3 Event Generation for FullMC and FastMC

Events for the Full Detector Monte Carlo samples (FullMC) are generated with `PYTHIA` version 6.409 and PDF lib CTEQ6L1. To generate the spectator particle interactions (the underlying event), we use the "tune A" version of `PYTHIA`, verified by the CDF collaboration using RunI data in 1987[53], with the standard initial-state radiation and final-state radiation (FSR) are turned on.

The events are generated for the `GEANT` FastMC and the data FastMC in slightly different ways.

For the `GEANT` FastMC, which is used to simulate the `GEANT` FullMC, events are generated in exactly the same way as they are for the FullMC (using `PYTHIA`)[20].

For the data FastMC, `PYTHIA` does not simulate the p_T spectrum sufficiently. No single generator includes complete QCD and EW corrections. Therefore, events are generated with `RESBOS`[3] + `PHOTOS`[21]. At low boson transverse momentum, the p_T spectrum is dominantly driven by QCD emission of multiple soft gluons, described well by `RESBOS`. The dominant electroweak (EW) effect is final state radiation (FSR) photons which originate directly from the W decay, `PHOTOS` is run with a limit of two FSR photons, and the effect of additional photons is absorbed into the calibration of the electron energy scale based on $Z \to ee$ events (Section 7.3.3.2). Initial state radiation (ISR) and other EW effects are not simulated, but the systematic uncertainty due to their absence has been determined from studies using the generators `WGRAD`[56] and `ZGRAD`[55], which do include those effects.

For both data and `GEANT` FastMC, Zero Bias and Minimum Bias are each selected from libraries, however unlike for the FullMC, they are libraries of the reconstructed vector momenta of the jets and electrons in the event, not distributions of raw cell energies.

---

[3] Software version dated Feb 8, 2011

Chapter 5

DATA RECONSTRUCTION

5.1 Data Samples

After triggering and removal of bad data [1], RunIIb34 has 3.7 fb^{-1} of data. [2] The purpose of the offline data reconstruction is to convert detector energy measurements into higher level objects such as electrons, jets, and other energy sums; the characteristics of these objects are used to select candidate events. The raw data has already been filtered by the DZero triggers, the highest level of which is the single electron trigger. We further process events that have passed this final trigger to derive useful quantities to characterize events. Some quantities characterize the electron candidates(s) in the event: Energy and momentum measurements of the electron candidate(s), shape and spatial characteristics of the detector signals, and association with a charged particle track. Other quantities characterize the full event: Scalar Energy sums and momentum sums (equivalent to missing energy).

None of these quantities can be measured perfectly, of course. The electron energy deposited in the calorimeter is not perfectly isolated from the hadronic recoil energy, and both of these quantities may be modified by FSR (Section 3.1). Besides the collision of interest, every event has additional contributions from pileup (other proton-antiproton interactions) and the spectator particle interactions. In addition, the energy from all these products are modified by detector response and detector noise. With the exception of the Dead Material Correction (Chapter 6), these effects are modeled by the Fast MC (Chapter 7). As RunIIb12 had a much higher instantaneous luminosity than RunIIa, the W mass measurement from that data required a great effort dealing with the effect of multiple interactions (pileup) as

---

[1] I.e. data taken at low energy, or during detector failure or beam malfunction.

[2] For comparison, RunIIa had 1.0 fb^{-1} of data, and RunIIb12 had 4.3 fb^{-1} of data.

well as significant variation in calorimeter gain at high beam intensity. The measurement with RunIIb34 data, taken at even higher luminosity, required similar techniques and effort.

5.2 Observables for Electron Identification

5.2.1 Preliminary Electron Energy and Momentum Measurements

In the CC, the measured raw electromagnetic energy $E_{\text{EM}}^{\text{raw}}$ associated with an electron is defined as the energy contained in the electron reconstruction window, or "cone", i.e. the EM calorimeter cells whose centers are within 0.2 radians in the (ϕ, η) plane of the center of the highest transverse energy tower.

In the CC, the measured raw total energy $E_{\text{Tot}}^{\text{raw}}$ associated with an electron is defined as the raw electromagnetic energy plus the energy in the hadronic calorimeter cells within two "nearest neighbor" cells of the same highest transverse energy tower mentioned in the previous paragraph.

The above two quantities are defined to test whether an electron passes the EMF requirement (Section 5.2.2). If it passes, another quantity is defined, simply called the raw electron energy $E^{e,\text{raw}}$. This quantity is equal to the raw electromagnetic energy plus the energy in the first fine hadronic layer cells of the calorimeter, in the same window defined in the previous paragraph.

The raw electron vector momentum is given by

$$\vec{p}^{e,\text{raw}} = E^{e,\text{raw}} \begin{pmatrix} \sin\theta^e \cdot \cos\phi^e \\ \sin\theta^e \cdot \sin\phi^e \\ \cos\theta^e \end{pmatrix} \tag{5.1}$$

The raw electron transverse energy (we refer to the electron energy and momemtum interchangeably, since its mass is negligible) is defined as $p_T^{e,\text{raw}} = E^{e,\text{raw}} \sin\theta^e$.

Corrected quantities $\vec{p}^e$ and E^e will be obtained later in the reconstruction procedure by applying the Dead Material Correction (Chapter 6).

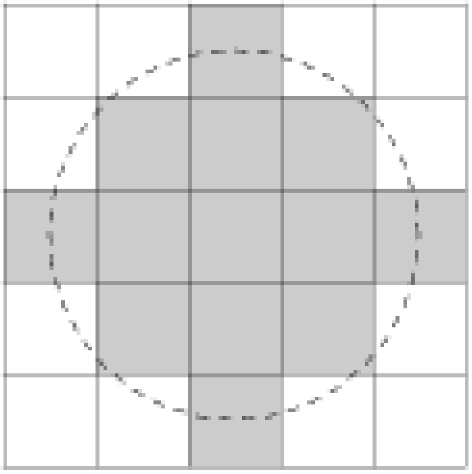

Figure 5.1: The electron reconstruction window, defined in the CC as the thirteen towers whose centers are contained in a radius $\Delta R = 0.2$ cone centered on the tower with the highest transverse energy[6].

5.2.1.1 Electron Energy Window in the Endcap Calorimeter

Due to the geometry of the EC, the calorimeter cells are closer to the beam line than in the CC. Therefore, the electron window has a more complex definition here. There are two conditions. The first depends on the hottest cell in the cluster's distance from the beam axis and its depth in the calorimeter (because the density of calorimeter cells varies with distance from the beam line). To be included in the electron cluster, an EC calorimeter cell must satisfy

$$\Delta\bar{R} \leq 1 + \frac{64}{2\pi} \cdot \frac{r_{\mathrm{EC}}}{r_{\mathrm{est}}} \tag{5.2}$$

where $r_{\mathrm{EC}} = 10\,\mathrm{cm}$, $r_{\mathrm{est}} = \sqrt{x_{\mathrm{hot}}^2 + y_{\mathrm{hot}}^2}$ and $\Delta\bar{R}$ is measured in nearest-neighbor cells. In addition (because a cell based count alone would result in a deformed cone), the cell coordinate must satisfy

$$\sqrt{(x_{\mathrm{hot}} - x_{\mathrm{proj}})^2 + (y_{\mathrm{hot}} - y_{\mathrm{proj}})^2} < r_{\mathrm{EC}} \tag{5.3}$$

where $x, y_{\mathrm{proj}} = x, y_{\mathrm{cell}} \times \frac{z_{\mathrm{hot}}}{z_{\mathrm{cell}}}$.

5.2.2 EM Energy Fraction

Electrons deposit nearly all of their energy in EM layers, therefore we expect the electromagnetic energy fraction

$$f_{\mathrm{EM}} \equiv \frac{E_{\mathrm{EM}}^{\mathrm{raw}}\left(\Delta R < 0.2\right)}{E_{\mathrm{Tot}}^{\mathrm{raw}}\left(\Delta R < 0.2\right)} \tag{5.4}$$

to be close to one.

5.2.3 Electron Spatial Characteristics

5.2.3.1 H-Matrix Criterion

An important observable used in the identification of electrons is the H-Matrix criterion which quantifies the degree to which the shower shape of an electron candidate looks like that of an ideal electron shower.[3] Detailed Monte Carlo simulations have been shown to model electron showers correctly. From large number S MC generated electron shower samples, an N-dimensional covariance matrix is built for N observables describing an electron shower.

$$M_{ij} = S^{-1} \sum_{s=1}^{S} \left(x_i^s - \bar{x}_i\right)\left(x_j^s - \bar{x}_j\right) \tag{5.5}$$

The inverse of this matrix $H = M^{-1}$ is used with a candidate signal in the calorimeter, to calculate a quantity χ_t^2 whose inverse is a measure of how electron-like a cluster is.

$$\chi_t^2 = \sum_{i=1,j=1}^{N} \left(x_i^t - \bar{x}_i\right) H_{ij} \left(x_j^t - \bar{x}_j\right) \tag{5.6}$$

To understand how χ_t^2 can describe how electron-like a cluster is, consider the effect of the measurement of the i-th observable on the sum above. The closer it is to the “average”

---

[3] It is referred to as “EMID” in many publications, however we will always refer to it as H-Matrix in this dissertation.

value, $\bar{x}_i$ of the observable (relative to the variance of the observable, M_{ii}), the smaller the contribution to χ_t^2. But, it does not have to be too close to the average for the cluster to get a good score. If it and the j-th are different from the average in a way that is typical for an electron cluster, the (i, j) and (j, i) elements of the sum will cancel the (i, i) and (j, j) to some degree - the more typical the variation, the better the cancellation.

H-Matrix7 is built from: EM fractions in layers 1, 2, 3, and 4, shower energy weighted RMS in the ϕ direction, $\log E^{\text{raw}}_{\text{Tot}}$, and $\frac{z_{\text{vtx}}}{\sigma_z}$. To pass the H-Matrix criterion in the CC, we require that the electron satisfy H-Matrix7<12.

H-Matrix8 uses the same observables as H-Matrix7, plus the shower energy weighted RMS in z. To pass the H-Matrix criterion in the EC, we require that the electron satisfy H-Matrix8<20.

5.2.3.2 Electron Loose and Tight Track Matching

Since an electron is a charged particle, it is likely to leave a track in the CTD. Tracks are constructed from SMT and CFT hits (see Section 2.3.1) and an (η, ϕ) direction is obtained. Tracks are matched to electron candidates based on the difference between the candidate cluster center and the expected position of the cluster based on the track direction extrapolated to the third layer of the EM calorimeter. There are various ways to form observables describing the positional difference:

$$\Delta\theta = \theta^{\text{cluster}} - \theta_{\text{track}} \tag{5.7}$$

$$\Delta\eta = \eta^{\text{cluster}} - \eta_{\text{track}} \tag{5.8}$$

$$\Delta\phi = \phi^{\text{cluster}} - \phi_{\text{track}} \tag{5.9}$$

$$\Delta z = z^{\text{cluster}} - z_{\text{track}} \tag{5.10}$$

A track is defined as satisfying the "loose track matching" criterion if the separation of the cluster centroid and track satisfies $\Delta\eta < 0.05$ and $\Delta\phi < 0.05$.

The track is defined as satisfying the "tight track matching" criterion if it has at least one SMT hit and

$$P(\chi^2) > 0.01 \ \text{(or } \chi^2 < 0.95) \tag{5.11}$$

where the parameter χ^2 is based on the angular difference between the tracker-determined position of the electron and the calorimeter determined position:

$$\chi^2_{\mathrm{TM}} \equiv \left(\frac{\Delta\phi}{\sigma_\phi}\right)^2 + \left(\frac{\Delta z}{\sigma_z}\right)^2 \tag{5.12}$$

where σ_ϕ and σ_z are the measured RMS widths of the $\Delta\phi$ and Δz distributions.

Matched tracks are required to satisfy $p_T^{\mathrm{track}} > 10\,\mathrm{GeV}$. This excludes low momentum charged particles which are dominated by background and which would otherwise need to be checked for a track match. A good track match implies that the track momentum and the calorimeter cluster momentum are similar.

5.2.3.3 Isolation

Electron showers are narrow, therefore

$$f_{\mathrm{iso}} \equiv \frac{E^{\mathrm{raw}}_{\mathrm{Tot}}(\Delta R < 0.4) - E^{\mathrm{raw}}_{\mathrm{EM}}(\Delta R < 0.2)}{E^{\mathrm{raw}}_{\mathrm{EM}}(\Delta R < 0.2)} \approx 0 \tag{5.13}$$

The isolation requirement strongly rejects hadronic jets, which have a wider shower than electrons. FSR and pileup can also cause an electron to fail the isolation requirement.

5.2.4 Calorimeter Fiducial Requirements

The North and South sides of the CC are divided radially into thirty-two modules, each two cells wide, and therefore there is an inter-module crack every $\frac{2\pi}{32}$ radians. The position relative to the boundaries of the local module is given by $\phi_{\mathrm{mod}} = \mod\left(\phi, \frac{2\pi}{32}\right)$. A Full MC simulation of electrons was used to study the effect of the inter-module cracks on the determination of the calorimeter cluster centers. The difference between the expected location of an electron in EM3 as extrapolated from its track, $\phi^{\mathrm{trk}}_{\mathrm{mod}}$, and the location of the associated calorimeter cluster, $\phi^{\mathrm{EM}}_{\mathrm{mod}}$, is shown in Figure 5.2, and a clear bias towards

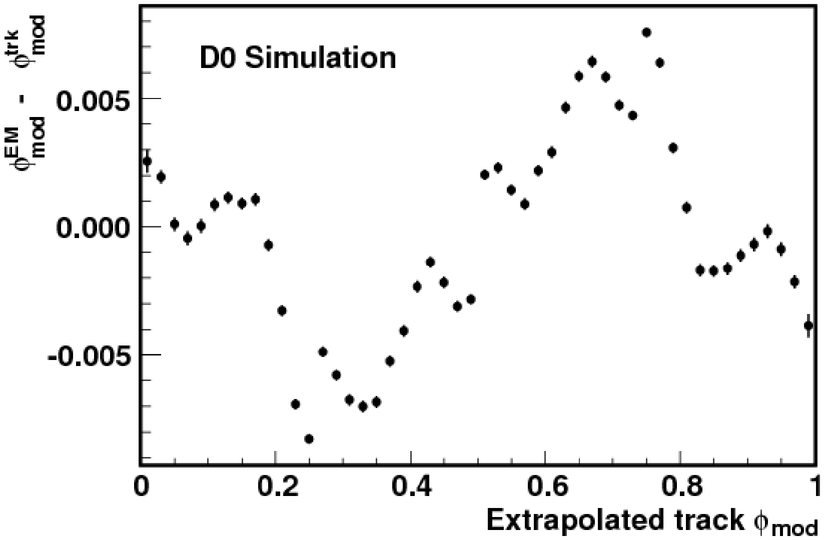

Figure 5.2: Average discrepancy between tracker-based (extrapolated to EM3 layer) $\phi^{\rm trk}$ and calorimeter-based $\phi^{\rm EM}$ measurements, in units of the calorimeter module width, as function of $\phi^{\rm trk}_{\rm mod}$[6].

the centers of the cells for the cluster centroid can be seen. In addition, if electrons fall too close to the cracks, they are unlikely to be reconstructed, as can be seen from the $\phi_{\rm mod}$ electron-reconstruction efficiency, determined from collider data and shown in Figure 5.3.

A correction is applied during track-matching to compensate for the relatively small bias in the ϕ measured from the calorimeter cluster. The sharp drop in efficiency near the calorimeter cracks could create a dangerous η-dependent bias, and the small fraction of electrons near the cracks which are reconstructed have poorly measured energy. Therefore, we impose the following requirements on the electron location:

$$0.1 < \phi_{\rm mod} < 0.9 \tag{5.14}$$

The only restriction on η is that it must fall within the CC ($\eta < 1.05$) or the EC ($1.5 < \eta < 2.3$).

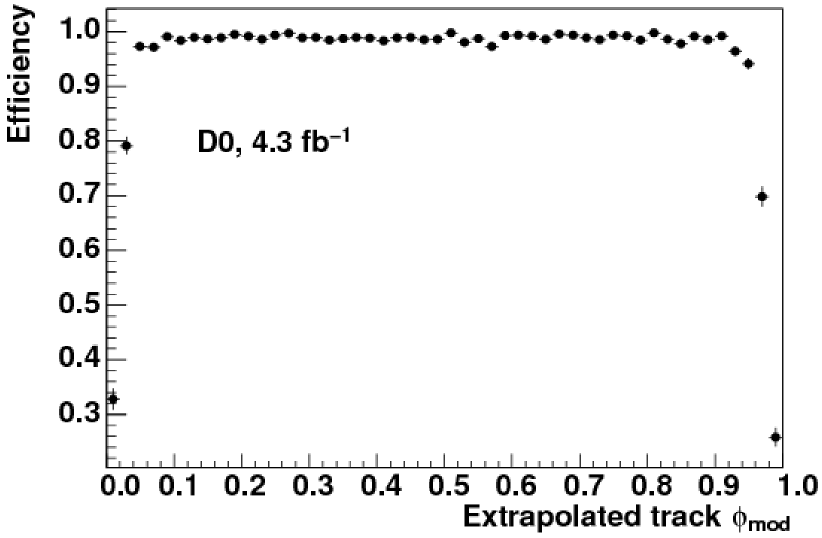

Figure 5.3: Electron reconstruction efficiency as a function of (tracker-based) $\phi_{\mathrm{mod}}^{\mathrm{trk}}$. Note the steep drop in efficiency near the module boundaries. Due to this drop in efficiency, we include only events where electrons satisfy $0.1 < \phi_{\mathrm{mod}} < 0.9$[6].

5.2.5 Vertex Reconstruction

An accurate vertex determination is crucial to an accurate determination of transverse hadronic recoil momentum (but not for electron transverse momentum, which is calculated using the individual track direction). To reconstruct the vertex (production point) z_{vtx} of the W boson, a first attempt is made using the D0 primary vertex algorithm. This method uses a Kalman filter algorithm with the charged particle tracks to identify a vertex. However, there maybe be additional $p\bar{p}$ collisions producing charged particles detected by the tracker, so the primary vertex chosen by the online vertexing algorithm may not be the one corresponding to the W or Z boson production. Thefore, during reconstruction, when the electron(s) from the W or Z decay have been identified and associated with track(s), the point of closest approach to the beam line (or average of two points of closest approach in the case of the Z boson) is compared with the D0reco primary vertex. If they agree to within 2 cm, the more accurate D0reco primary vertex is used. If they disagree, the point of closest approach (or average) is the most accurate option, and is used. For both the W and Z bosons, we require $|z_v| < 60\,\text{cm}$.

5.3 Energy and Momentum Measurements Used for Analysis

During the initial reconstruction, candidate electrons are required to satisfy $E_T^{\text{raw}} > 1.5\,\text{GeV}$, $f_{\text{EM}} > 0.9$, and the loose track-matching requirement, $\Delta R < 0.2$.

After we have selected $W \to e\nu$ and $Z \to ee$ candidate events (Section 5.4), we switch to working with the quantity $E^{e,\text{raw}}$ which we defined in Section 5.2.1. We use this quantity with FH1 included in order to fully contain the up to 10% leakage from the electromagnetic shower. After the dead material correction is applied to the electron energy (Chapter 6), this corrected energy is defined as E^e.

In this analysis the direction of the electron is defined as the direction of the matched track:

$$\theta^e = \theta_{\text{track}} \tag{5.15}$$

$$\phi^e = \phi_{\text{track}} \tag{5.16}$$

The electron corrected vector momentum is given by

$$\vec{p}^e = E^e \begin{pmatrix} \sin\theta^e \cdot \cos\phi^e \\ \sin\theta^e \cdot \sin\phi^e \\ \cos\theta^e \end{pmatrix} \tag{5.17}$$

The transverse energy is defined as $p_T^e = E^e \sin\theta^e$.

5.3.1 Raw Missing E_T and Recoil Reconstruction

The raw missing energy vector in the transverse plane is calculated by taking the negative vector sum of cell energies.

$$\vec{\not{E}}_T^{\text{raw}} = -\sum_i E_i^{\text{raw}} \sin\theta_i \begin{pmatrix} \sin\theta^e \cdot \cos\phi^e \\ \sin\theta^e \cdot \sin\phi^e \\ \cos\theta^e \end{pmatrix} = -\sum_i \left(\vec{E}_T^{\text{raw}}\right)_i \tag{5.18}$$

The sum is over all calorimeter cells that were read out, except cells in the CH and ICD, since they would introduce undesirable noise. ϕ_i and θ_i are the azimuth and polar angle of the center of cell i with respect to the primary vertex.

The recoil transverse momentum, $\vec{u}_T^{\text{raw}}$, for a W/Z boson event is the vector sum of calorimeter energies outside of the electron reconstruction window. We calculate it by taking the difference between the transverse energy imbalance (negative missing transverse energy) and the electron transverse momentum. For W boson events, this is:

$$\vec{u}_T^{\text{raw}} = -\vec{\not{E}}_T^{\text{raw}} - \vec{p}_T^{\text{raw}} \tag{5.19}$$

while for Z boson events, it is:

$$\vec{u}_T^{\text{raw}} = -\vec{\not{E}}_T^{\text{raw}} - \left(\vec{p}_T^{\text{raw}}\right)_{e1} - \left(\vec{p}_T^{\text{raw}}\right)_{e2} \tag{5.20}$$

We do not apply a hadronic energy scale correction. The interaction of hadrons with the dead material, and the distribution of hadronic energy in the calorimeter, is more complicated than that of electrons. Therefore, the hadronic response of the detector, about 65% on average for the D0 detector with W/Z bosons produced at the Tevatron, is instead modeled in the fast MC (Section 7.4). Therefore, we set

$$\vec{u}_T \equiv \vec{u}_T^{\text{raw}} \tag{5.21}$$

5.3.2 Scalar Transverse Energy Reconstruction

The scalar transverse energy (SET) is defined as the scalar sum of the transverse energies of all calorimeter cells except CH and ICD

$$\mathrm{SET} = \sum_i E_i^{\mathrm{raw}} \sin\theta_i \tag{5.22}$$

excluding cells in the electron reconstruction window, defined in Section 5.2.1. This quantity is strongly correlated with the instantaneous luminosity.

5.3.3 Corrected Missing Transverse Energy Reconstruction

The corrected $\vec{\not{E}}_T$ is calculated from $\vec{u}_T$ and corrected $\vec{p}_T^{\,e}$.

$$\vec{\not{E}}_T = -\vec{u}_T - \sum_e \vec{p}_T^{\,e} \tag{5.23}$$

The effect of this calculation is to apply the dead material correction to the contribution of energy deposited in the calorimeter in the electron window, which would otherwise contribute (as it does in the raw vector sum) to the MET calculation. However, the MET still has a contribution from missed hadronic recoil energy which is not corrected for (and is instead modeled in fast MC), as noted in section 5.3.1. In $Z \to ee$ events, the imperfect response of the detector to hadronic energy is the only source of MET.

5.4 Event Selection Summary

W and Z boson events are selected with the following requirements:

- Vertex requirement:
  - $|z_v| < 60$cm
- Electron requirements:

  - id= 10 or ±11 [4]
  - $f_{\mathrm{EM}} > 0.9$, $f_{\mathrm{ISO}} < 0.15$
  - H-Matrix7 < 12 in CC and H-Matrix8 < 20 in EC (EC electrons are only used for "tag and probe" type efficiency studies using Z events)
  - In calorimeter fiducial region in η and ϕ
  - $p_T > 25\,\mathrm{GeV}$
  - The associated track must have at least one SMT hit, $p_T > 10\,\mathrm{GeV}$ and a good track match (track match probability $P\left(\chi^2_{\mathrm{TM}}\right) > 0.01$).

- $Z \to ee$ candidate selection requirements:
  - At least one electron passes requirements of all three trigger levels.
  - Both electrons in CC: $|\eta_{\mathrm{det}}| < 1.05$ (Z events in "tag and probe" type efficiency studies may have one EC electron, with $1.5 < |\eta_{\mathrm{det}}| < 2.3$)
  - $u_T < 15\,\mathrm{GeV}$
  - $70 < m_{ee} < 110\,\mathrm{GeV}$

- $W \to e\nu$ candidate selection requirements:
  - The electron passes requirements of all three trigger levels.
  - $\vec{\not\!\!E}_T > 25\,\mathrm{GeV}$
  - Electron $|\eta_{\mathrm{det}}| < 1.05$
  - $u_T < 15\,\mathrm{GeV}$
  - $50 < m_{ee} < 200\,\mathrm{GeV}$

---

[4] These ids indicate that a cluster satisfying the isolation, EMfraction, and p_T criteria has been found using EMAnalyze[29], or a cluster satisfying at least the isolation criterion has been found using SEMReco[30].

In RunIIb34, there are roughly 50K $Z \to ee$ candidates with both electrons in the CC, and roughly 1.5 M $W \to e\nu$ events with the electron in the CC. These Z candidates are used to determine the EM calibration, and the W candidates to determine M_W.

Chapter 6

DEAD MATERIAL CORRECTION TO THE ELECTRON RESPONSE

The full material simulation, `GEANT`, described in Section 4, does not quite simulate electron showers at the precision necessary for an accurate W mass measurement. In addition, the FullMC simulation does not have a perfect model of the detector material in front of the calorimeter. In total, there are of 3.7 radiation lengths (X_0) of material at normal incidence, before the CC: $0.2X_0$ from the inner detector, $0.9X_0$ from the solenoid, $1.3X_0$ from the preshower detector ($1.0X_0$ of which is due to the preshower detector lead), and $1.3X_0$ from the cryostat walls and support structures. This is called "dead material" because it causes charged particles to radiate but does not measure the shower energy. As a result, the CC does not sample the full shape or energy content of the particle shower. As can be seen in Figure 6.1, an η_{phys}-dependent fraction of the beginning of the shower is not detected. There is also a significant non-linear dependence on the energy of the showering particle, as shown in Figure 6.5.

To account for this loss of signal, we can either simulate the effect of the dead material in the FastMC, or apply a correction to the electron energy during the reconstruction procedure for collider data samples. The effect was well-modeled for the RunIIa analysis, and, despite the addition of increased pileup in RunIIb and the addition of an inner silicon tracking layer (the SMT, which only added $\approx 0.003X_0$), it has not changed enough since then to re-derive the correction, as shown in Figure 6.2. In addition, we would like the reconstructed data to be as similar as possible as to the FullMC (which does not include the extra Dead Material), so that the FastMC simulations of FullMC and data can also be similar. Therefore, it is easiest to apply the correction during the reconstruction procedure,

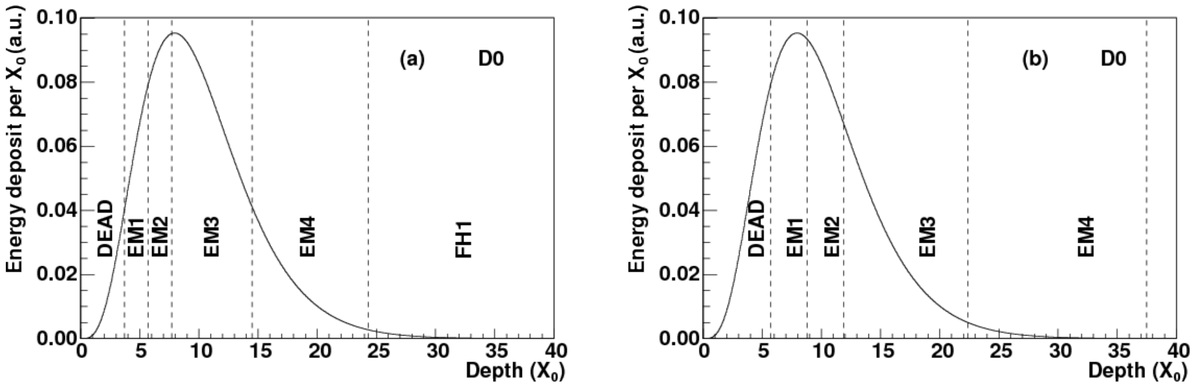

Figure 6.1: Mean shower profile of simulated 45 GeV electrons in the CC, at (normal) incidence $\eta = 0$ (left) and (non-normal) incidence $\eta = 1$ (right). The depths of the dead material and calorimeter layers are indicated as measured along the shower axis.

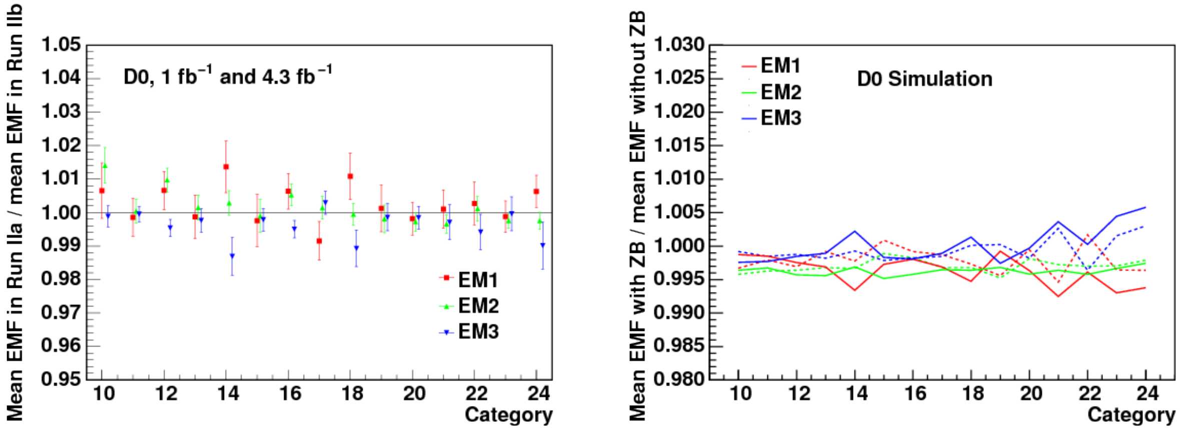

Figure 6.2: Comparison between RunIIa and RunIIb for the mean and variation in the three EM layers of the calorimeter[6].

and not waste computing resources by including it in the FastMC.

There are two main parts to the Dead Material Correction. The first is a set of correction functions derived by simulating the effect of a concentric copper cylinder in an improved FullMC simulation, the second is a residual correction applied to the energy

bin 0:	$\lvert\eta_{\rm phys}\rvert < 0.2$
bin 1:	$0.2 \leq \lvert\eta_{\rm phys}\rvert < 0.4$
bin 2:	$0.4 \leq \lvert\eta_{\rm phys}\rvert < 0.6$
bin 3:	$0.6 \leq \lvert\eta_{\rm phys}\rvert < 0.8$
bin 4:	$0.8 \leq \lvert\eta_{\rm phys}\rvert$

Table 6.1: Definition of bins in electron $|\eta_{\rm phys}|$.

measured in each layer of the calorimeter. The correction is derived from a $Z \to ee$ event sample, generated with a version of the FullMC which has an improved shower description relative to the default `GEANT`) simulation[1] This was done for the Run IIa ($1\,{\rm fb}^{-1}$) analysis and revalidated for RunIIb12; it is revalidated again for RunIIb34, as seen in Figure 6.2.

6.1 Tuning the Thickness of the Copper Cylinder

We start the tuning procedure by examining the fractions of energy (EMF) deposited by $Z \to ee$ electrons in the first three electromagnetic layers of the CC, EM1, EM2, and EM3. The energy deposited in EM4 and FH1 is negligible and is not used in the tuning. Because the electron energy loss in each layer depends on angle of incidence (compare the two plots in Figure 6.1), we divide the Z electron sample into categories based on angles of incidence of the two electrons. To minimize kinematic biases, each electron is categorized based on the angle of incidence of both electrons in the event, and leading and subleading electrons are treated equally. There are five $\eta_{\rm phys}$ bins (see Table 6.1), or fifteen possible categories for a given event, because there are two electrons per event (see Table 6.2).

The ratio of data to FullMC mean EMF per layer, per category, are plotted in Figure 6.3 (left). We can see significant disagreement between data and FullMC. Specifically

---

[1] The improvements are described in detail in [43]. They require an 80x increase in computing power, and therefore are only used for determining the required amount of dead material and layer-dependent gains.

Category	Combination of η_{phys} bins
10	0 - 0
11	0 - 1
12	0 - 2
13	0 - 3
14	0 - 4
15	1 - 1
16	1 - 2
17	1 - 3
18	1 - 4
19	2 - 2
20	2 - 3
21	2 - 4
22	3 - 3
23	3 - 4
24	4 - 4

Table 6.2: Definition of η_{phys} categories for $Z \to ee$ events.

the EMF in EM1 is too low in the FullMC, and the EMF in EM3 is too high in the FullMC. This is the effect one would expect if the layers start to sample energy from the showers in Figure 6.1 later in the shower development than is simulated in the standard FullMC. We also see no significant intra-layer dependence on the η_{phys} categories; therefore a longitudinally symmetric cylinder is an appropriate choice for modeling the dead material. (Though there is an η_{phys} dependence on amount of material traversed, the relative increase is uniform.)

We wish to find the thickness of the copper cylinder which maximizes the agreement between a high-quality FullMC simulation and data for the EMFs in all layers and

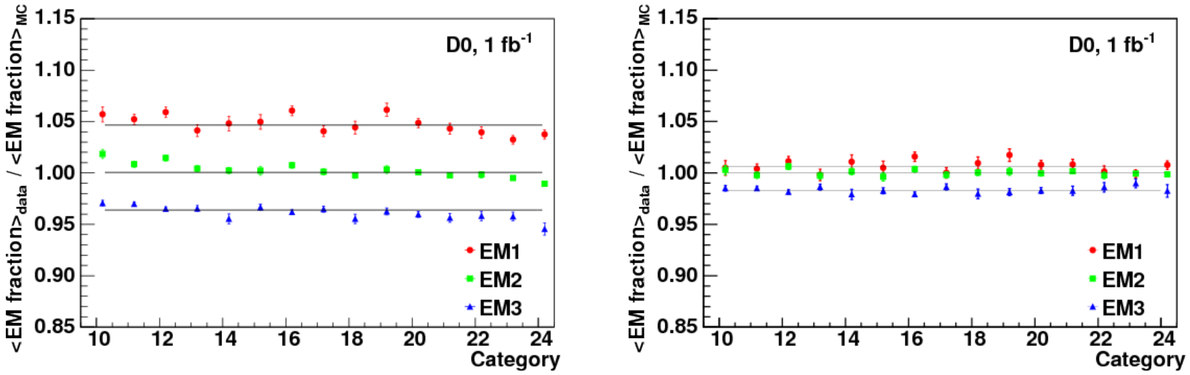

Figure 6.3: The ratio between the EMF in each layer for $Z \to ee$ events in data vs. FullMC, for each of the fifteen categories of η_{phys}, before (left) and after (right) the additional material has been added to the simulation. The mean EMF ratio for each layer is shown as a horizontal line.

categories. To do this, we simulate $Z \to ee$ events using the improved `GEANT` model with a range of thicknesses of the simulated copper cylinder. From these simulations, we create a parameterized model of the mean EMF and its fluctuations around the average as function of the copper thickness (measured in nX_0). Using this parametrization, we form a χ^2 discriminant based on the difference (in all categories) between the EMF in the simulations, and the EMF in the data:

$$\chi^2 = \sum_i \sum_j \left[\frac{f_{ij}^{\text{EML}} - \bar{f}_i^{\text{EML}}}{\sigma_{ij}^{\text{EML}}} \right] \tag{6.1}$$

where f_{ij}^{EML} and σ_{ij}^{EML} are the data/FullMC ratio and uncertainty of the mean energy fraction of layer i for electrons in category j, and $\bar{f}_i^{\text{EML}}$ is the mean of the energy fraction in all categories for layer i. The value of nX_0 that minimizes χ^2 is the optimal value. To validate our result, we also check that the χ^2 minimization, applied separately for each layer, results in thickness values that agree with the full optimized result. The results of the minimization procedures are shown in Figure 6.4.

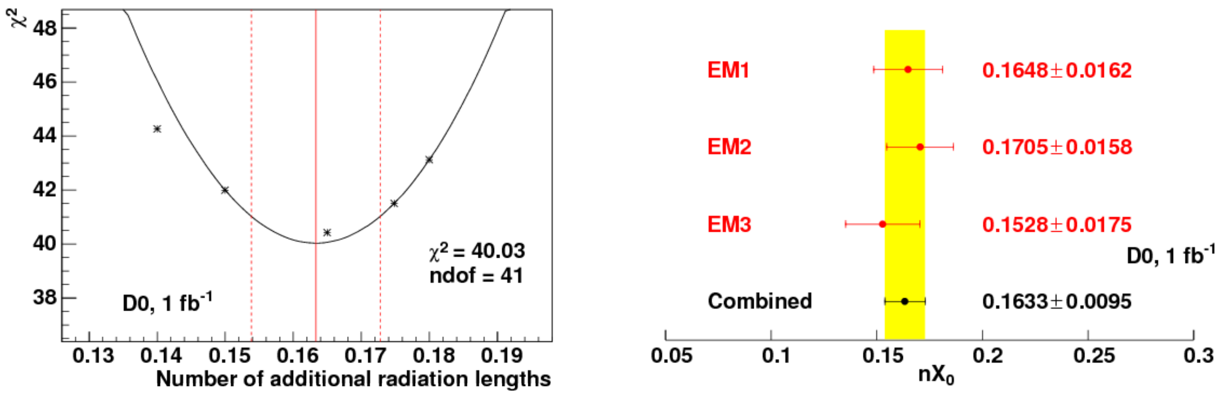

Figure 6.4: Left, the χ^2 discriminant (based on the difference between improved FullMC and data for EMFs in layers and η-bins) as a function of the thickness of the copper cylinder. The optimal value of the thickness and its one-σ uncertainty is shown. Right, the results of the χ^2 minimization process for the individual layers, showing agreement with the result for minimizing χ^2 simultaneously for all three layers[6].

6.2 Applying the Correction

Figure 6.3 (right) shows the EMF data/FullMC ratios for $Z \to ee$ events at the optimized thickness of the copper cylinder. We can see that the agreement is still not perfect. We interpret the small residual deviations as layer-dependent gain factors, and correct for these in the data reconstruction procedure, to bring the data into agreement with the FullMC.

Once we have determined the best thickness for our simulated copper cylinder, we derive correction functions to be applied in the reconstruction procedure with a single-electron FullMC simulation. We derive separate correction functions for data and FullMC, using the standard `GEANT` detector simulation for the FullMC correction and the improved material model (which matches data more closely) for the data correction. The correction functions are η_{phys} and p_T^e dependent and are derived by comparing the truth and reconstructed values of the electron energies. Figure 6.5 shows an example of some of the functions as measured for the FullMC sample.

Figure 6.6 shows the EMF data/FullMC ratios for W events simulated with standard `GEANT` with the correction functions applied, divided into the same η_{phys} bins (since there is only one electron per W event) we used to categorize the Z events. Since this sample has higher statistics, we see non-negligible deviations from unity that we could not deduce from the limited, high-precision, Z sample. To be precise, though the EMF ratio in all five η_{phys} bins averages to unity - confirming that the mean thickness of the cylinder is correct - it is likely that there is some η dependence not accounted for by the longitudinally uniform cylinder. However, correctly optimizing the dead material correction beyond our simple cylindrical model would be too resource intensive, so we will account for these higher order corrections with our FastMC tune, described in detail in Chapter 7.3.3.

The systematic uncertainty in the W boson mass due to modeling error is determined by calibrating FastMC toy models to FullMC simulations with the copper layer thickness varied up and down by its one-σ uncertainty (as seen in Figure 6.4, left), and measuring the resulting variation in m_W.

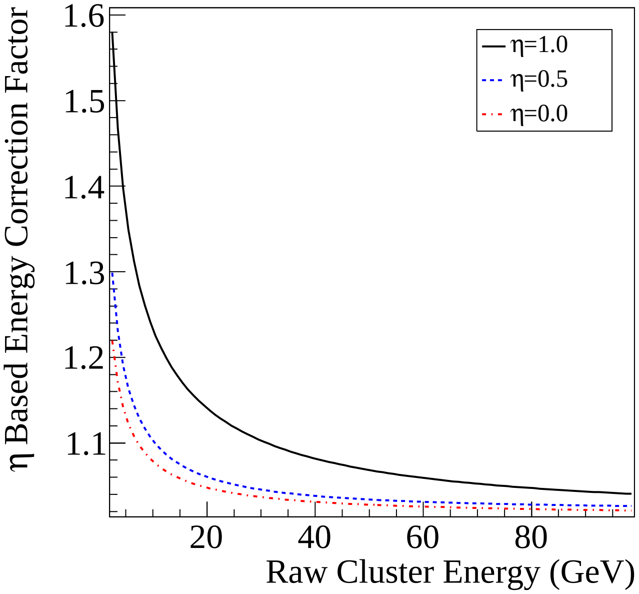

Figure 6.5: A few examples of the correction functions applied to the energy measurement of reconstructed electrons in collider data in order to correct for energy loss in upstream dead material, as a function of electron p_T^{raw}, for various values of η_{phys}

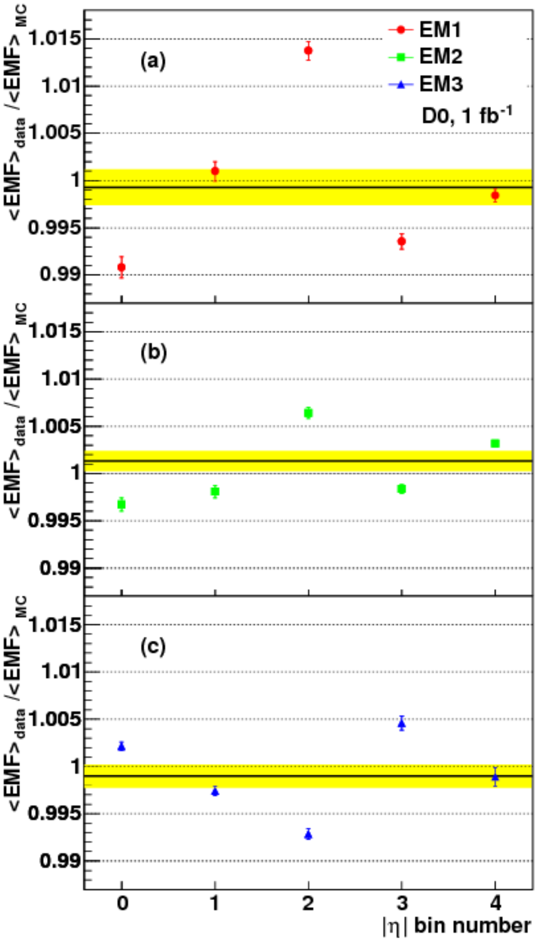

Figure 6.6: The ratio between the EMF in each layer for $W \to e\nu$ events in data vs. FullMC, for each of the five electron η_{phys} bins, after the additional material has been added to the simulation and the intra-layer calibration factors has been applied. The mean EMF ratio for each layer is shown as a horizontal line, with the yellow band indicating the combination of systematic and statistical uncertainty in the mean. (a), (b), and (c) correspond, respectively, to EM layer 1, 2, and 3.

Chapter 7

DETERMINATION OF FAST SIMULATION PARAMETERS

In order to create a large number of templates for the W mass measurement, we need to be able to quickly create large samples of simulated events. Simulating the physics of the decay of the vector boson with a given initial transverse momentum (described in Section 4.3) does not require large computing sources, so we use the same generator to create sets of events for both the FullMC and FastMC simulations. However, simulating the interaction of the decay products with the detector, is very resource intensive, because it requires simulating particle showers in the detector and calculating the energy deposit in each calorimeter cell. (Because of this, the "reconstruction" process is applied in the same way for both collider and FullMC data.) We need a way to simulate the results of the reconstruction procedure, which gives us simplified observables such as reconstructed energy and momentum sums.

The FastMC must therefore transform the generator level "truth" values into simulated reconstruction values. From the generated true values of the electron and W boson transverse momentum (Section 4.3), simulated initial vertex position (Section 7.1), simulated final state radiation (FSR) (Section 7.3.1), contributions from the underlying event described by Minimum Bias events (MB) (Section 7.4.2), and energy levels in the detector described by Zero Bias events (ZB) and InstLumi (Section 7.4.2), it must provide us with simulated values of the reconstructed electron p_T and reconstructed hadronic recoil u_T, from which the additional measurement observables, reconstructed W boson transverse mass m_T and reconstructed transverse momentum imbalance $\vec{\not{E}}_T$, are calculated. A schematic of these energy values are shown in Figure 7.1. The FastMC must also simulate the inefficiencies of the reconstruction procedure (Section 7.2), by "failing" to reconstruct the event at the same rate, and with the same dependences on event variables, as the reconstruction procedure

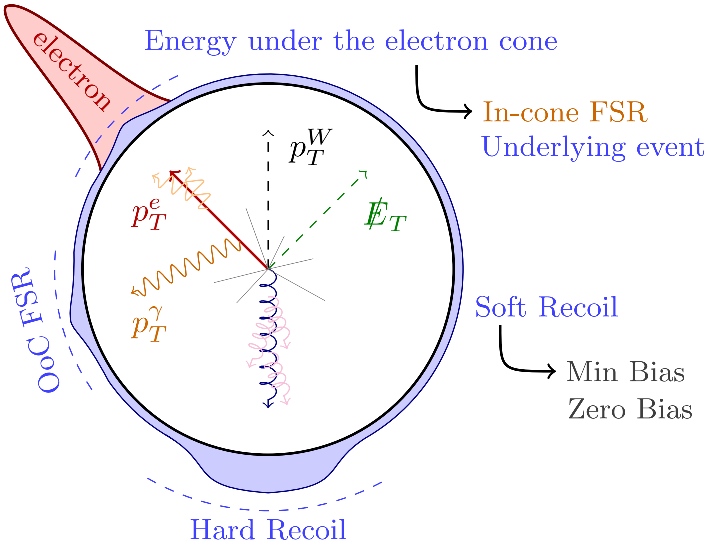

Figure 7.1: Schematic of transverse quantities $W \to e\nu$ events with more details than Figure 3.1. These details include energy from FSR, spectator particle interactions, and other $p\bar{p}$ events.

fails to reconstruct the event from collider data or FullMC. This is necessary to get accurate template shapes with which we measure the mass from collider data, as described in Section 3.2.

We create two main versions of a FastMC simulation that we use to measure a W mass. The first, which we will call the "`GEANT` FastMC", is "tuned" (by adjusting its parameters) to match the FullMC sample as well as possible. The second, which we will call the "data FastMC", is tuned to match the collider data sample as well as possible. The `GEANT` FastMC is not used to measure the real W mass in collider data, but is instead used to test the accuracy of our method.

For this test, we treat the FullMC sample as mock data, and use the `GEANT` FastMC to measure the W mass from this simulated sample, using the technique described in Chapter 3. If we can get back an accurate measurement of the mass used to simulate the FullMC W

events, we have achieved "MC closure", and we trust that our method can be used to get an accurate measurement of the W mass from the collider data.

If we achieve MC closure, we can use the second version of the FastMC to measure the physical W mass from the collider data. Its base tune is derived from FullMC, but, because the FullMC simulation is different enough from collider data that it cannot be used to measure the W mass at the precision we require, we make adjustments, based on collider data measurements, to more accurately simulate W events in the collider data.

Understanding correlations between sensitive observables is important to accurately model these observables. As we tune the models, we ensure an optimal parametrization by comparing distributions of observables from the FastMC to the same distributions in the FullMC or collider data. It is important to derive the parametrizations for the various steps of the FastMC simulation with respect to the order in which they are applied, because the parametrization of a specific step depends on the characteristis of the sample to which it is applied, and those characteristics depend on which steps have already been applied. The parameterizations are presented here in roughly the same order in which they are applied.

7.1 Primary Vertex Parametrization

The longitudinal coordinate of the primary vertex, z_{vtx} is used (along with η_{phys}) to calculate η_{det}, and the FastMC must therefore accurately simulate its distribution. For the FullMC and the `GEANT` FastMC, the beam shape is modeled by the convolution of a Gaussian bunch length in z with center $z_0 = 0$ and width $\sigma_z = 25\,\text{cm}$, and a Lorentz distribution set by the accelerator β^* functions in transverse directions $x - y$ with center at $x_0 = y_0 = 0$. For the data FastMC, the longitudinal shape parameters are determined from the vertex distribution of a sample of randomly triggered beam crossings.

7.2 Electron Efficiency Parametrization

The electron (event) efficiency for a specific requirement, or "cut", with respect to a defined base sample, is defined as the fraction of electrons (events) in the sample that pass the cut. The various selection cuts we apply to electrons and events to get the final sample of candidate events have been described in Chapter 5. If the selection cut is based on observables that the FastMC does not simulate, such as the detailed distribution of calorimeter energy in the case of the H-Matrix cut, or the difference between track based and calorimeter based position in the case of the track-matching cuts, we need to simulate the dependence of the cut's efficiency on relevant kinematic, geometric, and environmental observables. If the selection cut is based on an observable that the FastMC does simulate, the efficiency is implicit and does not need to be simulated.

As one example of an efficiency dependence, the probability for an electron to pass the trigger has a strong correlation with the electron energy. However, the inefficiency[1] of a single selection criterion may have multiple sources, which in turn may have dependencies on multiple correlated variables. For example, the electron identification (H-Matrix) cut, which is based on the electron shower shape as described in Section 7.3.5, depends on variables including electron p_T, η_{phys}, and η_{det}, which are strongly correlated with each other. To avoid double-counting the efficiency dependence on correlated variables, we measure it simultaneously for the correlated variables. Somewhat counterintuitively, by "measure simultaneously" we mean we split the sample into bins of all correlated variables and measure the efficiency individually in all those bins, wheareas to measure the efficiency dependence on a single, uncorrelated variable, we measure the efficiency in bins of that variable only.

We usually simulate the efficiency of a cut on an electron or event by choosing a random number between zero and one, and keeping the event if the random number is below the value of that efficiency at the value of the dependent variable for that electron or event. Since the modeled efficiency has some dependence on electron or event observables, this has the effect of shaping the distribution of that observable for the electrons or events. In some cases, when the dependent variable is chosen randomly from a distribution and has

---

[1] "Inefficiency" and "efficiency" are essentially interchangeable terms in this note. We always use "efficiency" to describe the curves used in simulating whether an electron or event passes or fails a certain criterion, but when we discuss sources of this effect, we often say "inefficiency".

not yet been determined, such as for the $\Delta u_{\parallel}$ efficiency described in Section 7.4.1, we can avoid discarding events by re-simulating the dependent variable until the electron or event passes the cut simulated by the random number process. This is equivalent to adding an extra dimension to the distribution from which the stochastic variable is selected, multiplying the distribution by the efficiency in that dimension. The average magnitude of the electron efficiency does not affect the final distributions apart from the statistical sample size, so when measuring the efficiency dependencies, we often normalize the efficiency shape to have its maximum value at one.

Because of correlations between an electron or event surviving a given cut and the value of other observables for that electron or event, the characteristics of the base sample relative to which the efficiency is measured affect the shape of the efficiency. Therefore, the form of the efficiencies depend on the order in which they are to be applied, and must be measured accordingly. In determining the efficiencies, we make an assumption that they are factorizable, that is, that the dependence on some variables can be measured independently from the dependence on others. This is not perfectly true, and can result in double-counting, an effect mitigated by final "residual" corrections.

The efficiencies can depend on electron or event level observables. For the `GEANT` FastMC that is used to test for closure, the electron selection efficiencies are measured from a FullMC sample of $Z \to ee$ events. However, as the FullMC is not identical to the collider data, we must measure the (small) differences in efficiencies and apply these residual corrections in the data FastMC in order to accurately simulate the data. When measuring efficiencies from collider data, we need some way to exclude the background (non-signal events) from our efficiency measurement.

There are three main tactics we use when measuring efficiency for this analysis: The "tag-and-probe" method involves identifying signal $Z \to ee$ events by finding an electron that satisfies some criterion, for example passing a trigger, and testing whether the other electron passes or fails the criterion for which the efficiency is being measured. The tag-and-probe method is sometimes used on FullMC in order to match the efficiency measurement on collider data. The "background-subtraction" method involves splitting events which may or may not be signal events into groups of passing or failing events. The groups are placed into histograms in some observable in which it is possible to subtract the background using a template. It is not possible to say for sure which events signal and which or not, but it is possible to estimate the number of signal events which pass, or fail, the cut. These numbers are then used to calculate the efficiency. The "background-subtraction" method is used to determine residual corrections to the H-Matrix and track-matching efficiencies for data, as described in Section 7.2.8.

We can measure efficiencies in data via the tag-and-probe and/or background subtraction method when we have enough statistics, or for final corrections, by taking the ratio of FullMC or collider data vs. FastMC distributions of the dependent variable. The "ratio" method is used for small residual efficiency corrections,[2] and is essentially a reweighting method. The distribution for the dependent observable is compared between data (`GEANT`) FastMC and collider data (FullMC), and any difference between the shapes, which shows up as a ratio that is not completely flat, are interpreted as the efficiency to be applied. These efficiencies are named according to their dependent variable, e.g. the $u_{\|}$ and electron-ϕ efficiencies.

The overall efficiency can be written as the product of the following terms:

$$\begin{aligned}\epsilon \;=\;& \epsilon_{\text{trig}}(p_T^e, \mathcal{L}) \cdot \epsilon_{\text{FSR}}(X, \Delta R, \eta_{\text{phys}}, p_T^e, \mathcal{L}) \qquad (7.1)\\ & \cdot \epsilon_{\text{hmatrix}}(\eta_{\text{phys}}, p_T^e) \cdot \epsilon_{\text{trk,loose}}(z_{\text{vtx}}, \eta_{\text{phys}}, p_T^e) \cdot \epsilon_{\text{trk,tight}}(z_{\text{vtx}}, \eta_{\text{phys}}, p_T^e)\\ & \cdot \epsilon_{\phi}(\phi^e) \cdot \epsilon_{\text{SET}}(\text{SET}, p_T^e, \eta_{\text{det}}, \mathcal{L}, u_{\|}) \cdot R_1(\text{SET}, \mathcal{L}, \eta_{\text{det}}, z_{\text{vtx}}, p_T^e) \cdot R_2(u_{\|})\end{aligned}$$

Each term in the above expression will be described in the following sections.

---

[2] It can adjust for efficiency dependence that was missed, or double-counted.

7.2.1 Trigger Efficiency

There were two triggers used in RunIIb34, a 25 GeV and a 27 GeV trigger.[3] For a given event, if both triggers are live, then the trigger with the lowest p_T threshold is considered the "active" trigger (because any trigger with a higher threshold will have negligible effect on the sample) for that event. Because the energy measured at the trigger level is different than the energy measured during offline reconstruction, there is a "turn-on" in the efficiency as a function of reconstructed p_T, where the efficiency rises from an initial low level at the threshold p_T, to unity as the reconstructed p_T increases.

The trigger efficiency ϵ_{trig} is derived from data $Z \to ee$ candidate events, using the tag-and-probe method. The tag electron is allowed to be in the CC or the EC (because the neutrino in $W \to e\nu$ events can be in the CC or the EC), and is required to satisfy all selection requirements, including passing the trigger. The probe electron is required to be in the CC, and must satisfy all selection requirements, except passing the trigger. The rate at which the probe electron passes the trigger, relative to the other selection requirements, is the trigger efficiency, ϵ_{trig}.

The trigger efficiency is measured as a function of reconstructed electron p_T. It is measured separately for RunIIb3 and RunIIb4, for the two trigger thresholds, and for InstLumi<3 and InstLumi>3. Note that the measurement of the trigger efficiency was redone in attempt to fix the problem of disagreement between RunIIb3 and RunIIb4 discussed in Chapter 10 and shown in Figure 10.1. A small difference was found in the slope between the first and second attempt, but this change was not enough to fix the disagreement.

7.2.2 FSR Efficiency

In this analysis, we define Final State Radiation (FSR) as the process by which the outgoing electron radiates one or more photons before interacting with any material[4],

---

[3] The 27 GeV was used when InstLumi rose above about 5, in order to limit the number of recorded events.

[4] i.e. it does not include Bremsstrahlung, which is accounted for in the Dead Material Correction described in Chapter 6.

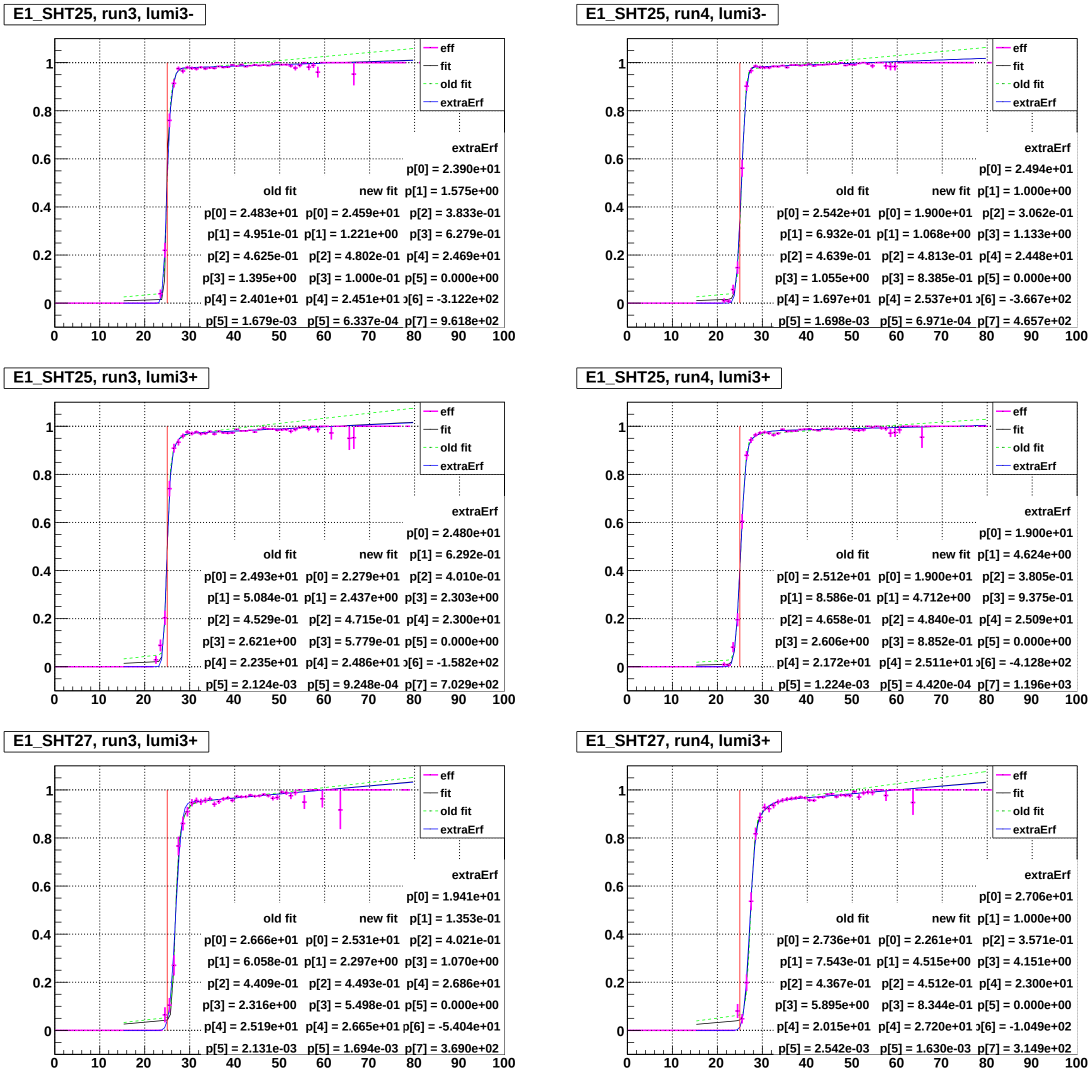

Figure 7.2: Efficiency turn-ons for the 25 GeV and 27 GeV triggers derived from data $Z \to ee$ events. Left column is RunIIb3, right column is RunIIb4. Top row is the 25 GeV trigger at InstLumi<3, center row is the 25 GeV trigger at InstLumi>3, bottom row is the 27 GeV trigger at InstLumi>3. NOTE: This figure is from the author's own work. At the time of writing, it has not been approved by the D0 collaboration for general public use beyond this dissertation.

which can affect the electron energy measurement. The FSR photon energy can be partially or totally absorbed by dead material in front of the calorimeter. If the FSR photon reaches the calorimeter, it might fall entirely outside the electron cone, in which case its energy will not be included in the electron energy measurement, but will instead contribute to the hadronic recoil energy measurement. If it instead falls inside the electron cone, it can change the shape of the electron's energy deposit in the calorimeter, affecting the shower-shape based identification, track-matching, and isolation of the electron. If it falls on the edge, a combination of all these effects can occur.

The effect of FSR energy loss on the reconstructed electron energy is discussed in Section 7.3.1. The inefficiency in electron identification, track-matching, and isolation due to FSR is modeled in the FastMC via the FSR efficiency. It is parametrized as a function of electron true energy, electron incidence angle (η_{phys}), the fraction of energy carried by the leading photon (X), InstLumi, and electron-photon separation, defined as

$$\Delta R(e,\gamma) = \sqrt{\left[\phi_{\mathrm{phys}}(e) - \phi_{\mathrm{phys}}(\gamma)\right]^2 + \left[\eta_{\mathrm{phys}}(e) - \eta_{\mathrm{phys}}(\gamma)\right]^2} \tag{7.2}$$

The FSR efficiency is derived by comparing two FullMC samples. The first is a simulation of electrons with kinematics matching those from $W \to e\nu$ decays and FSR turned on. The second is the same sample, but with the FSR photons removed and their energy added back to the electron, equivalent to turning off the FSR. Both samples have ZB turned on, which is the same ZB as in the main FullMC simulation.

Figure 7.3 shows the dependence of the FSR efficiency on energy fraction X and ΔR, for a single η_{phys}, InstLumi, and p_T^e bin: The first three plots show the dependence on X in the lowest ΔR bins. Here, the photon is close to electron, modifying the shower shape to decrease its recognition by the H-Matrix criterion as an electron shower. The photon energy can also modify the calorimeter-based estimation of the electron position which degrades the quality of the track match.

The last three plots show the dependence on X in the highest ΔR bins. Here, the photon is well outside the electron reconstruction window, where it does not interfere with shower shape and track-matching, except when X is very large. In that case, the energy of the electron has been lowered to levels that the reconstuction algorithm is not well-equipped to deal with, and the electron is not reconstructed.[5]

The rest of the plots correspond to the "transition region" (intermediate ΔR bins). Here, the cluster isolation requirement is important. Most of these plots show, in addition to the monotonic decrease related to track-matching and shower shape requirements, two dips at $X \approx 0.25$ and $X \approx 0.75$, separating three ranges of X. The lower bump in X corresponds to the range where the photon, despite being in the isolation region, is of such low energy that it does not make electron fail isolation cut. The bump at intermediate X corresponds to the range where the electron and photon are identified as a single large cluster, so that neither trigger the isolation cut. The small bump at high X corresponds to the range where the photon energy is high enough that the FSR is mistaken for the electron by the clustering algorithm and the electron energy is low enough that the isolation criterion is not failed. A decrease in FSR efficiency with increasing X can still be seen in these plots, as track-matching tends to veto high X photon clusters when ΔR is not small, and track-matching and shower shape requirements tend to veto the oddly shaped clusters at intermediate X[46].

7.2.3 Preselection, EM Identification (Hmatrix) Efficiency, and Track-Matching Efficiencies

The requirements for preselection, H-Matrix, and loose and tight track-matching, are described in detail in Section 5.2.3.1 and Section 5.2.3.2. The efficiencies for these criteria, including track-reconstruction efficiency, are determined as described in the following sections, and are modeled individually in the FastMC.

---

[5] It would also be excluded by the lower limit on the electron p_T .

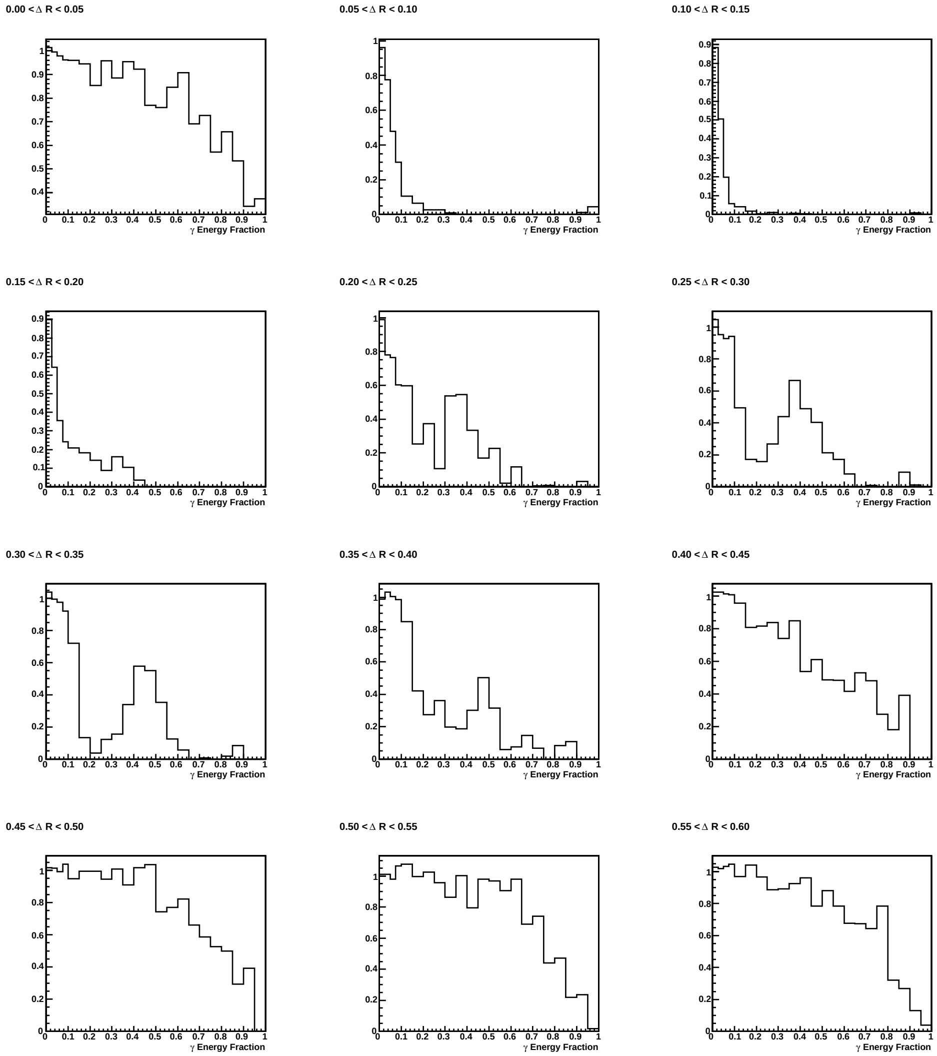

Figure 7.3: Electron identification efficiency as a function of X, the fraction of electron energy carried by the leading photon, measured from FullMC samples. For discussion, see Section 7.2.2. This is only a subset of the FSR efficiency dependence measurements, in bins with $0.1 < |\eta_{\text{phys}}| < 0.3$, $3 <$ InstLumi < 3.5, $37.5 < p_T^e < 45\,\text{GeV}$, and ΔR specified by the label on each plot[20]. NOTE: This figure is from a D0 internal note. At the time of writing, it has not been approved by the D0 collaboration for general public use beyond this dissertation.

7.2.3.1 Preselection Efficiency

The preselection efficiency can be measured from FullMC or data $Z \rightarrow ee$ events with a tag-and-probe method. The events are first selected by requiring an identified electron (which must pass the trigger, in data) with a loosely matched track, and a second track with $p_T > 12\,\mathrm{GeV}$, limited nearby track energy, and extrapolated track position in the EC or CC region, with invariant mass of the EM cluster and track between 70 and 110 GeV. The efficiency is the fraction of events where the second track loosely matches an EM cluster with $p_T > 15\,\mathrm{GeV}$. The dependence of this efficiency on η_{det} is found to be indistinguishable from unity in the fiducial region, and there are no other relevant dependences (i.e. the p_T^e dependence of the preselection criteria occurs only outide the measurement range). Therefore, this efficiency does not need to be simulated.

7.2.3.2 H-Matrix Efficiency

The efficiency for a single electron to pass the H-Matrix requirement is parametrized as a two-dimensional function of electron p_T^e and incident angle η_{phys}, because the ability of the H-Matrix technique to recognize the shape of an electron shower depends strongly on the energy and angle of incidence of the electron. The H-Matrix efficiency is measured relative to the preselection efficiency. First, the η_{phys} dependence is determined from from a sample of FullMC $Z \rightarrow ee$ events which have passed the preselection efficiency, by measuring the fraction of these events that pass the H-Matrix requirement. Then, the p_T^e dependence of the full H-Matrix efficiency, including EMF and isolation requirements, is measured from a sample of FullMC single-electron events.

7.2.3.3 Loose Track-Matching Efficiency

The loose track-matching efficiency is parametrized as a three-dimensional function of InstLumi, z_{vtx}, and η_{phys}. InstLumi affects the track-matching in two ways: pileup in the calorimeter can cause a mismeasurement of the cluster position, and a large number of track hits can cause an incorrect determination of the track position. z_{vtx} and η_{phys} together describe the angle of incidence within, and distance from $z = 0$ the electron passes through, the tracker and calorimeter, both of which affect the quality of the track match. The loose track-matching efficiency is measured relative to the H-Matrix efficiency, described in the previous section. It is measured with a tag-and-probe method using a sample of FullMC $Z \to ee$ events where both electrons pass the H-Matrix requirements, and at least one (the tag) passes the loose track-matching requirement. The efficiency is then the fraction of probe electrons which pass the loose track-matching requirement.

7.2.3.4 Tight Track-Matching Efficiency

Whereas the wider ΔR cone of the loose track-matching efficiency has a significant probability of contamination by luminosity-dependent pileup in the calorimeter, there is no significant InstLumi dependence found for the tight track-matching efficiency. Thus, the tight track-matching efficiency is parametrized as a two-dimensional function of z_{vtx} and η_{phys}, and is measured relative to the loose track-matching efficiency. It is measured with a tag-and-probe method on FullMC $Z \to ee$ events, in the same way the loose track-matching efficiency is measured. Figure 7.4 shows the tight track-matching efficiency for the RunIIb4 sample.

7.2.3.5 Additional p_T Dependence of Loose and Tight Track-Matching Efficiency

There is an additional dependence of the loose and tight track-matching efficiencies of the track reconstruction efficiency on p_T^e that was not included in the parametrization described in the previous two sections. This dependency is measured from a FullMC single electron sample, in order to have a good range of energies that is not limited by the kimatics of a $Z \to ee$ sample. Because the shape of the p_T^e dependence varies with η_{phys}, it is parametrized as a two-dimensional function η_{phys} and p_T^e. The p_T^e dependence is derived in bins of η_{phys}, as shown in Figure 7.5, and the efficiency in each η_{phys} bin is normalized so the efficiency at $p_T^e = 45\,\mathrm{GeV}$ is one. This roughly removes the η_{phys} dependence that is already

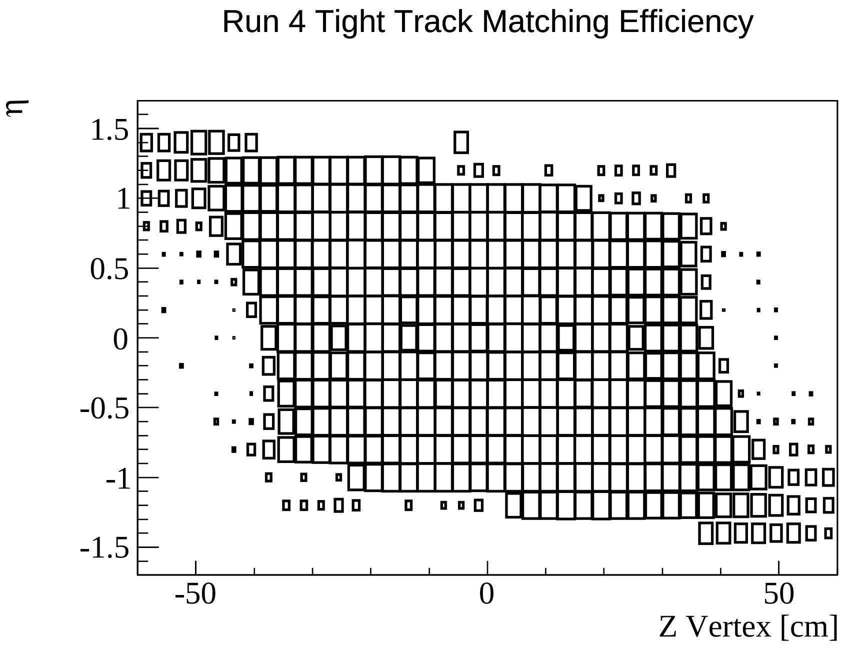

Figure 7.4: RunIIb4 Tight Track-Matching efficiency dependence on η_{phys} and z_{vtx}. Note the drop of efficiency as electrons get closer to the North and South boundaries of the tracker and calorimeter[20]. NOTE: This figure is from a D0 internal note. At the time of writing, it has not been approved by the D0 collaboration for general public use beyond this dissertation.

included in the H-Matrix and track-matching efficiency models. A perfect normalization is not possible, since the p_T^e distribution in the single electron sample does not match the kinematics of Z events, but normalizing at $p_T = 45\,\text{GeV}$, near the Jacobian edge, is a good first approximation, which will be corrected by the residual efficiency corrections.

7.2.4 Scalar E_t Dependent Efficiency

The Scalar Transverse Energy (SET) efficiency model describes the efficiency dependence on underlying energy contamination from spectator particle interactions (MB), pileup from other $p\bar{p}$ interactions (ZB), and the hadronic recoil from the vector boson in the

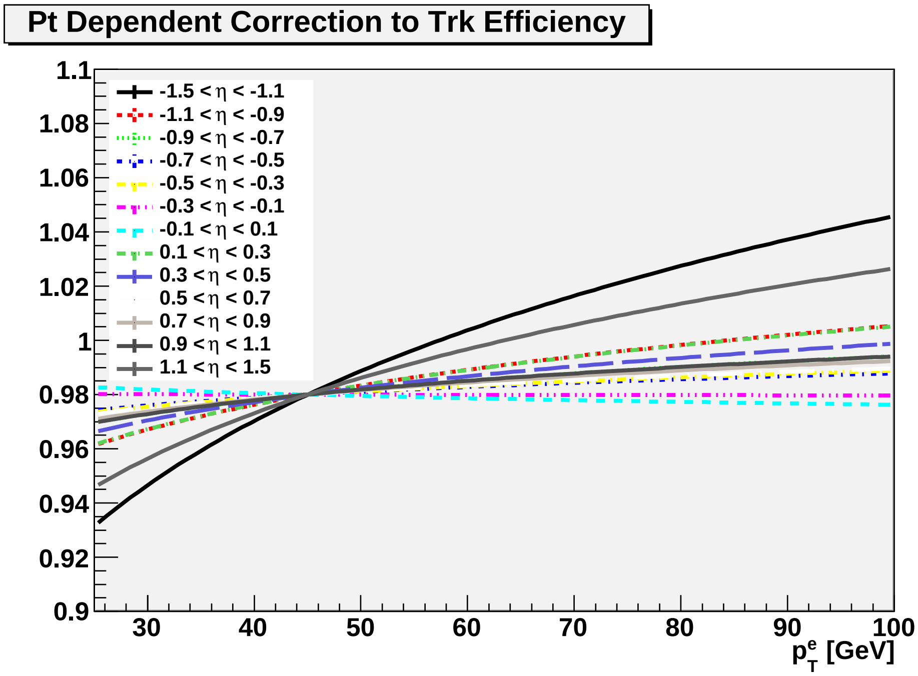

Figure 7.5: Additional p_T Dependence of Loose and Tight Track-Matching Efficiency, in bins of η_{phys}. Note that the curves are normalized to the same value at $p_T^e = 45\mathrm{GeV}$ in order to preserve the η_{phys} that has already been derived[20]. NOTE: This figure is from a D0 internal note. At the time of writing, it has not been approved by the D0 collaboration for general public use beyond this dissertation.

interaction of interest. In the earliest measurement using RunIIa data, the dependence was sufficiently parametrized as a function of the SET and the p_T^e, which have opposite effects on the efficiency. The SET reflects average background energy which, as it increases, degrades electron reconstruction based on cluster isolation and shower shape, whereas the higher the p_T of an electron, the easier it is to see against the background. In RunIIb, the luminosity increased to high enough values to modify the calorimeter gains significantly, which also affects identification. The high luminosity also means higher statistics, which makes possible a higher precision measurement if we also decrease the systematic uncertainty of our model correspondingly. Therefore we also allow a dependence on $u_{\|}$, the hadronic recoil relative to the electron direction. A high recoil is correlated with a highly boosted boson, and electrons which travel opposite the direction of the recoil are highly boosted as well, with high p_T and high reconstruction efficiency, but electrons which travel opposite the direction of the boost, in the same direction as the hadronic recoil, have low p_T and low reconstruction efficiency.

Therefore, In RunIIb, the SET efficiency model is now parametrized as a five-dimensional function of SET, p_T^e, $\eta_{\rm det}$, InstLumi, and $u_\parallel$. It is derived separately for W and Z events as a function of these five variables from FullMC samples with the u_T upper limit relaxed from 15 GeV to 30 GeV. The strongest dependence of the (so-called) SET efficiency is on the SET and the p_T^e, where larger values of SET decrease the efficiency and larger values of p_T^e increase the efficiency. Essentially, the efficiency depends most strongly on the ratio SET$/p_T^e$. Therefore, the SET efficiency is parametrized as a function of this ratio, in bins of the other variables.

The tuning is done in two steps: First, a reweighting is applied in the FastMC to make the distribution of the ZB contribution to the SET (SET$^{\rm ZB}$) versus the truth p_T^e agree with the same distribution in FullMC. We do not use the total value of the SET and the reconstructed value of the p_T^e, because they are contaminated by underlying energy, and to tune based on these observables would result in overcorrection and a bias. However, the dependent variables in the parametrization must be the final simulated observables, so for the second step, we create a parametrization based on the ratio between the (total value of the) SET and the reconstructed p_T^e. The second step is performed separately in bins of p_T^e, $\eta_{\rm det}$, InstLumi, and $u_\parallel$. For each bin in this four-dimensional set, we create a polynomial parametrization of the ratio between the SET$/p_T^e$ distributions in the reweighted FastMC and the original FullMC. Then we normalize the parametrized curve to have average value of unity and multiply it by overall ratio for each (p_T^e, $\eta_{\rm det}$, InstLumi, and $u_\parallel$) bin.

7.2.5 $U_\parallel$ Efficiency

While the SET dependent parametrization described in the previous section is a good model of the inefficiencies arising from the overall magnitude of the underlying energy, it does not fully describe the dependence of efficiency on the distribution of underlying energy, most importantly, the relative distribution of the hadronic recoil energy and the electron energy. When the hadronic recoil is close to the electron, it significantly affects the reconstruction and the identification efficiency of the electron. Therefore, we model an additional correction to the efficiency which depends on the "u-parallel" variable $u_{\|}$, which is the projection of hadronic energy on the direction of the electron momentum, defined by

$$u_{\|} = \vec{u}_T \cdot \frac{\vec{p}_T^e}{p_T^e} \tag{7.3}$$

The $u_{\|}$ efficiency is modeled as a slope with a turn-on (or "kink-point")[13] at slightly positive $u_{\|}$. In addition, we are experimenting with an additional slope and kink-point to model some dependence at negative $u_{\|}$. It used to be measured with a tag-and-probe method performed on a sample of FullMC $Z \to ee$ events, but this method overestimates the pure $u_{\|}$, because there are significant correlations with p_T and SET. In addition, the $u_{\|}$ efficiency is slightly different for $Z \to ee$ than for $W \to e\nu$ events. Therefore, we use the "ratio method", modeling an efficiency measured from the ratio between the FastMC (without the $u_{\|}$ efficiency simulated) and the FullMC or collider data. The discrepancy prior to the correction is shown in Figure 7.6. The $u_{\|}$ efficiency is measured from the data $W \to e\nu$ sample in four bins of InstLumi. The determination of the correction parameters is shown in Figures 7.8 and 7.10. Figures 7.9, 7.11, and 7.7 show the same ratios calculated after the efficiency has been applied.

7.2.6 ϕ-mod Efficiency

The ϕ-mod efficiency does not need to be simulated because of the calorimeter fiducial requirements, described in Section 5.2.4.

7.2.7 Electron ϕ Efficiency

The electron ϕ-dependent efficiency is due to imperfections such as dead tracker pixels and dead calorimeter cells. There is also an overall sinusoidal effect due to the difference

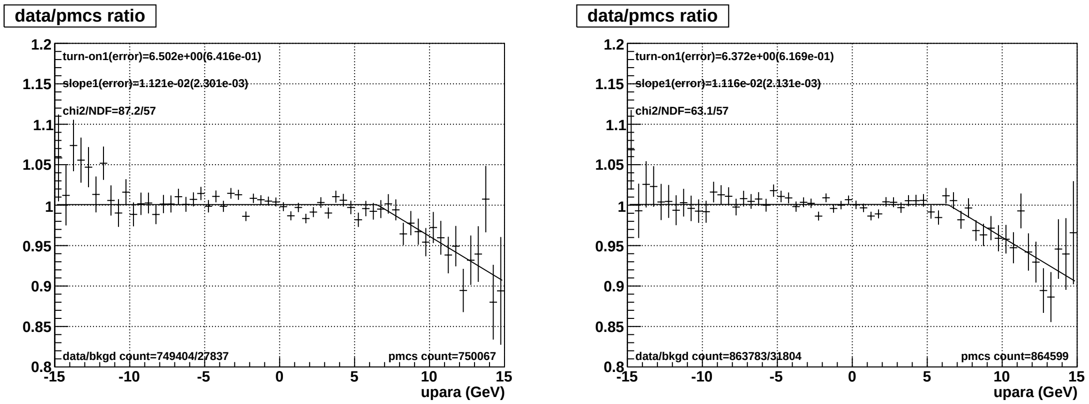

Figure 7.6: Data/FastMC ratio vs. $u_{\|}$, before correction. RunIIb3 is left, RunIIb4 is right. InstLumi<4 is left, 4<InstLumi<999 is right. Full InstLumi range is bottom. NOTE: This figure is from the author's own work. At the time of writing, it has not been approved by the D0 collaboration for general public use beyond this dissertation.

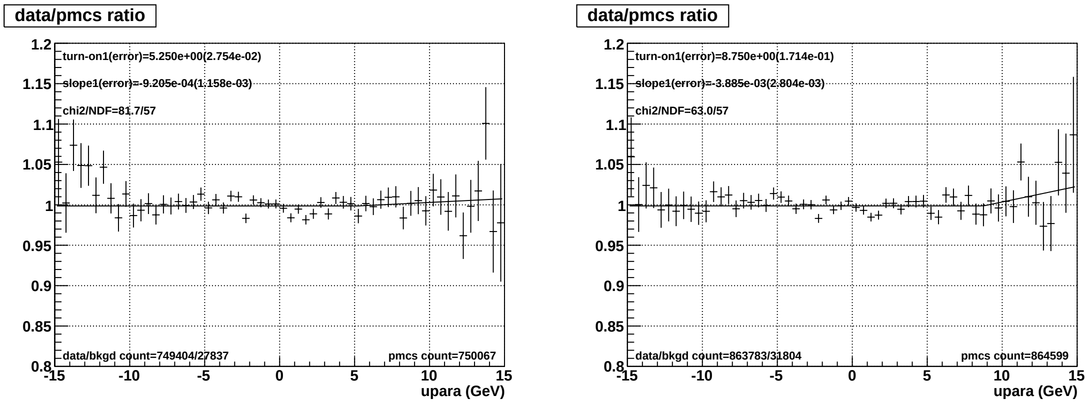

Figure 7.7: Data/FastMC ratio vs. $u_{\|}$, after correction F applied. RunIIb3 is left, RunIIb4 is right. InstLumi<4 is left, 4<InstLumi<999 is right. Full InstLumi range is bottom. NOTE: This figure is from the author's own work. At the time of writing, it has not been approved by the D0 collaboration for general public use beyond this dissertation.

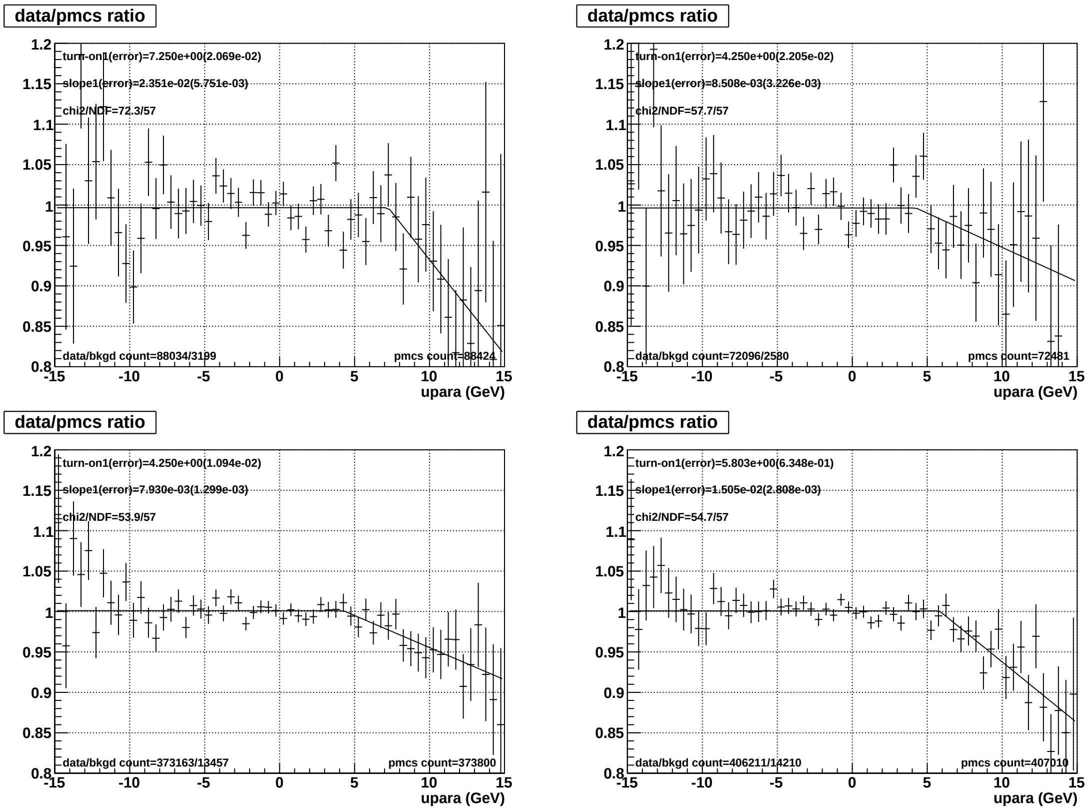

Figure 7.8: Data/FastMC ratio vs. $u_{\|}$, before correction. RunIIb3 is left, RunIIb4 is right. InstLumi<2 is top row, 2<InstLumi<4 is bottom row. NOTE: This figure is from the author's own work. At the time of writing, it has not been approved by the D0 collaboration for general public use beyond this dissertation.

in readout time between the top and bottom of the detector. Because we do not expect any significant correlation between electron ϕ and other variables, this efficiency is derived by dividing the sixtyfour-bin ϕ distribution in $W \rightarrow e\nu$ data or FullMC by the distribution from the corresponding FastMC distribution, to get a value for each ϕ module. It is shown for RunIIb4 in Figure 7.12.

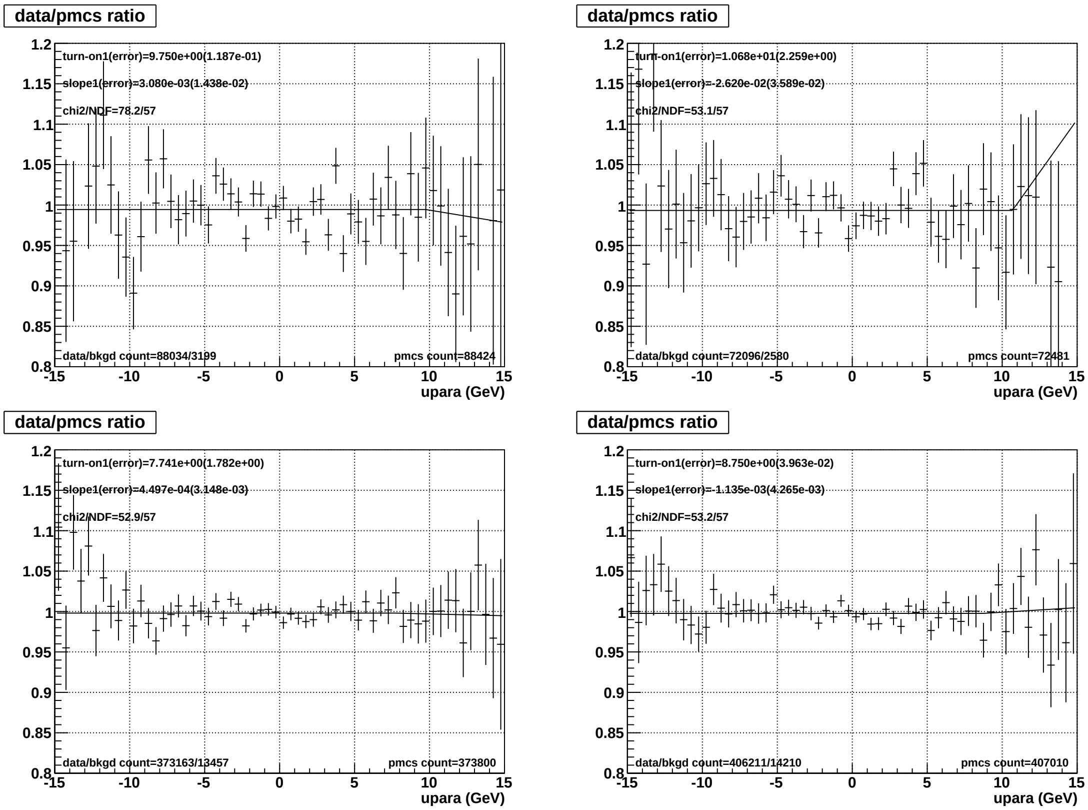

Figure 7.9: Data/FastMC ratio vs. $u_{\|}$, after correction F applied. RunIIb3 is left, RunIIb4 is right. InstLumi<2 is top row, 2<InstLumi<4 is bottom row. NOTE: This figure is from the author's own work. At the time of writing, it has not been approved by the D0 collaboration for general public use beyond this dissertation.

7.2.8 Residual Corrections to the H-Matrix and Track-Matching Efficiencies

We have determined the dependences of the H-Matrix and Track-Matching efficiencies on electron p_T, SET, InstLumi, electron η_{det}, and η_{phys} in the FullMC $Z \to ee$ sample, as described in Section 7.2.3. These are used in the `GEANT` FastMC, and also form the basis for the data FastMC. However, the efficiency dependence in the collider data are found to have non-negligible differences from those in the FullMC. Therefore, we must determine these differences and add a modification to the FastMC, in the form of parameterized correction

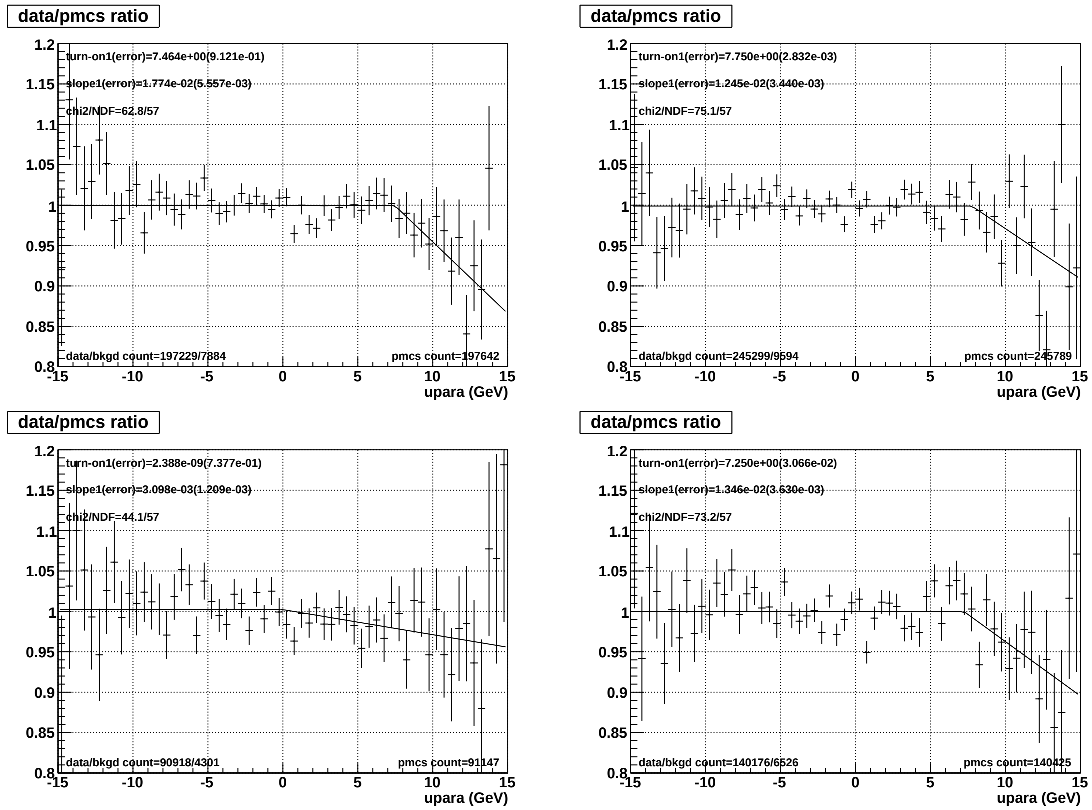

Figure 7.10: Data/FastMC ratio vs. $u_{\|}$, before correction. RunIIb3 is left, RunIIb4 is right. 4<InstLumi<6 is top row, 6<InstLumi<999 is bottom row. NOTE: This figure is from the author's own work. At the time of writing, it has not been approved by the D0 collaboration for general public use beyond this dissertation.

functions which are applied in the same manner as efficiencies, using random numbers. The base sample we use to determine the efficiency of the three cuts is a sample of events in collider data which have satisfied the following criteria:

Base selection criteria applied to $Z \rightarrow ee$ events for the H-Matrix efficiency study:

- The event has at least two reconstructed electrons. If more than two, we take the leading two according to $p_T(e)$.

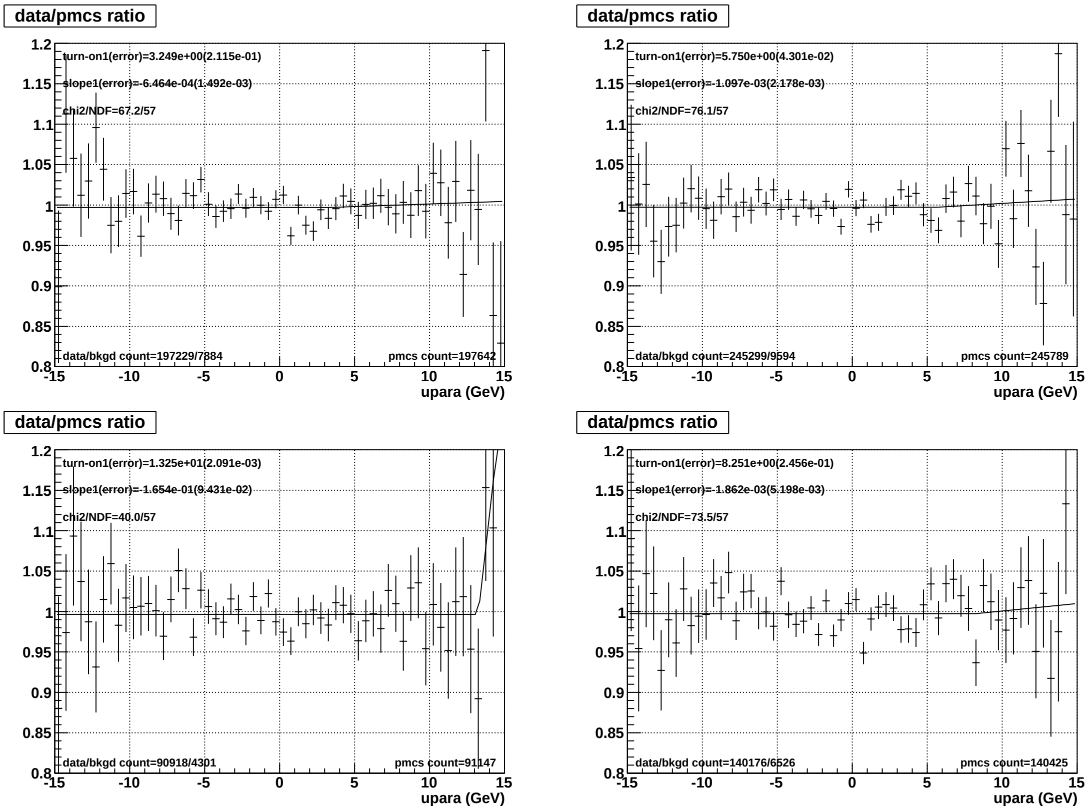

Figure 7.11: Data/FastMC ratio vs. $u_{\|}$, after correction F applied. RunIIb3 is left, RunIIb4 is right. 4<InstLumi<6 is top row, 6<InstLumi<999 is bottom row. NOTE: This figure is from the author's own work. At the time of writing, it has not been approved by the D0 collaboration for general public use beyond this dissertation.

- The invariant mass, M_{ee}, is between 60 and 130 GeV.
- Recoil p_T (u_T) satisfies $u_T < 30$ GeV.
- Both electrons do not fall in Phi Cracks (calorimeter inter-module gaps in ϕ).
- Both electrons satisfy $p_T(e) > 25$ GeV.
- Both electrons satisfy EMF>0.9.

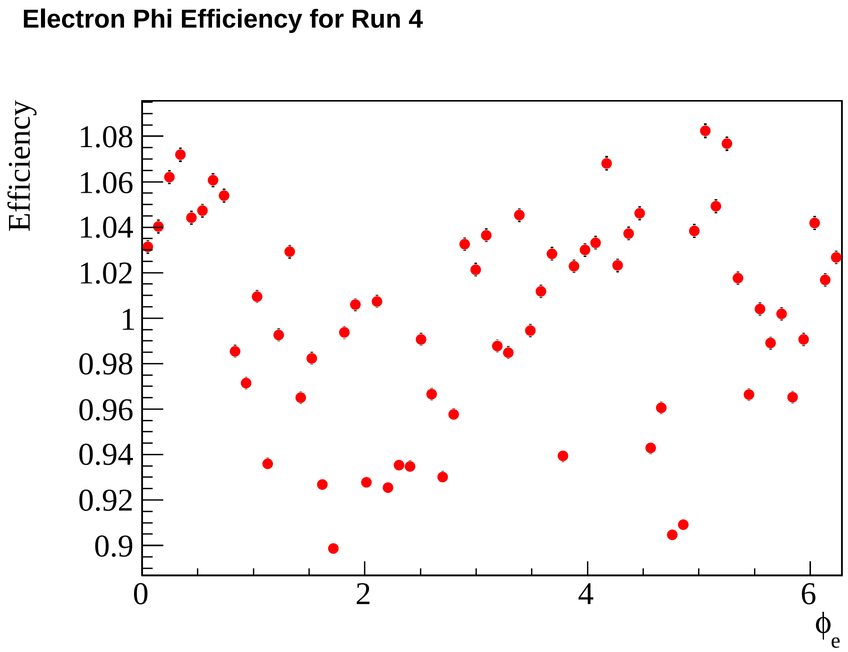

Figure 7.12: Electron ϕ efficiency used in `GEANT` FastMC, determined from the ratio of the ϕ distributions of FullMC and FastMC. It looks “noisy” because each point corresponds to a single ϕ-module, and the efficiency depends in part on peculiarities to the individual modules[20]. NOTE: This figure is from a D0 internal note. At the time of writing, it has not been approved by the D0 collaboration for general public use beyond this dissertation.

- Both electrons satisfy ISO<0.15.
- Electrons can be either in CC or in EC. If in EC, it must pass the H-Matrix criterion.
- **Pass:** *this electron* is in CC, passes H-Matrix, its reconstruction window does not contain dead cells, and *the other electron* passes the trigger.
- **Fail:** *this electron* is in CC, passes H-Matrix, its reconstruction window does not contain dead cells, and *the other electron* passes the trigger.

Base selection criteria applied to $Z \rightarrow ee$ events for the loose track-match efficiency study:

- The event has at least two reconstructed electrons. If more than two, we take the leading two according to $p_T(e)$.
- The invariant mass M_{ee} is between 60 and 130 GeV.
- Recoil p_T (u_T) satisfies $u_T < 30$ GeV.
- Both electrons do not fall in Phi Cracks (calorimeter inter-module gaps in ϕ).
- Both electrons satisfy $p_T(e) > 25$ GeV.
- Both electrons satisfy EMF>0.9.
- Both electrons satisfy ISO<0.15.
- Both electrons pass the H-Matrix criterion.
- Electrons can be either in CC or in EC.
- **Pass:** *this electron* is in CC, passes the loose track-matching criterion, its reconstruction window does not contain dead cells, and *the other electron* passes the trigger.
- **Fail:** *this electron* is in CC, fails the loose track-matching criterion, its reconstruction window does not contain dead cells, and *the other electron* passes the trigger.

Base selection criteria applied to $Z \to ee$ events for the tight track-match efficiency study:

- The event has at least two reconstructed electrons. If more than two, take the leading two according to $p_T(e)$.
- The invariant mass M_{ee} is between 60 and 130 GeV.
- Recoil p_T (u_T) satisfies $u_T < 30$ GeV.

- Both electrons do not fall in Phi Cracks (calorimeter inter-module gaps in ϕ).
- Both electrons satisfy $p_T(e) > 25$ GeV.
- Both electrons satisfy EMFraction>0.9.
- Both electrons satisfy ISO<0.15.
- Both electrons pass the H-Matrix criterion.
- Both electrons pass the loose track-matching criterion.
- Electrons can be either in CC or in EC.
- **Pass:** *this electron* is in CC, passes tight-track-match criterion, and its reconstruction window does not contain dead cells; and *the other electron* pass trigger.
- **Fail:** *this electron* is in CC, fails tight-track-match criterion, and its reconstruction window does not contain dead cells; and *the other electron* pass trigger.

Note that we include events where one electron is in the EC to more closely match the kinematics of $W \to e\nu$ events. However, we only measure the efficiency of electrons which are in the CC. We do not allow the electron being tested to have dead cells, as this would predispose it to failing any of the cuts, and in the case of the p_T dependent efficiency, place the electron in the wrong efficiency bin, due to mismeasurement of the p_T.

The residual correction is determined simultaneously for z_{vtx} and η_{phys} for the H-Matrix and the tight track-matching efficiencies. For the loose track-matching efficiency, it is necessary to determine a three-dimensional z_{vtx}, η_{phys}, and InstLumi correction due to correlations. We have found that no η_{det} or p_T^e correction is needed. In this dissertation, we present the calculation of the dependence of the H-Matrix and loose and tight track-matching efficiency correction on the correlated SET and InstLumi observables, but with the InstLumi dependence of the loose track-matching efficiency correction removed, because it is already included in the three-dimensional z_{vtx}, η_{phys}, and InstLumi correction to the loose track-matching efficiency.

7.2.8.1 Problems with the Traditional "Tag-and-Probe" Method

Unlike the FullMC sample, which is pure signal, the collider data is contaminated by background, and we do not have access to the true values of the observables in the collider data. Therefore, we need some other way of separating signal from background. We cannot use the traditional version of the "tag-and-probe" method here, because it results in a bias. This bias is illustrated in Figure 7.13, which shows the efficiency to pass electron ID, measured in FullMC from every electron in the sample (red), and measured only from electrons in an event where the other electron passes electron ID (blue). Above the Jacobian edge, the efficiencies have the same dependence on electron true p_T. Below the Jacobian edge, they deviate from each other, for the following reason: In the "tag-and-probe" method, an electron is a probe - is tested for passing the electron ID - only if it has a partner electron which is a tag - passes electron ID. when the probe electron has low p_T, it is likely that the tag electron is highly boosted, having a high p_T in the opposite direction of the recoil. This means that the probe electron is likely to be contaminated by the recoil, and likely to fail electron ID due to its own low p_T. If we treat all electrons equally, the partner electron is not required to pass electron ID, and a smaller fraction of the low-p_T electrons which are tested will be so contaminated by recoil that they fail electron ID. This effect is accounted for in the recoil model and the $u_{\parallel}$-dependent efficiencies; to avoid double-counting, it must not be included in this part of the efficiency model.[6]

---

[6] It is true that the effect of the double-counting is not quite as large as implied by Figure 7.13, because we would actually be correcting based on the ratio between the efficiency in collider data and FullMC. However, there are differences in the recoil model between data and FullMC, and some portion of those differences would be double-counted.

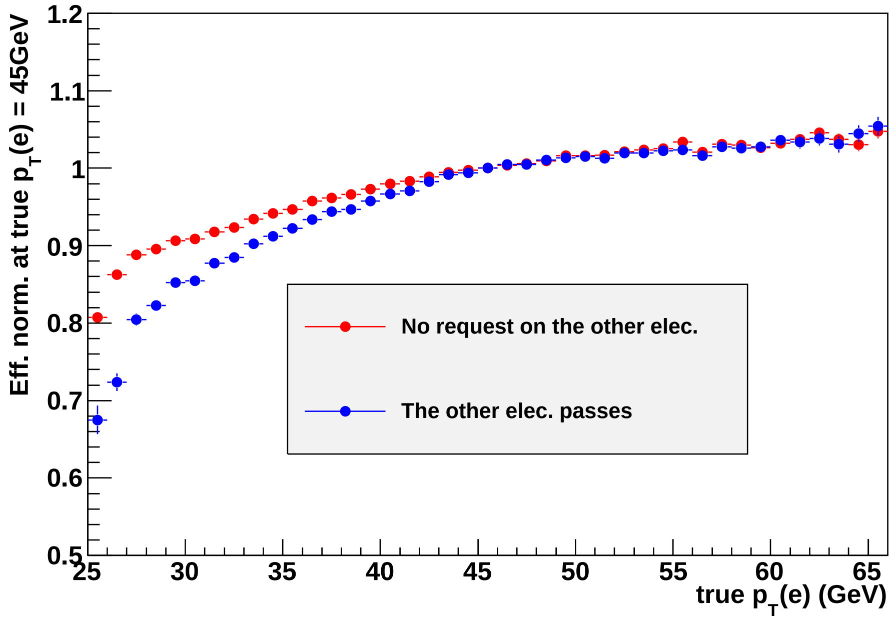

Figure 7.13: Illustration of the bias in the efficiency measured by the traditional tag-and-probe method. See 7.2.8.1 for discussion[41]. NOTE: This figure is from a D0 internal note. At the time of writing, it has not been approved by the D0 collaboration for general public use beyond this dissertation.

7.2.8.2 Alternative "Tag-and-Probe" Method with Background Subtraction

Since we cannot safely identify signal events by tagging electrons with the electron ID requirement, we need another way to determine how many events in a given bin, which pass or fail a given cut, are signal. We do not need to identify the specific signal events, only count them, and we can use a "background-subtraction" method for this purpose. This method requires creating normalized templates which describe the shape of the signal (Section 7.2.8.4) and background (Section 7.2.8.3) distribution in a given observable, in this case, the invariant mass M_{ee} of the candidate electrons. We then find the best fit to the distribution of the following parametrized function

$$F\left(x;N,f\right) = N \cdot \left[f \cdot S\left(x\right) + \left(1-f\right) \cdot B\left(x\right)\right] \tag{7.4}$$

where $S\left(x\right)$ is the signal template, $B\left(x\right)$ is the background template, f is the best-fit estimate of the fraction of the distribution that is signal, and N is the integral of the parametrized function. N is allowed to float to within 10% of the integral of the distribution to allow the fit more freedom to optimize f. $S\left(x\right)$ contains two additional floating parameters (a "shift" and a "smear") which are simultaneously determined with f and N in the fit of $F\left(x;N,f\right)$. The role of these parameters in the form of $S\left(x\right)$ is described in Section 7.2.8.4. The shape $B\left(x\right)$ is determined first in a separate fit, described in Section 7.2.8.3.

The signal templates are created using FullMC or FastMC samples. When we use the FastMC, it can be the `GEANT` version or an earlier tune of the data version; the subtle differences between the two tunes are negligible for the determination of this efficiency correction. However, in some cases we find that the FullMC provides a better model of the failing signal distribution, because the FastMC is tuned to model the distributions for electrons which pass all cuts whereas the FullMC simulates both passing and failing electrons.

To estimate the shape of the passing and failing signal spectrum in the dependent variable M_{ee}, we use a data sample with a relaxed set of selection requirements, particularly, we remove the selection requirements of the cut whose efficiency we are trying to measure. This results in a data sample that includes signal electrons which pass the cut, signal electrons which fail the cut, and background. Then, since we cannot identify whether individual electrons are signal electrons or not, we use a template method to estimate the number of signal electrons passing or failing a given selection cut.

7.2.8.3 Creating Templates for Background Subtraction

The background template for a specific bin is derived from collider data in that bin with selections applied to exclude signal events. It will most likely also exclude some background events, but this is acceptable since we need the shape of the background spectrum, but not its magnitude, for our template. The selection criteria applied to the data samples to select background events are similar to the selection criteria for the full sample, but with the EMF criterion removed. For the H-Matrix background, both electrons must fail the loose track-matching requirement. For the loose track-matching background, both electrons must fail the H-Matrix criterion and fail the tight track-matching criterion. For the tight track-matching background, both electrons must fail the Hmatrix criterion. The full set of cuts used to select the backgrounds for the H-Matrix, Loose Track-Matching, and Tight Track-matching efficiencies are:

Base selection criteria applied to $Z \to ee$ events to select pure background for H-Matrix efficiency study:

- The event has at least two reconstructed electrons. If more than two, take the leading two according to $p_T(e)$.
- The invariant mass $M(ee)$ is between 60 and 130 GeV.
- Recoil p_T (u_T) satisfies $u_T < 30$ GeV.
- Both electrons do not fall in Phi Cracks (calorimeter inter-module gaps in ϕ).
- Both electrons satisfy $p_T(e) > 25$ GeV.
- Both electrons satisfy EMFraction > 0.9 .
- Both electrons satisfy ISO < 0.15 .
- Both electrons can be either in CC or EC. There is no requirement for both electrons to be in CC at the same time.
- Both electrons fail loose-track-match criterion.

- Both electrons fail tight-track-match criterion.

- **Pass:** *this electron* is in CC, HMx7<12 , and its reconstruction window does not contain dead cells. *Other* electron must pass trigger.

- **Fail:** *this electron* is in CC, HMx7>12 , and its reconstruction window does not contain dead cells. *Other* electron must pass trigger.

Base selection criteria applied to $Z \rightarrow ee$ events to select pure background for loose-track-match efficiency study:

- The event has at least two reconstructed electrons. If more than two, take the leading two according to $p_T(e)$.

- The invariant mass $M(ee)$ is between 60 and 130 GeV.

- Recoil p_T (u_T) satisfies $u_T < 30$ GeV.

- Both electrons do not fall in Phi Cracks (calorimeter inter-module gaps in ϕ).

- Both electrons satisfy $p_T(e) > 25$ GeV.

- Both electrons satisfy ISO < 0.15 .

- Both electrons fail H-Matrix criterion.

- No EMFraction criterion for both electrons.

- **Pass:** *this electron* is in CC, pass loose-track-match criterion, and its reconstruction window does not contain dead cells. *Other* electron must pass trigger.

- **Fail:** *this electron* is in CC, fail loose-track-match criterion, and its reconstruction window does not contain dead cells. *Other* electron must pass trigger.

Base selection criteria applied to $Z \rightarrow ee$ events to select pure background for tight-track-match efficiency study:

- The event has at least two reconstructed electrons. If more than two, take the leading two according to $p_T(e)$.
- The invariant mass $M(ee)$ is between 60 and 130 GeV.
- Recoil p_T (u_T) satisfies $u_T < 30$ GeV.
- Both electrons do not fall in Phi Cracks (calorimeter inter-module gaps in ϕ).
- Both electrons satisfy $p_T(e) > 25$ GeV.
- Both electrons satisfy ISO < 0.15 .
- Both electrons fail H-Matrix criterion.
- Both electrons pass loose-track-match criterion.
- No EMFraction criterion for both electrons.
- **Pass:** *this electron* is in CC, pass tight-track-match criterion, and its reconstruction window does not contain dead cells. *Other* electron must pass trigger.
- **Fail:** *this electron* is in CC, fail tight-track-match criterion, and its reconstruction window does not contain dead cells. *Other* electron must pass trigger.

These background requirements are identical to the requirements used in the RunIIb12 analysis, with the exception of the requirement that the other electron passes the trigger. This requirement was found to be necessary to properly fit to the full sample at low M_{ee}.

Once the background is selected, it is fit with an ad-hoc template function consisting of the sum of a gaussian and a tenth order polynomial:

$$B(x) = p_0 \cdot e^{-\frac{(x-p_1)^2}{2p_2^2}} + \sum_{i=3}^{13} p_i \cdot x^{i-3} \tag{7.5}$$

where p_0 to p_{13} are the parameters allowed to float in the fit. After fitting, the template is then normalized to one.

7.2.8.4 Creating Templates to Model the Signal with the "Kernel Estimation Procedure"

The signal template for the background subtraction procedure is derived from either a FastMC or FullMC sample of $Z \to ee$ events.[7] The Monte Carlo samples do not perfectly describe the signal in collider data, because the energy resolution and response of the detector is not perfectly modeled as a function of the efficiency dependent variables. Therefore, we use a modified version of the "Kernel Density Estimation Method", described in detail in [39] and [27] where we include a shift and smearing parameter that we allow to float. The shift and smearing parameters are applied as follows:

The Monte Carlo sample for the signal template is put into a histogram of 1 GeV bins in M_{ee} . This histogram is converted into a function where every M_{ee} bin is replaced by a Gaussian function with peak position equal to the bin center, magnitude equal to the bin content, and width equal to 1 GeV . Parameters are added to allow the peak to shift and the Gaussian to widen, while keeping the magnitude (i.e. the number of $Z \to ee$ events) the same. Thus the function representing the signal spectrum template is

$$S(x; s, \sigma) = \frac{1}{N} \sum_{i=1}^{m} \frac{n_i}{\sqrt{2\pi (h_i + \sigma)^2}} e^{-\frac{[(x-s)-t_i]^2}{2(h_i+\sigma)^2}} \tag{7.6}$$

$$h_i = \frac{1}{2} \cdot (\frac{4}{3})^{\frac{1}{5}} \cdot \sqrt{\frac{\Delta x_i}{3\sqrt{2}}} \cdot \sqrt{\frac{N}{n_i}} \tag{7.7}$$

---

[7] The fast Monte Carlo sample was originally used for the signal template in all cases, because it contains residual data corrections and should in theory match the data signal shape better. However, it was found that PMCS does not describe electrons which fail cuts, particularly the loose track-matching cut, as well as full Monte Carlo does, so for those data cuts, full Monte Carlo was used for the signal template.

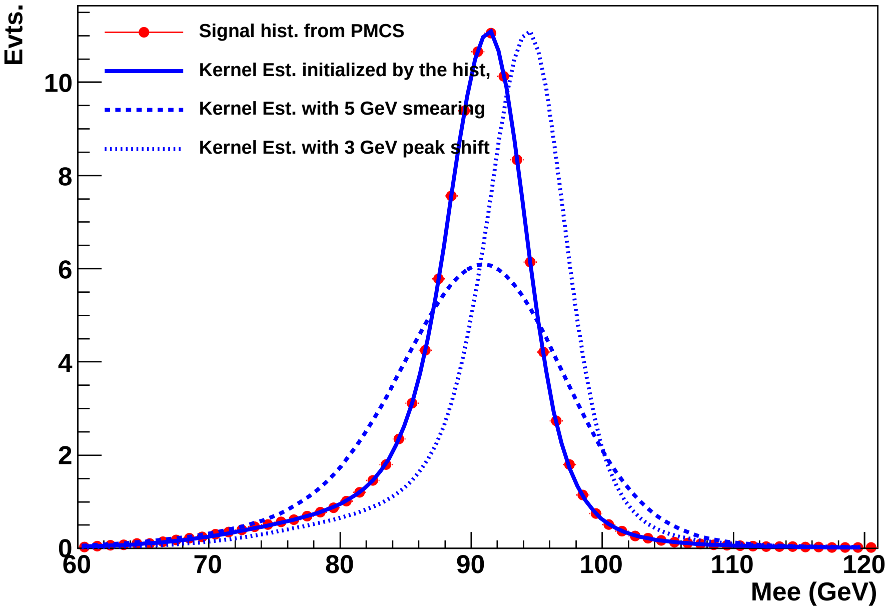

Figure 7.14: Illustration of the signal template with the effect of "smearing" by 5 GeV and "shifting" by 3 GeV shown[41]. NOTE: This figure is from a D0 internal note. At the time of writing, it has not been approved by the D0 collaboration for general public use beyond this dissertation.

where the Δx_i is the bin width of the ith bin. The form of this template function is such that it is automatically normalized to one[41][2].

7.2.8.5 Calculating the Estimated Signal in an Efficiency Bin

The signal and background templates are normalized and fit to the data spectrum with the `Root MINUIT` fitter. For fitting stability, the overall magnitude of the data spectrum is allowed to float between 0.9 and 1.1 times the magnitude of the input data histogram. The signal fraction is the coefficient of the signal template in Section 7.4. The estimated signal count is calculated via:

$$n = N_{\rm eff} - k_{\rm eff} \cdot (1-f) \cdot N_{\rm fit} \ . \tag{7.8}$$

$$k_{\rm eff} = \frac{N_{\rm eff}^{\rm bkg}}{N_{\rm fit}^{\rm bkg}} \ , \tag{7.9}$$

$$\sigma_{k_{\rm eff}}^2 = \frac{(N_{\rm fit}^{\rm bkg})^2 \cdot N_{\rm eff}^{\rm bkg} + (N_{\rm eff}^{\rm bkg})^2 \cdot N_{\rm fit}^{\rm bkg}}{(N_{\rm fit}^{\rm bkg})^4} = \frac{k_{\rm eff}}{N_{\rm fit}^{\rm bkg}} \cdot (1 + k_{\rm eff}) \ , \tag{7.10}$$

where $N_{\rm eff}^{\rm bkg}$ or $N_{\rm fit}^{\rm bkg}$ is the number of background in the pure background histogram.

Therefore, the error of n^+ or n^- is given by:

$$\sigma_n^2 = N_{\rm eff} + k_{\rm eff}^2 \cdot (1-f)^2 \cdot N_{\rm fit} + k_{\rm eff}^2 \cdot N_{\rm fit}^2 \cdot \sigma_f^2 + (1-f)^2 \cdot N_{\rm fit}^2 \cdot \sigma_{k_{\rm eff}}^2 . \tag{7.11}$$

The background subtraction procedure is performed once for passing electrons, and once for failing electrons, in all bins of the variable whose efficiency dependence we are measuring.

7.2.8.6 Deriving the Correction for the Data Efficiency

To determine the necessary correction to the data FastMC, we must also measure the FullMC efficiency in the same bins we used to measure the efficiency from collider data. This is a much easier task, since the sample is all signal, and we do not need to perform a background subtraction. The efficiency measured from collider data is divided by that measured from the FullMC sample, and the resulting values are converted to a polynomial function to modify the efficiency applied in the FastMC. As usual, we conserve efficiency by scaling the overall efficiency shape to never be larger than one. Figure 7.15 shows the efficiency correction for the correlated dependent variables SET and InstLumi, for RunIIb3 and RunIIb4.

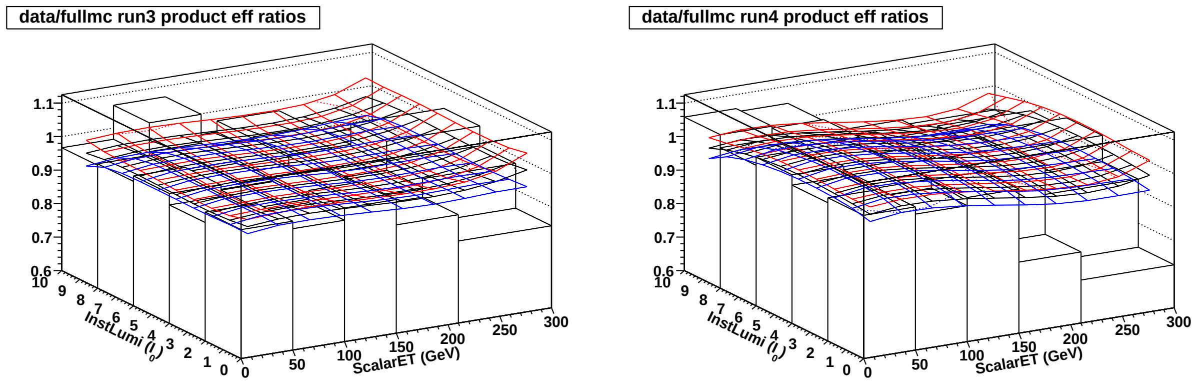

Figure 7.15: Ratio between data efficiency and FullMC efficiency vs. SET and InstLumi (2D "Lego" plot). Residual efficiency correction fit to the ratio and applied in data FastMC (black 2D curve), with upper (red) and lower (blue) 68% confidence intervals of the curve. NOTE: This figure is from the author's own work. At the time of writing, it has not been approved by the D0 collaboration for general public use beyond this dissertation.

7.2.8.7 Systematic Uncertainty Due to Efficiency Correction

The estimated residual corrections contain an inherent uncertainty due to the limited statistics of the data sample, as well as the fact that a polynomial function may not be a perfect model of the dependence. The uncertainty is measured by the covariance matrix from the fit, which describes the uncertainties of the individual parameters, as well as their correlations. The uncertainties can be visualized in various ways. For example, Figure 7.16 shows the SET (upper row) and InstLumi (lower row) dependent factors of the efficiency parameterization in black. The plots also show the same curve with the parameter of the first order (red), second order (green), and third order (blue), varied up and down by their uncertainty. However, the variation is misleadingly large in this visualization, because the correlations described by the covariance matrix are not accounted for.

Figure 7.15 shows the confidence intervals of the parametrized function. The confidence interval at a given point for our parametrized function is the amount of uncertainty

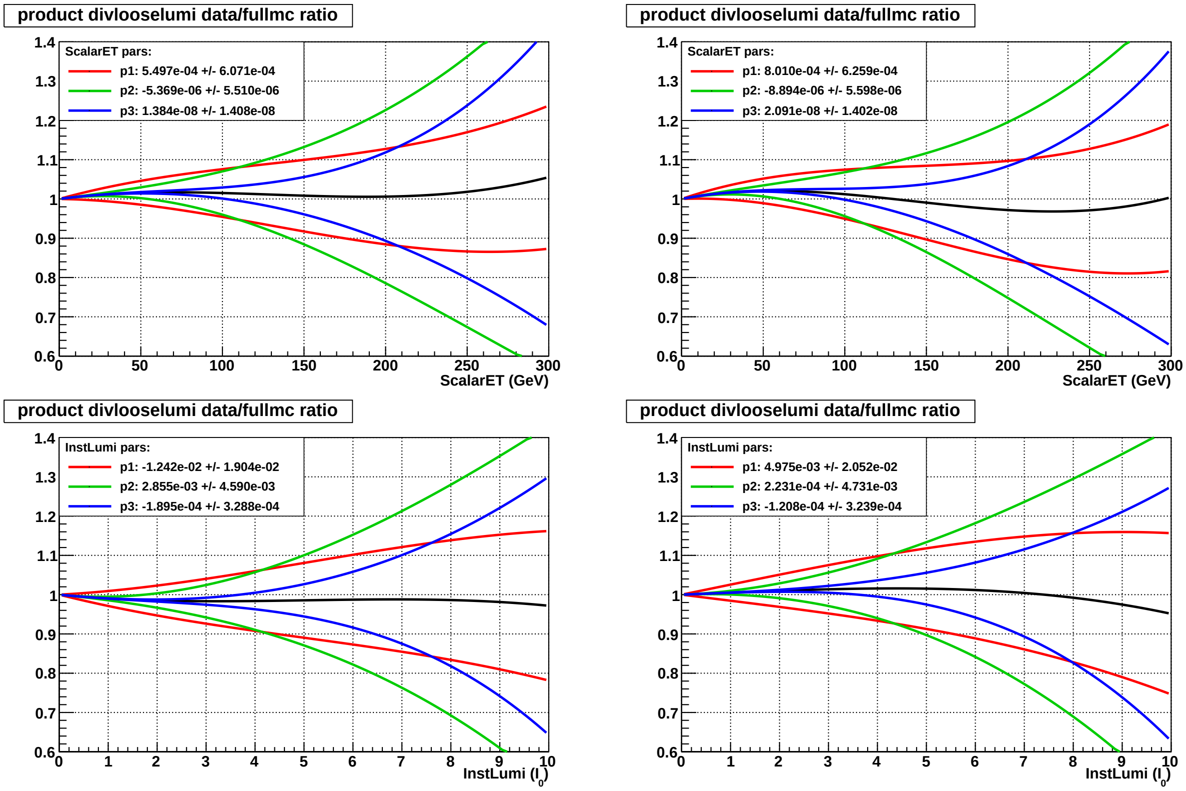

Figure 7.16: The SET (upper row) and InstLumi (lower row) dependence of the residual efficiency correction (black), with p_1 (red), p_2 (green), and p_3 (blue) varied up and down by one σ. RunIIb3 left, RunIIb4 right. NOTE: This figure is from the author's own work. At the time of writing, it has not been approved by the D0 collaboration for general public use beyond this dissertation.

in the value of the function given the uncertainty in the value of the parameters. Therefore, the standard 68%[8] confidence interval is calculated via

$$(\delta F(x,y))^2 = \sum_{i,j} \frac{\partial F(x,y)}{\partial p_i} C_{ij} \frac{\partial F(x,y)}{\partial p_j} \tag{7.12}$$

To properly describe our confidence in the measurement of the W mass, we need

---

[8] To get a different confidence level, the above equation is multiplied by a factor that depends on the degrees of freedom of the fit and desired confidence level.

to calculate the systematic uncertainty due to uncertainty in the parameters in our model. The uncertainty in the W mass due to all the parameters in a single residual correction is the product of the W variations with the covariance matrix that came from the fit of the parametric function for the measured residual correction of the data efficiency. The calculation is described by the following equation:

$$\frac{\delta M_W}{\delta p_i} C_{ij} \frac{\delta M_W}{\delta p_j} \tag{7.13}$$

where C_{ij} is the (i, j)th element of the covariance matrix, and $\frac{\delta M_W}{\delta p_i}$ and $\frac{\delta M_W}{\delta p_j}$ describe the dependence of the value of the W mass on the ith and jth parameters. The dependence of the W mass on the nth parameter is determined by taking a series of measurements of the W mass, using FastMC samples as pseudodata, and with the parameter varied up and down in steps of $\frac{1}{2}\sigma_n$, where $\sigma_n = \sqrt{C_{nn}}$ is the uncertainty in the nth parameter. As can be seen in Figure 7.17, the slope is determined by a linear fit to the W mass measurement as a function of δp_n. The calculation described in Equation 7.13 is performed for the W mass measurement for each of the three measurement observables.

In order to get the pure dependence of the W mass measurement on the parameters, we must remove the effect of statistical variation between the samples. To accomplish this, we generate all the pseudodata samples simultaneously, and apply the $5N$ (where N is the number of parameters) variations of the efficiency to each event as multiplicative weights instead of using random numbers. Then, the only difference between the samples is due to the variation in the efficiency, and we can disregard the statistical uncertainty in the individual measurements when performing the linear fits.

We have performed this calculation by using templates generated from the central values of the parameters of the fit, and varying the parameters to generate multiple samples of pseudodata, because this is analogous to the effect we wish to measure, the dependence of the outcome of our measurement of the W mass on the “true” value of the parameters. However, to first order, we have verified that we can get the same value by using the central values of the parameters of the fit to generate a single sample of pseudodata, which can be seen in Figure 7.18. The samples generated by varying the parameters are then used to generate the templates, and the same linear fit is done as before, now varying the templates used to measure the W mass points instead of varying the pseudodata. The fact that these calculations give roughly the same result is useful, because if we want to check that the our uncertainty calculation from pseudodata is similar to that which we get from data, we can only use the method where we vary the templates (having only access to a single data sample). The calculation performed on the data in this manner can be seen in Figure 7.19.

7.3 Electron Response Parametrization

The electron response describes the relationship between the true value of the electron energy and the value that is read out of the detector. An overall scale (multiplicative factor) and resolution ("smearing" factor) are determined, and there is also an angular dependence to this response. However, not all the effects are purely due to calorimeter response; there is an effect due to electron energy loss to FSR, there is an effect of the electron energy reconstruction technique, which simply counts all the energy in a "cone" around the electron cluster in the calorimeter and may not get it all, and which counts extra energy not due to the electron. The following subsections describe the techniques used to model all these effects.

7.3.1 Photon Radiation Effects

The parametrization of the inefficiency caused by FSR was described in Section 7.2.2. Here we describe the simulation of the effect of FSR on the reconstructed electron energy. First, production of zero, one, or two FSR photons is simulated at generator level. Production of three or more FSR photons has a negligible contribution. The same two FullMC samples as were described in Section 7.2.2 are used.

Energy loss due to FSR photons outside the electron window is modeled as a function of p_T, η_{phys}, ΔR, and X, where X is the fraction of electron energy carried by the photon, and ΔR is as defined in Equation 7.2.

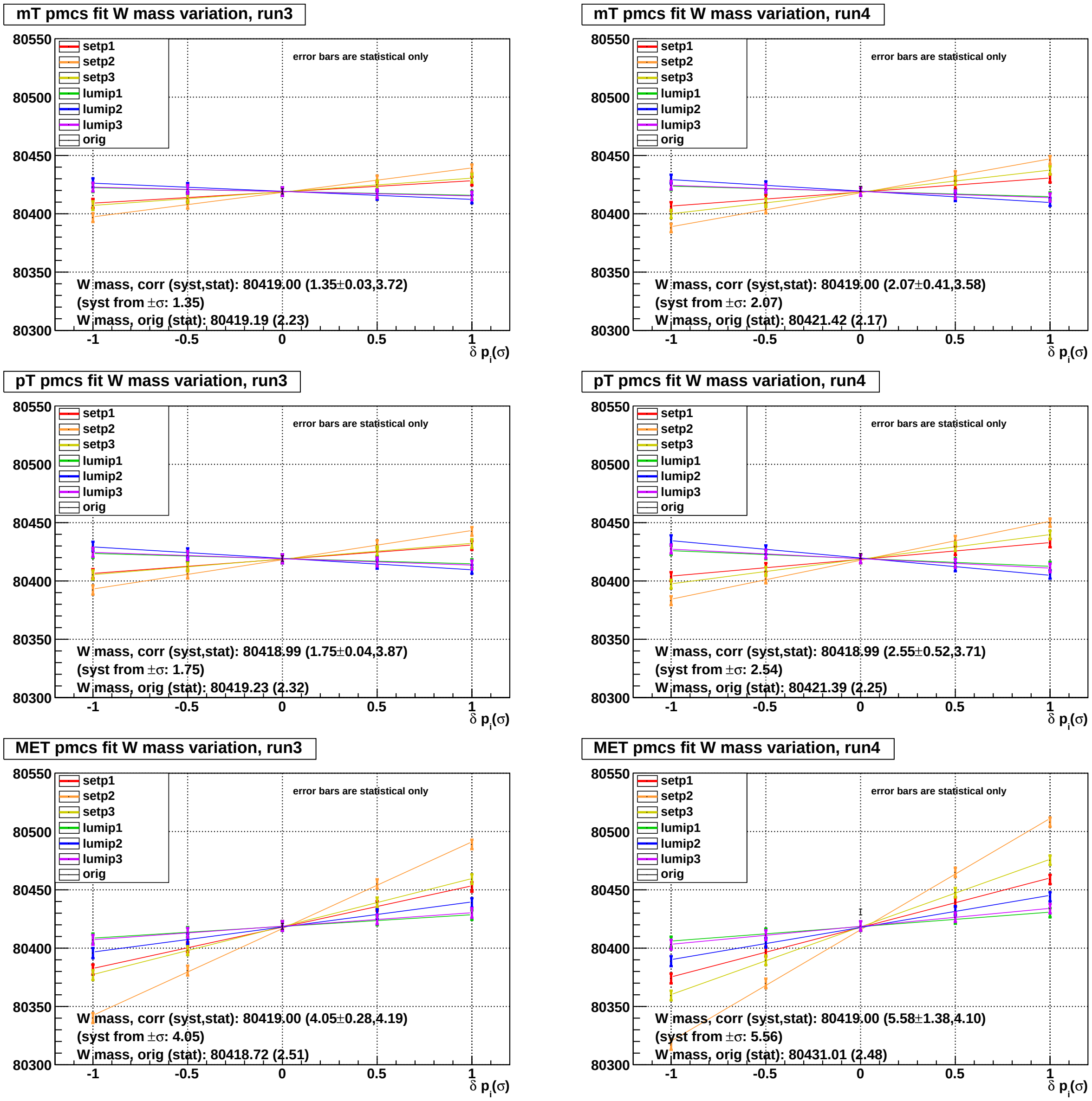

Figure 7.17: The central values and variation (by varying the pseudodata) of the W boson mass in pseudodata with the parameters from the SET-InstLumi dependent efficiency correction. Top row is m_T based measurement, middle row is p_T^e based measuerment, bottom row is MET based measurement. Left column is RunIIb3, right column is RunIIb4. NOTE: This figure is from the author's own work. At the time of writing, it has not been approved by the D0 collaboration for general public use beyond this dissertation.

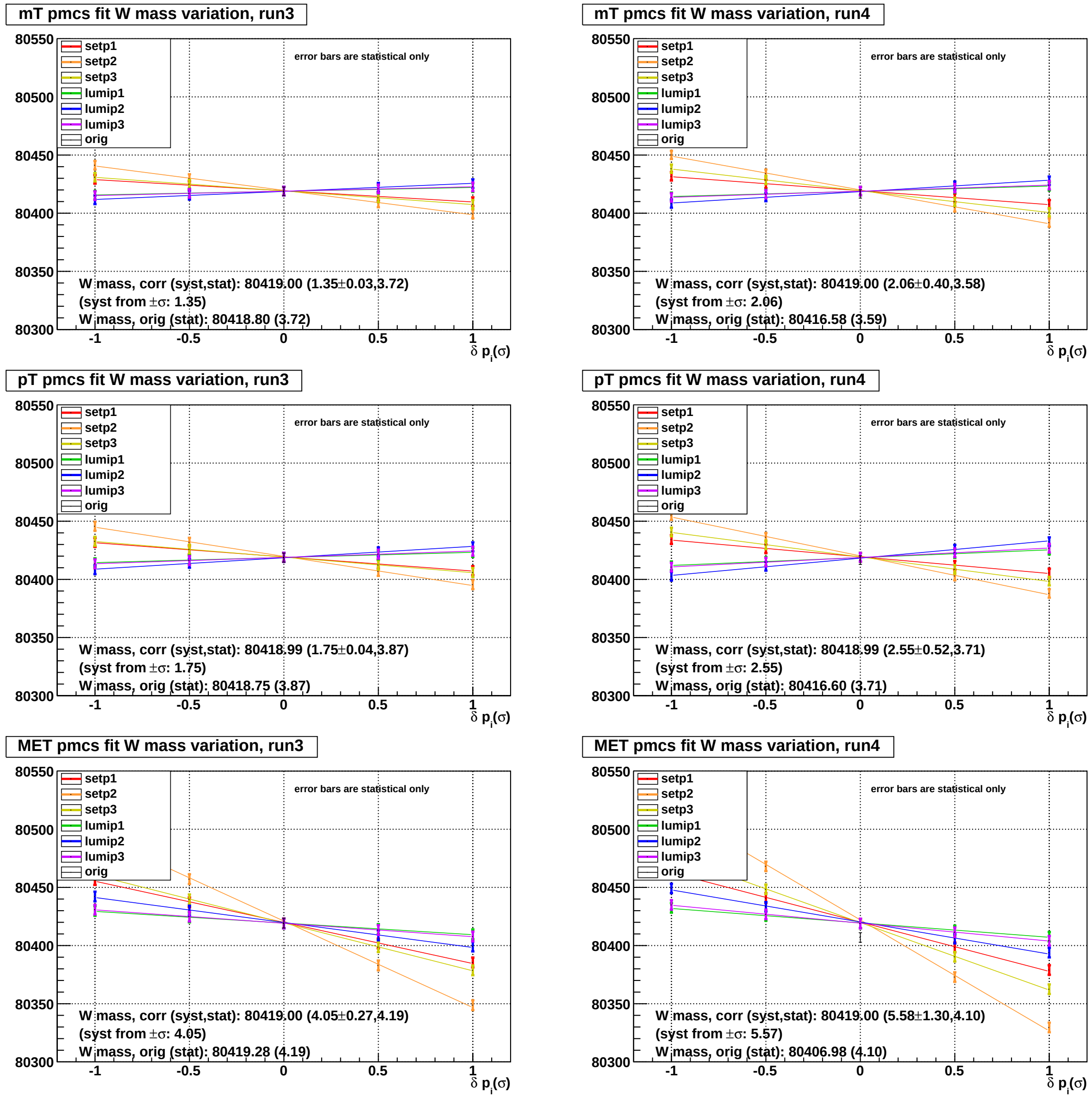

Figure 7.18: The central values and variation (by varying the template) of the W boson mass in pseudodata with the parameters from the SET-InstLumi dependent efficiency correction. Top row is m_T based measurement, middle row is p_T^e based measuerment, bottom row is MET based measurement. Left column is RunIIb3, right column is RunIIb4. NOTE: This figure is from the author's own work. At the time of writing, it has not been approved by the D0 collaboration for general public use beyond this dissertation.

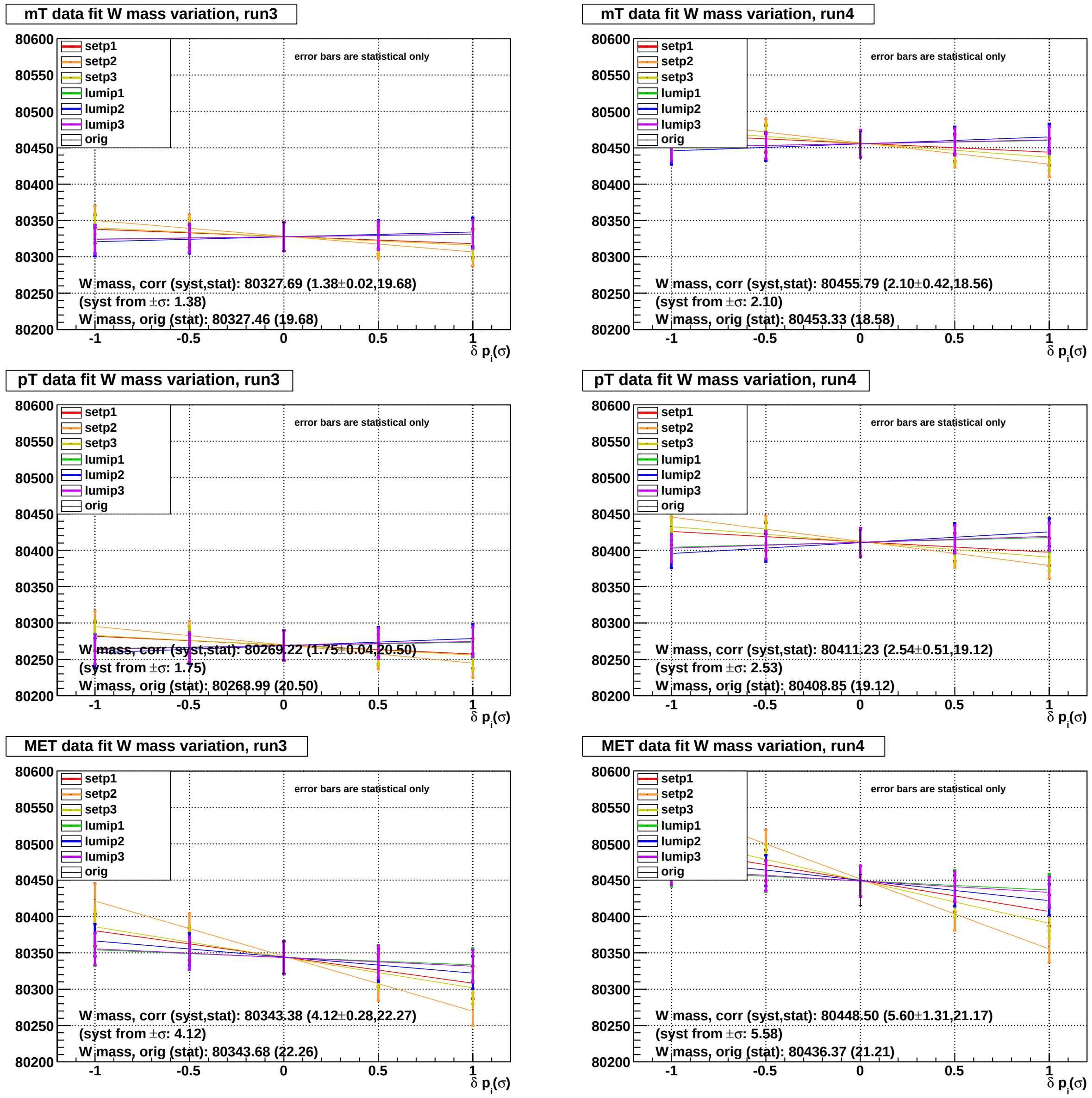

Figure 7.19: The central values and variation (by varying the template) of the blinded W boson mass in collider data with the parameters from the SET-InstLumi dependent efficiency correction. Top row is m_T based measurement, middle row is p_T^e based measeuerment, bottom row is MET based measurement. Left column is RunIIb3, right column is RunIIb4. NOTE: This figure is from the author's own work. At the time of writing, it has not been approved by the D0 collaboration for general public use beyond this dissertation.

The relationship between the difference in electron reconstructed energy due to the radiated photon and the true amount of energy carried by the photon is described by κ:

$$\begin{aligned} \kappa &= -\frac{E_{\text{reco}}^{\text{no FSR}} - E_{\text{reco}}}{E_{\text{true}}^{\text{no FSR}} - E_{\text{true}}} && (7.14) \\ &= -\frac{E_{\text{reco}}^{\text{no FSR}} - E_{\text{reco}}}{X \cdot E_{\text{true}}^{\text{no FSR}}} && (7.15) \end{aligned}$$

where $E_{\text{reco}}^{\text{no FSR}}$ is what the reconstructed electron energy would be if the electron had not undergone FSR, and $E_{\text{true}}^{\text{no FSR}}$ is what the true electron energy would be if the electron had not undergone FSR. That is, the denominator is the true energy of the radiated photon, and the numerator is the reconstructed energy of the radiated photon.

The plots in Figure 7.20 show κ dependence in agreement with the following expectations: At high ΔR, we expect $\kappa = -1$ since the photon falls entirely outside of the electron reconstruction window. At large values of X and intermediate ΔR, that is, when the photon is close enough and of high enough energy that the cluster is reconstructed around it, we expect $\kappa \approx 0$ since the energy remaining to the electron is much less than the photon energy in the denominator. At low ΔR, when the electron and the photon are approximately collinear, we expect negative values of κ, the magnitude of which depends on X: at high X, dead material losses are less significan, since the photon loses energy slower than the electron, and the numerator is close to 0, but at low X, dead material losses are more significant and the numerator is larger. The numerator in this case represents the magnitude of the FSR energy that survives after traveling through the dead material, and hence κ is the fraction of the FSR energy that survives.

If an electron passes the FSR efficiency cut, its energy loss via FSR is simulated by combining the true post-FSR energy of the electron with the true energy of the FSR photon multiplied by κ. This preliminary value of the reconstructed electron energy (called "FSR photon merged") will be modified by additional response parametrizations at a later stage.

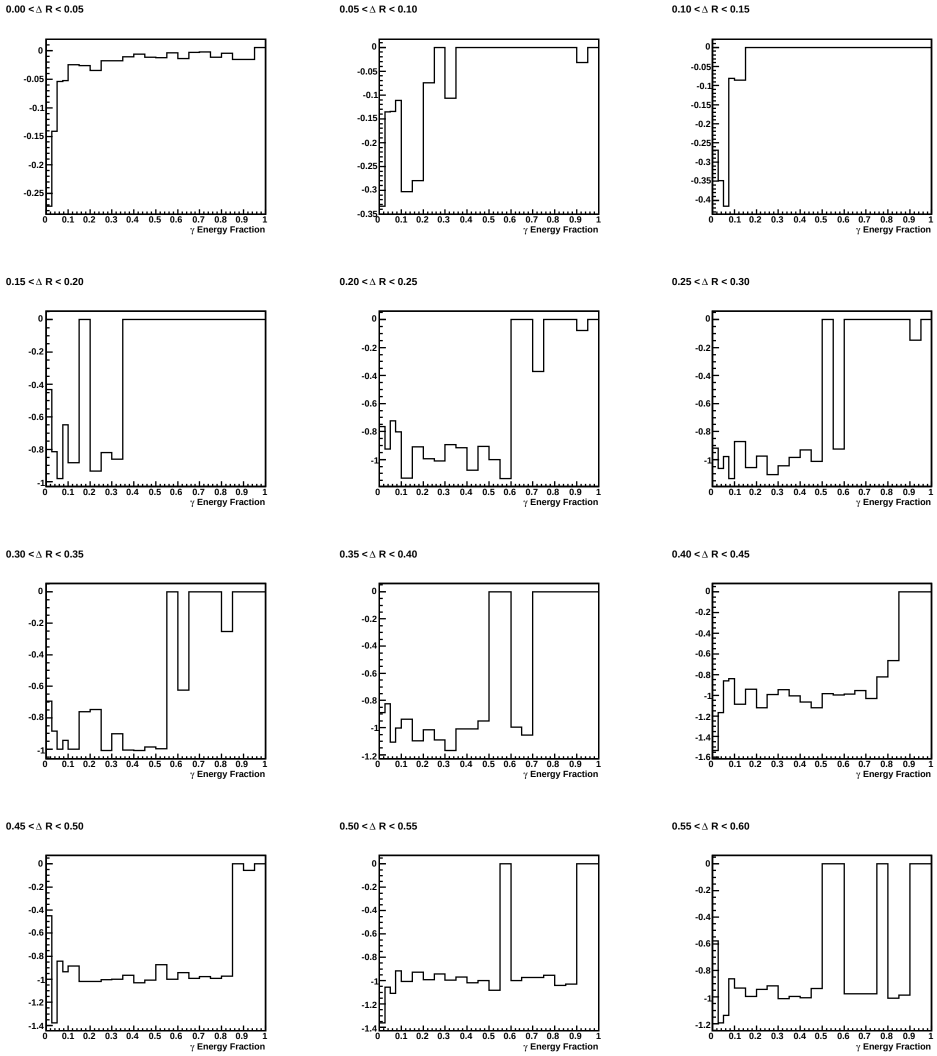
$0.00 < \Delta R < 0.05$

$0.05 < \Delta R < 0.10$

$0.10 < \Delta R < 0.15$

$0.15 < \Delta R < 0.20$

$0.20 < \Delta R < 0.25$

$0.25 < \Delta R < 0.30$

$0.30 < \Delta R < 0.35$

$0.35 < \Delta R < 0.40$

$0.40 < \Delta R < 0.45$

$0.45 < \Delta R < 0.50$

$0.50 < \Delta R < 0.55$

$0.55 < \Delta R < 0.60$

Figure 7.20: Fraction of FSR photon energy κ that is lost by the electron as a function of photon energy fraction X in bins of ΔR. Dependence is discussed in Section 7.3.1. This is only a subset of the FSR response measurements, corresponding to the bin with $0.1 < |\eta| < 0.3$, $3 <$ InstLumi < 3.5, and $37.5 < p_T^e < 45\,\mathrm{GeV}$[20]. NOTE: This figure is from a D0 internal note. At the time of writing, it has not been approved by the D0 collaboration for general public use beyond this dissertation.

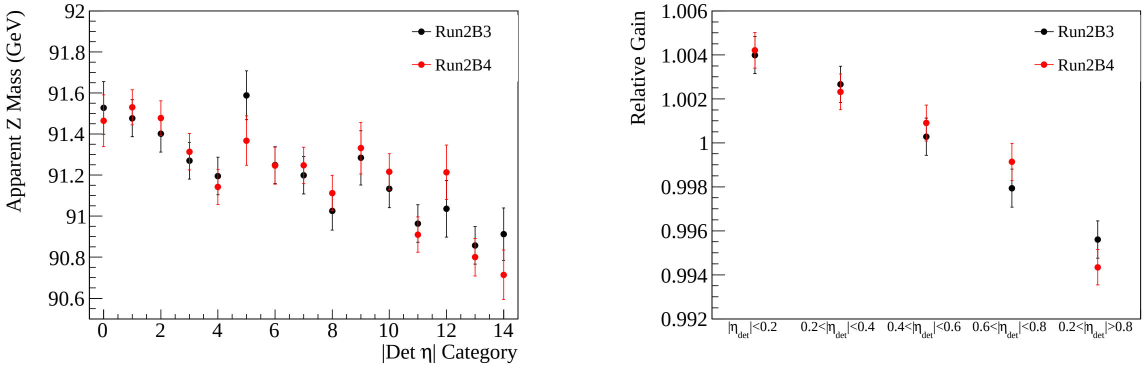

Figure 7.21: Left: Value of the Z boson mass determined from collider data for each $\eta_{\rm det}$ category, before $\eta_{\rm det}$-dependent gain constants have been applied. Right: The $\eta_{\rm det}$-dependent gain constants, derived as described in Section 7.3.2[21]. NOTE: This figure is from a D0 internal note. At the time of writing, it has not been approved by the D0 collaboration for general public use beyond this dissertation.

7.3.2 Dependence of the Calibration on Detector η

The energy responses of the the towers at different $\eta_{\rm det}$ values are not exactly the same. Therefore we calibrate the FastMC to the calorimeter with five gain parameters corresponsing to the five $\eta_{\rm det}$ categories. We optimize the gain parameters by maximizing the agreement between the known value of the Z mass and its value measured from data (using FastMC templates derived with those gain parameters), for all fifteen samples each corresponding to one of the $\eta_{\rm det}$ categories in Table 6.2.

7.3.3 Energy Response and Resolution

After the effect of FSR on the electron energy is simulated, as described in Section 7.3.1, the next step is to simulate the energy response and resolution of the detector. The reconstructed electron energy is calculated via

$$E = R_{EM}(E_0) \otimes \sigma_{EM}(E_0) + \Delta E \tag{7.16}$$

where E_0 is the FSR photon merged true electron energy (Section 7.3.1), E is the reconstructed energy, $R_{EM}(E_0)$ is the calorimeter response (Section 7.3.3.1), σ_{EM} is the electron energy resolution (Section 7.3.3.2), and ΔE is the term correcting for electron reconstruction window effects (Section 7.3.5).

7.3.3.1 Response

The energy response of the EM calorimeter for electrons is modeled as

$$R_{EM}(E_0) = \alpha \cdot \left(E_0 - \bar{E}_0\right) + \beta + \bar{E}_0 \tag{7.17}$$

where α and β are the scale and offset of the calorimeter response to electrons, and $\bar{E}_0 \equiv 43\,\mathrm{GeV}$ is the mean transverse energy of electrons in $Z \rightarrow ee$ events. α and β are determined separately for FullMC and data using the standard samples of FullMC and data $Z \rightarrow ee$ events. The constant $\bar{E}_0$ has no physical interpretation; its purpose is to improve the stability of the fit to determine the model parameters.

If the FSR simulation is perfectly accurate, the electron response parameters will not include any contribution from FSR. However if it is poorly simulated, the missing dependence may be partially absorbed by the scale and/or the offset. Likewise, at this stage, the underlying event, other $p\bar{p}$ interactions, and energy loss in upstream material have already been simulated by the MB/ZB model and the dead material correction. The scale and offset are intended to adjust for small imperfections in earlier components of the model, and we therefore expect $\alpha \approx 1$ and $\beta \approx 0$. These approximations are confirmed by the measurement.

The calorimeter response parameters, α and β are determined by using a log-likelihood method[9] to maximize the agreement between FastMC templates, generated with

---

[9] This is a computationally intensive method requiring a parametrization of each bin's dependence on α and β. See [15] for more information.

a range of values for α and β, and FullMC or data of the two-dimensional distribution of m_Z^{reco} and f_Z^{reco}, two quantities which describe the dependence of the Z mass pole shape on the electron energies. The significance of m_Z^{reco}, is obvious: it is the reconstructed mass of the Z boson, measured by calculating the dilepton center-of-mass from the electron energies and their opening angle:

$$m_Z^{\text{reco}} = m_{ee} = \sqrt{2E^{e_1}E^{e_2}\left(1-\cos\omega\right)} \tag{7.18}$$

The meaning of f_Z is more obscure, so we will first define it and then describe its significance:

$$f_Z = \frac{\left(E_0^{e_1}+E_0^{e_2}\right)\cdot\left(1-\cos\omega\right)}{m_Z} \tag{7.19}$$

The parameter f_Z is sensitive to the opening angle and the energy of the electrons, and is therefore a good variable for describing the kinematics of the decay.[10] The dependence of the m_{ee} peak position on f_Z is sensitive to β. This can be shown by taking the following Taylor expansion of m_{ee}, using the fact that $\alpha - 1 \ll 1$ and $\beta \ll E^{e_i}$:

$$\begin{aligned}
m_{ee} &= \sqrt{2\left(\alpha\cdot\left(E_0^{e_1}-\bar{E}_0\right)+\beta+\bar{E}_0\right)\left(\alpha\cdot\left(E_0^{e_2}-\bar{E}_0\right)+\beta+\bar{E}_0\right)\left(1-\cos\omega\right)} && (7.20)\\
&= \sqrt{2\left(\alpha E_0^{e_1}+\beta+\left(1-\alpha\right)\bar{E}_0\right)\left(\alpha E_0^{e_2}+\beta+\left(1-\alpha\right)\bar{E}_0\right)\left(1-\cos\omega\right)} && (7.21)\\
&\equiv \sqrt{2\left(\alpha E_0^{e_1}+\beta'\right)\left(\alpha E_0^{e_2}+\beta'\right)\left(1-\cos\omega\right)} && (7.22)\\
&= \alpha\cdot\sqrt{2E_0^{e_1}E_0^{e_2}\cdot\left(1-\cos\omega\right)}+\beta'\cdot\frac{\left(E_0^{e_1}+E_0^{e_2}\right)\left(1-\cos\omega\right)}{\sqrt{2E_0^{e_1}E_0^{e_2}\cdot\left(1-\cos\omega\right)}}+\mathcal{O}\left(\beta'^2\right) && (7.23)\\
&= \alpha m_Z+\beta'\cdot\frac{\left(E_0^{e_1}+E_0^{e_2}\right)\left(1-\cos\omega\right)}{m_Z}+\mathcal{O}\left(\beta'^2\right) && (7.24)\\
&= \alpha m_Z+\beta' f_Z+\mathcal{O}\left(\beta'^2\right) && (7.25)
\end{aligned}$$

where $\beta' = \beta + \left(1-\alpha\right)\bar{E}_0$, and m_Z is the truth value of the Z boson mass. Note that this expansion is only to illustrate the relationship between the fit parameters, α and β, and the dependent variables of the distribution used for the fit, m_{ee} and f_Z; Equation 7.18 is the one

---

[10] In principle one could derive the scale and offset from the m_Z distribution only, but this variable is not sensitive enough given the available statistics. One could also use a 3D distribution, substituting e.g. η^{e_1} and η^{e_2} for f_Z, but this would severely decrease the statistics per bin, as well as increase the computational intensity of the fit.

used to calculate the reconstructed Z boson mass variable that is used for tuning. Also note that the Taylor expansion leads to an expression for f_Z that depends on the true electron energies; we tune α and β using f_Z^{reco} which behaves very similarly.

To account for the dependence of the response on luminosity, particularly at high lumonsity due to anomalous currents described in Section 2.3.6.5, α and β are determined in four InstLumi bins, separately for RunIIb3 and RunIIb4. Their best fit values and their covariance can be seen in Figure 7.22.

7.3.3.2 Resolution

The energy resolution of the EM calorimeter for electrons is modeled as

$$\frac{\sigma_{EM}\left(E_0\right)}{E_0} = \sqrt{C_{EM}^2 + \frac{S_{EM}^2}{E_0} + \frac{N_{EM}^2}{E_0^2}} \tag{7.26}$$

where C_{EM}, S_{EM}, and N_{EM} are the constant, sampling, and noise terms for the EM calorimeter.

The sampling term does not have the “textbook” $(\sin\theta)^{-\frac{1}{2}}$ form, due to the significant amount of upstream material in which early parts of the electron showers are lost. After a very intensive study[54], the following functional form was determined, dependent on the electron energy and incident angle:

$$S_{\text{EM}} = \left(S_1 + \frac{S_2}{\sqrt{E_0}}\right) \cdot \frac{e^{S_{\text{exp}}/\sin\theta}}{e^{S_{\text{exp}}}} \tag{7.27}$$

where

$$S_{\text{exp}} = S_3 - S_4/E_0 - \left(S_5/E_0\right)^2 \tag{7.28}$$

In the FullMC simulation, C_{EM} and N_{EM} are both negligible. Therefore the sampling term S_{EM} can be determined independently from the distribution of the ratio of reconstructed to

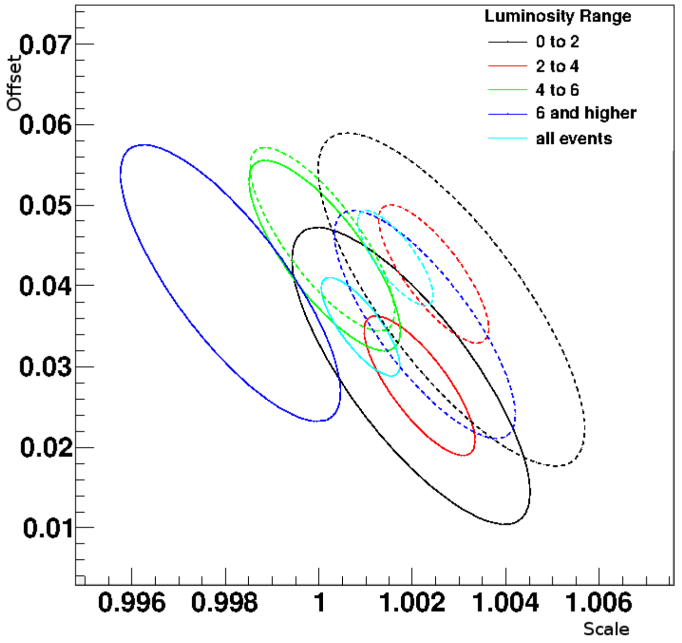

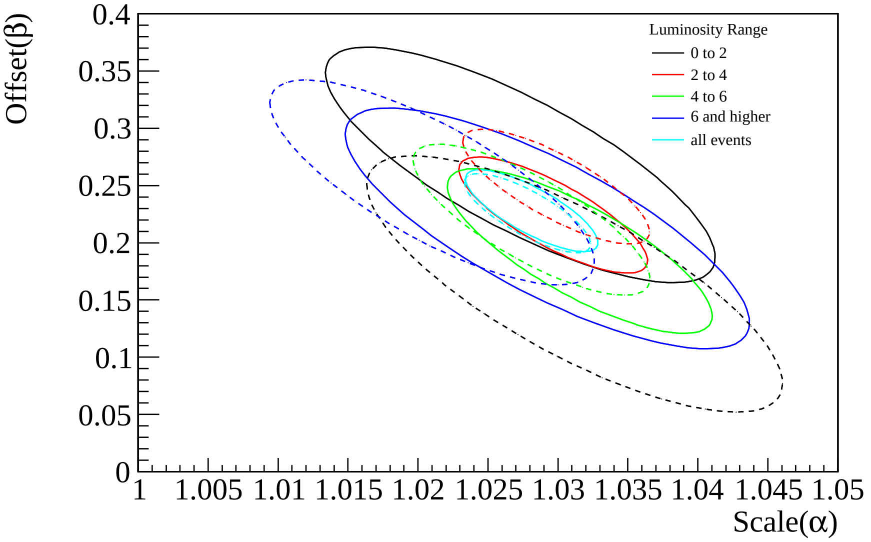

Figure 7.22: One-σ contours for the energy scale α and offset β derived from the template fit to the (M_Z,f_Z) distribution, in FullMC (top) and data (bottom) for RunIIb3 (solid lines) and RunIIb4 (dashed lines)[20][21]. NOTE: This figure is from a D0 internal note. At the time of writing, it has not been approved by the D0 collaboration for general public use beyond this dissertation.

truth energy in a FullMC simulation of single electrons. The parameters S_i are found to be:

$$\begin{aligned} S_1 &= 0.152035 && (7.29) \\ S_2 &= 0.151266 && (7.30) \\ S_3 &= 1.39247 && (7.31) \\ S_4 &= 1.45474 && (7.32) \\ S_5 &= 10.3506 && (7.33) \end{aligned}$$

with negligible errors.

These parameters are used in both the `GEANT` and data FastMC. A small adjustment to the sampling resolution will be made for both data and FullMC, and is described in Section 7.4.5.

Detector noise is relatively small at the Z and W decay energies and most of it is included in the Soft Recoil model described in Section 7.4.2. Any residual effects are negligible and therefore we can also set the noise term $N_{EM} = 0$ in data.

The constant term C_{EM} is extracted by comparing the width of the reconstructed Z mass peak to its true width. As stated above, in FullMC it is found to be negligibly small, $(0.29 \pm 0.08)\,\%$, but in the data it is found to be

$$C_{EM} = (2.00 \pm 0.07)\,\% \tag{7.34}$$

The difference between FullMC and data is due to the fact that the constant term arises mainly from cell-to-cell gain variations which are not simulated in FullMC. However, the term is still kept in the FastMC for the FullMC closure test, in order to absorb any small "missing energy smearing"[42].

7.3.4 Angular Resolution

The electron angular resolution is modeled in FastMC using two "smearing" parameters:

$$\eta_{smear} = \eta_{gen} \otimes \sigma_\eta \tag{7.35}$$

$$\phi_{smear} = \phi_{gen} \otimes \sigma_\phi \tag{7.36}$$

where σ_η and σ_ϕ are the η and ϕ resolutions of the tracking system. σ_η and σ_ϕ are measured in FullMC to be $\sigma_\eta = 2 \times 10^{-3}$ and $\sigma_\phi = 0.4$ mrad.

7.3.5 Electron Window Effects

The electron reconstruction window is a cone of radius 0.2 in (η, ϕ). Of course, the boundary of this cone is not perfectly respected by the electron(s) and hadronic recoil of a $W \to e\nu$ $(Z \to ee)$ decay. Some of the electron energy might fall outside of the edge of the cone, and energy from the underlying event, including the hard recoil, can fall inside the cone's boundaries. Therefore, we need the electron energy bias term, ΔE, to account for energy in the electron cone which comes from sources other than electron and FSR photons, and energy outside the electron cone which comes from the electron. This term includes contributions from the hard recoil, spectator parton interactions, and additional $p\bar{p}$ interactions. Zero-suppression effects are also included implicitly. Note that since ΔE describes energy leakage across the electron window boundary, which affects the energy budget on both sides, it is related to the hadronic recoil energy bias, $\Delta u_\parallel$, which we describe here and discuss in Section 7.4.4.

To model $\Delta u_\parallel$, we examine the energy deposition in "empty windows" of $W \to e\nu$ events. An "empty window" is a region bounded by the shape of an electron reconstruction cone pointed in a random direction which does not overlap with the actual electron reconstruction. We create libraries of these energy deposition values as a function of the SET, InstLumi, $u_\parallel$, η_{phys}, and η_{det} of the event. Then, from the libraries, we create a histogram of the energy deposition for each bin of SET, InstLumi, $u_\parallel$, η_{phys}, and η_{det}. We do this separately for FullMC and data. During the simulation, $\Delta u_\parallel$ is determined by randomly selecting an energy deposition value from the histogram corresponding to the SET, InstLumi, $u_\parallel$, η_{phys}, and η_{det} of the current event. A fraction of the events, the $\Delta u_\parallel$ "zero-fraction", will not have any contribution in the "empty window" and the histograms reflect this.

In addition to its magnitude, we also need to model the effect of $\Delta u_\parallel$ being so large that it prevents our reconstruction procedure from identifying the electron. This efficiency is determined, using the `wmass_CAEPfilter` samples described later in this section, in bins of p_T^e and η_{phys}, as a function of the ratio $\Delta u_\parallel / p_T^e$, and applied using an iterative stochastic method.[11]

To model ΔE, we need a way to convert from the $\Delta u_\parallel$ which is subtracted from the recoil to the ΔE which is added to the electron. The two values are not equivalent, because the electron energy is corrected for dead material energy loss while the hadronic recoil energy is not, and also because zero-suppression affects large concentrated energy deposits such as ΔE differently than it affects diffuse background energy such as $\Delta u_\parallel$.

Three closely related FullMC samples are used. The first is just the "full sample" of complete $W \to e\nu$ events. The other two are created simultaneously using the `wmass_CAEPfilter` package. The "electron only" sample contains only the electron and FSR photons, and the "no electron" sample contains everything else, specifically the hard recoil, spectator parton interactions, and additional $p\bar{p}$ interactions. All three versions are run through the full detector simulation, and are passed through the standard reconstruction procedure, including noise suppression. Then for individual events, the electron energy bias calculated via

$$\Delta E = E_2 - E_1 \tag{7.37}$$

where E_1 is the pure electron signal (including FSR) measured in the "electron only" sample, and E_2 is the energy deposition in the "full sample", both measured in the electron window

---

[11] See slide 7 of [40] more details.

only. The recoil energy bias $\Delta u_{\parallel}$ is likewise measured from the "no electron" sample.

From these measurements, we can relate ΔE and $\Delta u_{\parallel}$ to each other. For non-zero $\Delta u_{\parallel}$, ΔE is determined via the parametrized function

$$\Delta E = p_0 + p_1 \cdot \frac{\Delta u_{\parallel}}{\sin(\theta)} \tag{7.38}$$

where p_0 and p_1 are determined from fits to the ΔE vs. $\Delta u_{\parallel}$ distribuion, measured individually in bins of η_{phys}, p_T^e, $u_{\parallel}$, InstLumi, and SET. We validate our model by comparing the ΔE dependence on InstLumi, SET, electron energy, η_{det}, and η_{phys} in the Fast and the FullMC.

7.4 Hadronic Recoil Parametrization

Accurate modeling of the Hadronic Recoil is crucial to determining the $\not\!\!E_T$ and m_T distributions. The true momentum of the hadronic recoil from the production of a W or Z boson is expected to be exactly opposite that of the boson produced. However, the measured quantities do not exactly balance each other, due to the low response and large fluctuations of the calorimeter. In addition to the "hard" component of the recoil (defined as the true recoil) there are overlaid "soft" components which are included in the measurement of the hadronic energy.

The hadronic recoil is an umbrella term covering everything other than the decay products of the vector boson: the hard recoil of the spectator partons left over from the proton-antiproton collision that produced the vector boson, the collisions of other proton-antiproton collisions. It is modeled as having four components, which will be discussed in subsequent sections: Hard recoil (Section 7.4.1), soft recoil (Section 7.4.2), and electron window effects, the last of which is split up into non-FSR related leakage of electron or recoil energy across the electron window boundary (Section 7.4.3), and leakage out of the electron window due to FSR (Section 7.4.4).

$$\vec{u}_T = \vec{u}_T^{\,\text{Hard}} + \vec{u}_T^{\,\text{Soft}} + \vec{u}_T^{\,\text{Elec}} + \vec{u}_T^{\,\text{FSR}} \tag{7.39}$$

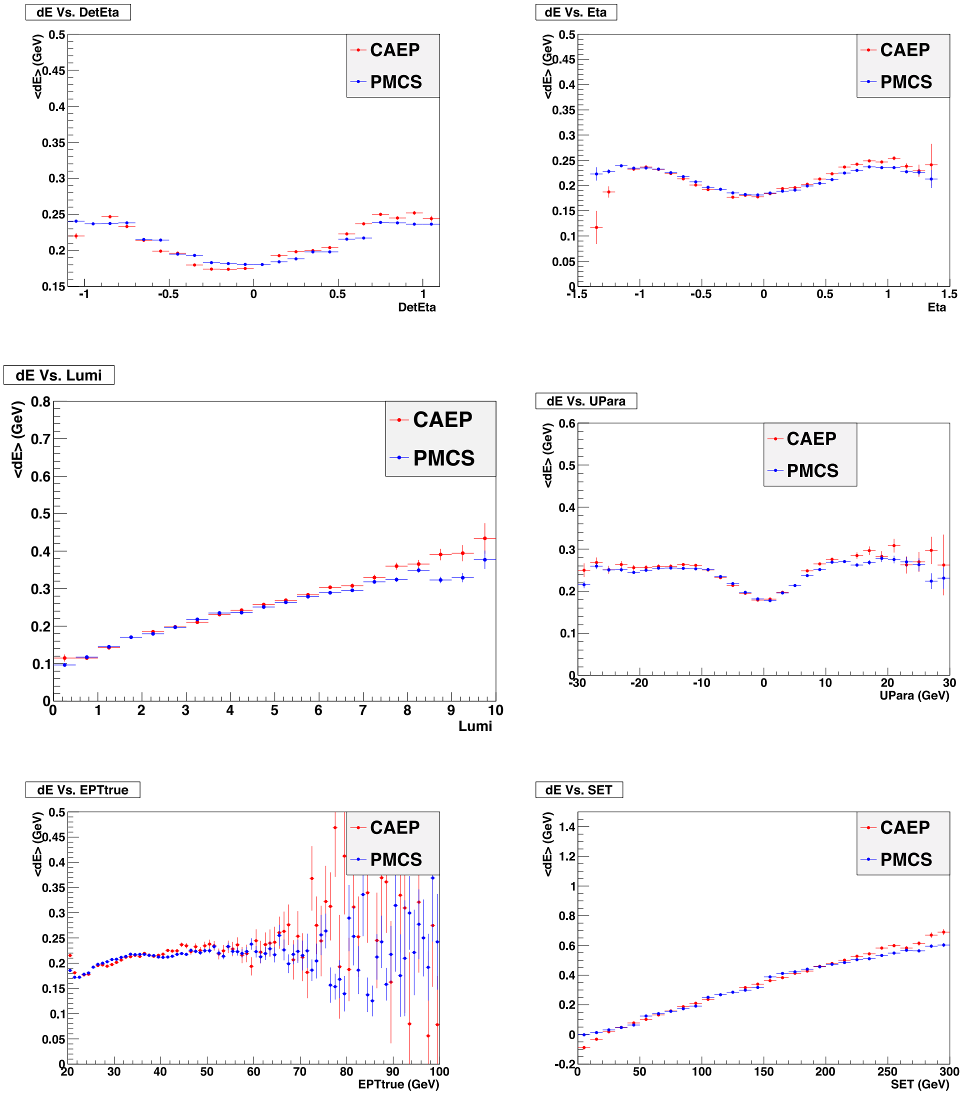

Figure 7.23: Comparing mean ΔE between FullMC (`wmass_CAEPfilter` samples) and FastMC toy model for RunIIb4, as a function of electron η_{det} (top left), electron η_{phys} (top right), InstLumi (middle left), $U_{\parallel}$ (middle right), true electron energy (bottom left), and SET (bottom right)[20]. NOTE: This figure is from a D0 internal note. At the time of writing, it has not been approved by the D0 collaboration for general public use beyond this dissertation.

7.4.1 Hard recoil model

The hard recoil is the part of the hadronic response that balances the boson momentum, modified ("smeared") by the detector response and resolution:

$$\vec{u}_T^{\text{Hard}} = \vec{q}_T^{\text{smeared}}\left(\vec{q}_T\right) \tag{7.40}$$

where $\vec{q}_T = -\vec{p}_T^{\,Z}$ is the true recoil vector and $\vec{u}_T$ is smeared recoil vector. It is parametrized as a function of the true hadronic recoil from the vector boson, $\vec{q}_T = -\vec{p}_T(W/Z)$, the luminosity, and SET. The parametrization function $f\left(\vec{q}_T\right)$ is derived from a sample of FullMC $Z \rightarrow \nu\nu$ events with Minimum Bias turned off, and with a Zero Bias overlay. Since the neutrinos deposit no energy in the detector, all energy other than ZB energy is due to the recoil of the Z boson. The Zero Bias overlay is necessary because of the significant effect of pileup modifying the measured fractional energy response to hadronic recoil, shown in Figure 7.24. Specifically, a cell with pure hard recoil energy and ZB energy contributions that are each below the zero suppression level may surpass the zero suppression level when the two contributions are combined, an important effect which would be lost if the hard recoil energy were simulated alone. We require the $Z \rightarrow \nu\nu$ events to satisfy $|\eta_\nu| < 1.3$ to match the kinematics of $Z \rightarrow ee$ events.

To obtain the parametrized model for the detector response to the hard recoil, we use a technique called "ZB/MB cell-by-cell subtracted reconstruction".[12] A sample is generated in FullMC, where each event corresponds to an event in the FullMC $Z \rightarrow \nu\nu$ sample, but only has the ZB of that event, and not the boson decay. For each event, the simulated cell-energies for the ZB-only event are subtracted from the simulated cell-energies for the Z boson decay. The difference is then the effective contribution to calorimeter energy measurement from the Z boson decay. Histograms created from the ZB subtracted event sample are then used to model the detector's response and resolution to the hadronic recoil energy, as well as the hard recoil contribution to the SET.

---

[12] It is somewhat confusingly referred to as the "single neutrino subtraction" in many references, because the easiest way to generate a ZB sample is to simulate single neutrino events. (The neutrino has no significance or effect on the sample.)

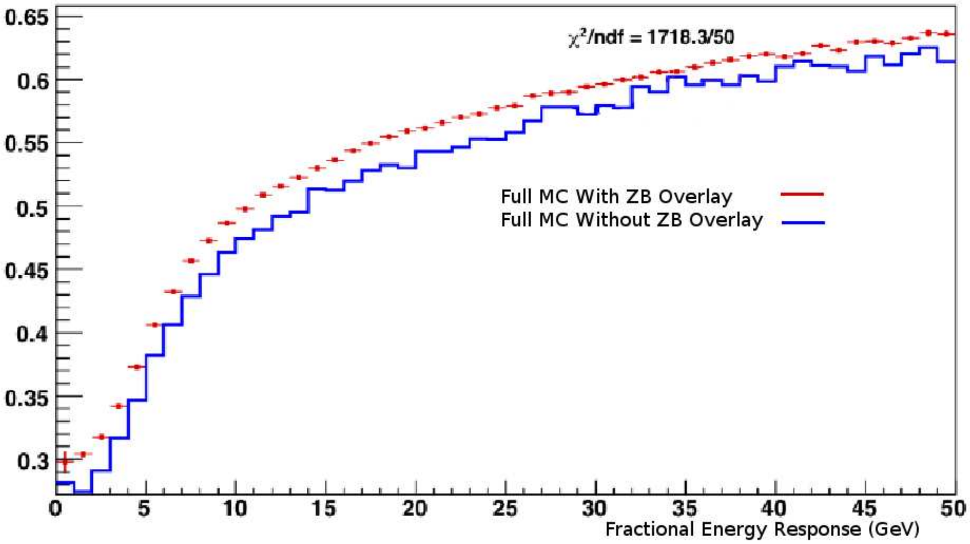

Figure 7.24: Fractional energy response of hadronic recoil in FullMC $Z \to \nu\nu$ events, measured relative to transverse momentum of Z vector boson. With (red, dotted) and without (blue, solid) ZB overlay[20]. NOTE: This figure is from a D0 internal note. At the time of writing, it has not been approved by the D0 collaboration for general public use beyond this dissertation.

Our procedure for modeling the detector response models the response resolution with three sets of probability density functions (PDFs) which describe the correlation between the true recoil, ZB SET, $\Delta\phi$, and u_T/q_T. A single histogram is generated for each p_T^Z-InstLumi bin. Two examples can seen in Figure 7.25. To simulate the response for a given event, we select the histogram with the appropriate p_T^Z and InstLumi, and take the horizontal cross section of the histogram at the appropriate ZB SET. This cross section serves as a PDF from which the u_T/q_T is randomly selected.

Once the response has been determined, the recoil angular (ϕ) resolution is modeled in a similar way, using 2D histograms of $\Delta\phi/\pi$ vs. u_T/q_T, each corresponding to a bin of p_T^Z and ϕ. Two examples can be seen in Figure 7.26. Now a vertical cross section of the histogram, at the value of u_T/q_T which was just selected, is used as the PDF from which a

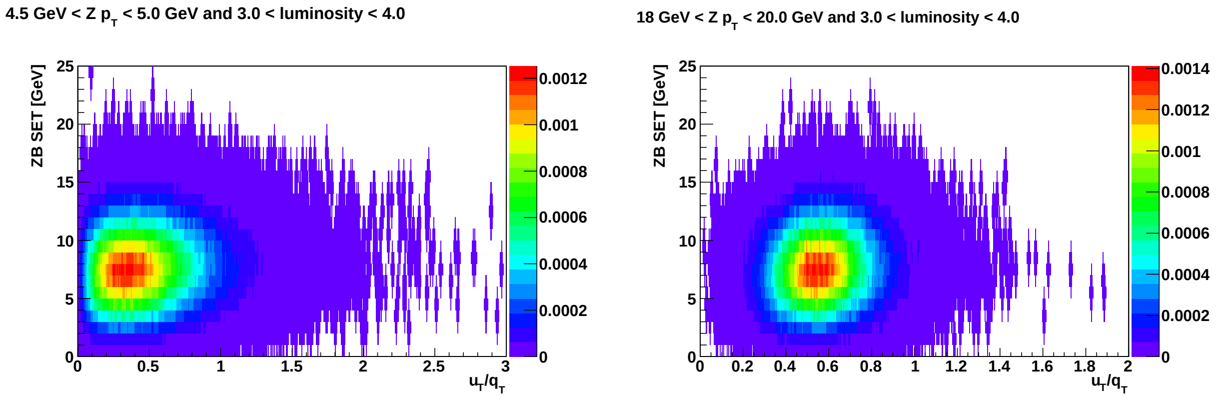

Figure 7.25: Examples of histograms which describe the correlation between ZB SET and u_T/q_T, and which are used to select random values of u_T/q_T for events[20]. NOTE: This figure is from a D0 internal note. At the time of writing, it has not been approved by the D0 collaboration for general public use beyond this dissertation.

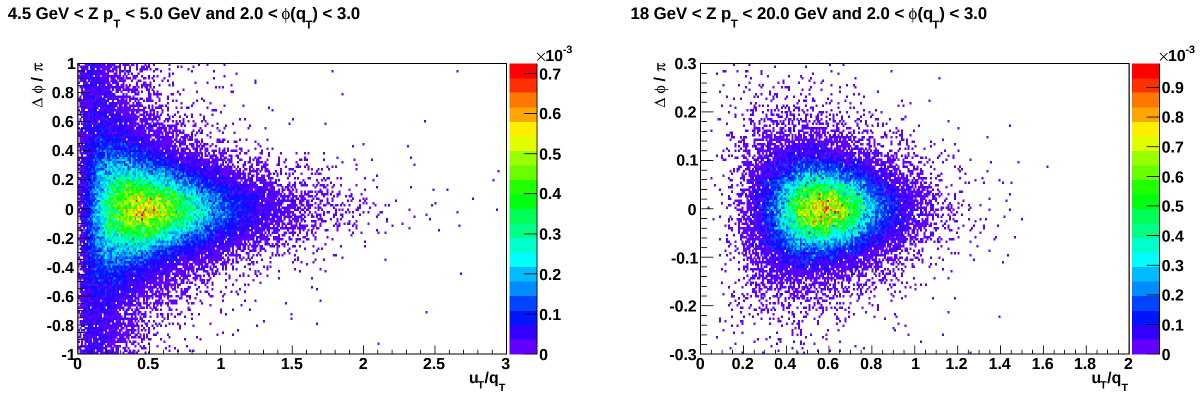

Figure 7.26: Examples of histograms which describe the correlation between $\Delta\phi/\pi$ and u_T/q_T, and which are used to select random values of $\Delta\phi$ for events[20]. NOTE: This figure is from a D0 internal note. At the time of writing, it has not been approved by the D0 collaboration for general public use beyond this dissertation.

value of $\Delta\phi$ is randomly selected.

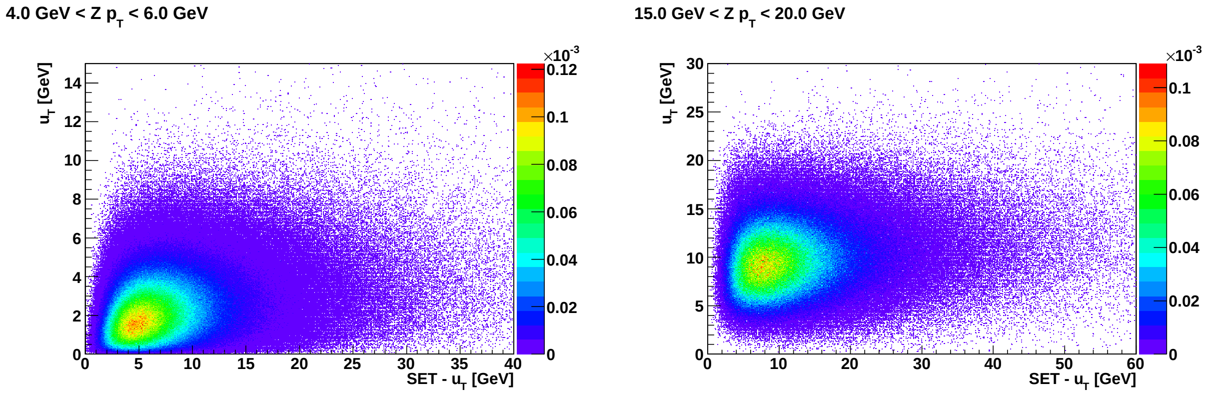

Figure 7.27: Examples of histograms which describe the correlation between u_T and SET$-u_T$, and which are used to select random values of SET $- u_T$ for events[20]. NOTE: This figure is from a D0 internal note. At the time of writing, it has not been approved by the D0 collaboration for general public use beyond this dissertation.

Finally, the contribution to the SET due to the (vector) hard recoil must be simulated. Again, we use 2D histograms, now describing the correlation between u_T and SET$-u_T$, in bins of p_T^Z. Two examples can be seen in Figure 7.27. A horizontal slice at the appropriate u_T gives the PDF from which the value of SET $- u_T$ is randomly selected.

So far, this model is determined using FullMC generated samples. After some fine tuning, described in Section 7.4.5, it can be applied to FullMC or collider data[14].

7.4.2 Soft recoil model

The soft recoil model describes the energy contribution from the spectator partons, also called the “underlying event”, or Minimum Bias (MB), and additional energy in the detector from other proton-antiproton interactions from the current or previous events, which is also called “pileup” and is the main contributor to the Zero Bias (ZB). It also includes a contribution from detector noise. It cannot be modeled from first principles; therefore we build MB and ZB event libraries from which we can look up the soft recoil contribution to our simulated events. For FullMC, underlying event energy is modeled using a library of MB events generated in FullMC with ZB overlay, with the ZB subtracted using the "ZB/MB cell-by-cell subtracted reconstruction" procedure described in Section 7.4.1. For data, we use collider MB events which are triggered by an inelastic reaction, and which have at most one PV. For both data and FullMC, the energy contribution from other $p\bar{p}$ interactions is modeled using a lookup table for the $\vec{E}_T$ (i.e. the vector sum of transverse momenta) from ZB events recorded in non zero-suppressed mode, selected from collider data with the ZB trigger requirement. The library (indexed by run number) of these events is used both in the Full and FastMC, so that the luminosity profiles of the Full and FastMC are identical, and very similar to the luminosity profile of the collider data (but not exactly the same, since different ZB events are not used to measure the W mass).

For both data and FullMC, the MB events also need to be reweighted so that the SET spectrum (sum of hard, ZB, and MB components) in the FastMC simulation matches the SET spectrum of the FullMC generated $Z \to \nu\nu$ events. The reweighting is performed by adding the MB events to the library based on the MB SET to some (non-zero) power. A fraction of events, the MB "zero-fraction", in the library will also have no contribution from MB, due to there being no inelastic collisions in the event. The values of the power and the MB zero-fraction are varied until maximal agreement (via the χ^2 method) between the Fast and FullMC is achieved. The χ^2 dependence on these two parameters for RunIIb3 and RunIIb4 can be seen in Figure 7.28.

Some effects, such as detector noise and soft interactions without a primary vertex, will be included in both the ZB and the MB model. To remove the effect of this double-counting, we "de-weight" the MB contribution with the ad-hoc multipurpose correction factor α_{MB}. It is "multipurpose" because it is also used to remove the double-counting of detector noise and soft interactions without a primary vertex, and to fine-tune the soft recoil resolution. α_{MB} is determined simultaneously with some other fine-tuning parameters, using width of the η imbalance of $Z \to ee$ events, as described in Section 7.4.5.

After rescaling of the MB library and determination of α_{MB}, the soft recoil momen-

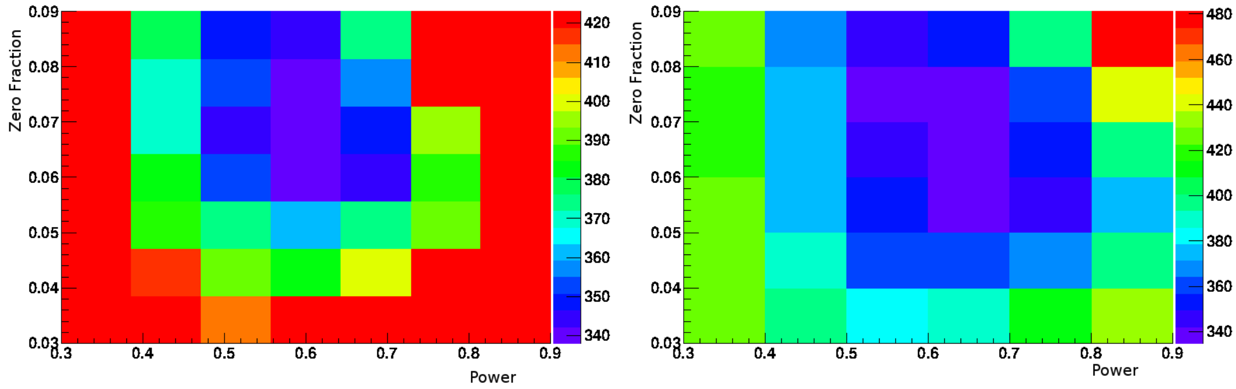

Figure 7.28: RunIIb3 (left) and RunIIb4 (right) χ^2 distributions used to find the best values of the zero-fraction and the MB SET power. These values are used when building the MB library[20]. NOTE: This figure is from a D0 internal note. At the time of writing, it has not been approved by the D0 collaboration for general public use beyond this dissertation.

tum contribution to an event is simulated in the FastMC with the following parametrization,

$$\vec{u}_T^{\text{Soft}} = -\sqrt{\alpha_{\text{MB}}} \cdot \vec{\not{E}}_T^{\text{MB}} - \vec{\not{E}}_T^{\text{ZB}} \tag{7.41}$$

7.4.3 Electron Window Effects (non-FSR leakage)

The contribution to the hadronic recoil energy measurement from electron window effects is modeled as

$$\vec{u}_T^{\text{ELEC}} = \sum_e \left[-\Delta u_{\parallel} \cdot \hat{p}_T\left(e\right) + \vec{p}_T^{\text{LEAK}}\right] \tag{7.42}$$

where the first term in the sum is the hadronic energy that falls in the electron reconstruction window and is therefore not counted in the recoil measurement, and the second term is the electron energy that falls outside the electron reconstruction window and is therefore included in the recoil measurement. The determination of $\Delta u_{\parallel}$ was discussed in Section 7.3.5, and $\hat{p}_T(e)$ is the direction of the smeared electron[32].

The second term is the electron energy that leaks outside the electron reconstruction window, and is therefore included in $\vec{u}_T$ even though it is not part of the recoil. The electron energy leakage is parametrized as a function of p_T^e and η_{det}, and determined from a single electron FullMC simulation. The cases with and without in-cone FSR photons are treated separately, since in-cone FSR almost doubles the leakage rate. Out-of-cone FSR contributions to $\vec{u}_T$ are discussed in the next section.

7.4.4 Electron Window Effects (FSR leakage)

The FSR contribution to the reconstructed transverse recoil,

$$\vec{u}_T^{\mathrm{FSR}} = \sum_{\gamma} \vec{p}_T(\gamma) \tag{7.43}$$

is FSR energy that falls outside the electron window and is therefore not included in electron energy measurement, but is included in the recoil measurement. This contribution to the recoil energy has been studied with a FullMC simulation of single photon events with a ZB overlay, with the “ZB/MB cell-by-cell subtracted reconstruction” procedure described in Section 7.4.1 applied. The FSR “leakage” out of the electron window and into the hadronic recoil region is interpolated from a 4D “histogram”[13] in the photon pseudorapidity $\eta_{\mathrm{phys}}(\gamma)$, photon true energy in the transverse plane $p_T(\gamma)$, the fraction of the electron’s energy carried by the photon X, and the event SET. The probability that the FSR photon will be lost entirely is interpolated from a 2D “histogram” in $p_T(\gamma)$ and $\eta_{\mathrm{phys}}(\gamma)$.

7.4.5 Fine-tuning the Recoil Model

The hard recoil model described so far is based on simulations of the recoil from simulated neutrino events. However, for our FullMC and collider data, the response and resolution are slightly different due to the underlying event and additional energy typical of a vector boson production and decay. To account for the differences in the recoil from a massive vector boson, we fine-tune the model with the following correction.

---

[13] Not a histogram in the statistical sense, but an array of values stored in the same software structure we use for histograms.

The component of the hadronic recoil in the direction of the vector boson momentum,

$$u_{\parallel}^{\nu\nu} = u_T^{\nu\nu} \cos\left(\Delta\phi\right) \tag{7.44}$$

is modified via

$$\frac{u_{\parallel}^{\mathrm{HARD}}}{q_T} = \left(r_0 + r_1 e^{-q_T/\tau_{\mathrm{HAD}}}\right) \left\langle \frac{u_{\parallel}^{\mathrm{HARD}}}{q_T} \right\rangle + \sigma_0 \left(\frac{u_{\parallel}^{\nu\nu}}{q_T} - \left\langle \frac{u_{\parallel}^{\mathrm{HARD}}}{q_T} \right\rangle \right) \tag{7.45}$$

while the perpendicular component of the hadronic recoil,

$$u_{\parallel}^{\mathrm{HARD}} = u_T^{\nu\nu} \sin\left(\Delta\phi\right) \tag{7.46}$$

is not modified.

In the first term of the correction to the parallel part of the recoil, r_0 is the "relative scale" and r_1 is the "relative offset" which is important at low values of the recoil momentum relative to the exponential term τ_{HAD}. The form of this part of the correction was determined by comparing a FullMC pure recoil ($Z \rightarrow \nu\nu$ without ZB overlay) sample with a FullMC $Z \rightarrow ee$ sample. In the second term, σ_0 is a relative sampling term used to adjust the hadronic energy resolution. The mean values, $\left\langle \frac{u_{\parallel}^{\mathrm{HARD}}}{q_T} \right\rangle$, are determined from the histograms shown in Figure 7.26.

The parameters of this ad-hoc model are tuned using the mean and width of two diagnostic variables, described first in Section 3.6. The first, the η imbalance,

$$\eta_{\mathrm{imb}} = \left[\vec{u}_T + \vec{p}_T\left(ee\right)\right] \cdot \hat{\eta} \tag{7.47}$$

is the discrepancy (or "imbalance") between the directly measured recoil of the Z boson and its transverse momentum as measured from the two electrons, projected onto the inner bisector of the angle between the two electrons, $\hat{\eta}$. The second is the perpendicular component of the imbalance,

$$\xi_{\mathrm{imb}} = \left[\vec{u}_T + \vec{p}_T\left(ee\right)\right] \cdot \hat{\xi} \tag{7.48}$$

The hard and soft recoil contributions are modeled independently, however they have correlations, mainly due to noise suppression, that must be correctly modeled in the

FastMC simulation. The multi-purpose parameter, α_{mb}, introduced in Section 7.4.2, also provides a "de-weighting" effect to remove double-counting of effects present in both the hard recoil and the MB.

We simultaneously tune all five parameters (r_0, r_1, τ_{HAD}, σ_0, and α_{MB}) by creating high statistics templates of the η_{imb} distribution from FastMC samples generated with a range of values of for all the parameters. We create two χ^2 statistics, one for the mean of the η imbalance in ten equally weighted smeared $p_T\,(ee)$ bins, and one for the RMS width of the η imbalance in the same ten bins. We fine-tune the response parameters (r_0, r_1, τ_{HAD}) by minimizing the χ^2 for the mean of the η imbalance and fine-tune the resolution parameters (σ_0, and α_{MB}) by minimizing the χ-square for the width of the η imbalance. This tuning is done separately for FullMC and data. The comparisons between the FullMC and `GEANT` FastMC are shown in Figure 7.29. As usual, we place a 30 GeV upper limit on recoil magnitude during tuning.

The best fit values for the RunIIb3 `GEANT` tuning of the FastMC are found to be $\sigma_0 = 1.00497 \pm 0.01531$, $\alpha_{\mathrm{MB}} = 1.15512 \pm 0.02085$, $r_0 = 1.01104 \pm 0.002575$, $r_1 = 0.40043 \pm 0.05896$, and $\tau_{\mathrm{HAD}} = 3.47072 \pm 0.31335$.

The best fit values for RunIIb4 `GEANT` tuning of the FastMC are found to be $\sigma_0 = 1.00087 \pm 0.01359$, and $\alpha_{\mathrm{MB}} = 1.26481 \pm 0.01786$, $r_0 = 1.01239 \pm 0.002464$, $r_1 = 0.329769 \pm 0.09765$, and $\tau_{\mathrm{HAD}} = 3.41273 \pm 0.32878$.

The complete correlation matrix, used for systematic error estimation, for the RunIIb3 `GEANT` tuning of the FastMC is:

	σ_0	α_{MB}	r_0	r_1	τ_{HAD}
σ_0	1	−0.6084	0.3086	−0.005799	−0.1888
α_{MB}	−0.6084	1	−0.0952	−0.1444	0.09492
r_0	0.3086	−0.0952	1	−0.05547	−0.4877
r_1	−0.005799	−0.1444	−0.05547	1	−0.4851
τ_{HAD}	−0.1888	0.09492	−0.4877	−0.4851	1

The complete correlation matrix, used for systematic error estimation, for the

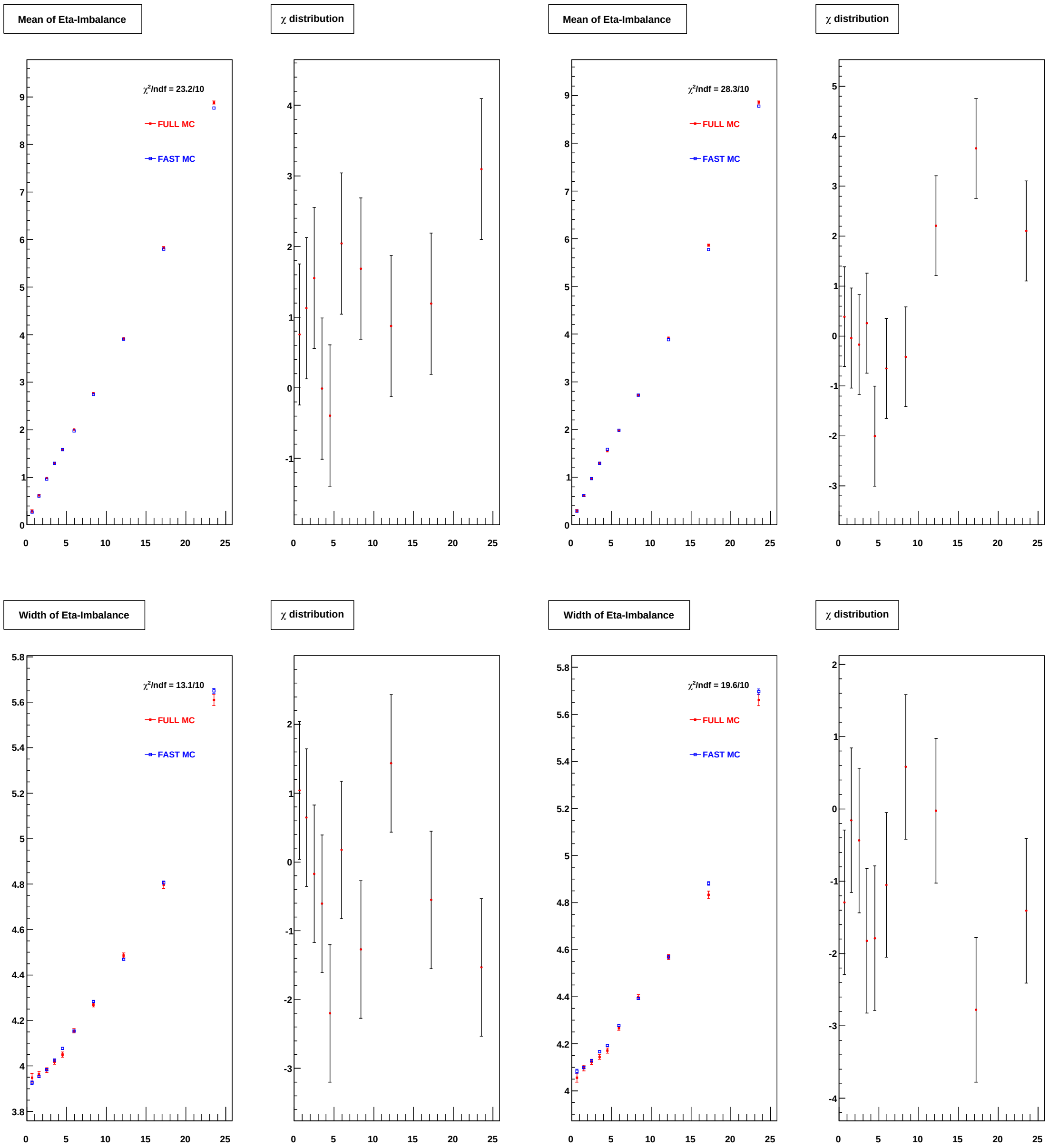

Figure 7.29: RunIIb3 (left two plots) and RunIIb4 (right two plots) FullMC vs. FastMC comparison (first and third) and difference (second and fourth) of the mean (top) and width (bottom) of the η imbalance for the ten $p_T\,(ee)$ bins used for fitting[20]. NOTE: This figure is from a D0 internal note. At the time of writing, it has not been approved by the D0 collaboration for general public use beyond this dissertation.

RunIIb4 `GEANT` tuning of the FastMC is:

	σ_0	α_{MB}	r_0	r_1	τ_{HAD}
σ_0	1	-0.533	0.3172	0.105	-0.2118
α_{MB}	-0.533	1	-0.07399	-0.4181	0.3105
r_0	0.3172	-0.07399	1	0.09593	-0.4152
r_1	0.105	-0.4181	0.09593	1	-0.7885
τ_{HAD}	-0.2118	0.3105	-0.4152	-0.7885	1

The best fit values for RunIIb34 data (parameters were derived for combined runs to take advantage of combined statistics) tuning of the FastMC are estimated in preliminary studies to be $\sigma_0 = 1.10558$, and $\alpha_{\mathrm{MB}} = 0.646$, $r_0 = 0.984521$, $r_1 = 0.647967$, and $\tau_{\mathrm{HAD}} = 5.10032$.

7.5 Bias in W Mass from Tuning with Z Events

As can be seen in Figure 7.30, the electrons produced in W boson decays and the electrons produced in Z boson decays occupy different bands in η vs. electron energy space. Therefore, if flaws in the energy loss correction lead to a mismeasurement of the energy scale (which is tuned with FullMC and data Z boson events), a bias in the W mass will result. We quantify the size of this bias with the following calculation.

First, we compare the fractional discrepancy between truth and reconstructed electron energy for simulated $W \to e\nu$ and $Z \to ee$ events, and take the difference, shown in the lower plot of Figure 7.31. The FastMC is tuned to model this translation from truth to reconstructed energy for Z events, therefore any differences between the two distributions illustrate the inability of the Z-tuned FastMC parametrization to correctly model W events. The upper plot in Figure 7.31 is the true electron energy distribution of $W \to e\nu$ events. The convolution of the lower plot with the upper plot applies the disrepancy in the lower plot to the upper plot, modifying the true electron energy distribution to what it would look like if it were only modified by the “energy scale mistake”. The W mass derived from the

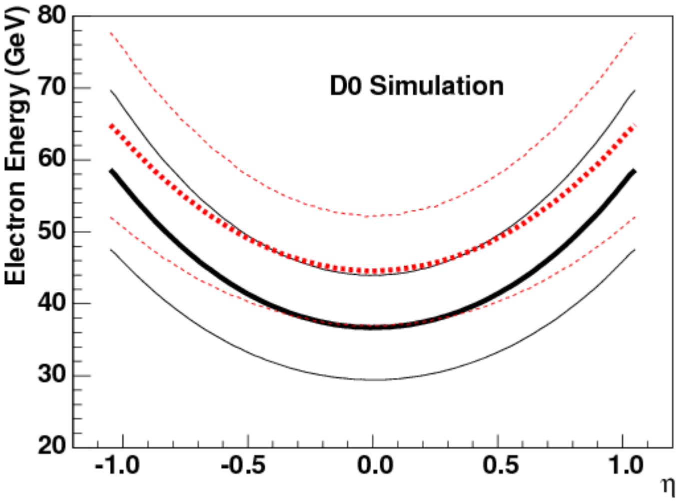

Figure 7.30: Mean and one-σ boundary of electron energy vs. η distribution for lower energy $W \rightarrow e\nu$ (black, solid) and higher energy $Z \rightarrow$ (red, dashed) events. Because of the different distributions for the W and Z electrons, we must determine the systematic uncertainty from measuring the W mass from templates tuned with Z events. [7]

convolved energy distribution is compared with the W mass derived from the unmodified energy distribution, and the difference is a measure of the bias in the W mass resulting from using Z events in the tuning process. This bias, of order 5 MeV, is included in the systematic uncertainty due to the electron energy loss model.

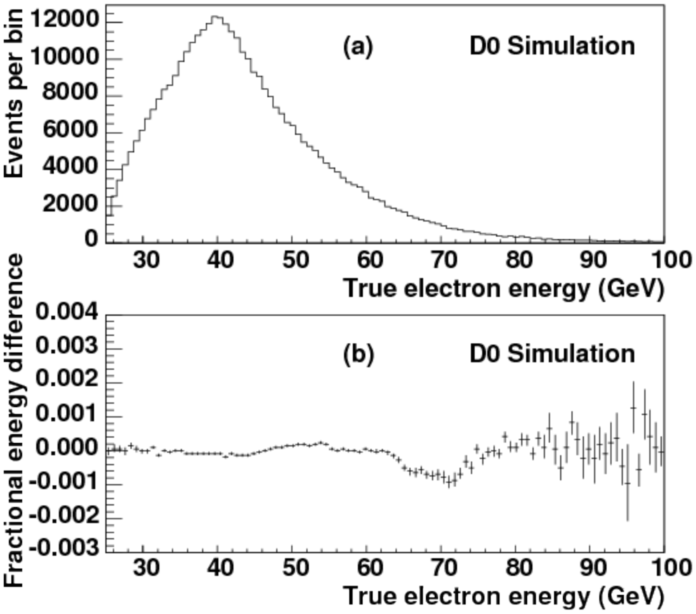

Figure 7.31: True energy distribution of $W \to e\nu$ electrons (top). Difference between the fractional discrepancies between truth and reconstructed electron energy for simulated $W \to e\nu$ and $Z \to ee$ events (bottom). The difference between the relationship of the reconstructed to the truth electron energy of W vs. Z events is a measure of the bias in the W mass resulting from the use of Z events to tune the measurement templates. [7]

Chapter 8

BACKGROUNDS

There are three non-negligible sources of background in the $W \rightarrow e\nu$ event sample: QCD multi-jet (mostly di-jet), "heavy lepton" W decays ($W \rightarrow \tau\nu \rightarrow e\nu\nu\nu$), and di-lepton Z boson decays (almost entirely $Z \rightarrow ee$). These types of events pass the selection cuts at a rate high enough to affect the shape of the distributions used to measure the W mass, and we must therefore account for these events by predicting and subtracting their contribution to the m_T, p_T^e, and $\not{E}_T$ histograms. The QCD and Zee background are determined from collider data, while the decay of background τ leptons must be simulated in FullMC.

8.1 $Z \rightarrow ee$ Background

$Z \rightarrow ee$ decays mimic $W \rightarrow e\nu$ decays when one electron is misidentified - usually because it landed in ICD region - and the mismeasurement results in substantial MET (because the ICD region is excluded from MET measurement).

To estimate the background contribution by $Z \rightarrow ee$ events we use the "ABCD" method: assuming the probability that an electron will have a reconstructed track is independent of the probability that an electron will have a reconstructed jet, we can use the expected relationship between the number of electrons with both a track and a jet, the number of electrons with a track but no jet, the number of electrons with a jet but no track, and the number of electrons with neither a track nor a jet to predict 1) the independent probabilities and 2) the number of electrons with neither a track nor a jet.

We extract $Z \rightarrow ee$ candidates directly from the $W \rightarrow e\nu$ data sample by selecting events that have one good electron and a second object which is a jet. This does not select all of the $Z \rightarrow ee$ events that look like $W \rightarrow e\nu$ because some $W \rightarrow e\nu$ candidates that are truly $Z \rightarrow ee$ events will not satisfy these criteria: we must correct for the Z acceptance and the efficiency to detect an electron as an EM object, a jet, or a track. In addition, QCD events can mimic $Z \rightarrow ee$ events (which mimic $W \rightarrow e\nu$ events), and these events must be subtracted. Therefore, the contribution to background by $Z \rightarrow ee$ events can be written as

$$N(Z \rightarrow ee) = \frac{N^{Z\rightarrow ee}(e, \text{jet}) - N^{QCD}(e, \text{jet})}{\epsilon_{\text{jet}} \times A(e, \text{jet})} \tag{8.1}$$

where $N^{Z\rightarrow ee}(e, \text{jet})$ is the number of $Z \rightarrow ee$ events that look like (e,jet) pairs, $N^{QCD}(e, \text{jet})$ is the number of QCD events that look like (e,jet) pairs (and also like $Z \rightarrow ee$ events), ϵ is jet-finding efficiency with respect to a track-based sample (i.e. probability of finding a jet where there is a track), and $A(e, \text{jet})$ is acceptance of the invariant mass window cut (see below) for the (e,jet) pairs.

We use the jet-finding efficiency with respect to tracks (as opposed to the track-finding efficiency with respect to jets), because there are more tracks reconstructed than there are jets, and therefore more tracks without jets than jets without tracks. This in turn gives better statistics for the "failing" contribution, to which the efficiency is most sensitive, in the denominator of the efficiency calculation (Equation 8.6).

Most often, the second object is in the ICD region, corresponding to a large contribution to the missing energy (because this region is not included in the definition of MET (Section 5.3.1). In this region, EM objects are always track based and their efficiency with respect to tracks is 100%. Therefore, we must use jets as our second object.

By design of the selection requirements, the fraction of QCD events in the (e,jet) sample is negligible, so $N^{QCD}(e, \text{jet})$ can be omitted, i.e.

$$N(e, \text{jet}) - N^{QCD}(e, \text{jet}) = N^{Z\rightarrow ee}(e, \text{jet}) \approx N(e, \text{jet}) \tag{8.2}$$

so that we have

$$N(Z \rightarrow ee) = \frac{N(e, \text{jet})}{\epsilon_{\text{jet}} \times A(e, \text{jet})} \tag{8.3}$$

Because we have to apply mass cuts to strongly exclude non-Z events, the jet-finding efficiency that we can measure is not exactly ϵ_{jet}, which is the efficiency to find a jet *at any invariant mass of the* (e, jet) *pair* given a track *at any invariant mass of the* $(e, track)$ *pair.* What we measure instead is the efficiency ϵ'_{jet} to find a jet *in the jet mass window*[1] given that we have found a matching track *in the track mass window*:

$$\epsilon'_{\text{jet}} = \epsilon_{\text{jet}} \times A(e, \text{jet})/A(e, \text{trk}) \tag{8.4}$$

Therefore, we write

$$N(Z \to ee) = \frac{N(e, \text{jet})}{\epsilon'_{\text{jet}} \times A_(e, \text{trk})} \tag{8.5}$$

where $A(e, \text{track})$ is acceptance of the invariant mass window cut (see below) for the (e,track) pairs. We measure ϵ'_{jet} by taking the ratio of the sizes of the two populations shown in Figure 8.1:

$$\epsilon'_{\text{jet}} = \frac{N^{Z\to ee}(e, \text{jet} + \text{track})}{N^{Z\to ee}(e, \text{track})} \tag{8.6}$$

where $N^{Z\to ee}(e, \text{jet} + \text{track})$ is the number of $Z \to ee$ events that pass both the jet-based and track-based selection, and $N^{Z\to ee}(e, \text{track})$ is the number of $Z \to ee$ events that pass the track based selection.

The selection requirements for (e,track) $Z \to ee$ events in the $W \to e\nu$ sample are:

- $\Delta\phi(e, \text{track}) > 2.5$
- $p_T^{\text{track}} > 25\,\text{GeV}$
- $1.0 < |\eta_{\text{det}}\,(\text{track})| < 1.5$
- $\left|z^{DCA}_{\text{track}} - z^{reco}_{\text{PV}}\right| < 1\,\text{cm}$
- track and electron have opposite charge

---

[1] At the time of writing, it is not clear to the author whether the EM object corresponding to the jet must also lie in the track mass window. If this is the case, the jet and track requirements have been selected such that the numerator in the following equation is still $\epsilon_{\text{jet}} \times A(e, \text{jet})$. See [22] for more information.

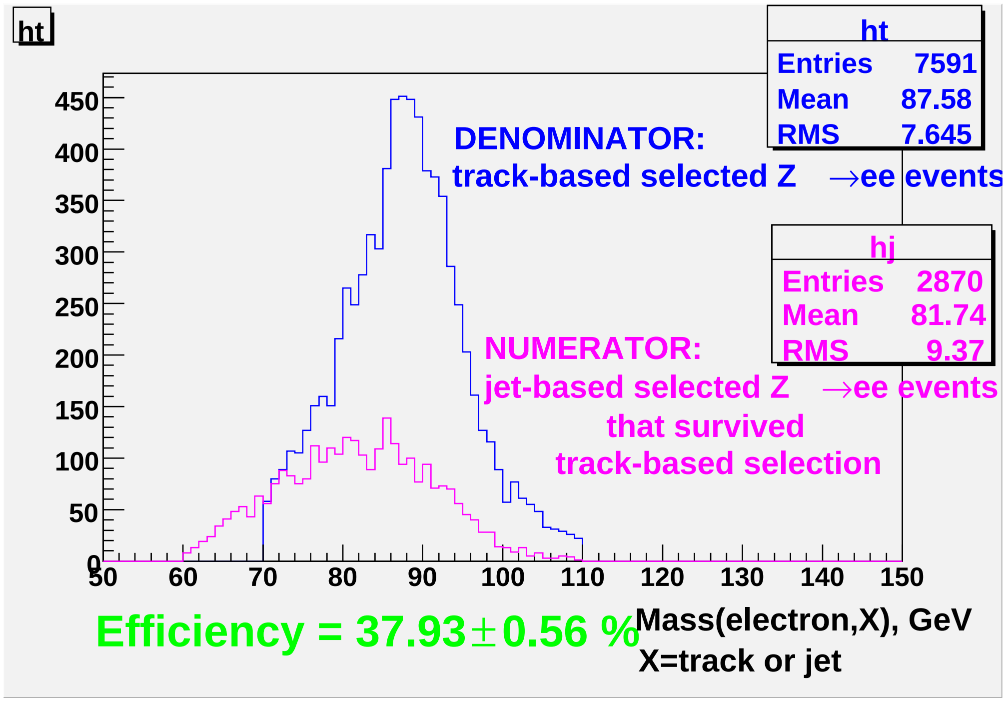

Figure 8.1: The numerator (magenta, plotted as a function of jet-based invariant mass) is the number of (e,jet) $Z \rightarrow ee$ pairs that also satisfy the (e,track) requirements. The denominator (blue, plotted as a function of track-based invariant mass) is the number of (e,track) $Z \rightarrow ee$ events. Note that the measured jet- and track-based invariant masses are not necessarily the same - this is the reason that the magenta "numerator" curve - the distribution of (e,jet) $Z \rightarrow$ events - is not sharply cut off at 70 GeV; it would be, if the track-based invariant mass were plotted instead of the jet-based invariant mass[22]. NOTE: This figure is from a D0 internal note. At the time of writing, it has not been approved by the D0 collaboration for general public use beyond this dissertation.

- $\sum\limits_{\Delta R<0.4} p_T^{\mathrm{track}} < 4\,\mathrm{GeV}$
- $70\,\mathrm{GeV} < m_{\mathrm{inv}}(\mathrm{track}, \mathrm{electron}) < 110\,\mathrm{GeV}$

Selection requirements for (e,jet) $Z \rightarrow ee$ events in the $W \rightarrow e\nu$ sample:

- $\Delta\phi(e, \mathrm{jet}) > 2.5$
- $p_T^{\mathrm{jet}} > 20\,\mathrm{GeV}$
- $1.0 < \left|\eta_{\mathrm{det(jet)}}\right| < 1.5$
- Jet ID selections: jetEMFrac<0.5, jetCHFrac<0.15, n_{tracks} <10, 2<jetN90<25, jetHCR<6
- $N_{\mathrm{jets}}^{p_T > 8\,\mathrm{GeV}} \leq 4$
- $\Delta R(\mathrm{jet}, \mathrm{track}) < 0.3$
- $60\,\mathrm{GeV} < m_{\mathrm{inv}}(\mathrm{track}, \mathrm{electron}) < 110\,\mathrm{GeV}$

Non-ICD (e,jet) and (e,track) events in $W \to e\nu$ sample are negligible[22].

The uncertainty in the $Z \to ee$ background is determined by measuring the W mass with the background increased and decreased by its standard deviation. The uncertainty contribution from the $Z \to ee$ background determination is quoted as half the variation in the W mass.

8.2 Multijet Background

The QCD background is measured in collider data. Multijets can pass the $W \to e\nu$ cuts if one jet is mis-identified as an electron and another jet is mismeasured so that the event appears to have a large MET.

If the efficiency with which $W \to e\nu$ events in the loose sample pass the tight track-matching cut (ϵ_W^{t}) is known, and the efficiency, or "fake-rate", with which QCD events pass the track-matching cut ($f_{\mathrm{QCD}}^{\mathrm{t}}$) is known, then the number of true $W \to e\nu$ events can be determined via the matrix method[22]:

$$N^{\mathrm{l}} = N_W^{\mathrm{l}} + N_{\mathrm{QCD}}^{\mathrm{l}} \tag{8.7}$$

$$N^{\mathrm{t}} = \epsilon^{\mathrm{t}} N_W^{\mathrm{l}} + f^{\mathrm{t}} N_{\mathrm{QCD}}^{\mathrm{l}} \tag{8.8}$$

where N_W^{l} is the number of $W \to e\nu$ candidates passing the loose requirement, $N_W^{\mathrm{t}} = \epsilon^{\mathrm{t}} N_W^{\mathrm{l}}$ is the number of $W \to e\nu$ candidates passing the tight requirement, $N_{\mathrm{QCD}}^{\mathrm{l}}$ is the number of QCD candidates passing the loose requirement, and $N_{\mathrm{QCD}}^{\mathrm{t}} = f^{\mathrm{t}} N_{\mathrm{QCD}}^{\mathrm{l}}$ is the number of QCD candidates passing the tight requirement. For simplicity, in this section only, we define $\epsilon \equiv \epsilon^{\mathrm{t}}$ and $f \equiv f^{\mathrm{t}}$.

Solving the system of equations above results in

$$N_W^{\mathrm{l}} = \frac{N^{\mathrm{t}} - f \cdot N^{\mathrm{l}}}{\epsilon - f} \tag{8.9}$$

$$N_{\mathrm{QCD}}^{\mathrm{l}} = \frac{\epsilon \cdot N^{\mathrm{l}} - N^{\mathrm{t}}}{\epsilon - f} \tag{8.10}$$

and

$$N_W^{\mathrm{t}} = \epsilon \cdot N_W^{\mathrm{l}} = \epsilon \cdot \left(\frac{N^{\mathrm{t}} - f \cdot N^{\mathrm{l}}}{\epsilon - f} \right) \tag{8.11}$$

$$N_{\mathrm{QCD}}^{\mathrm{t}} = f \cdot N_{\mathrm{QCD}}^{\mathrm{l}} = f \cdot \left(\frac{\epsilon \cdot N^{\mathrm{l}} - N^{\mathrm{t}}}{\epsilon - f} \right) \tag{8.12}$$

where the numbers after the tight selection are the quantities we are interested in. In order to propagate uncertainties we must transform to the statistically independent quantities $N^1 = N^{\mathrm{l}} - N^{\mathrm{t}}$ and $N^2 = N^{\mathrm{t}}$. Then,

$$\begin{aligned} \Delta N_W^{\mathrm{t}} &= \left(\left(\frac{\partial N_W^{\mathrm{t}}}{\partial \epsilon} \right)^2 \Delta\epsilon^2 + \left(\frac{\partial N_W^{\mathrm{t}}}{\partial f} \right)^2 \Delta f^2 + \right. \qquad (8.13) \\ &\qquad \left. \left(\frac{\partial N_W^{\mathrm{t}}}{\partial N_1^2} \right)^2 \Delta N_1^2 + \left(\frac{\partial N_W^{\mathrm{t}}}{\partial N_2^2} \right)^2 \Delta N_2^2 \right)^{1/2} \\ \Delta N_{\mathrm{QCD}}^{\mathrm{t}} &= \left(\left(\frac{\partial N_{\mathrm{QCD}}^{\mathrm{t}}}{\partial \epsilon} \right)^2 \Delta\epsilon^2 + \left(\frac{\partial N_{\mathrm{QCD}}^{\mathrm{t}}}{\partial f} \right)^2 \Delta f^2 + \right. \qquad (8.14) \\ &\qquad \left. \left(\frac{\partial N_{\mathrm{QCD}}^{\mathrm{t}}}{\partial N_1^2} \right)^2 \Delta N_1^2 + \left(\frac{\partial N_{\mathrm{QCD}}^{\mathrm{t}}}{\partial N_2^2} \right)^2 \Delta N_2^2 \right)^{1/2} \end{aligned}$$

where ϵ and f are determined using similar techniques as described in Section 7.2.3,[2] and described in more detail in [22] and [46]. $\Delta N_i = \sqrt{N_i}$ when statistics satisfy $N_i \gtrsim 25$.

---

[2] The efficiencies used for subtracting the background are measured with fewer dependent variables than the efficiency used for signal modeling.

The fake rate f is measured from an “EM+JET” sample, composed of dijet events where one jet is misidentified as an electron. These events are skimmed from RunIIb34 data by requiring an EM cluster that satisfies H-Matrix and loose track-matching requirements (see Sections 5.2.3.1 and 5.2.3.2), and is back-to-back with a jet passing the following JET ID requirements:

- jetN90>1
- $p_T^{\rm jet}$ >20GeV
- 0.05<jetEMFrac<0.95
- jetCHFrac<0.4
- jetHCRatio<10.
- jetTracks>0
- $\eta_{\rm det}$ <0.8 or ($\eta_{\rm det}$ >1.5 and $\eta_{\rm det}$ <2.5)

The fake rate is the fraction of these events where the “EM cluster” is found to have a track satisfying the tight track-matching requirement. In the RunIIa analysis, it was sufficient to use a constant fake rate because the strongest dependency, on p_T, was negligible compared to the statistical fluctuations of the background sample, and in the RunIIb12 analysis, a 1D dependence on p_T was used because the next strongest dependence, on $\eta_{\rm det}$, was negligible in comparison.

The p_T dependence is the most important for QCD background shape and fraction, because the kinematic spectrum shape is used to measure W mass. In the RunIIb34 analysis, we find that the fake rate and electron efficiency strongly depend on $\eta_{\rm det}$ and $z_{\rm vtx}$, but because there is not strong correlation of $z_{\rm vtx}$ with the background shape, we have tried to parameterize the fake rate and electron efficiency as a function of only p_T and $\eta_{\rm det}$. However, we have found that we need to consider not only the dependence on η_{det} and p_T, but also on ϕ, due to a non-negligible difference in tracker performance in the top and bottom of the detector. This variation with ϕ is due to the failure of more and more tracker modules over time.

8.3 $W \to \tau\nu \to e\nu\nu\nu$ Background

Some of the electrons from W boson decays did not come directly from a $W \to e\nu$ decay, but instead came from the process $W \to \tau\nu \to e\nu\nu\nu$. These could in principle be treated as signal with different kinematics than the $W \to e\nu$ electrons, but since the number of τ events we detect is relatively small and they have a poor mass resolution due to the subsequent decay to three leptons, we simplify the analysis by treating them as a background.

$W \to \tau\nu$ background is estimated with generated events processed by a FastMC simulation. $W \to \tau\nu$ decays are generated with `RESBOS`. Hadronic τs which can fake $W \to e\nu$ events are negligible and so these are not simulated. In RunIIa, the $W \to \tau\nu$ decays were generated by `PYTHIA`,[3] but the boson p_T spectrum shape was narrower than seen in data. `RESBOS`, the more complete simulation, was found to have a broader spectrum shape, as seen in Figure (8.2).

After being generated by `RESBOS`, τ leptons are passed to `TAUOLA` which simulates their decay to electrons and neutrinos. `PYTHIA` assumes uniform polarization of the τ, which is results in an incorrect angular distribution of the decay products, an extreme example of which can be seen in Figure 8.3. Therefore, we always use `TAUOLA` to decay the τ particles.[4]

To determine the number of background τ particles we expect to see in a given sample, we need to measure the relative acceptance of τ vs. e events,

$$A \equiv \frac{n_\tau}{n_e} \tag{8.15}$$

---

[3] In RunIIa, they were also processed with the full detector simulation "d0gstar".

[4] Other analyses have fixed this problem used reweighting of the p_T spectrum, which is not acceptable for this analysis, as it has a non-negligible effect on important distributions such as boson η.

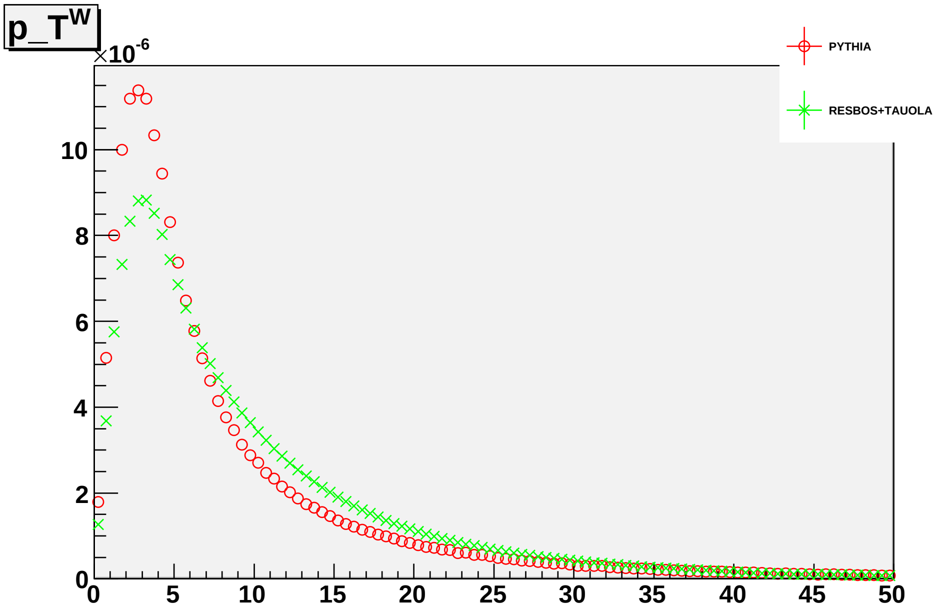

Figure 8.2: Comparison of the W boson p_T spectrum simulated by `PYTHIA` (red) vs. `RESBOS+TAUOLA` (green). The latter was found to better match the spectrum shape measured at the Tevatron. NOTE: This figure is from a D0 internal note. At the time of writing, it has not been approved by the D0 collaboration for general public use beyond this dissertation.

where n_τ is the number of $W \to \tau\nu \to e\nu\nu\nu$ events in the sample, and n_e is the number of $W \to e\nu$ events in the sample. Then,

$$n_\tau = \frac{N^{\text{PASS}}_{W\to\tau\nu\to e\nu\nu\nu}}{N^{\text{gen}}_{W\to\tau\nu\to e\nu\nu\nu}} \cdot \mathcal{L} \cdot \sigma_W \cdot \text{BR}\,(W \to \tau e) \cdot \text{BR}\,(\tau \to e\nu\nu) \tag{8.16}$$

and

$$n_e = \frac{N^{\text{PASS}}_{W\to e\nu}}{N^{\text{gen}}_{W\to e\nu}} \cdot \mathcal{L} \cdot \sigma_W \cdot \text{BR}\,(W \to e\nu) \tag{8.17}$$

where $N^{\text{PASS}}_{W\to\tau\nu\to e\nu\nu\nu}$ and $N^{\text{PASS}}_{W\to e\nu}$ were derived from FastMC simulations of one billion $W \to e\nu$ events and 651 million $W \to \tau$ events, and $N^{\text{gen}}_{W\to\tau\nu}$ and $N^{\text{gen}}_{W\to e\nu}$ are the numbers of simulated events (which passed the generator level cuts) that were simulated with the FastMC. $\mathcal{L}$ is the integrated luminosity for the sample in question, σ_W is the cross-section to produce a W

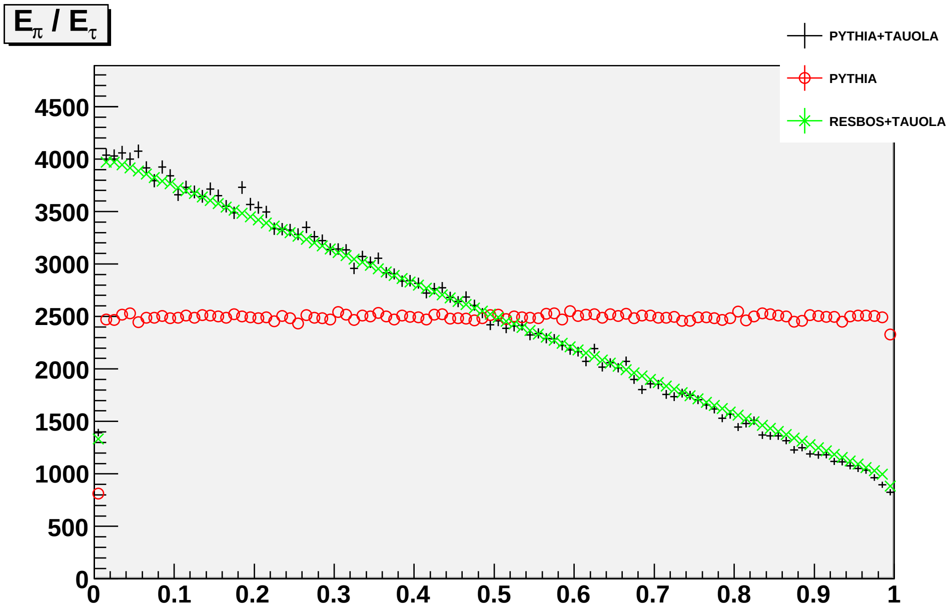

Figure 8.3: Example of the effect of neglecting to simulate, as seen in the standard version of `PYTHIA` (red), vs. simulating, as seen in `PYTHIA`+`TAUOLA` (black) and `RESBOS`+`TAUOLA`, (green), the polarization of the τ. NOTE: This figure is from a D0 internal note. At the time of writing, it has not been approved by the D0 collaboration for general public use beyond this dissertation.

boson at the Tevatron, and BR means “branching ratio”. Then,

$$\frac{n_\tau}{n_e} = \frac{N^{\text{PASS}}_{W\to\tau\nu\to e\nu\nu\nu}}{N^{\text{PASS}}_{W\to e\nu}} \cdot \frac{N^{\text{gen}}_{W\to e\nu}}{N^{\text{gen}}_{W\to\tau\nu\to e\nu\nu\nu}} \cdot \frac{\text{BR}\,(W\to\tau\nu)\cdot\text{BR}\,(\tau\to e\nu\nu)}{\text{BR}\,(W\to e\nu)} \tag{8.18}$$

The branching ratios are:

$$\text{BR}\,(\tau\to e\nu\nu) = 17.83 \pm 0.04\% \tag{8.19}$$

$$\text{BR}\,(W\to\tau\nu)\,/\text{BR}\,(W\to e\nu) = 1.046 \pm 0.023\% \tag{8.20}$$

and thefore we have:

$$\frac{\text{BR}\,(\tau\to e\nu\nu)\cdot\text{BR}\,(W\to\tau)}{(W\to e\nu)} = 18.65 \pm 0.04\% \tag{8.21}$$

From these calculations, we expect the m_T, p_T^e, and MET distributions to respectively contain 1.722%, 1.701%, and 1.716% of $W \rightarrow \tau\nu$ events. These fractions apply to both the FullMC and collider data, since by design the FullMC has the same InstLumi profile as the data.

The τ background uncertainty comes from two main sources: uncertainty in the the W mass used to simulate the τ background, and uncertainty in the branching ratio for the $W \rightarrow \tau\nu$ decay. The W mass affects the τ background by changing the kinematic shape of background, which also affects the relative acceptance and thus the overall contribution of the background. However, the uncertainty from both these sources is negligible, by the reasoning in the following paragraphs.

The dependence of the τ background fraction on the input mass in RunIIb34 is shown in Figure 8.4. It also shows the change in the τ background fraction due to varying the branching ratio up and down by the uncertainty quoted in Equation 8.21. We see that a change of about 0.1 GeV in the m_W used for the τ background results in less than a 0.01% change in the size of the τ background, which is of a similar magnitude to that found in the RunIIb12 analysis.

In studies done for the RunIIb12 analysis, it was found that changing the m_W used to generate the τ background by 4 GeV (and but leaving the input W mass for the FastMC the same) resulted in less than a 3 MeV change in the fitted m_W. If we assume that the default W mass in `RESBOS` (80.419 GeV) is within 40 MeV of the true W mass, we expect a maximum error of 0.003 MeV from the kinematic shape, which is negligible compared to other uncertainties in this measurement[22].

A larger uncertainty is due to the branching ratio. There is a 0.04% uncertainty in the size of the τ background due to the uncertainties in the branching ratios quoted above. This is at most an order of magnitude larger than the uncertainty due to the input W mass to the τ background, and is therefore also considered to be negligible.

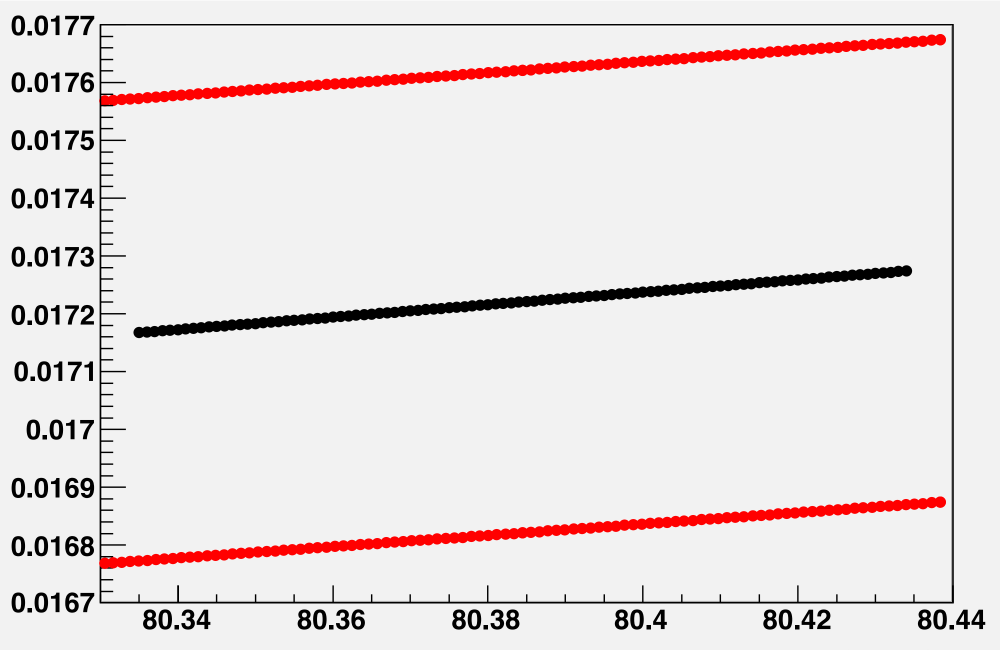

Figure 8.4: The dependence of the τ background fraction on the input W mass to the τ model. The black line comes from using the central value of the branching ratio, the red lines come from varying the branching ratio up and down by the uncerta. Horizontal axis is M_t in GeV, vertical axis is $W \rightarrow \nu\tau$ background fraction[47]. NOTE: This figure is from a D0 internal presentation. At the time of writing, it has not been approved by the D0 collaboration for general public use beyond this dissertation.

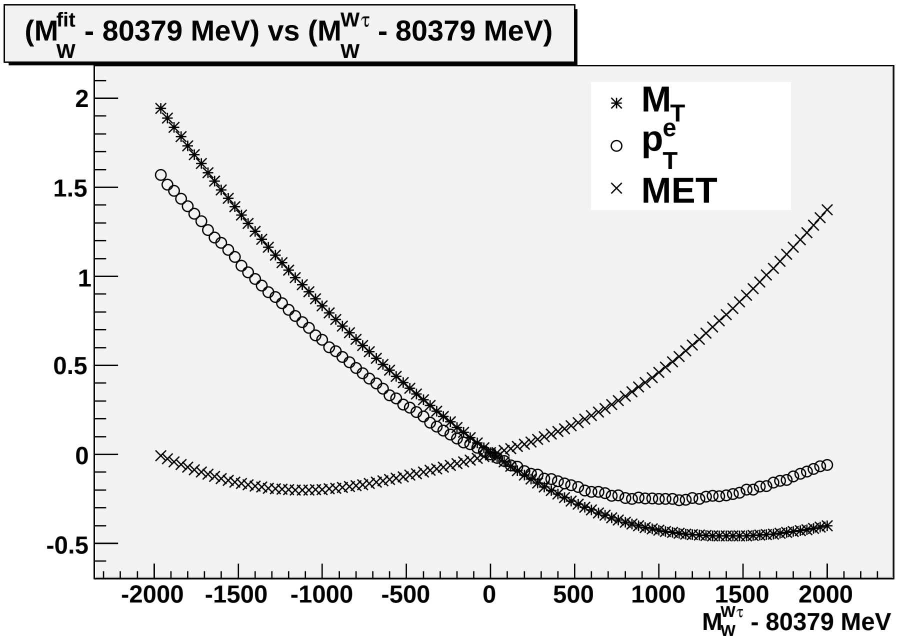

Figure 8.5: Dependence of W mass measured from the three measurement observables on the value of the input W mass used to determine the τ background[22]. NOTE: This figure is from a D0 internal note. At the time of writing, it has not been approved by the D0 collaboration for general public use beyond this dissertation.

Chapter 9

MEASURING THE W MASS FROM A FULL MC SAMPLE

An important step in the measurement of the W mass is to test that our measurement technique is accurate. To do this, we perform our measurement technique on FullMC samples, treating them as mock data, with the reconstrucion proceeding in exactly the same way as it does with collider data. If the result of our measurement of the boson mass agrees with the value used in the simulation, we trust the accuracy of our measurement. We measure both the W and Z boson masses, with differences in success between the two measurements being due to errors in the translation from efficiencies and responses measured from electrons with $Z \rightarrow ee$ kinematics to simulation of electrons with $W \rightarrow e$ kinematics.

9.1 Z Boson Closure Test

Since the main tuning of the FastMC was performed using $Z \rightarrow ee$ events, an important first step in testing for closure is to confirm that the FastMC can accurately simualte $Z \rightarrow ee$ events. Therefore, we compare the FullMC and FastMC versions of some important distributions in the $Z \rightarrow ee$ sample. Figures 9.1 and 9.2 show the comparisons between FullMC and FastMC of the distributions of the Z mass (top left), the Z p_T (top right), the electron p_T (bottom left), and the hadronic recoil (bottom right), for RunIIb3, and RunIIb4, respectively. We see good agreement, both visually and from the χ^2/ndf values.

We then perform a measurement of the Z mass using our measurement strategy, with the invariant mass of the decay electrons, M_{ee}, as our observable. The results are shown in Table 9.1 and Figure 9.3. We see good agreement in all InstLumi bins and for the full InstLumi range with the input value of 91.188 GeV. Therefore our FastMC passes the closure test for simulation of $Z \rightarrow ee$ events and the measurement of the Z boson mass.

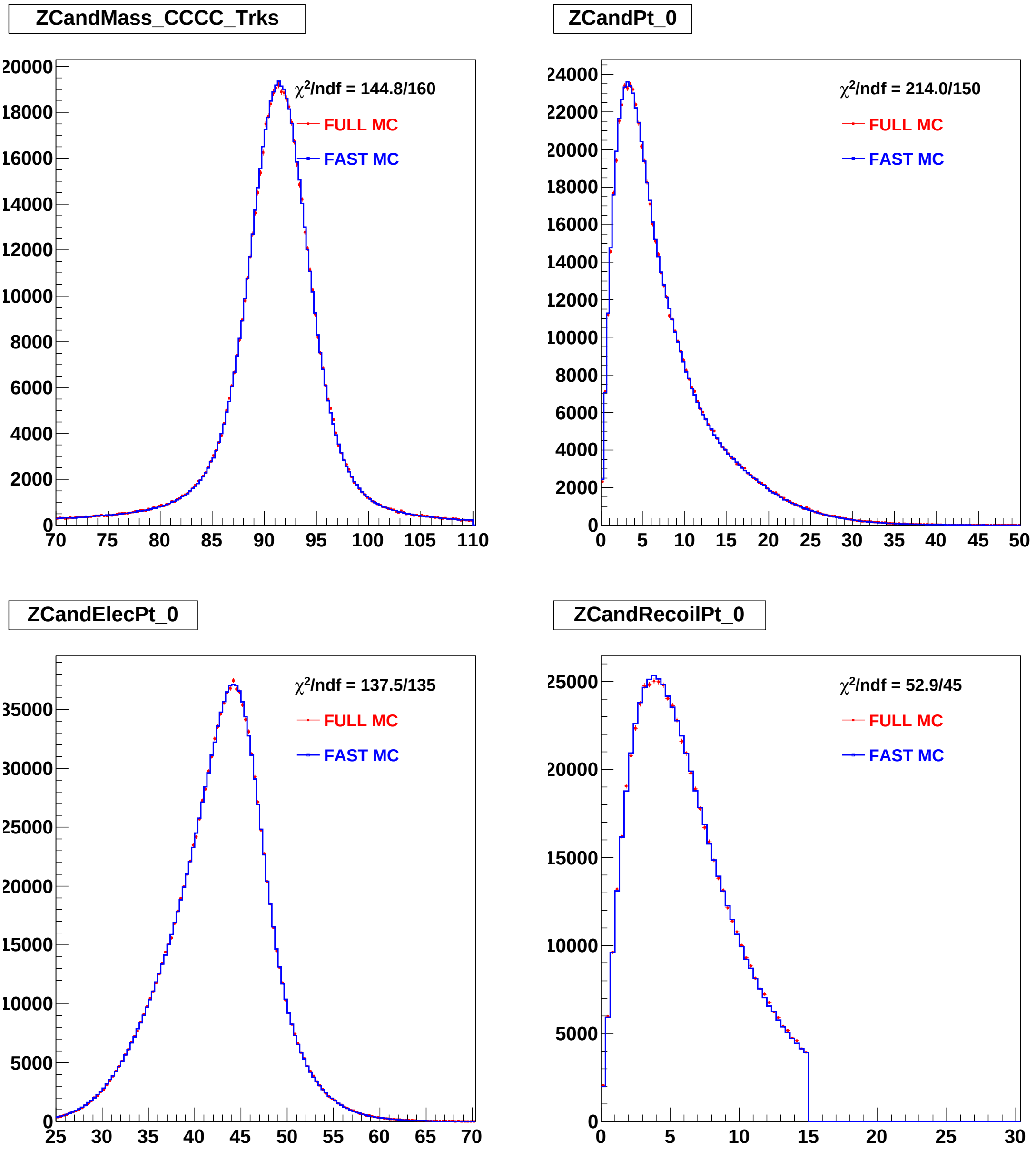

Figure 9.1: RunIIb3 comparisons between FullMC and FastMC of the distributions of the Z mass (top left), the Z p_T (top right), the electron p_T (bottom left), and the hadronic recoil (bottom right). Note the good χ^2 agreement[20]. NOTE: This figure is from a D0 internal note. At the time of writing, it has not been approved by the D0 collaboration for general public use beyond this dissertation.

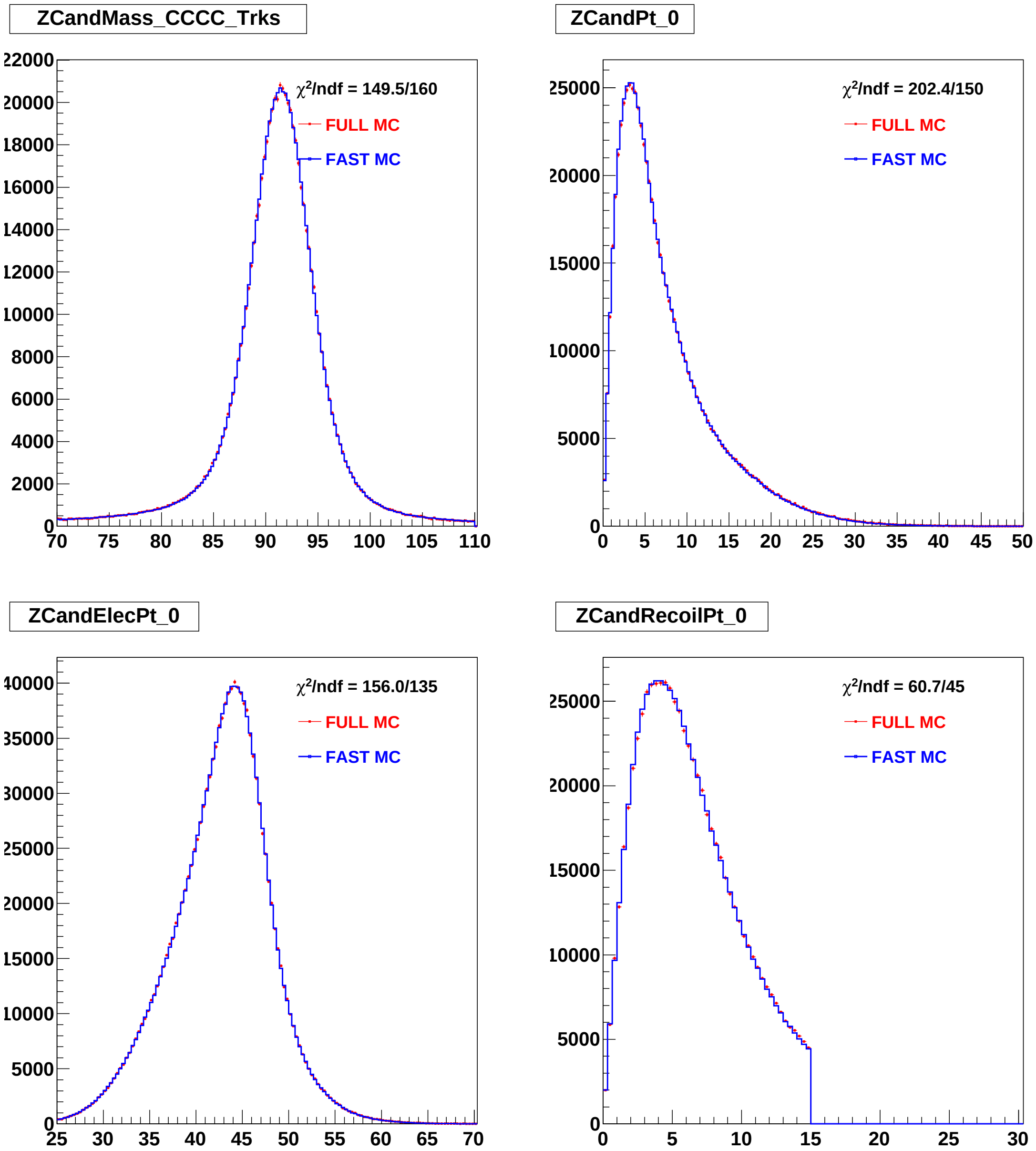

Figure 9.2: RunIIb4 comparisons between FullMC and FastMC of the distributions of the Z mass (top left), the Z p_T (top right), the electron p_T (bottom left), and the hadronic recoil (bottom right). Note the good χ^2 agreement[20]. NOTE: This figure is from a D0 internal note. At the time of writing, it has not been approved by the D0 collaboration for general public use beyond this dissertation.

$\mathcal{L}$	Z mass RunIIb3	Z mass RunIIb4
All $\mathcal{L}$	91.191 ± 0.005	91.194 ± 0.004
$0 < \mathcal{L} < 2$	91.188 ± 0.014	91.191 ± 0.016
$2 < \mathcal{L} < 4$	91.190 ± 0.006	91.187 ± 0.006
$4 < \mathcal{L} < 6$	91.189 ± 0.009	91.190 ± 0.008
$\mathcal{L} > 6$	91.191 ± 0.013	91.193 ± 0.010

Table 9.1: Result of the fit of the Z mass in bins of InstLumi. The input Z mass value is 91.188 GeV. RunIIb3 and RunIIb4 fit values are in good agreement with the input value. NOTE: This figure is from a D0 internal note. At the time of writing, it has not been approved by the D0 collaboration for general public use beyond this dissertation.

9.2 W Boson Closure Test

Next, we test the ability of the FastMC to accurately simulate $W \to e\nu$ events. We compare the distributions of the three measurement observables: the transverse W mass, m_T (Figure 9.4), the electron transverse momentum, p_T (Figure 9.5), and the missing transverse energy, $\not{E}_T$ (Figure 9.6), between FullMC and FastMC, for RunIIb3 and RunIIb4. The comparison is shown in the top half, and the χ^2 distribution is shown in the bottom half, of each figure. There is good agreement for all three measurement observables.

Finally, we perform measurements of the W mass using our measurement strategy, for both runs, in each measurement observable. The results are shown in Tables 9.2 and 9.3, and in Figure 9.7. We see good agreement in all InstLumi bins and for the full InstLumi range with the input value of 80.450 GeV. Therefore our FastMC passes the closure test for simulation of $W \to e\nu$ events and the measurement of the W boson mass.

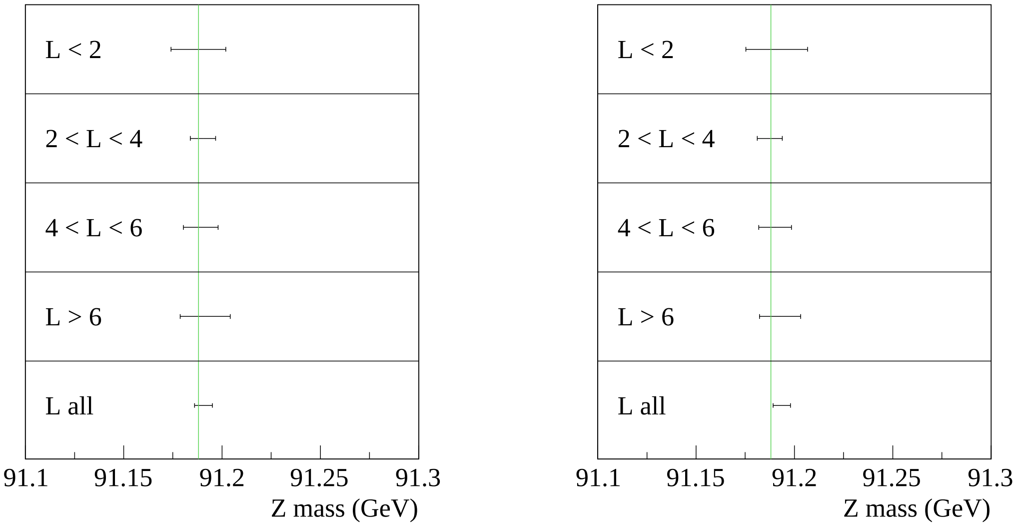

Figure 9.3: Results from measuring the Z mass from the Full MC $Z \to ee$ RunIIb3 (left) and RunIIb4 (right) samples, in bins of InstLumi and for the full InstLumi range. The vertical line shows the input Z mass value of 91.188 GeV[20]. NOTE: This figure is from a D0 internal note. At the time of writing, it has not been approved by the D0 collaboration for general public use beyond this dissertation.

9.3 Monte Carlo Closure

Because our FastMC is able to model both $Z \to ee$ and $W \to e\nu$ events well, and we are able to measure the correct mass of the boson that was simulated, we trust that our technique can, in principle, be used to measure the W mass from collider data. Of course, accurate measurement of the W mass from the data requires that the modifications we have made to our FastMC tune to model collider data are correct. In the next and final chapter, we discuss the status of the measurement in collider data.

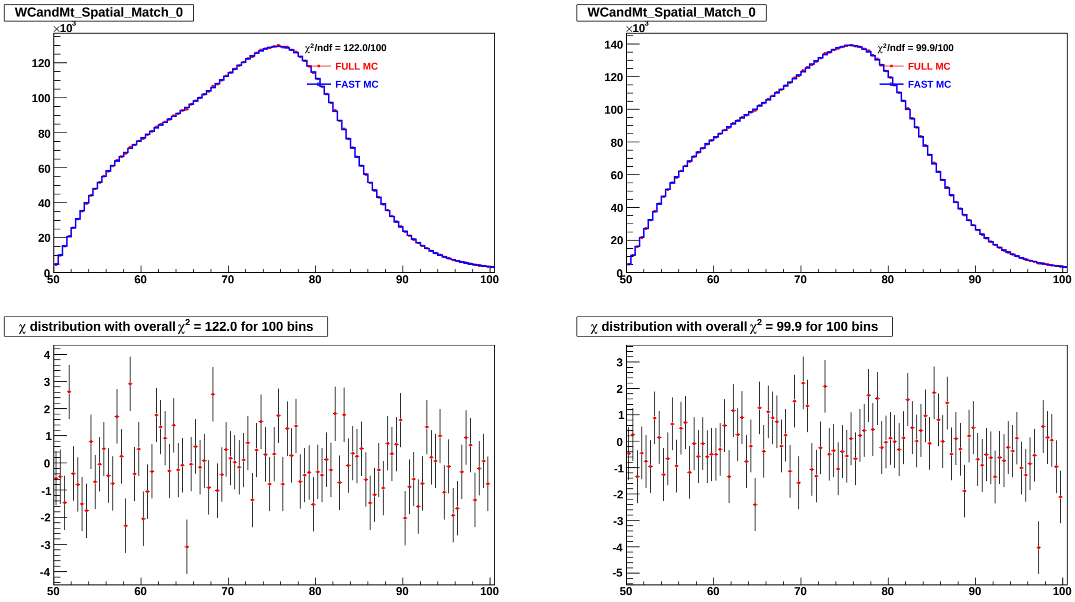

Figure 9.4: RunIIb3 (left) and RunIIb4 (right) comparison (top) and difference (bottom) plots of the transverse W mass[20]. NOTE: This figure is from a D0 internal note. At the time of writing, it has not been approved by the D0 collaboration for general public use beyond this dissertation.

$\mathcal{L}$	m_T	$p_T(e)$	MET
All $\mathcal{L}$	80.451 ± 0.006	80.450 ± 0.006	80.439 ± 0.008
$0 < \mathcal{L} < 2$	80.446 ± 0.018	80.457 ± 0.019	80.421 ± 0.021
$2 < \mathcal{L} < 4$	80.454 ± 0.009	80.454 ± 0.009	80.444 ± 0.011
$4 < \mathcal{L} < 6$	80.454 ± 0.012	80.442 ± 0.011	80.443 ± 0.016
$\mathcal{L} > 6$	80.416 ± 0.018	80.439 ± 0.016	80.418 ± 0.026

Table 9.2: Result of the MC closure test for RunIIb3, in bins of InstLumi and for the full InstLumi range. The input W mass value is 80.450 GeV. NOTE: This figure is from a D0 internal note. At the time of writing, it has not been approved by the D0 collaboration for general public use beyond this dissertation.

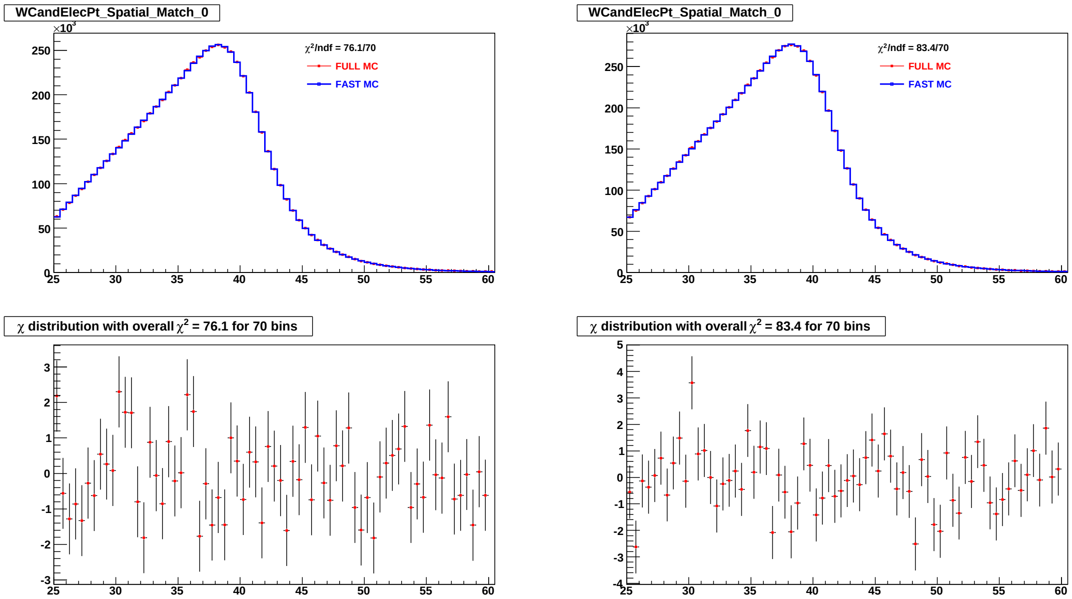

Figure 9.5: RunIIb3 (left) and RunIIb4 (right) comparison (top) and difference (bottom) plots of the transverse W electron momentum[20]. NOTE: This figure is from a D0 internal note. At the time of writing, it has not been approved by the D0 collaboration for general public use beyond this dissertation.

$\mathcal{L}$	m_T	$p_T(e)$	MET
All $\mathcal{L}$	80.454 ± 0.006	80.452 ± 0.006	80.448 ± 0.008
$0 < \mathcal{L} < 2$	80.460 ± 0.021	80.476 ± 0.021	80.431 ± 0.024
$2 < \mathcal{L} < 4$	80.463 ± 0.009	80.459 ± 0.008	80.457 ± 0.011
$4 < \mathcal{L} < 6$	80.454 ± 0.012	80.452 ± 0.011	80.424 ± 0.016
$\mathcal{L} > 6$	80.434 ± 0.015	80.445 ± 0.013	80.467 ± 0.021

Table 9.3: Result of the MC closure test for RunIIb4, in bins of InstLumi and for the full InstLumi range. The input W mass value is 80.450 GeV. NOTE: This figure is from a D0 internal note. At the time of writing, it has not been approved by the D0 collaboration for general public use beyond this dissertation.

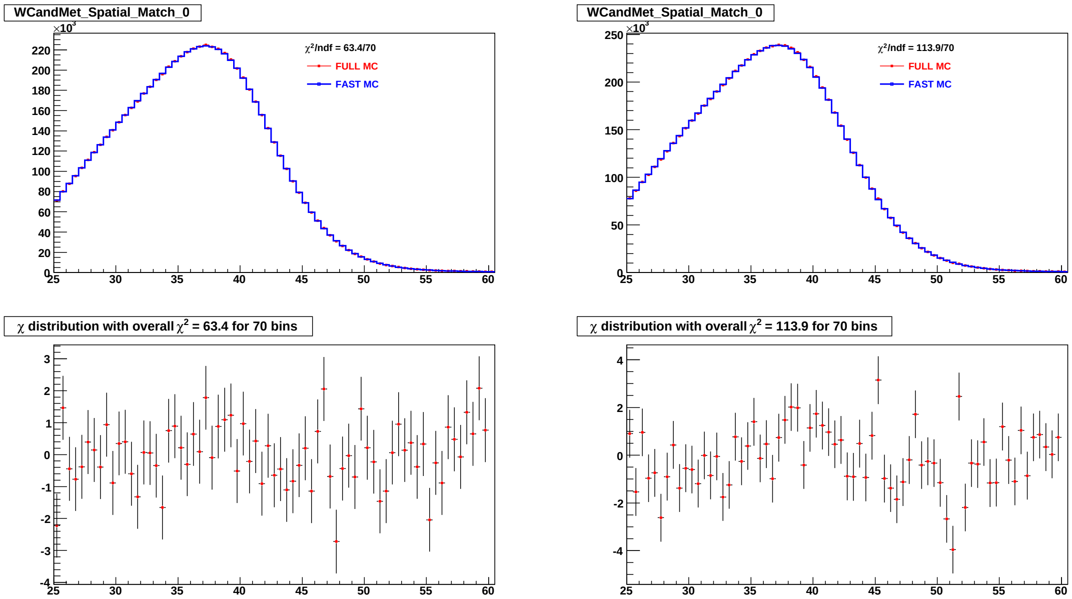

Figure 9.6: RunIIb3 (left) and RunIIb4 (right) comparison (top) and difference (bottom) plots of the missing transverse energy[20]. NOTE: This figure is from a D0 internal note. At the time of writing, it has not been approved by the D0 collaboration for general public use beyond this dissertation.

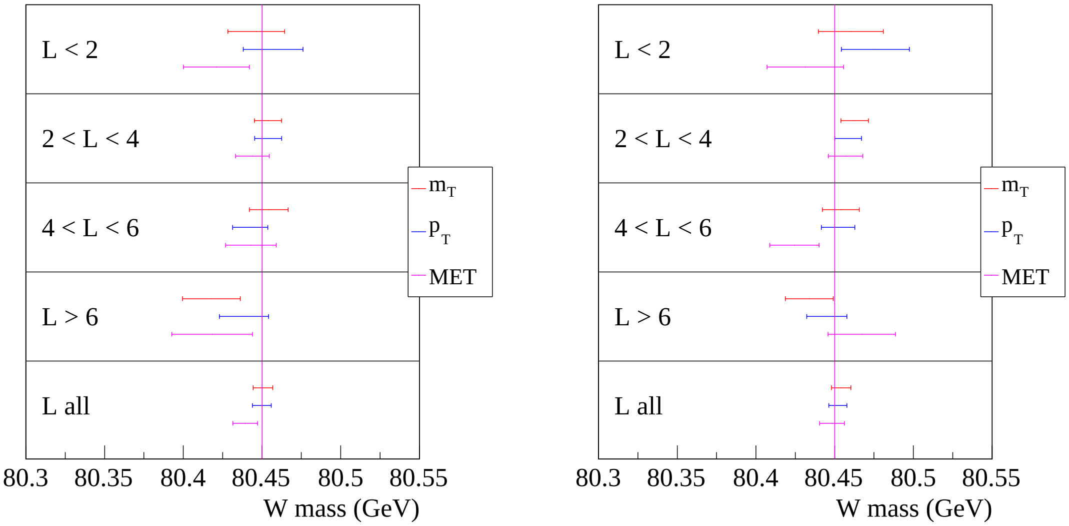

Figure 9.7: Results from measuring the W mass from the Full MC $W \to e\nu$ RunIIb3 (left) and RunIIb4 (right) samples, in bins of InstLumi and for the full InstLumi range. The vertical line shows the input W mass value of 80.450 GeV[20]. NOTE: This figure is from a D0 internal note. At the time of writing, it has not been approved by the D0 collaboration for general public use beyond this dissertation.

Chapter 10

DISCUSSION AND CONCLUSIONS

10.1 Uncertainties in the Current Measurement

We have not yet reached the point where we are ready to unblind (Section 3.3) our measurement of the W mass from the RunIIb34 data. We have not achieved a satisfactory FastMC model of the collider data, with significant discrepancies between the data and the FastMC model, and between the RunIIb3 and the RunIIb4 versions of the FastMC models. Because of these problems, which we discuss in Section 10.2, we do not have a final value of the W mass to present in this dissertation.

However, there is a small amount preliminary information to share that is interesting, namely the contributions to the W mass measurement uncertainty from a small subset of the parameters of our model. These can give a sense of the amount by which this measurement (if possible to complete) can increase the precision of the worldwide average of the W mass measurement. Because the model is not finalized, these are estimates which may be different from the final values of the uncertainties. Because in general we tend to wait until we have a satisfactory model to perform the full uncertainty analysis, we do not have estimates for all the components of the model.

The uncertainties that are available from the current measurement are the QCD uncertainties, a subset of the recoil uncertainties, and the uncertainties due to the SET-InstLumi dependent residual efficiency correction.

The uncertainty contribution from the recoil parametrization is calculated from the five parameter covariance for the RunIIb3 data sample, and from the ten parameter covariance matrix (because different parameters were used for each subset of data) for the combined RunIIb34 data sample. The uncertainty contribution for the RunIIb4 data sample

Source	m_T	p_T^e	$\not{E}_T$
PDF	14.54	20.78	16.15
QCD (Boson p_T)	1.71	6.41	1.42

Table 10.1: Expected contribution from QCD model uncertainty to the combined RunIIb34 measurement of the W mass in each measurement observable[28]. NOTE: This figure is from a D0 internal note. At the time of writing, it has not been approved by the D0 collaboration for general public use beyond this dissertation.

Source	m_T	p_T^e	$\not{E}_T$
RunIIb3 Residual Efficiency Correction	1.35	1.75	4.05
RunIIb4 Residual Efficiency Correction	2.07	2.55	5.58

Table 10.2: Estimated contribution to the uncertainty, from the SET-InstLumi dependent residual efficiency correction, for individual RunIIb3 and RunIIb4 measurements of the W mass in each measurement observable. NOTE: This figure is from the author's own work. At the time of writing, it has not been approved by the D0 collaboration for general public use beyond this dissertation.

is not available at this time, and the uncertainties are only presented for the m_T observable based measurement. For RunIIb3 we estimate a 10.3 MeV contribution to the uncertainty, and for the combined RunIIb34 measurement we estimate a 6.4 MeV contribution to the uncertainty[33].[34]

The uncertainty contributions from the parameterization of the residual efficiency correction for data as a function of SET and InstLumi, which are calculated as described in Section 7.2.8.7, are shown in Table 10.2.

The expected statistical uncertainty in the measurements measured by the fitting software, and verified as described in [44] and [37], are shown in Table 10.3.

Source	m_T	p_T^e	$\not{E}_T$
Statistical	17	17	20

Table 10.3: Estimated statistical uncertainty for the combined RunIIb34 measurement of the W mass in each measurement observable[44][37]. NOTE: This figure is from a D0 internal presentation. At the time of writing, it has not been approved by the D0 collaboration for general public use beyond this dissertation.

The values that have just been presented can be compared with the uncertainties from the RunIIb12 measurement, arranged in Table 10.4. They are all comparable in size, providing some assurance that, in the absence or mitigation of the problems described in Section 10.2, we can achieve a similar quality of measurement for the RunIIb34 data as for the RunIIb12 data.

10.2 Current Status of the Measurement

There is currently a tension of about 80 MeV between our measurement of the W mass performed on RunIIb3 data and RunIIb4 data, with RunIIb4 having the larger value. There is actually about a 150 MeV tension between the value of the W mass measured from data taken early and data taken late in the RunIIb4 data taking period, with the later value being larger. We do not know the tension between the measurement and the world estimate of the mass, because the measurement is blinded (to the same value for both RunIIb3 and RunIIb4). In this section, we will discuss the possible reasons for this tension and the implications for the completion of the measurement.

The problem can be seen in Figure 10.1. There is a noticable difference between RunIIb3 and RunIIb4 in the peaks of the distributions of all three measurement observables, when $u_\parallel > 0$. There is also a mysterious disagreement at low p_T, which is visible in all InstLumi bins, and was originally thought to be caused by the trigger efficiency simulation, but this theory was disaffirmed by a close study of the trigger efficiencies, described in Section

7.2.1. While the problem of disagreement at low p_T is concerning, and ideally would be solved, it is outside the range of the measurement, so is less of a problem than the disagreement at the peak. This discussion therefore focuses only on the problem of the disagreement at the peak.

The problem can be further localized to particular regions of the detector, namely the top part, as can be seen by the splitting of the $p_T(e)$ distribution into electron ϕ bins as is done in Figure 10.2. The effect is strongest in the top part of the detector, approximately where $\frac{\pi}{2} < \phi < \frac{\pi}{2}$.

When we take a closer look at the electron p_T plot, as in Figure 10.1, we notice that the "missing" events, indicated by the violet arrow, could conceivably have been "smeared" (via a lower than expected resolution) into the region of higher electron p_T, indicated by the red arrow. In addition, we can further subdivide the RunIIb4 data by time, into an "early" part, and a "late" part, as shown in Figure 10.3. The plot was initially used in a study of calorimeter currents, however here it is simply used to describe the subdivision of the RunIIb4 data.

Figure 10.4 shows the same plots which compare RunIIb3 and RunIIb4 data. However, now, the RunIIb4 data has been split into an early (left) and a late (right) sample. The difference at the peaks is slightly more pronounced in late RunIIb4 data, and the smearing, indicated by the violet arrow, becomes very noticeable in the late sample.

The problem is still visible when we combine $u_\parallel > 0$ and $u_\parallel < 0$ events, as in the comparisons of the total electron p_T (Figure 10.5), W transverse mass m_T (Figure 10.6), and electron ϕ (Figure 10.7). The deficit in events at the top of the detector can be seen in the last plot to increase from the early to the late period in RunIIb4.

If the hypothesis that the difference between RunIIb3 and RunIIb4 is due to a "smearing" of events away from the peak is correct, this loss in resolution could be caused by the energy measurement, by the measurement of the direction, or both of these combined. However, it is also possible that it is due to an electron p_T-dependent inefficiency that is not (yet) modeled. This inefficiency could be due to the H-Matrix cluster identification,

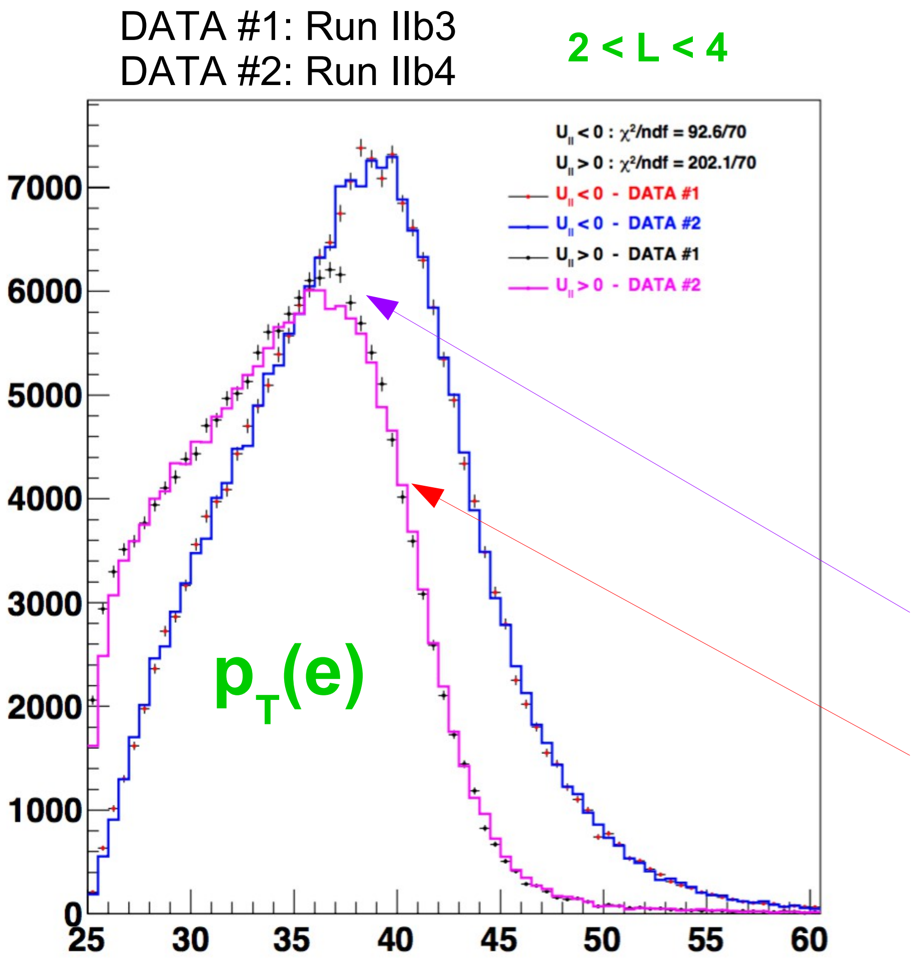

Figure 10.1: A close look at the electron p_T distribution, split into $u_\parallel > 0$ and $u_\parallel > 0$, and compared between RunIIb3 and RunIIb4. There is a disagreement in p_T between RunIIb3 and RunIIb4 when $u_\parallel > 0$ (black points vs. magenta line). The disagreement can also be seen in the m_T (left) and MET (right) distributions. Note there is also a mysterious disagreement at low p_T, which is visible in all InstLumi bins, and was originally thought to be caused by the trigger efficiency simulation, but this theory was disaffirmed by a close study of the trigger efficiencies, described in Section 7.2.1. NOTE: This figure is from a D0 internal presentation. At the time of writing, it has not been approved by the D0 collaboration for general public use beyond this dissertation.

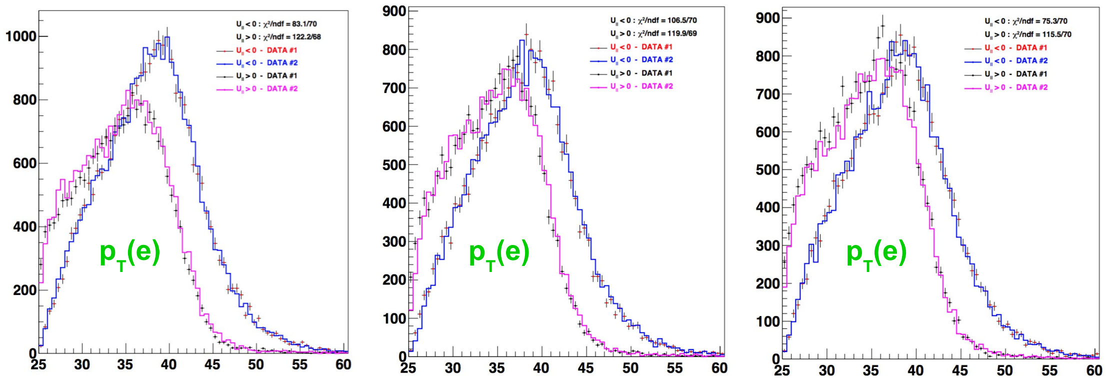

0 < electron phi < 0.785 0.785 < electron phi < 1.570 1.570 < electron phi < 2.355

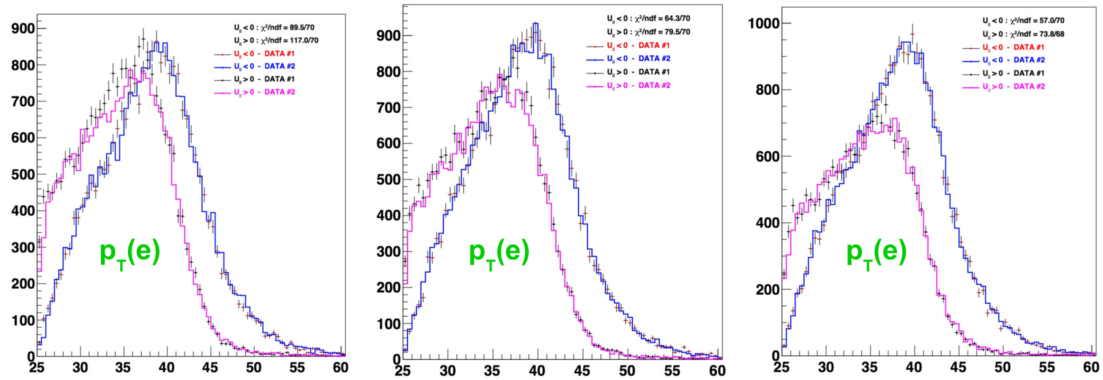

2.355 < electron phi < 3.140 3.140 < electron phi < 3.925 3.925 < electron phi < 4.710

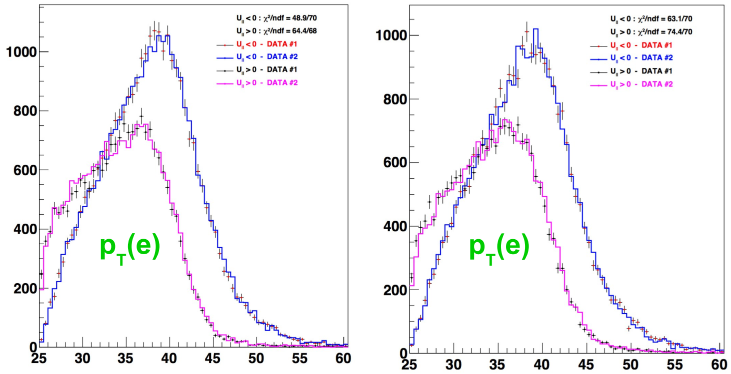

4.710 < electron phi < 5.495 5.495 < electron phi < 6.280

Figure 10.2: The electron p_T distribution, as in Figure 10.2, broken into ϕ bins. The second through fourth plots show the most disagreement between RunIIb3 and RunIIb4. NOTE: This figure is from a D0 internal presentation. At the time of writing, it has not been approved by the D0 collaboration for general public use beyond this dissertation.

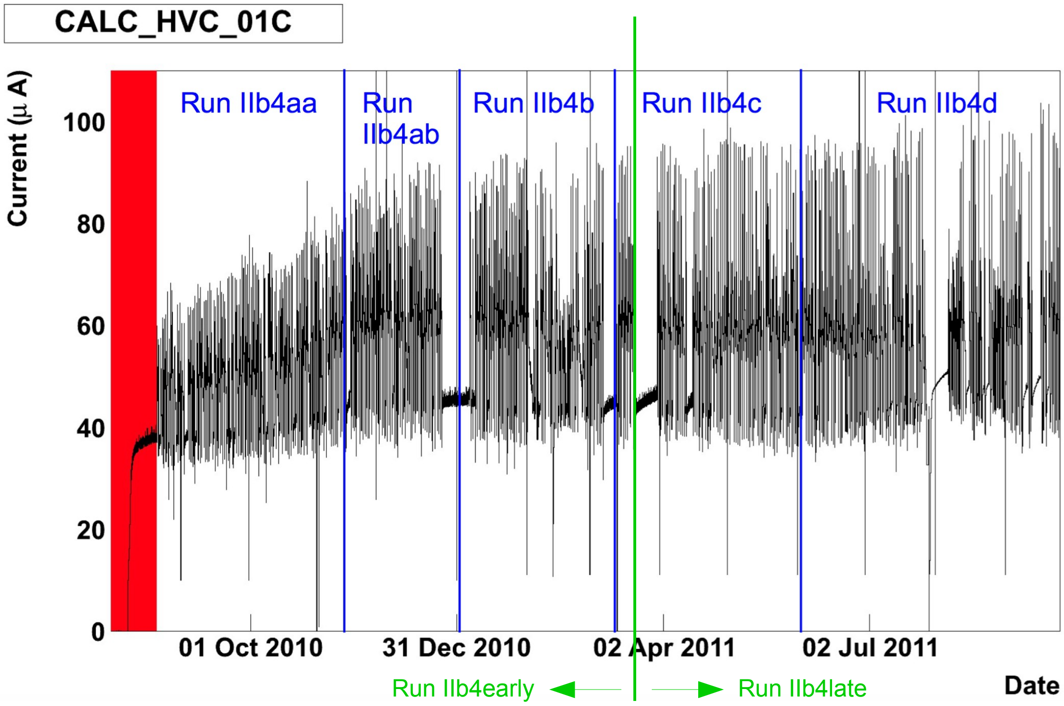

Figure 10.3: Illustration of the splitting of RunIIb4 into an "early" and a "late" data taking period, for the purposes of investigating the evolution of spectrum shapes over time. Evolution of the calorimeter currents over time are shown, but they are not relevant to the current discussion. NOTE: This figure is from a D0 internal presentation. At the time of writing, it has not been approved by the D0 collaboration for general public use beyond this dissertation.

a tracker inefficiency, or some track-matching based effect.[1] To try to pin down the cause of the discrepancy in the late RunIIb4 sample, we make comparisons again of the $p_T(e)$ distributions, but zoom a bit, and also look at the $E(e)$ distribution as well, still with

---

[1] Such an efficiency dependence could conceivably have been seen in the author's own studies in working towards the residual efficiency correction. However, those studies were done before the problem was well described. While the ratio between the data and FullMC efficiency was noisy, it did not show more obvious p_T dependence than in RunIIb12, when the dependence was considered unnecessary to model. Now that we know of the need to split RunIIb4 into early and late samples, and azimuthally, we may be able to more accurately describe the efficiency correction.

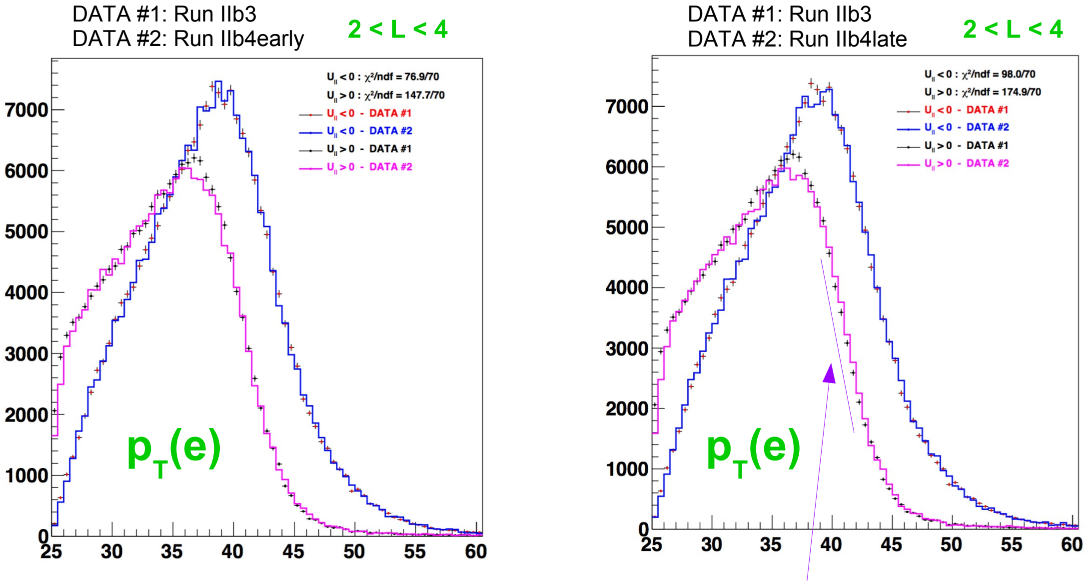

Figure 10.4: An enlarged view of the electron p_T distribution, split into $u_{\|} > 0$ and $u_{\|} > 0$, and compared between RunIIb3 and RunIIb4 early (left) and late (right). NOTE: This figure is from a D0 internal presentation. At the time of writing, it has not been approved by the D0 collaboration for general public use beyond this dissertation.

$u_{\|} > 0$, as seen in Figure 10.8. From the shape of the difference between RunIIb3 and RunIIb4 in the $E(e)$ distribution, we deduce that there is a slight energy shift. To get a better sense of the energy scale difference between the two samples, we compare the Z mass peaks, and see that there is a small scale difference, as indicated in the circled best fit values in Figure 10.9. Figure 10.10 shows the electron p_T and E distributions, as in Figure 10.8, but with the energy scale of RunIIb4 late scaled up to match RunIIb3. We see that there is still a problem with the p_T distribution, but the E distribution does not appear to have any problems, in particular, it does not appear more smeared in RunIIb4 late than in RunIIb3. Therefore, we conclude that the primary problem is that there is something wrong with the tracker measurements.

This is most likely due to failure of the tracker elements which increases during

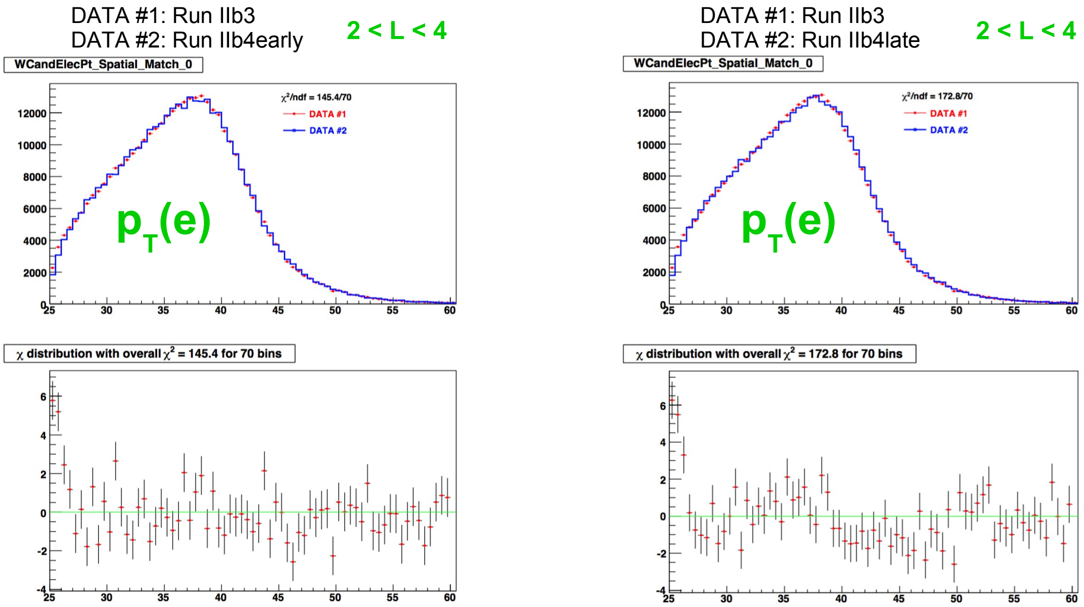

Figure 10.5: Comparison (top) and difference (bottom) plots of electron p_T between RunIIb3 and RunIIb4 early (left) and late (right), with combined $u_{\parallel} > 0$ and $u_{\parallel} < 0$ events. The discrepancy can still be seen, and it increases in the late RunIIb4 period. NOTE: This figure is from a D0 internal presentation. At the time of writing, it has not been approved by the D0 collaboration for general public use beyond this dissertation.

RunIIb4. This failure happens mostly in the upper portion of the tracker, which can be seen via the ϕ-dependent discrepancies seen in electron p_T, and which can also be seen in the recoil u_T measurements.

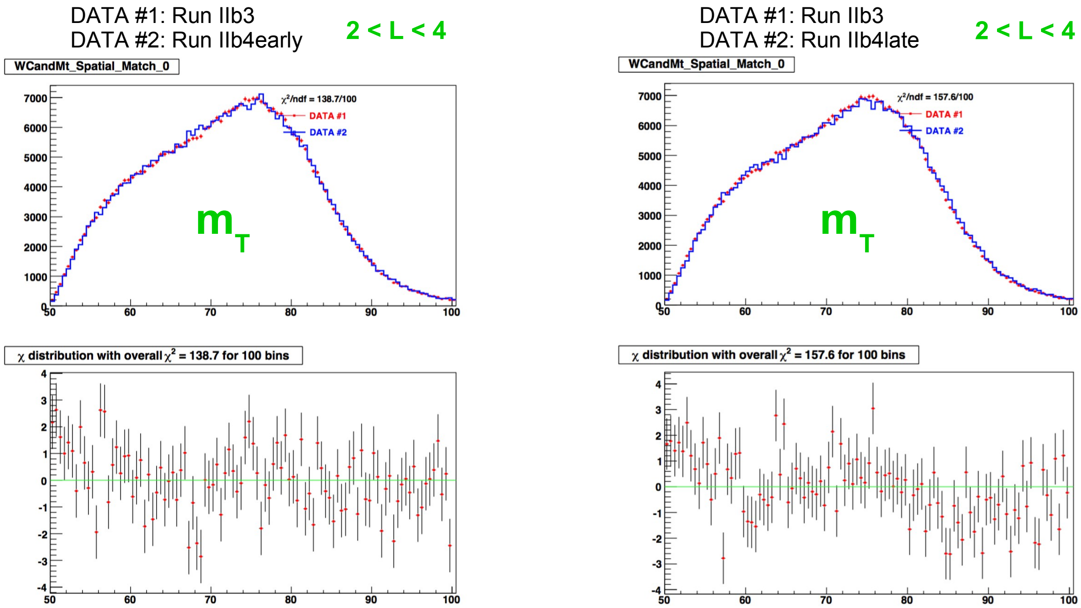

Figure 10.6: Comparison (top) and difference (bottom) plots of event m_T between RunIIb3 and RunIIb4 early (left) and late (right), with combined $u_\parallel > 0$ and $u_\parallel < 0$ events. The discrepancy can still be seen, and it increases in the late RunIIb4 period. NOTE: This figure is from a D0 internal presentation. At the time of writing, it has not been approved by the D0 collaboration for general public use beyond this dissertation.

There are three options to proceed:

- Measure the W mass only from RunIIb3 data (possibly including early RunIIb4 data).
- Attempt to account for the tracker failure in our simulation (with a combination of simulation and error estimation) and measure the W mass from both RunIIb3 and RunIIb4 data.
- Do not continue with the analysis.

Discussions as to which is the best option are ongoing at the time of writing.

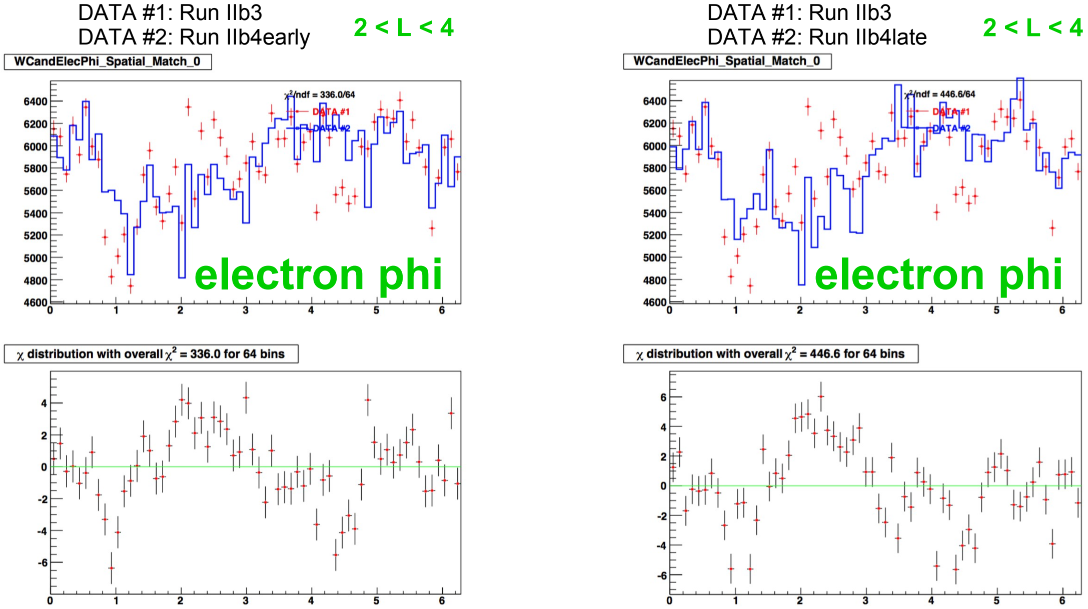

Figure 10.7: Comparison (top) and difference (bottom) plots of electron ϕ between RunIIb3 and RunIIb4 early (left) and late (right). NOTE: This figure is from a D0 internal presentation. At the time of writing, it has not been approved by the D0 collaboration for general public use beyond this dissertation.

10.3 Summary

A template method has been used with D0 detector data from RunIIb34 to measure the W boson mass based on distributions of three observables of the electron-neutrino decay channel: the electron transverse momentum, p_T^e, the W boson transverse mass, m_T, and the missing transverse energy corresponding to the neutrino transverse momentum, $\not{E}_T$. A parametrized Fast Monte Carlo simulation to match the Full Monte Carlo simulation has been created and verified by achieving Monte Carlo Closure. Progress has been made in tuning a parametrized Fast MC simulation to match the collider data, however, at the time of writing, we have not yet successfully achieved a W boson mass measurement from the collider data.

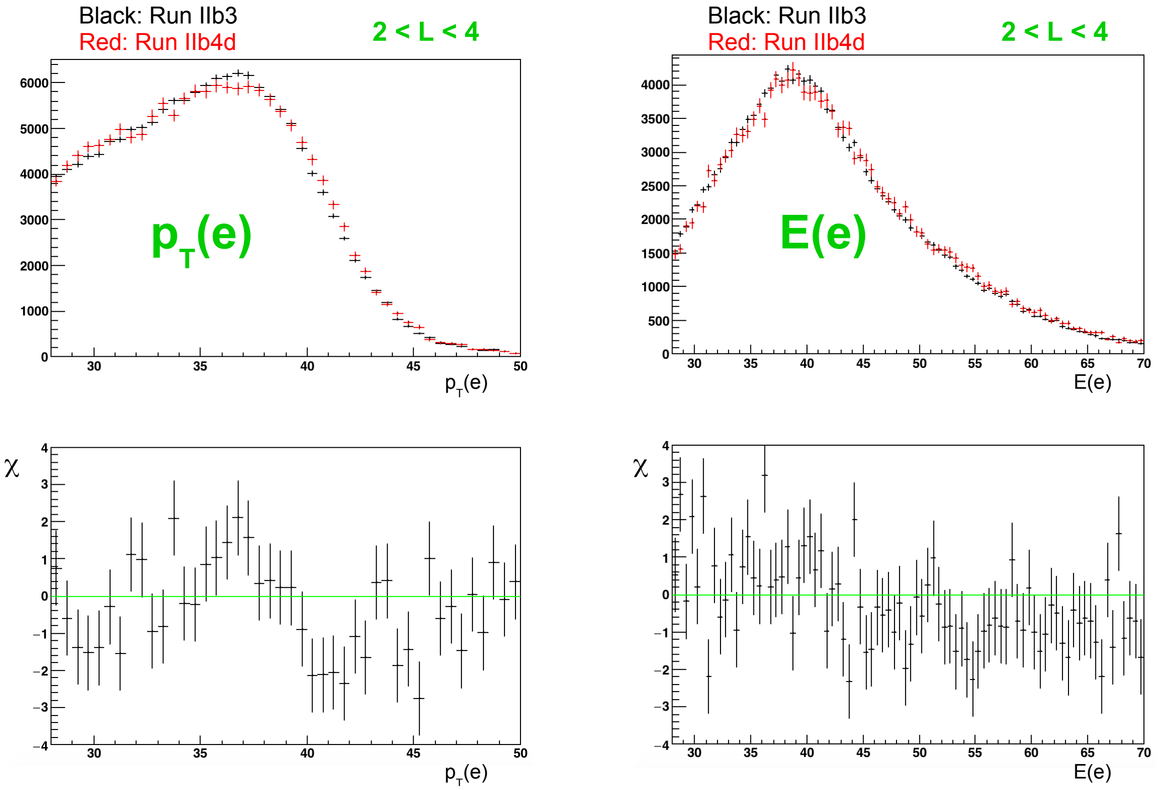

Figure 10.8: Comparison of the electron p_T (left) and E (right) distributions between RunIIb3 and RunIIb4 (late), all with $u_{\|} > 0$, without the scale correction from the $Z \rightarrow ee$ dilepton mass measurement applied. NOTE: This figure is from a D0 internal presentation. At the time of writing, it has not been approved by the D0 collaboration for general public use beyond this dissertation.

Source	m_T	p_T^e	$\not{E}_T$
Experimental:			
Electron Energy Scale	16	17	16
Electron Energy Resolution	2	2	3
Electron Shower Model	4	6	7
Electron Energy Loss	4	4	4
Recoil Model	5	6	14
Electron Efficiencies	1	3	5
Backgrounds	2	2	2
$\sum$ Experimental	18	20	24
W Production and Decay Model:			
PDF	11	11	14
QED	7	7	9
Boson p_T	2	5	2
$\sum$ Model	13	14	17
$\sum$ Systematic	22	24	29
Statistical	13	14	15
Total	26	28	33

Table 10.4: Contributions to the uncertainty in the RunIIb12 measurement[6].

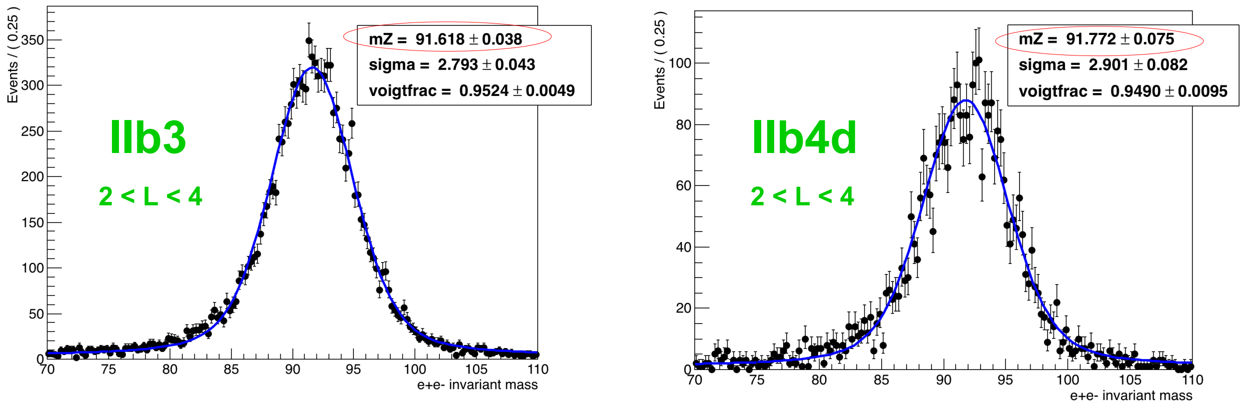

Figure 10.9: Fits to the invariant Z mass from the RunIIb3 (left) and RunIIb4 (right) $Z \rightarrow ee$ sample. A small difference in peak position between the two run periods can be seen. NOTE: This figure is from a D0 internal presentation. At the time of writing, it has not been approved by the D0 collaboration for general public use beyond this dissertation.

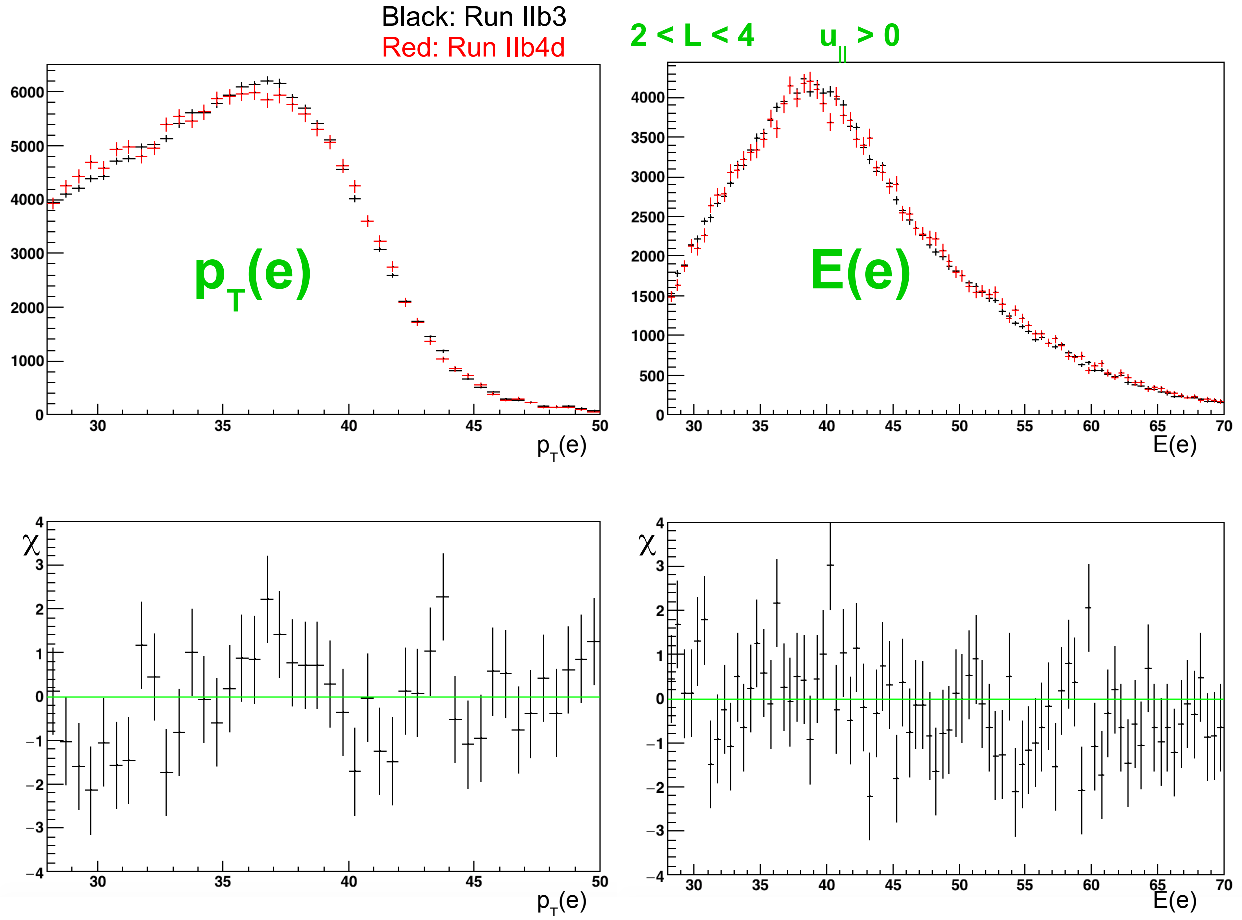

Figure 10.10: Comparison of the electron p_T (left) and E (right) distributions between RunIIb3 and RunIIb4 (late), all with $u_{\parallel} > 0$, with the scale correction from the $Z \rightarrow ee$ dilepton mass measurement applied. NOTE: This figure is from a D0 internal presentation. At the time of writing, it has not been approved by the D0 collaboration for general public use beyond this dissertation.

BIBLIOGRAPHY

[1] 2012 update of the combination of CDF and D0 results for the mass of the W boson. arXiv:1204.0042.

[2] Kernel density estimation. *Wikipedia*. available at `https://en.wikipedia.org/wiki/Kernel_density_estimation`.

[3] Precision electroweak measurements on the Z resonance. October 2005.

[4] T. Aaltonen et al. Precise measurement of the W boson mass with the CDF II detector. *Phys. Rev. Lett.*, 108:151803, 2012, arXiv:1203.0275.

[5] V. Abazov et al. The upgraded D0 detector. *Nucl. Instrum. Meth.*, A565:463537, 2006, arXiv:physics/0507191.

[6] V. M. Abazov et al. Measurement of the W boson mass with the D0 detector. *Phys. Rev. Lett.*, 108:151804, 2012, arXiv:1203.0293.

[7] V. M. Abazov et al. Measurement of the W boson mass with the D0 detector. *Phys. Rev. Lett.*, 108:151804, 2012, arXiv:1203.0293.

[8] G. Abbiendi et al. Measurement of the mass and width of the W boson. *Eur. Phys. J.*, C45:307335, 2006, arXiv:hep-ex/0508060.

[9] J. Abdallah et al. Measurement of the mass and width of the W boson in e^+e collisions at $\sqrt{s} = 161$ GeV to 209 GeV. *Eur. Phys. J.*, C55:138, 2008, arXiv:0803.2534.

[10] P. Achard et al. Measurement of the mass and the width of the W boson at LEP. *Eur. Phys. J.*, C45:569587, 2006, arXiv:hep-ex/0511049.

[11] C. Albajar et al. Studies of intermediate vector boson production and decay in UA1 at the CERN proton-antiproton collider. *Z. Phys.*, C44:1561, 1989.

[12] J. Alitti et al. An improved determination of the ratio of W and Z masses at the CERN pp collider. *Phys. Lett. B*, 276:354–364, 1992.

[13] T. Andeen. U-para efficiency. *D0 Internal Note*, 5686, February 2009.

[14] T. Andeen et al. Modeling the hadronic recoil for a precision measurement of the W mass in the RunIIa analysis at D0 (method I). *D0 Internal Note*, 5668, May 2008.

[15] T. Andeen et al. Fit for the electron response model. *D0 Internal Note*, 5662, March 2009.

[16] M. Awramik, M. Czakon, A. Freitas, and G. Weiglein. Precise prediction for the W boson mass in the Standard Model. *Phys. Rev.*, D69:053006, 2004. arXiv:hep-ph/0311148 [hep-ph].

[17] M. Baak et al. The electroweak fit of the Standard Model after the discovery of a new boson at the LHC. *Eur. Phys. J.*, C72:2205, 2012, arXiv:1209.2716.

[18] M. Begel, D. Edmunds, P. Laurens, and R. Partridge. D0 luminosity in RunII: Delivered. *D0 Internal Note*, 3970, March 2003.

[19] D. Boline et al. Measurement of the W boson mass using RunIIb (4.3fb^{-1}) data. *D0 Internal Note*, 6268, January 2012.

[20] D. Boline et al. W test mass measurement in full GEANT Monte Carlo in RunIIb34. *D0 Internal Note*, 6480, 2016.

[21] D. Boline et al. Measurement of the W boson mass in RunIIb3/4 data. *D0 Internal Note*, 6481, forthcoming.

[22] D. Boline and A. Melnitchouk. Background model for RunIIb W mass measurement. *D0 Internal Note*, 6084.

[23] J. Bystricky et al. Algorithms and architecture for the L1 calorimeter trigger at D0 RunIIb. *IEEE Trans. Nucl. Sci.*, 51:351355, 2004.

[24] B. Casey et al. The D0 RunIIb luminosity measurement. *Nucl. Instrum. Meth.*, A698:208223, 2013, arXiv:1204.0461.

[25] S. Chekanov et al. Measurement of high q^2 charged current cross-sections in e^- p deep inelastic scattering at HERA. *Phys. Lett.*, B539:197217, 2002, arXiv:hep-ex/0205091.

[26] J. Collins, D. E. Soper, and G. Sterman. Transverse momentum distribution in Drell-Yan pair and W and Z boson production. *Nucl. Phys. B*, 250:199–224, 1985. available at `http://www.sciencedirect.com/science/article/pii/0550321385904791`.

[27] K. S. Cranmer. Kernel estimation in high-energy physics. *Comput. Phys. Commun.*, 136:198, 2001, hep-ph/0005309 and hep-ex/0011057.

[28] J. Cuth and M. Schott. Estimation of theoretical QCD uncertainties for RunIIb34 W-mass measurement at D0. *D0 Internal Note*, November 2016. available at `https://indico.fnal.gov/getFile.py/access?contribId=1&resId=0&materialId=slides&confId=13358`.

[29] F. Fleuret. The D0 electron/photon analysis package EMAnalyze. *D0 Internal Note*, 3888, April 2001.

[30] F. Fleuret. The D0 soft electron reconstruction package SEMReco. *D0 Internal Note*, 3872, July 2001.

[31] A. Freitas, W. Hollik, W. Walter, and G. Weiglein. Electroweak two loop corrections to the W-Z mass correlation in the Standard Model. *Nucl. Phys.*, B632:189–218, 2002. arXiv:hep-ph/0202131 [hep-ph].

[32] F. Guo et al. Studies of energies below electron window for W mass measurement. *D0 Internal Note*, 5661, February 2009.

[33] J. Holzbauer. Recoil fit uncertainties, first pass. *D0 Internal Presentation*, January 2015. available at `https://indico.fnal.gov/getFile.py/access?contribId=2&resId=0&materialId=slides&confId=8555`.

[34] J. Holzbauer. Recoil fit uncertainties, revisited. *D0 Internal Presentation*, March 2015. available at `https://indico.fnal.gov/getFile.py/access?contribId=2&resId=0&materialId=slides&confId=9227`.

[35] F. Jegerlehner, M. Y. Kalmykov, and O. Veretin. MS versus pole masses of gauge bosons: Electroweak bosonic two loop corrections. *Nucl. Phys.*, B641:285326, 2002. arXiv:hep-ph/0105304 [hep-ph].

[36] F. Jegerlehner, M. Y. Kalmykov, and O. Veretin. MS versus pole masses of gauge bosons. 2. Two loop electroweak fermion corrections. *Nucl. Phys.*, B658:49112, 2003. arXiv:hep-ph/0212319 [hep-ph].

[37] J. Kraus. Stat uncertainty update. *D0 Internal Presentation*, July 2014. available at `https://indico.fnal.gov/getFile.py/access?contribId=2&resId=0&materialId=slides&confId=8527`.

[38] F. Landry, R. Brock, P. M. Nadolsky, and C.P. Yuan. Tevatron RunI Z boson data and Collins-Soper-Sterman resummation formalism. *Phys. Rev.*, D67:073016, 2003. arXiv:hep-ph/0212159 [hep-ph].

[39] H. Li. Higgs recoil mass and cross-section analysis at ILC and calibration of the CALICE SiW ECAL prototype (doctoral dissertation). LAL-09-118, October 2009.

[40] H. Li. Update again, dUPara model. *D0 Internal Presentation*, February 2011. available at `https://indico.fnal.gov/getFile.py/access?contribId=s1t1&resId=0&materialId=0&confId=D0_a11240`.

[41] H. Li and J. Stark. W mass measurement in full GEANT Monte Carlo in RunIIb. *D0 Internal Note*, 6266, February 2012.

[42] H. Li, J. Stark, and S. Yacoob. Electron window effect correction for the D0 RunIIb W mass measurement. *D0 Internal Note*, 6265, 2012.

[43] R. Lopes de Sá. Measurements of the W boson mass with the D0 detector (doctoral dissertation). August 2013.

[44] R. Lopes de Sá. About wzfitter and the statistical uncertainty in the D0 W mass measurement. *D0 Internal Presentation*, April 2014. available at `https://indico.fnal.gov/getFile.py/access?contribId=2&resId=1&materialId=slides&confId=7903`.

[45] W. Marciano and A. Sirlin. Radiative corrections to neutrino induced neutral current phenomena in the SU(2)×U(1) theory. *Phys. Rev.*, D22:2695, 1980.

[46] D0 W mass group. Measurement of the W boson mass using RunIIa data. *D0 Internal Note*, 5868, March 2009.

[47] M. Rominsky. Backgrounds. *D0 Internal Presentation*, March 2013. available at `https://indico.fnal.gov/getFile.py/access?contribId=0&resId=0&materialId=slides&confId=6453`.

[48] S. Schael et al. Measurement of the W boson mass and width in e^+e^- collisions at LEP. *Eur. Phys. J.*, C47:309335, 2006, arXiv:hep-ex/0605011.

[49] V. Shiltsev et al. Beam-beam effects in the Tevatron. *Phys. Rev. ST Accel. Beams 8*, page 101001, October 2005.

[50] V. Shiltsev et al. Experimental studies of compensation of beam-beam effects with Tevatron electron lenses. *New Journal of Physics*, April 2008. available at `https://arxiv.org/pdf/0802.0504.pdf`.

[51] A. Sirlin. Radiative corrections in the SU(2) × U(1) theory: A simple renormalization framework. *Phys. Rev.*, D22:971981, 1980.

[52] A. Sirlin and A. Ferroglia. Radiative corrections in precision electroweak physics: A historical perspective. *Rev. Mod. Phys.*, 85:263–297, February 2013. available at `http://link.aps.org/doi/10.1103/RevModPhys.85.263`.

[53] T. Sjstrand and M. V. Zijl. Multiple parton-parton interactions in an impact parameter picture. *Phys. Lett. B*, 188:149, 1987.

[54] J. Stark. Understanding and modelling the CAL energy resolution. *D0 Internal Presentation*, January 2006. available at `https://indico.fnal.gov/getFile.py/access?contribId=s1t0&resId=1&materialId=0&confId=D0_a0651`.

[55] S. Keller U. Baur and D. Wackeroth. A Monte Carlo program for the calculation of electroweak radiative corrections to W boson production at hadron colliders. available at `http://ubpheno.physics.buffalo.edu/~dow/wgrad.html`.

[56] S. Keller U. Baur and D. Wackeroth. Electroweak radiative corrections to W boson production in hadronic collisions. *Phys. Rev. D*, 59, 1999.

[57] Z.Q. Zhang. A determination of electroweak parameters at HERA. *PoS*, HEP2005:293, 2006.